

https://dspace.org/

Investigation of defects in diamond implanted with N-O molecular ions

Matindi, Tresor Balembo

2020
https://hdl.handle.net/10539/31608

Downloaded from a DSpace repository. https://dspace.org/

UNIVERSITY OF THE
WITWATERSRAND,
JOHANNESBURG



INVESTIGATION OF DEFECTS IN DIAMOND IMPLANTED WITH N-O MOLECULAR IONS

by

Tresor Balembo Matindi

Supervisor: Prof. S.R. Naidoo

Co-supervisor: Prof. O.M. Ntwaeaborwa

A thesis submitted to the Faculty of Science, in fulfilment of the requirements for the degree of Doctor of Philosophy.

University of the Witwatersrand, Johannesburg

December 2019

Declaration

I declare that this thesis is my own unaided work. It is being submitted for the Degree of Doctor of Philosophy at the University of the Witwatersrand, Johannesburg. It has not been submitted before for any degree or examination in any other University

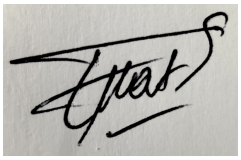

Tresor Balembo Matindi, 1138396

December 3, 2019

Abstract

The incorporation of shallow n-type dopants in diamond is one of the major challenges for its electronic applications. n-Type behavior in diamond has been observed for substitutional phosphorus and nitrogen, with activation energies of approximately 0.62 eV and 1.7 eV respectively. Both nitrogen and phosphorus are deep lying substitutional impurity states in diamond. It has been theoretically demonstrated that the substitution of the N-O molecule into the diamond lattice forms a stable defect in the band gap and in the negatively charged state induces a shallow defect below the conduction band edge which may lead to n-type conductivity.

In this project, surface characterization and optical spectroscopy were carried out to investigate the nature and behavior of the defects induced by the implantation of N-O ions into type IIa Chemical Vapor Deposition (CVD) diamond samples. Photoluminescence peaks attributed to N-O complexes were observed at 293.3 nm, 297.3 nm, 305.9 nm, 309.8 nm, 314.4 nm for the sample which was implanted with N-O molecular ions and annealed at 600 °C. The mechanism of electronic transitions leading to emission of photoluminescence of these peaks is proposed. In addition, a peak at 533 nm was observed on the cathodoluminescence spectrum of the same sample and was tentatively attributed to a radiative recombination of a shallow n-type defect and a deep lying p-type defect in the middle of the band gap, associated to vacancy-related states. The results presented extends the knowledge on defects leading to shallow n-type dopants in diamond. We believe that this thesis creates a paradigm for future studies on the search for alternative suitable shallow dopants, which is the sine qua non for potential application of diamond-based electronic devices.

Dedication

This is for you, BM. Thanks for always being there for me. And for El elyon-elyora "la source de ma force et de mon inspiration"..

Acknowledgements

Through this intense, sometimes painful, but constantly rewarding experience that is a doctoral thesis, a multitude of meetings made possible the completion of this vast project, from long hours to too short years tirelessly spent living "diamond" .... My sincere thanks to all those who contributed towards making this project a success.

Thanks be to the almighty God for making this happen and giving me the strength to keep going. It would have not been possible without you.

A special acknowledgment goes to the DST/NRF Centre of Excellence in Strong Materials (COE) for the financial support throughout my studies. I owe gratitude and so much more.

My sincere heart felt thank you to my supervisor Prof S.R. Naidoo, my co-supervisor Prof M. Ntwaeaborwa. I simply could not have done it without you. Thank you for taking your the time to share the wisdom and for your continued support. You have been more than supervisors to me. You have been mentors.

I would also like to thank all staff members in the school of Physics, especially, Dr R. Erasmus and Prof D.Wamwangi, I am grateful for everything that I have learned from you.

I also want to thank Prof A. Strydom (University of Johannesburg) for his help regarding electrical measurement, Prof L. Coetsee-Hugo (University of the Free State) for the XPS measurements and Prof T. Kroon (University of the Free State) for the Cathodoluminescence measurements. I felt most prepared to tackle the unknown physics problems when I knew I was going to get assistance from you.

To my colleagues, friends and all postgraduate students at the school of physics, I was blessed to

work with a team of ambitious people who continuously strived for excellence and maintaining a positive working environment. I have learned a lot from your wealth of experience. Thank you for your support and friendship.

To my parents, Joseph and Marceline Matindi, everything I am today and all I might become tomorrow, is all for the sacrifices you have made. I am the person I am today because of you both and for that I will forever be grateful. To my brothers and sisters, you have always been the inspiration behind my endeavors.

Contents

1 Introduction and aims **1**

1.1 Introduction 1

1.2 Aims 2

1.3 Outline of thesis 3

2 Diamond **5**

2.1 Carbon hybridization and allotropes 5

2.2 Diamond 7

2.2.1 Properties of diamond and its applications 8

2.3 Production of Synthetic Diamond 13

2.3.1 High-Pressure High-Temperature (HPHT) diamonds 13

2.3.2 Chemical vapour deposition (CVD) diamonds 14

2.4 Classification of Diamonds 16

2.4.1 Type I diamonds 17

2.4.2 Type II diamonds 18

2.5 Doping of Diamond 19

2.5.1 Impurities in diamond 19

2.5.2 Doping techniques 22

3 Defects in Diamond **25**

3.1 Defects in a diamond crystal 25

3.1.1 Ideal crystal 25

3.1.2 Defects in the real crystal 27

3.2 Luminescent defects in diamond 31

3.2.1 Nitrogen defects 31

3.2.2 Carbon defects 39

3.2.3 Boron defect 41

3.2.4 Hydrogen defect 41

3.2.5 Oxygen defects in diamond 42

3.3 Background on N-O complex in diamond 46

4 The Physics of ion implantation **49**

4.1 Principle of doping by ion implantation 49

4.2 Advantages and disadvantages of ion implantation techniques 52

4.3 Stopping power 53

4.3.1 Atomic displacements 56

4.3.2 The stopping range 58

4.4 Defects caused by ion implantation 60

4.5 Simulation 61

4.6 Post-implantation thermal annealing 63

4.6.1 Isothermal annealing 63
4.7 Channeling 64

5 Experimental and characterization techniques 66

5.1 Sample preparation 66
5.2 Ion implantation 67
5.3 Radio frequency (RF) furnace 69
5.4 Surface characterizations 70
5.4.1 Scanning electron microscopy 70
5.4.2 X-ray photoelectron spectroscopy 71
5.5 Optical spectroscopy 78
5.5.1 Raman spectroscopy 79
5.5.2 Absorption spectroscopy 85
5.5.3 Fourier-transform infrared spectroscopy 87
5.5.4 Photoluminescence spectroscopy 91
5.5.5 Cathodoluminescence 94

6 Results 96

6.1 Simulation of damage caused by ion implantation 96
6.2 Surface morphology 99
6.3 XPS analysis 101

6.3.1 Analysis of survey spectrum . . . 101
6.3.2 XPS high resolution spectra . . . 103
6.4 Raman measurements . . . 115
6.5 UV-visible absorption measurements . . . 119
6.6 Fourier-transform infrared spectroscopy measurements . . . 121
6.7 Photoluminescence measurements . . . 126
6.7.1 Room temperature photoluminescence measurements obtained with 248 nm excitation wavelength . . . 126
6.7.2 Low temperature photoluminescence measurements obtained with 248 nm excitation wavelength . . . 129
6.7.3 Low temperature photoluminescence measurements obtained with 458 nm excitation wavelength . . . 142
6.7.4 Low temperature photoluminescence measurements obtained with 514.5 nm excitation wavelength . . . 145
6.7.5 Proposed mechanism of electronic transitions leading to PL emission of N-O . . . 150
6.8 Cathodoluminescence (CL) measurements . . . 152

7 Conclusion **157**

7.1 Summary . . . 157
7.2 Conclusion . . . 159
7.3 Future work . . . 160

A Room temperature photoluminescence measurements obtained with 458 nm excitation wavelength **161**

B Room temperature photoluminescence measurements obtained with 514 nm excitation wavelength **164**

References **194**

List of Figures

2.1 Hybrid orbitals of carbon: (a) three hybridizations sp, (b) sp^2 and (c) sp^3 [21] . 6

2.2 Diamond structure. 7

2.3 Representation of hexagonal structure of lonsdaleite. 8

2.4 (a) Schematic representation of a hydraulic press for diamond synthesis by HPHT method. (b) Description of different components of a hydraulic press. 14

2.5 Carbon phase diagram [58]. 15

3.1 Energy band diagram of a an ideal crystal. 26

3.2 Illustration of different point defects in a crystal lattice. (a) vacancy defect,(b) self-interstitial defect, (c) interstitial and substitutional impurity atoms [104]. . . 28

3.3 Illustration of association of point defects in a crystal. (a) Schottky defect and (b) Frenkel defect [105]. 29

3.4 Band diagram of a real crystal showing the hole and electron traps as well as the recombination centers. 30

3.5 Infrared spectrum of type IaA diamond showing the presence of isolated substitutional nitrogen atoms (C centre) with peaks at 1130 and 1344 cm^{-1} [113]. . . . 32

3.6 Infrared spectrum of type IaA diamond showing the A centre signature peaks at 1212 and 1282 cm^{-1} [113]. 33

3.7 Infrared spectrum of type IaB diamond showing the B centre signature peaks at 1010,1096, 1180 and 1332 cm^{-1} [113]. 34

3.8 Typical photoluminescence spectra of 389 nm centre taken at low and room temperature (bold line) from as-irradiated CVD diamond [125]. 36

3.9 Illustration of NV centre in a diamond crystal lattice. (a) Neutral form of NV centre and (b) negatively charged state of NV centre [125]. 38

3.10 Typical CL spectra of 5RL centre recorded at liquid nitrogen temperature of as-irradiated CVD diamond film and single crystal diamond HPHT diamond. The 175, 193 and 237 meV are the three local vibrational modes [106]. 40

3.11 (a) Geometry of different charge states of substitutional oxygen defect (b) Symmetry and varous charge transition levels of substitution oxygen defects [141] . . 44

3.12 Defect related band structure of different charged froms of the nearest substitutional pair of N-O in diamond [11]. This figure shows the occupied shallow level which is less than 0.3 eV below the conduction band. 46

4.1 Diagram showing the interaction processes of the implanted ions with the target material [149]. 50

4.2 Typical diagram of an ion implanter [150]. 52

4.3 Schematic illustration of a collision between a projectile of mass M_1 and a target atom of mass M_2 54

4.4 Schematic illustration of (a) non-local electronic stopping power and (b) local electronic stopping power. 55

4.5 Representation of different displacements of atoms of the host material upon ion implantation [160]. 57

4.6 Transport of ions in matter (TRIM [97]) simulation showing the distribution of defects and implanted ions as a function of depth. TRIM simulation for 9 keV C^+ ion implantation in diamond 61

4.7 Schematic describing the evolution of the in-depth distribution of defects, implanted impurities and impurities on substitutional sites [160]. 64

4.8 Schematic describing the tilt and twist angles used during the implantation in order to limit the channeling phenomenon [167]. 65

5.1 Picture of the 200-20A2F ion implanter (iThemba LABS, Gauteng). 68

5.2 Image of RF furnace used for annealing. 70

5.3 Illustration of the photoelectric process [174] 72

5.4 (a) Evolution of the binding energies of the 1s carbon peak for graphite, PECVD diamond film and DLC films obtained at different laser intensities,(b) XPS deconvolution of carbon peak C1s of a DLC film deposited a 7.1×10^8 and 0.9×10^8 W·cm^{-2} [183] 76

5.5 Diagrammatic illustration of absorption and emission of a photon by an atom or a molecule. 78

5.6 Typical Raman spectrum of diamond excited at 228.9 nm at room temperature showing first, second and third order Raman peaks [106]. 83

5.7 Optical path diagram showing the light path permutations of the Jobin-Yvon T64000 model spectrometer (T64000 User manual October 2009) 85

5.8 Diagrammatic illustration of principle of absorption methods. 86

5.9 Illustration of a dual-beam UV-vis spectrophotometer. 87

5.10 Typical IR absorption spectra of different types of diamond films. (a) Type Ia and Ib diamonds samples, showing nitrogen related features. (b) Type IIa and IIb diamond samples, showing boron related features. Image courtesy: Magilabs Oy [196]. 89

5.11 Schematic diagram of an FTIR spectrometer 90

5.12 Different recombination processes in a semiconductor. 92

5.13 Photoluminescence scheme of (a) direct band gap semiconductor ,(b) an indirect band gap semiconductor. (Shaded areas indicate states that are occupied by electrons) [198]. 93

6.1 SRIM simulation showing the damage and N-O ion distribution profiles in diamond irradiated with 9 keV N^+ and O^+ ions. The damage peak is estimated at a depth of 8 nm while the ion distribution peak is approximately 13.2 nm from the sample surface. For a fluence of 1×10^{16} ions/cm^2 the simulated vacancy density is $\sim 2.4 \times 10^{23}$ vac/cm^3 at the surface of the diamond and this far exceeds the critical simulated damage density (amorphization threshold) of $5-9\times10^{22}$ vac/cm^3. 97

6.2 SEM images of (a) the unimplanted sample, (b) N-O implanted sample, (c) annealed carbon implanted sample and (d) N-O implanted and annealed sample. . 100

6.3 Wide-scan survey XPS of (a) unimplanted sample, (b) N-O implanted sample and (c) N-O implanted and annealed sample before (blue) and after (red) sputtering. 102

6.4 High resolution XPS spectra on C1s for (a) unimplanted sample, (b) N-O implanted sample and (c) N-O implanted and annealed sample recorded before the removal of air contaminant by argon etching. 107

6.5 High resolution XPS spectra of C1s on (a) unimplanted sample, (b) N-O implanted sample and (c) annealed N-O implanted sample recorded after the removal of air contaminants by argon etching. 109

6.6 XPS spectra of O1s on N-O implanted and annealed sample (a) before argon etching and (b) after argon etching. 111

6.7 XPS spectra of O1s on N-O implanted sample (a) before argon etching and (b) after argon etching. 112

6.8 (a) O1s XPS spectra of N-O implanted before argon etching and (b) after argon etching. 114

6.9 Raman spectra of (a) unimplanted sample, (b) N-O implanted sample, (c) N-O implanted and annealed sample and (d) carbon implanted sample recorded at room temperature with 514.5 nm excitation wavelength. The first order Raman peak at 1332 cm^{-1} is observed in all the samples. The N-O implanted sample shows the 1332 cm^{-1} diamond Raman peak on a broad Raman band starting at 1150 cm^{-1} and peaking at 1520 cm^{-1}. This is observed for high fluence ion implantation and the radiation damage is associated with amorphous carbon with a D band ($\sim 1350 cm^{-1}$) and G-band ($\sim 1500 - 1600$ cm^{-1}). The G mode arises from stretching from any pair of sp^2 sites from rings and chains, while the D mode is assigned to the breathing mode from sp^2 bonds in rings [98] 117

6.10 Raman spectrum of N-O implanted and annealed sample recorded at room temperature with 458 nm excitation wavelength. Peak at 1332 cm^{-1} is the first order Raman peak of diamond. Peaks observed previously at 728.5 and 1708.3 cm^{-1} on this sample while excited at 514.5 nm are not present anymore. However, new peaks can be observed at 478 and 1434 cm^{-1} and they are from photoluminescence lines. 118

6.11 Absorption spectra of unimplanted, N-O implanted, N-O implanted annealed, carbon implanted samples in the range of 200 to 800 nm. These spectra show the intrinsic absorption edge of diamond at 223 nm (5.5 eV). 120

6.12 Absorption spectra of unimplanted, N-O implanted, N-O implanted annealed and carbon implanted samples in the range of 750 to 2500 nm. 121

6.13 FTIR absorption spectrum of (a) unimplanted, (b) N-O implanted, (c) N-O implanted and annealed and (d) carbon implanted samples. 123

6.14 Expanded view of the FTIR spectra in the one-phonon absorption region, for (a) unimplanted, (b) N-O implanted, (c) N-O implanted and annealed and (d) carbon implanted samples. 124

6.15 Expanded view of the FTIR spectra in the three-phonon absorption region, for (a) unimplanted, (b) N-O implanted, (c) N-O implanted and annealed and (d) carbon implanted samples. 125

6.16 Typical PL spectra of (a) unimplanted sample, (b) N-O implanted sample, (c) annealed N-O implanted sample and (d) carbon implanted sample in the range 260 to 750 nm. These spectra were recorded at room temperature using 248 nm for excitation. All the spectra were normalized with the first order Raman peak at 251 nm. 128

6.17 Comparison of PL spectra of unimplanted sample (spectrum A), carbon implanted sample (spectrum B), N-O implanted sample (spectrum C) and annealed N-O implanted sample (spectrum D). These spectra were recorded at room temperature using 248 nm for excitation. The spectra are vertically offset for more convenience and were normalized with the first order Raman peak at 251 nm. 129

6.18 The typical PL spectra (262-335 nm) of (a) annealed unimplanted sample, (b) N-O implanted sample, (c) annealed N-O implanted sample and (d) annealed carbon implanted sample. These spectra were recorded at 77 K using 248 nm for excitation. All the spectra were normalized with the first order Raman peak at 251 nm 131

6.19 Comparison of PL spectra (262-335 nm) of annealed unimplanted sample (spectrum A), annealed carbon implanted sample (spectrum B), N-O implanted sample (spectrum C) and annealed N-O implanted sample (spectrum D). These spectra were recorded at 77 K using 248 nm for excitation. The spectra are vertically offset for convenience and were normalized to the first order Raman peak at 251 nm. Peaks at 293.3 nm, 297.3 nm, 305.9 nm, 309.9 nm and 314.2 nm are only present in the N-O implanted and annealed sample. 132

6.20 PL spectra (262-335 nm) of annealed N-O implanted sample (spectrum D), annealed oxygen implanted sample (spectrum E) and annealed nitrogen implanted sample (spectrum F). These spectra were recorded at 77 K using 248 nm for excitation. The spectra are arranged vertically for easy comparison and were normalized to the first order Raman peak at 251 nm. Peaks at 293.3 nm, 297.3 nm, 305.9 nm, 309.8 nm, and 314.4 nm do not appear in either the oxygen implanted sample or the nitrogen implanted sample. 135

6.21 Typical photoluminescence spectra (335-450 nm) of (a) unimplanted sample and (b) N-O implanted sample, obtained at 77 K using 248 nm laser excitation. The spectra were normalized with the first order Raman peak at 251 nm. 136

6.22 Typical photoluminescence spectra (335-450 nm) of (a) annealed N-O implanted sample, (b) annealed carbon implanted sample, (c) annealed nitrogen implanted sample and (d) annealed oxygen implanted sample, obtained at 77 K using 248 nm laser excitation. All the spectra were normalized to the first order Raman peak at 251 nm. 137

6.23 Photoluminescence spectra (450-650 nm) of (a) the annealed unimplanted sample and (b) N-O implanted sample obtained at 77 K using 248 nm laser excitation. . 138

6.24 Photoluminescence spectra (450-650 nm) of (a) the annealed N-O implanted sample, (b) annealed carbon implanted sample, (c) annealed nitrogen implanted sample and (d) annealed oxygen implanted sample, obtained at 77 K using 248 nm laser excitation. 140

6.25 (a) Comparison of photoluminescence spectra (450-650 nm) of N-O implanted and annealed (spectrum D), annealed carbon implanted sample (spectrum B), annealed oxygen implanted sample (spectrum E) and annealed nitrogen implanted sample (spectrum F) obtained at 77 K using 248 nm laser excitation. The inset shows the peak at 556.7 nm, which is only present in the annealed N-O implanted sample. (b) PL spectra of annealed unimplanted sample (spectrum A), N-O implanted sample(spectrum C) and annealed N-O implanted sample (spectrum D). 141

6.26 Typical 77 K PL spectra of (a) the unimplanted sample before annealing and (b) N-O implanted sample, recorded under 458 nm excitation. 143

6.27 Typical 77K PL spectra of (a) annealed N-O implanted sample, (b) carbon implanted sample before annealing, (c) unimplanted sample after annealing and (d) annealed carbon implanted sample, recorded under 458 nm excitation. 144

6.28 Comparison of PL spectra of unimplanted sample before annealing (spectrum A),carbon implanted sample before annealed (spectrum B), N-O implanted sample (spectrum C), annealed N-O implanted sample (spectrum D), annealed carbon implanted sample (spectrum G) and annealed unimplanted sample (spectrum H) obtained with 458 nm excitation wavelength in the range of 460 to 510 nm. All the spectra were normalized with the first order Raman peak at 487 nm 145

6.29 Typical 77 K PL spectra of unimplanted sample before annealing (a) and N-O implanted sample (b) recorded under 514.5 nm excitation. 147

6.31 Comparison of the PL spectra at 77 K of (A) unimplanted sample before annealing, (G) carbon implanted sample after annealing, (H) unimplanted sample after annealing, (D) annealed N-O implanted sample obtained at 77 K with 514.5 nm excitation wavelength in the range of 560 to 620 nm. This figure shows a pair of lines at 596.5 and 597.1 nm in all the spectra and a peak at 579.3 only present in the N-O implanted and annealed sample. All the spectra were normalized to the first order Raman peak at 552 nm. 147

6.30 Typical 77 K PL spectra of (a) annealed N-O implanted sample , carbon implanted sample before annealing (b), unimplanted sample after annealing (c) and carbon implanted sample after annealing (d) recorded under 514.5 nm excitation. 148

6.32 Schematic diagram of energy levels of N-O centre corresponding to photoluminescence spectra. 151

6.33 CL spectra of (a) unimplanted sample,(b) N-O implanted sample, (c) annealed N-O implanted sample and (d) carbon implanted sample, recorded at room temperature with the acceleration voltage set at 10 kV for all the measurements. . . 154

6.34 Deconvolution of the CL spectrum of the annealed N-O implanted sample, showing different components of the 533 nm feature. 156

6.35 (a) Comparison of CL spectra of (A) unimplanted sample, (B) Carbon implanted sample, (C) N-O implanted sample and (D) annealed N-O implanted sample. The spectra are vertically offset for more convenience. (b) Comparison of the intensities of CL spectra of unimplanted sample, N-O implanted sample and annealed N-O implanted sample. 156

A.1 Typical PL spectra of (a) unimplanted sample, (b) N-O implanted sample, (c) annealed N-O implanted sample and (d) carbon implanted sample in the range 460 to 700 nm. These spectra were recorded at room temperature using 458 nm for excitation. All the spectra were normalized with the first order Raman peak at 487 nm 162

A.2 Comparison of PL spectra of unimplanted sample (spectrum A), carbon implanted sample (spectrum B), N-O implanted sample (spectrum C) and annealed N-O implanted sample (spectrum D). These spectra were recorded at room temperature using 458 nm for excitation. The spectra are vertically offset for more convenience and were normalized with the first order Raman peak at 487 nm. 163

B.1 Typical PL spectra of (a) the unimplanted sample, (b) N-O implanted sample, (c) annealed N-O implanted sample and (d) carbon implanted sample. recorded under 514 nm excitation. All the spectra were normalized with the first order Raman peak at 552 nm. The inset shows peak at 577 nm and 579 nm. 165

List of Tables

2.1 General characteristics of diamond and silicon [20] 9

3.1 Different positions of oxygen defect energy levels in the band gap, calculated with an energy gap at 4.5 eV [3]. 43

3.2 Agregation energies for various charge states of the N-O defect in diamond. The values presented in this table have to be treated with some care as the band gap used for the calculation is 4.5 eV compared to the experimental value which is 5.47 eV. [11]. 47

5.1 Binding energy of the 1s peak of nitrogen for different bonds. 77

6.1 Implantations parameter 99

6.2 Atomic concentrations of elements on the surface of the samples before and after sputtering 104

6.3 Characteristics of the C1s peak components for the samples under investigation recorded before argon etched 106

6.4 Characteristics of the C1s peak components for the samples under investigation recorded after argon etched 110

6.5 Characteristics of the O1s peak components for the N-O implanted sample before and after argon etching 113

6.6 Characteristics of the N1s peak components for the N-O implanted sample after argon etching 115

6.7 Summary of defects observed from FTIR measurements. 125

6.8 Summary of defects observed from CL and PL measurements. 149

1. Introduction and aims

1.1 Introduction

Since their appearance in the 1960s, the performance of semiconductor-based electronic devices has been greatly improved and their complexity has increased. Currently, 95% of electronic devices are based on silicon technology [1]. However, the growing needs in the field of energy, transport and communications require the use of new materials that can withstand higher power and operate at higher frequencies. Diamond is the most suitable material for such purposes. Indeed, besides the fact that it is a gemstone of commercial value in the jewelery market, diamond is a material with a very high technological potential because of its extreme mechanical, thermal and electronic properties.

Impurities in diamond have been generating research interest due to their potential application in diamond-based electronic devices. Manufacturing diamond-based electronic devices is possible, for the reason that p-type and n-type donors do exist as substitutional impurities as they do for silicon. Many studies have demonstrated that nitrogen and boron form substitutional dopants in diamonds [2–6]. As a substitutional defect, boron gives an acceptor level at 0.37 eV above the valance band edge [7–10]. While nitrogen forms a deep donor level at 1.7 eV below the conduction-band edge [3, 11, 12] and it is not an effective n-type dopant in diamond [11, 12]. Among the attempts to achieve n-type doping in diamond, the incorporation of phosphorus via homoepitaxial growth has led to the n-type behaviour in diamond [13, 14]. Its activation energy is approximately 0.61 eV, which is still relatively high for room-temperature applications [8, 9, 15]. However, early work has suggested that oxygen could lead to n-type conductivity in diamond [15]. Electronic structure calculations [3] predict that defect levels related to oxygen are deep lying states. Alternatively, considering the significance of nitrogen in diamond, Lowther [11] reported that the formation of a suitable n-type conductivity could largely depend on nitrogen, given that

nitrogen is responsible for raising the effective Fermi energy in the band gap in diamond [11]. The theoretical work of Lowther [11] on the substitutional oxygen-nitrogen pair in diamond showed that N-O defects are stable in diamond, and in the negatively charged form they exhibit a shallow n-type defect behavior. Eyre et al. [16] also analyzed N-O pairs in diamond and found that the pair prefers nearest-neighbor sites and forms a deep donor in diamond. The N-O pair has been suggested to be responsible for two paramagnetic resonance centers labelled N3 and Ok1, with N3 as the first nearest neighbour to the N-O pair [17] while Ok1 is the second nearest neighbour to the pair [18].

The foregoing makes relevant the necessity of exploring and conducting an experimental investigation on the interaction between nitrogen and oxygen in diamond as well as related defects. This involves placing these atoms close to each other in the diamond lattice by means of the ion implantation, which has the advantage of providing greater accuracy of location and depth of ions in the host material.

1.2 Aims

This thesis was aimed at establishing if nitrogen and oxygen ions form molecular N-O complexes in diamond. This question has been addressed in this thesis by firstly creating a layer of higher density of N and O ions on the surface of the diamond sample. This was done by a choice of higher fluence and low energy used during the implantation. Optical and surface characterization techniques were then used to investigate the defects arising from implantation of N and O ions.

1.3 Outline of thesis

Chapter 2 presents a general introduction to diamond. After a brief description of carbon hybridization and allotropes as well as diamond structures, some of the properties of diamond with emphasis on its electronic properties are presented. Different modes of diamond synthesis and types of diamond were also examined. The final section focuses on the different modes of diamond doping, and in particular on the ion implantation technique used in our study.

Chapter 3 of this thesis is based on the study of defects in diamond. In the first part, several types of defects that often appear in the crystalline structure of diamond are presented. Knowledge of the defects is crucial for understanding many phenomena in a diamond crystal as most physical, chemical, optical and electronic properties depend on the position of the defects and the electronic and vibrational energy levels they create. Thereafter, the most common luminescence defects observed in chemical vapour deposition (CVD) diamond are reviewed. The last part of this chapter focuses on oxygen and nitrogen-oxygen complexes in diamond.

Chapter 4 discusses ion implantation, its advantages and disadvantages compared to diffusion doping methods. In addition, the generation of defects caused by ion implantation and how these defects can be annealed is discussed, including the activation and diffusion of implanted species.

In chapter 5, a description of the experimental techniques used in this study is presented. The theoretical principles of each characterization technique, especially in the context of their application to CVD diamond are presented.

Chapter 6 presents the results of analysis and research conducted in this study. The first part is a discussion of the results obtained from the stopping and range of ions in matter (SRIM) analysis, which is used to predict the damage caused by implantation and gives the distribution profile of the implanted N-O ions. Thereafter, the morphology of the samples obtained from scanning electron microscopy (SEM) analysis is presented. The electronic states and surface chemical

composition carried out by X-ray photoelectron spectroscopy (XPS) analysis is discussed. The results of Raman spectroscopy used to determine the crystalline quality and the study of sample amorphization by implantation is presented. Optical spectroscopy results (Photoluminescence and Cathodoluminescence) obtained at room and low temperature (77 K) using different excitation sources (248 nm, 458 nm and 514.5 nm) are included.

The conclusion of this thesis drawn from all the results obtained, and proposed extensions of this work are presented in chapter 7.

2. Diamond

If there is one single adjective that could describe the various properties of diamond as a material, it would be "exceptional". Exceptional properties that are related to this work will be discussed later in section 2.2. Additional information can be found in "The Properties of Natural and Synthetic Diamond" [19] and "Properties and Applications of Diamond" [20]. This chapter presents a review of carbon hybridization and allotropes, diamond structures as well as their intrinsics properties. The classification of diamond is discussed in term of its nitrogen content. A brief overview of diamond synthesis and how doping is achieved by ion implantation is given.

2.1 Carbon hybridization and allotropes

One of the most important chemical elements in nature is carbon. It plays an important role in the chemistry of life as it is present in the structures of living organisms and also in many things we use daily such as food, clothes, fuel, etc.

From an atomic point of view, the most stable form of carbon is carbon 12 (^{12}C) and it has six electrons. It has a ground state electron configuration of $1s^2\ 2s^2\ 2p^2$ or K^2L^4, meaning that there are four electrons at the $n = 2$ energy state, which is its highest energy level. The electrons of the upper shell ($2s$ and $2p$) are distributed on hybrid atomic orbitals called "sp" which combine the $2s$ and $2p$ orbitals. The electrons become unpaired, creating four chemical bonds which are called the sp^3 hybridized states. In the case of sp^3 hybridization, the four valence electrons are engaged in sp^3 hybrid orbitals directed along a tetrahedron and forming an angle of $109°28'$ to each other. The electrons can also hybridize the s and p orbitals and form hybridization states referred to as the sp and sp^2.

The sp^2 hybridized carbon has three valence electrons in sp^2 orbitals, at $120°$ from each other,

and an electron in a p orbital perpendicular to the sp^2 orbital plane. Finally, two sp orbitals at $180°$ to each other and two electrons in orthogonal p orbitals form the sp hybridization of carbon. Figure 2.1 shows different hybrid orbitals of carbon.

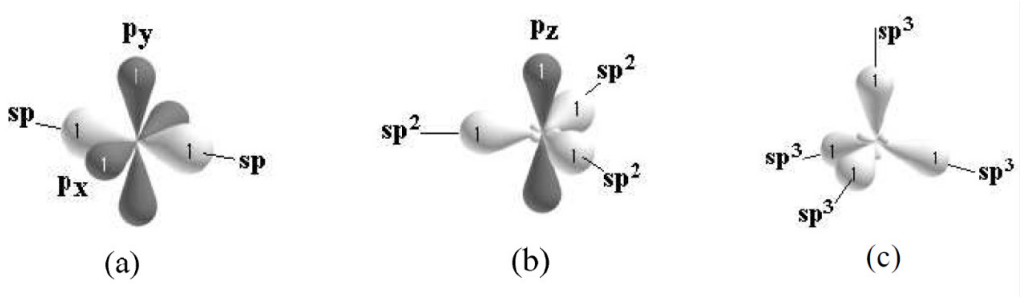

Figure 2.1 Hybrid orbitals of carbon: (a) three hybridizations sp, (b) sp^2 and (c) sp^3 [21]

The ability of carbon to form different types of covalent bonds such as sigma or pi-bonds allows it to generate structures of different dimensionality with a wide variety of physical and chemical properties [22–26]. The flexibility of forming such structures allows carbon to chemically bond in a range of ways. The ability to form such bonds is called catenation, which gives rise to large molecules, in particular the hydrocarbons.

Several carbon allotropes can be distinguished according to their hybridization. Thus, the three-dimensional connectivity of sp^3 carbon can give rise to the cubic structure of diamond, and also lonsdaleite 3-D hexagonal structure. The bonds between sp^2 hybridized carbons form planar structures whose stacking generates the structure of hexagonal or rhombohedral graphite. For the sp hybrid, the carbon can polymerize in linear form and give newly discovered compounds called carbyne. There are many other condensed forms where carbon atoms take intermediate degrees of hybridization sp^n and forms zero-dimensional solids (for instance the case of fullerenes and carbon nanotubes). Carbon also exists in the form of an amorphous or organized in short-distance, in which it is under several states of hybridization. This is the case of the so-called Diamond-Like Carbon (DLC).

2.2 Diamond

Diamond is a rare allotropic form of carbon found in nature. It consists of an assembly of carbon atoms in sp^3 hybridization, where each atom is bound to four carbon atoms by strong covalent σ-bonds. This three-dimensional assembly defines face-centered cubic lattices containing eight atoms, four of which are placed at the centres of four small cubes of volume equal to one-eighth of the primitive cell.

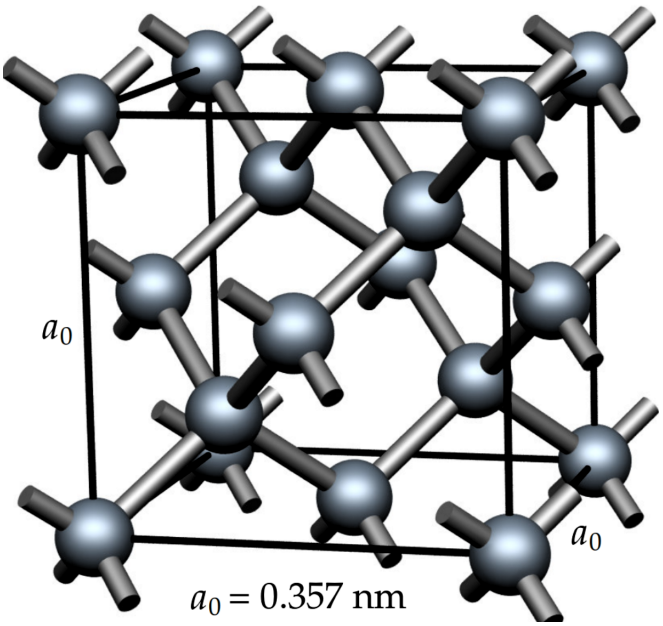

Figure 2.2 Diamond structure.

In a normal structure of diamond, the lattice parameter of the cubic unit cell is 0.357 nm. The shortest distance between two carbon atoms, i.e. the distance corresponding to a quarter of the diagonal of the lattice, is 0.154 nm. This makes the diamond crystal lattice very dense (1.76×10^{23} atoms.cm^{-3}) in comparison to other materials. The theoretical mass density for diamond is $\sim$ 3.515 g.cm^{-3}; it is obtained by the multiplication of the atomic density by the average atomic mass of a carbon. Figure 2.2 shows an illustration of diamond structure.

The hexagonal crystal structure of diamond, named lonsdaleite, is a rare polymorph of carbon [27], which was first synthesized in 1966 [28]. It was subsequently found in small quantities in meteorites [29, 30] or in diamond synthesized by shock waves of perfectly oriented graphite [31]. Figure 2.3 shows an illustration of hexagonal crystal structure of diamond.

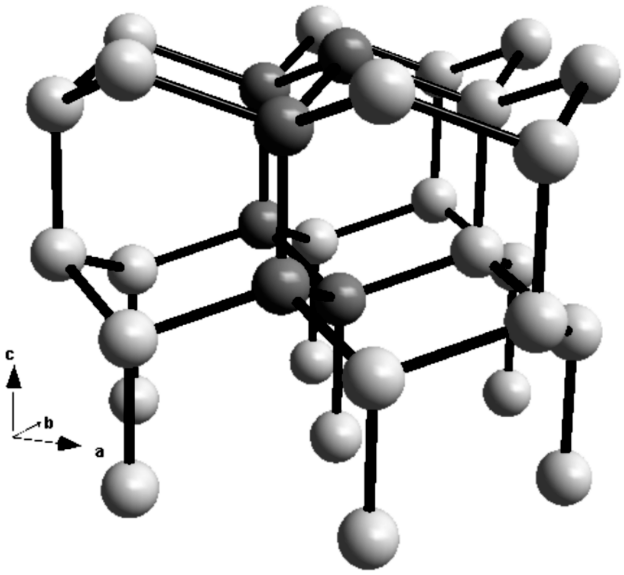

Figure 2.3 Representation of hexagonal structure of lonsdaleite.

2.2.1 Properties of diamond and its applications

Diamond is undoubtedly a material that combines an outstanding set of mechanical, chemical, thermal, acoustic, optical and electronic properties exceeding those of any other existing material. It offers a unique combination of properties such as high hardness, excellent thermal conductivity, chemical and thermal inertness, good abrasion resistance, transparency in a wide range of wavelengths, high electrical resistivity and semiconductor properties when doped. Table 2.1 summarizes the main properties of diamond that are compared to those of silicon, which is a semi-conductor with the same crystal structure as diamond and is widely used in electronics.

Table 2.1 General characteristics of diamond and silicon [20]

Property at 300 K	**Silicon**	**Diamond**
Atomic number Z	14	6
Crystal structure	Diamond cubic lattice	Diamond cubic lattice
Lattice parameter (nm)	0.543	0.357
Distance between nearest neighbor atoms (nm)	0.235	0.154
Number of atoms / unit vol. (10^{22}cm^{-3})	5.0	17.6
Density (g.cm^{-3})	2.33	3.515
Band gap (eV)	1.12	5.47
Melting point (K)	1688	4100
Thermal conductivity (W.cm^{-1}.K^{-1})	1.31	20-25
Refractive index	3.4-3.5	1.8-2.4
Relative dielectric constant	11	5.7
Intrinsic resistivity (Ω.cm)	3×10^5	$10^{12} - 10^{16}$
Saturation velocity ($\times 10^7$cm.s^{-1})	1.0	2.7
Coefficient of thermal expansion (K^{-1})	3×10^{-16}	2×10^{-16}

The fields of application of diamond are varied because of its many exceptional properties that make it an ideal material for many uses. Some of these properties and their application are summarized in sections 2.2.1.1 - 2.2.1.4 and two associated application highlighted in subsequent sections 2.2.1.5 and 2.2.1.6.

2.2.1.1 Mechanical properties

Diamond has a small inter-atomic distance, which gives it a high density of 3.515 g.cm^{-3} . This high density associated with its strong internal covalent bonds gives diamond a high hardness. Diamond has a deformation resistance of about 90 GPa. With a high resistance to abrasion and erosion, diamond is used as a tool for cutting and polishing. Natural diamond is not only used in jewelery but is mainly used for machining and polishing of hard materials (ceramics, alumina). Diamond coatings, even if their properties differ slightly from those of single crystal diamond, are also particularly well suited for many applications. In general, diamond coatings are used as protective layers, for example in chemical (valves subjected to very high temperatures) or energy (oil drilling) industries. They offer an excellent cutting efficiency, allow chip evacuation from the machined surface, increase the tool life (protection of the cutting surface) and can be used for the machining of various materials due to its chemical inertness. Diamond-coated knives are found in fields as diverse as metallurgy, surgery and the preparation of biological specimens [32].

It should be noted that the application of diamond in aggressive environments has a slight restriction on temperature of use, since diamond oxidizes in air at the temperatures greater than 900 K and turns into graphite around 1770 K under vacuum [33]. It is also chemically reactive with ferrous materials and is thus not suitable for machining iron based materials.

2.2.1.2 Optical properties

Due to its large band gap (5.47 eV at room temperature), high purity diamonds are transparent to a large part of the electromagnetic spectrum, particularly in the infrared (IR) and X-ray regions. This remarkable transparency allows diamond to be used as an optical window for high power lasers and optical fibers [33–35]. Diamond absorbs ultraviolet (UV) photons and the exploitation of this feature is the recent development of ultraviolet detectors for solar and space physics [36]. In addition, diamond is not always colorless, its color strongly depends on the impurities present. Infrared spectrometry measurements have made it possible to classify the different types of diamond [37, 38], as discussed in section 2.4.

2.2.1.3 Electronic properties

Pure diamond is an insulator with a high intrinsic resistivity even at high temperatures (between 10^{12} and 10^{16} Ω.cm) [39]. Its electrical resistance decreases rapidly with the presence of impurities and extended defects. The electronic characteristics of diamond are governed by doping impurities such as nitrogen, boron, phosphorus, and extended defects such as grain boundaries in the case of polycrystalline diamond [40]. The presence of impurites give diamonds the properties of n-type and p-type semiconductor materials. Due to its semi-conductive properties, it is possible to use diamond for innovative applications in electronics fields. Indeed, the exceptional electronic properties of diamond such as relative dielectrical constant $\epsilon_r = 5.7$, breakdown field of 10^7 V.cm^{-1}, high carrier mobility larger than 1060 and 2100 $\text{cm}^2 \cdot \text{V}^{-1} \cdot \text{s}^{-1}$ for electrons and holes, respectively at room temperature [41], saturation speed 2.7×10^7cm.s^{-1}) make diamond a superior candidate in the field of high power and high frequency electronics [42].

2.2.1.4 Thermal properties

Pure diamonds have a high thermal conductivity (W.cm^{-1}.K^{-1}) at room temperature [43] which is four times higher than that of copper [44]. The high thermal conductivity of diamond is exploited as a heat sink for electronic or optoelectronic components such as power transistors and laser diodes [45]. Diamond has a low heat capacity (6.195 J.mol^{-1}) and low thermal expansion coefficient (10^{-6} K^{-1} at 20°C), which means that its cooling capacity is higher than any natural material [46]. As an example, diamond is used to increase the power of laser diodes [47] by improving the evacuation of the heat generated by the emission. This improvement has simplified the complex encapsulation due to thermal constraints posed by the materials used previously.

2.2.1.5 Telecommunications

The high speed of propagation of sound in diamond (1.8 km.s^1 [48]) allows for its application in the field of telecommunications, and high-frequency telephony [49, 50]. The principle is to create a surface wave using an aluminum nitride (AIN) type piezoelectric actuator. This wave then propagates on the surface of the diamond to be converted into an electrical signal using a piezoelectric receiver. The frequency of use of the filter is proportional to the speed of sound in the diamond and inversely proportional to the inter-electrode distance. The speed of sound in diamond is five times higher than in the other materials conventionally used for this type of application, which makes it possible to reach frequencies of 2 to 3 GHz without resorting to expensive high-resolution lithography technologies.

2.2.1.6 Biology

Diamond by its chemical composition (carbon), is bio-inert [51] and can be used in the medical field, while commonly used semiconductor materials such as silicon or gallium arsenide are not

bio-inert. The electro-stimulation of neurons is one of the therapeutic techniques used in the context of diseases of neuronal deficiencies such as Parkinson's disease and also in the case of degeneration of photo-receptors which leads to loss of vision. In the case of loss of vision this is applicable provided that some of the photo-receptors are still able to function but the information is cut off at the level of the neurons which drive the information. The electro-stimulation of these cells after implantation of neuro-stimulators and of photo-receptors can give patients with vision impairment a chance to regain their vision [52, 53]. However, the semiconductor materials used in this field, such as silicon or gallium arsenide are not bio-inert. Thus, the interface between the non bio-inert materials used and the human cells can degrade over time, which will not be the case with the use of diamond. Diamond can provide the link between sensors and deficient cells and can be simultaneously used as an optical detector [54].

2.3 Production of Synthetic Diamond

2.3.1 High-Pressure High-Temperature (HPHT) diamonds

The first attempt to develop diamond synthesis was to replicate what nature has been doing for many years. For this, the manufacturing of diamond crystals started in 1953 by the electricity company ASEA (Allmänna Svenska Elektriska Aktiebolaget) in Sweden that developed a method called High Pressure and High Temperature (HPHT) (unpublished). This technique uses graphite mixed with a metal solvent such as iron or nickel which has the property of solubilizing the carbon strongly. This mixture is then brought to high pressure and temperature conditions using hydraulic presses equivalent to diamond synthesis from geological deposits. Figure 2.4 shows the illustration of a hydraulic press for diamond synthesis.

The first published result of the creation of synthetic diamond is attributed to General Electric which published a similar process as ASEA in the journal Nature in 1955 [55]. Bundy et al.

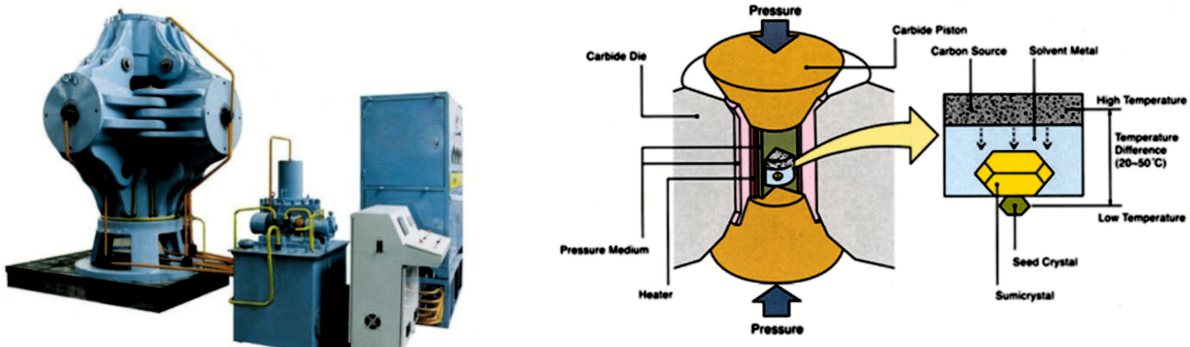

(a) **(b)**

Figure 2.4 (a) Schematic representation of a hydraulic press for diamond synthesis by HPHT method. (b) Description of different components of a hydraulic press.

established in 1955 the carbon phase diagram [55], presented in Figure 2.5, which defines the conditions of temperature and pressure necessary for the production of diamond, in thermodynamic equilibrium of diamond for different production techniques. Details of these conditions were reported in 1973 and 1996 [56, 57].

Most of the diamonds produced by HPHT synthesis have nitrogen as an impurity. Nitrogen present in the air-sealed capsule during HPHT diamond synthesis is incorporated into the diamond crystal giving it a yellow characteristic color. To grow large pure crystals by HPHT synthesis is possible, but the process is slow and takes a long time (6-7 mg/h [59]). Advances in the low pressure CVD technique is favored for manufacturing of single crystal diamonds of high quality.

2.3.2 Chemical vapour deposition (CVD) diamonds

The chemical vapour deposition (CVD) technique is the deposition of a solid on a surface from chemical reactions in the gas phase at the surface of a suitable substrate. This growth method was postulated in 1955 by Bridgman, a growth specialist [60]. It was tested for the first time

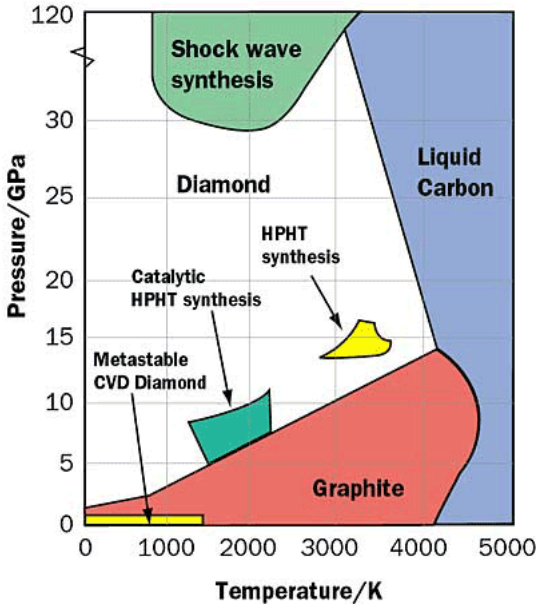

Figure 2.5 Carbon phase diagram [58].

in 1958, and then in 1968 [61, 62] resulted in the deposition of carbon atoms in the form of a polycrystalline layer of diamond. However, the growth rate was extremely slow, of the order of 1 nm/hour. Later, in 1982 Japanese researchers of the National Institute for Research in Inorganic Materials finally succeeded in growing a thin layer of polycrystalline diamond of 1 micron thickness with good quality at an acceptable growth rate in a hot filament reactor.

The CVD method of diamond growth involves synthesizing diamond by activating a hydrogen-rich H_2/CH_4 gas mixture from low to moderate pressure conditions, where the graphite phase is thermodynamically the most stable [63]. The production of atomic hydrogen plays an important role in the stabilization of the diamond phase by saturating the dangling bonds at the surface and ensuring the reduction of non-diamond phases that is co-deposited (carbon sp^2). The methyl radicals (CH_3) produced from the dissociation of methane are considered the principal carbon species precursor that subtends the sp^3 carbon bonding and initiates the diamond growth [64]. The growth of high quality diamond films at high growth rates is mainly based on the ability

to produce a large amount of atomic hydrogen in the vicinity of the growing surface [65]. CVD diamond growth techniques differ in the method used to activate the gas phase [66]. The two main types of external sources for the activation of the gas within a chamber (called a reactor) is a hot filament (HFCVD) and a microwave plasma (MWCVD). HFCVD is a thermal activation that uses a tungsten filament heated to high temperature (> 2273.15K). This technique allows to coat large areas at low cost but suffers from low growth rates and significant contamination by the constitutive metals of the filament. In a MWCVD reactor powers of 600 to 6 kW and working pressures of up to several hundred mbar lead to high gas temperatures (3500 K) in the center of the plasma discharge, thus promoting the dissociation of molecules to form a plasma composed of radicals such as H^+ or CH_3^+ and ionic species such as $C_xH_y^+$ necessary to initiate diamond growth. This technique yields reasonably high growth rates.

The advantage of the CVD technique over the HPHT technique is the growth of ultra-pure diamonds containing less than 1 parts per billion of nitrogen atoms incorporated in the layer. In addition, the introduction of gaseous species such as borane and phosphine makes it possible to intentionally dope or incorporate species in the growth phase to reproduce p-type or n-type diamond [67].

2.4 Classification of Diamonds

Originally, the classification of diamond was based on two criteria, namely ultraviolet transparency (type I diamonds are not transparent to ultraviolet, while type II are transparent to about 230 nm [68]) and to the middle infrared (4000-400 cm^{-1}) radiation. Recently, it is mainly from the absorption in the infrared that the classification of diamonds by type has been established. The classification is made according to the nitrogen content in the diamonds. Two categories of diamond have been introduced based on their nitrogen content. Beyond a concentration of 5 parts per million nitrogen atoms, the diamonds are called type I and below that, they are classified

as type II [69].

2.4.1 Type I diamonds

Type I diamonds are characterized by the presence of nitrogen. This is the main impurity present in the crystal lattice. Depending on whether the nitrogen atoms are isolated or aggregated, and based on their absorption characteristics, diamond can be distinguished into two feather subcategories within type I, namely type Ia and type Ib.

2.4.1.1 Type Ia diamonds

Type Ia diamonds contain aggregated nitrogen impurities up to 2500 ppm [70]. Nitrogen is present in the form of A aggregates (association of two nitrogen atoms substituting two neighboring carbon atoms) or B aggregates (a carbon vacancy surrounded by four nearest-neighbor nitrogen atoms). According to Koivula et al. [71], the majority of natural diamonds are of this type. These diamonds are divided into three subcategories: type IaA, type IaAB and type IaB, which are defined by their infrared spectral characteristics.

- **Type IaA diamonds**: This type of diamond contains only nitrogen impurities in the form of A aggregates. They are relatively common.
- **Type IaB diamonds**: Diamonds of this type only contain nitrogen impurities in the form of B aggregates. They are very rare.
- **Type IaAB diamonds** : Diamonds of this type contain nitrogen impurities in the form of A aggregates, B aggregates and platelets. This is by far the most common case for Type Ia diamonds.

2.4.1.2 Type Ib diamonds

Type Ib diamonds contain isolated, dispersed, paramagnetic nitrogen impurities located on a carbon site in the crystal lattice. Natural type Ib diamonds are rare, with 0.1% being the most frequently quoted figure [70]. It is in this type of diamond that one finds the bright yellow diamonds whose absorption spectrum does not have the Cape lines (Cape yellow diamonds-originally termed this way when they were first found in the Cape Province in South Africa). They are better known in the cosmetic jewelry trade under the name "canary diamonds".

2.4.2 Type II diamonds

Type II diamonds contain very little nitrogen ($<$ 5 ppm, [70]), that is, too little for detection using an infrared spectrometer. These diamonds are said to be the purest [72]. There are two categories in this group: Type IIa and Type IIb. The distinction is based on a criterion of electrical conductivity.

2.4.2.1 Type IIa diamonds

Type IIa diamonds, called "pure" diamonds, are electrical insulators. They are usually colorless unless they contain visible absorption defects. They are transparent in the ultraviolet up to 230 nm. The one phonon absorption (400 to 1332 cm^{-1}) of the infrared spectrum and the visible spectrum of this type of diamond does not show absorption. Mined diamonds are rarely type IIa, Many "big" diamonds found in diamond mines, including Cullinan, are of this type.

2.4.2.2 Type IIb diamonds

This category of diamond is characterized by the presence of boron in substitutional form, which induces a p-type conductivity. Natural diamonds belonging to this category are rare (less than 0.1%) and blue colored due to the presence of boron.

2.5 Doping of Diamond

Diamond is a semiconductor with a wide band gap (5.47 eV). It is intrinsically insulating but can become either semiconducting, metallic or superconductive if it is doped. The use of diamond as a semiconductor for electronics is closely related to the possibility of the realization of p-type or n-type doping to control its conductivity. This requires a good control of the doping levels.

Doping involves incorporating an impurity that results in the creation of an impurity level in the band gap of a semiconductor material. This new state in the band gap, by means of thermal excitation, can create holes in the valence band or electrons in the conduction band, depending on whether the dopant is an acceptor or electron donor, respectively.

In the following section, an overview of reported research done on the different impurities that can be used to dope diamond is presented.

2.5.1 Impurities in diamond

The high atomic density of the diamond lattice limits the number of potential dopants. The impurities are selected in relation to the energy required to ionize the associated electrical carriers, once the atom is placed in a suitable site, which is generally a substitutional site. This energy must be low enough to allow provision of a large number of charge carriers at room temperature. A brief overview of the main dopant impurities used in diamond and the associated results are discussed

below. The ionization levels associated with most of these atoms are deep. Consequently, the search for new impurities, allowing more efficient doping, is particularly needed.

2.5.1.1 p-type doping

Boron is the main impurity used for p-type doping of diamond. Natural diamond containing boron exists, but it is very rare (type IIb diamond). Boron gives the diamond its blue color and was identified as the impurity responsible for electrical conductivity in natural type IIb diamond [73]. Boron was therefore the first dopant used for the synthesis of p-type diamond. With a covalent radius of 0.085 nm, boron is incorporated fairly easily into a substitution site in diamond (covalent radius of carbon: 0.077 nm). Its ionization energy is 0.368 eV [73].

Its incorporation during CVD growth is achieved by adding a gaseous borated compound, for example (B_2H_6, $B(CH_3)_3$ or Trimethylborane (TMB), $B(C_2H_5)_3$), to the H_2/CH_4 mixture in the CVD reactor [74]. Boron is the most effective p-type dopant in diamond. It can be incorporated in concentrations sufficient for the production of electronic components in range extending from 10^{15} to some 10^{21} cm^{-3} [75–77].

Boron is incorporated more easily on the (111) and (110) faces than for the (100) [78] faces, but the best results in terms of mobility and compensation are obtained with (100) orientation. Its ionization energy being high, boron is only partially activated at room temperature. Complete activation is obtained from 600 °C [77].

Currently, the best hole mobility obtained at room temperature on the (100) orientation is 1840 $cm^2/V.s$ for a boron concentration of $6 \times 10^{17} cm^{-3}$ [79] and the compensation rate of 0.4% being the lowest [80].

Calculations based on the DFT-LDA (Density Functional Theory-Local Density Approximation) method have been carried out in an attempt to determine the ionization energies associated with

the atoms of group III, (aluminum (Al), gallium (Ga) and indium (In)) and the simulations give energies of 1.4 eV, 1.4 eV and 1.8 eV, respectively [81]. Due to its low mass (11 g/mol), boron is the dopant that gives the best results in ion implantation, for p-type diamond, creating less damage in the crystal than heavier atoms at the same energy and fluence.

2.5.1.2 n-type doping

Research on the donor dopants is mainly concentrated on the first element of group V of the periodic table: nitrogen (N), phosphorus (P) and arsenic (As).

Nitrogen, the first element of group V is a natural candidate for n-type doping of the diamond as it fits easily into substitutional sites, its covalent radius (0.079 nm) is close to that of carbon (0.077 nm). In contrast, its ionization energy of 1.7 eV which is too high to achieve acceptable conductivities, at least at room temperature. Because of its high ionization energy, it is generally not considered a dopant, but a deep trap. It could eventually find electronic applications at very high temperatures [82].

Phosphorus is the substitutional dopant that has been mostly studied for n-type doping in diamond and gave the most conclusive results at present [13,83]. This was done for the first time by CVD deposition on homoepitaxial oriented (111) [13] layers. Its ionization energy is $\sim$ 0.6 eV. This was measured by various methods: electrical measurements as a function of temperature [84] and photocurrent spectroscopy measurements [85]. The maximum incorporation obtained is approximately 5×10^{19} cm^{-3}. Phosphorus has a covalent radius (0.117 nm) much larger than that of carbon (0.077 nm) and therefore phosphorus causes a relaxation of the surrounding carbon atoms. This has the consequence of creating a deeper donor level than that calculated in the effective mass approximation (0.23 eV). The incorporation of the phosphorus is much less effective for epitaxial growth with orientation (100) than for those with (111) orientation. In 2004, however, an AIST (Association for Iron and Steel Technology) team [86] took a new step

in developing n-type doping diamond using phosphor as dopant with (100) orientation. This is a major advancement because it eliminates a restriction on the orientation of the substrate. This opens new perspectives for the development of diamond-based electronic components. At present, the best electron mobility obtained at room temperature for the (111) orientation is 660 cm$^2 \cdot$ V$^{-1} \cdot$ s^{-1} for a phosphorus concentration of 7×10^{16}cm^{-3} [87].

Arsenic (As) and **antimony** (Sb) are also potential substitutive donors in diamond. Their ionization energies, calculated by the ab-initio method [8], were about 0.4 eV for arsenic and 0.3 eV for antimony. However, until now, there has been no significant experimental evidence supporting these results. Only the implantation of arsenic was attempted, but gave no result in terms of activated dopant electrical conductivity [88].

2.5.2 Doping techniques

A brief overview of the main results concerning diamond doping by diffusion and by ion implantation recorded in the literature is provided. The hydrogen-terminated diamond surfaces which are reported to exhibit p-type conduction, will not be discussed [89, 90] as they are not relevant to the work presented here. Readers who want to know more are referred to [91].

2.5.2.1 Doping by diffusion

Few studies have been conducted on diffusion doping. This technique has so far been considered inefficient in the case of diamond because of the low diffusion coefficient values of most impurities in diamond. This is due in particular to the high atomic density of diamond. In many studies, the low diffusivity of dopants is accommodated by a high temperature, ranging from 1400 °C to 1900 °C [92, 93]. However, the temperature is limited by the conversion mechanism of diamond into graphite, which can start around 1500 °C in inert environments.

2.5.2.2 Doping by ion implantation

Ion implantation is a predominatly flexible doping technique from the point of view of the control of the concentration levels and the geometries of impurity profiles made. It has been decisive in the design of silicon components with complex geometries. It could appear, in the case of diamond, as a simpler solution than epitaxial doping at the level of implementation. The first attempts to dope diamond by ion implantation dates back to the 1960s [94]. The doping of diamond by ion implantation has attracted much research over the past fifteen years. One of the major obstacles to this technique is the metastable nature of C-C bonds of sp^3-type diamonds. Indeed, under normal temperature and pressure conditions, the stable configuration of the C-C bonds is a 2D configuration, sp^2 relative to graphite. Graphite is conductive, anisotropic and does not have the hardness of diamond.

The ion implantation process creates defects in the diamond lattice leading to the amorphization or recrystallization of sp^3 bonds to sp^2 bonds, the creation of vacancies, interstitials, dangling bonds and aggregates of defects. This can lead to the formation of a conductive layer inside the diamond samples [95]. From a certain concentration of implantation-related defects common to all dopants, the diamond tends to recrystallize in the graphitic phase during post-implantation annealing [96]. This critical simulated concentration of defects, evaluated using Stopping Range of Ions in Matter software (SRIM [97]), is $N_{critical} \simeq 1 - 9 \times 10^{22}$ cm^{-3}. The range of $1 - 9 \times 10^{22}$ $vac \cdot cm^{-3}$ is related to the energy range of the implantation. For keV energies the simulated damage density for amorphization post annealing is close to 1×10^{22} $vac \cdot cm^{-3}$, while for MeV energies it is closer to 9×10^{22} $vac \cdot cm^{-3}$ [98].

Post-implantation annealing allows movement of the implanted ion from interstitial sites to substitutional sites, in order to improve the charge carrier concentration. It must also repair the broken bonds created by the bombardment and reduce defects that compensate the carriers due to the active dopant. Conventional annealing has been shown to leave high defect rates in implanted

films [99]. The primary drawback in diamond is that it is difficult to annealing at temperatures higher than 1700 K because of the onset of graphitization at these high temperatures. Unless, it is short enough to avoid complete graphitization.

A further difficulty lies in the fact that the point defects created by the implantation can quickly diffuse to combine with each other and form aggregates of defects, which are more difficult to remove [100]. The post-implantation annealing is generally carried out under high vacuum or inert gas so as to prevent the combustion of diamond in contact with oxygen.

A possible route to improve doping of diamond by ion implantation is the CIRA (Cold Implantation Rapid Annealing) method [100, 101]. It was developed by Prins [101]. He proposed that because interstitials begin to migrate at room temperature, leaving behind a high density of vacancies that combine to create clusters of defects, the implantation should be done at low temperatures. The CIRA method of performing implantation at a low temperature (usually around 77 K, liquid nitrogen temperature), was to limit the diffusion of interstitials and vacancies. The sample is then rapidly annealed from 77 K to some higher predefined temperature, usually 700 K or higher. The idea was that this method would lead to an effective mopping up of the vacancy self interstitial defects thereby reconstituting the diamond and trapping the dopants at substitutional sites of the diamond lattice.

3. Defects in Diamond

Spectral analysis of light emitted by sample can be very valuable for characterizing semiconductors in general. In many wide-band gap semiconductors, defects generated during growth or after doping (grain boundaries, twins, dislocations, stacking defects, impurities, crystallographic defects) can act in different ways on the luminescence of the sample, based on defect levels they create in the band gap. In the case of diamond, luminescence spectra allow for the identification of donor and acceptor levels involved in the recombination of bound excitons. Several defects in diamond can therefore be studied from their luminescence spectra, and in particular by the position and the width of the peaks in a spectrum.

A variety of point defects and impurities in diamond can be present in high concentration and this can make their study very complex, particularly in CVD diamond layers. It was therefore challenging to make an exhaustive description of all of the luminescent centers in this thesis. Thus a brief overview of the most common point defects and impurities in CVD diamond, with a special emphasis on luminescent defects related to nitrogen, oxygen and nitrogen-oxygen complexes, is outlined in this thesis.

3.1 Defects in a diamond crystal

3.1.1 Ideal crystal

An ideal crystal is a solid whose structure consists of molecules or atoms in a periodic array. The lattice is obtained by translations in all directions of a basis unit. This basis unit is the smallest crystal volume of the lattice and is called a primitive cell. Each element of the lattice is associated with a well-defined site around which it can perform vibrational movements. Band

theory describes the electronic structure of a crystal [102]. This theory states that the periodicity of a crystalline lattice is related to the origin of an energy diagram including allowed bands and accessible to charge carriers and an energy gap. The last permitted energy band is called the conduction band (CB). The valence band (VB) is the penultimate band of the allowed energies. The valence electrons of atoms are located in this band. The two bands are separated by an energy gap E_g, called band-gap (BG). The energy E_g is a characteristic quantity of the material (see Figure 3.1) and represents the energy required for an electron in the valence band to access the conduction band for a direct band gap material.

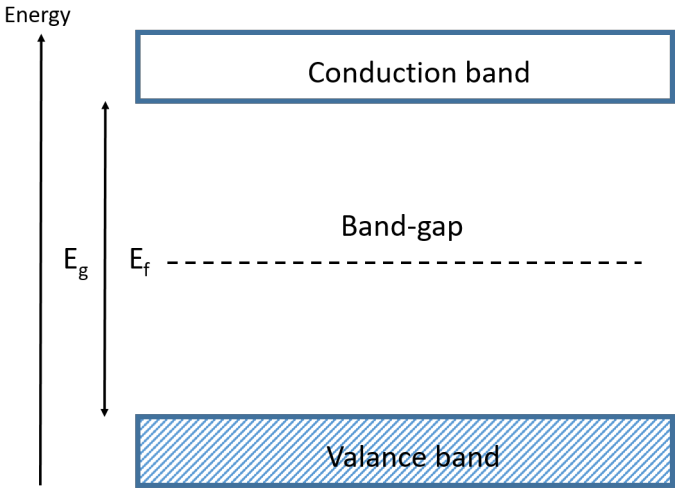

Figure 3.1 Energy band diagram of a an ideal crystal.

The Fermi energy level, E_f, sets the maximum energy level that electrons can reach at absolute zero temperature (0 K). The Fermi level position in the energy band diagram determines the category in which the material is classified. When the Fermi level is located in the conduction band, the material is conductive and its conduction band is partially filled with free electrons (up to the Fermi level). When the Fermi level is located between the valence band and the conduction band, it then distinguishes insulators whose conduction band is empty and semiconductors for which this same band is practically empty. Insulators have a high gap and thermal agitation does not allow electrons to pass through to the conduction band. Semiconductors can be considered

as insulators with a lower energy gap but have an impurity band close to the valence band for a p-type semiconductor and close to the conduction band for a n-type semiconductor. In this sense a semiconductor is not an ideal crystal because the dopant atoms are regarded as impurities in the crystal.

3.1.2 Defects in the real crystal

A real crystal is an arrangement of atoms whose periodicity is disturbed or broken by defects. If the disturbance is localized at the level of an atom or a unit cell, it is called a point defect [103]. When the disturbances are extended within the network, one speaks of extensive defects.

Point defects are of two types: intrinsic which involve only the host atoms and extrinsic, which involve impurities or foreign atoms. There are several types of point defects such as vacancies, self-interstitial atoms or chemical impurities (substitutional or interstitial).

The vacancy is the absence of an atom on a normally occupied site. This usually occurs because of imperfect packing of atoms during crystallization of the solid or due to the fact that an atom has been dislodged from the equilibrium position as a result of thermal vibrations at high temperatures. Vacancy defects facilitate the movement of atoms and thus are responsible for the diffusion process in the crystal. If there is a large number of vacancies, the atoms can diffuse easily through the crystal. The number of vacancies in a crystal can be calculated using the following formula:

$$n = N \exp\left[-\frac{E_v}{kT}\right]$$

where n is the number of vacancies per unit volume, N is the number of lattice atoms per unit volume, E_v is the formation energy for vacancy, k is the Boltzmann's constant and T is the absolute temperature [102].

Interstitial atoms are actually atoms that occupy abnormal (where no atom is supposed to occupy)

sites in the lattice. A self-interstitial defect, however, is when an atom of the host material is positioned at an interstitial site. The presence of chemical impurities refers to the presence of foreign atoms in the crystal lattice in the interstitial or in substitutional position (solute or impurity).

In the case of a crystal with several types of atoms, the replacement of an atom by an atom of another type in the crystal lattice is called an anti-site defect.

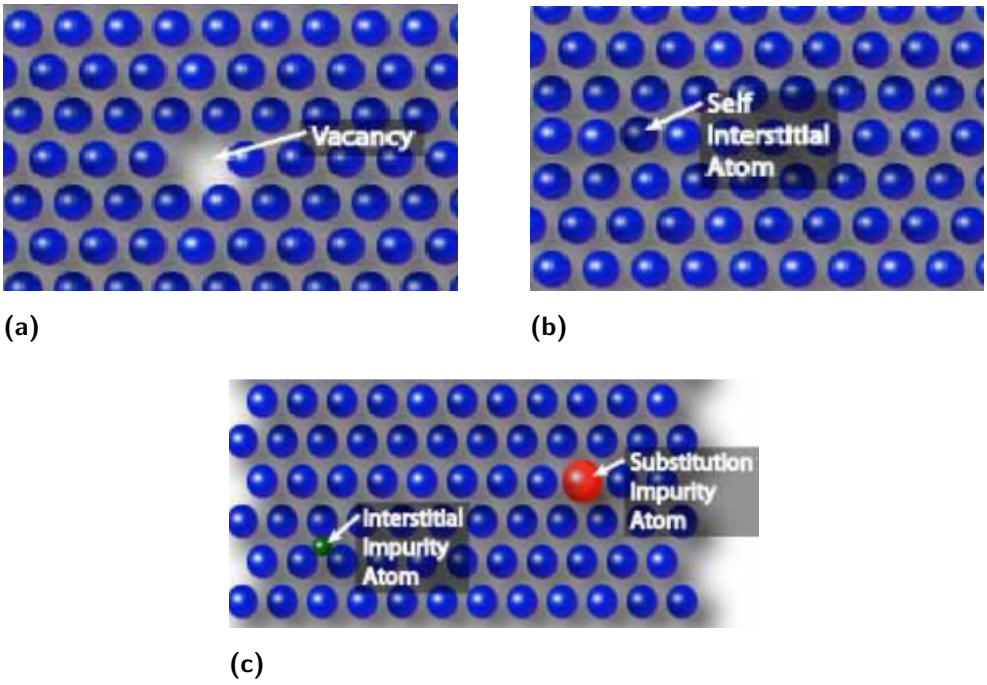

Figure 3.2 Illustration of different point defects in a crystal lattice. (a) vacancy defect,(b) self-interstitial defect, (c) interstitial and substitutional impurity atoms [104].

Figure 3.2 shows the different types of point defects that can be found in a crystal lattice.

Associations of point defects in a crystal lattice are possible as shown in Figure 3.3. In the case of an ionic crystal, it is possible to find association of an anionic vacancy and a cationic vacancy as illustrated in Figure 3.3a. This association is known as a Schottky defect. The Frenkel

defect corresponds to the displacement of a species of the crystal lattice from its site towards an interstitial position as illustrated in Figure 3.3b. It is therefore an association of a crystalline species in an interstitial position and a vacancy. Point defects give the crystal specific properties, such as the color of the crystal or the conduction of the electric current.

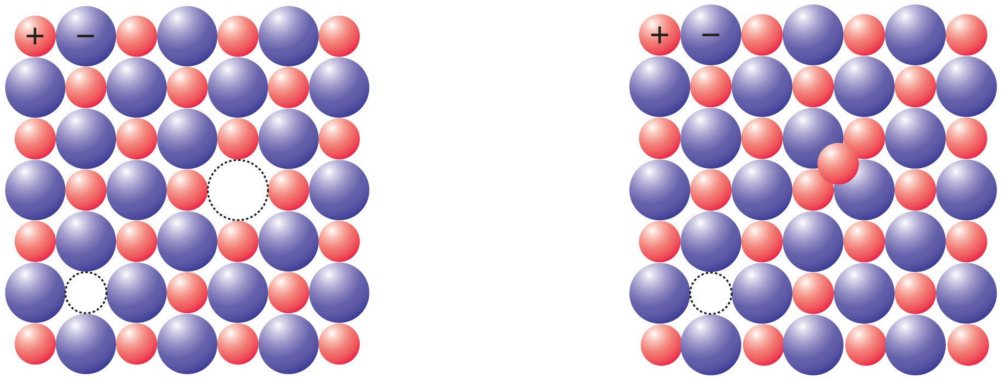

Figure 3.3 Illustration of association of point defects in a crystal. (a) Schottky defect and (b) Frenkel defect [105].

Among the extended defects, one distinguishes surface and volume defects as the grain boundaries. Grain boundaries can be defined as the juxtaposition of two grains. Stacking faults of atoms or planes modify the periodicity of the crystal lattice at the level of at least one chain of atoms. Thus the breaking of an atomic plane is called a dislocation.

The perturbations-induced defects introduce changes in allowed energy levels of a crystal. In some cases, the disturbance is large enough to produce an electronic state located in the band gap. These electronic levels are called traps. If a level has an electron capture cross-section much greater than that of the holes, $\sigma_e >> \sigma_h$, these electronic levels are called electron traps. Otherwise, the level is called a hole trap. Some of these traps may be the site of electron-hole recombinations, which is said to be a recombination center. Electron traps are electron donor levels in the conduction band. These donor levels are located below the conduction band, while

hole traps are near the valence band. Hole traps are also called electron acceptor levels. In the energy band diagram, traps sufficiently far from the conduction or valence bands are not disturbed in room temperature and are called metastable traps. The traps located near the Fermi level are characterized by an effective electron capture cross section very close to that of the holes ($\sigma_e \sim \sigma_t$,) and are therefore generally centers of recombination. However, depending on the temperature, the electron (hole) traps far away enough from the conduction (valence) band can become recombination centers.

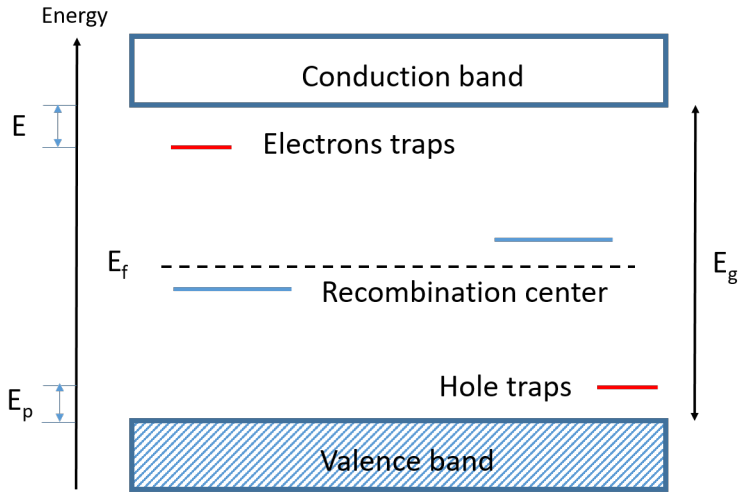

Figure 3.4 Band diagram of a real crystal showing the hole and electron traps as well as the recombination centers.

The band diagram in Figure 3.4 shows the case of an insulator with an electron trap located at an energy E below the bottom of the conduction band, a trap of holes at an energy E_p above edge of the valence band and two recombination centers located on either side of the Fermi level characterized by E_f. The energy E (E_p) corresponds to the energy required to bring the crystal to untrap an electron (a hole) from an electron (hole) trap to the conduction (valence) band . This energy is called activation energy of the trap or depth of the trap.

For this study, the focus is on point defects which play a key role in the optical and electrical

properties of diamond. These are now considerably discussed in sections 3.2 and 3.3, respectively.

3.2 Luminescent defects in diamond

Most of the point defects encountered in diamond involve atoms with a small radius covalent, such a nitrogen, boron, carbon, hydrogen and vacancies, but more rarely larger atoms, such as silicon, phosphorus, arsenic and transition metals. The diversity of existing defects being very large, it is difficult to make an exhaustive list here. In the handbook "Optical properties of diamond" [106], Zaitsev identifies several hundred optical transitions that are generally associated with one or more types of point defects. The reader can also consult the book entitled "The properties of natural and synthetic diamond" [19] which gives extremely abundant and instructive information on the nature of the defects encountered in diamond (HPHT, CVD, or natural), their possible evolution according to the treatments carried out (annealing and high pressure treatments) and their relation to observed optical transitions. It should also be noted that charge transfers are frequent between adjacent defects, which may complicate their observation or quantification. This section briefly describes the most frequently encountered defects and impurities in CVD diamond.

3.2.1 Nitrogen defects

Nitrogen is the most common impurity in diamond and the majority of defects are mainly related to substitution by nitrogen atoms and vacancies of carbon atoms in the diamond lattice. As discussed in section 2.4 on the diamond classification, nitrogen-containing diamonds are of type Ia, or Ib. The nitrogen concentrations of type II diamonds are known to be less than 5 ppm and in theory this can not be detected using a conventional infrared spectrometer [107].

Substitutional nitrogen is a deep donor with an ionization energy of 1.7 eV [108]. It has an infra-

red spectrum (IR) characterized by a peak around 1130 cm^{-1} as shown in Figure 3.5), and a sharp peak at 1344 cm^{-1} which is due to a local vibration and which is proportional to the amount of nitrogen present [109]. At temperatures around 1500 °C the nitrogen atoms become mobile and may associate with other nitrogen atoms to form A aggregates. This nitrogen aggregate (A aggregate) is present in type IaA and IaB diamonds. It has an electron donor level of energy 3.8 eV below the conduction band [110]. When the annealing temperature reaches 2600 °C under stabilizing pressure of 9.5 Gpa [111, 112], B aggregates are obtained. The B aggregate corresponds to the association of four nitrogen atoms around a carbon vacancy. This type of aggregate is visible in type IaA and IaB diamonds. The main common luminescence defects related to nitrogen and other impurities are discussed below.

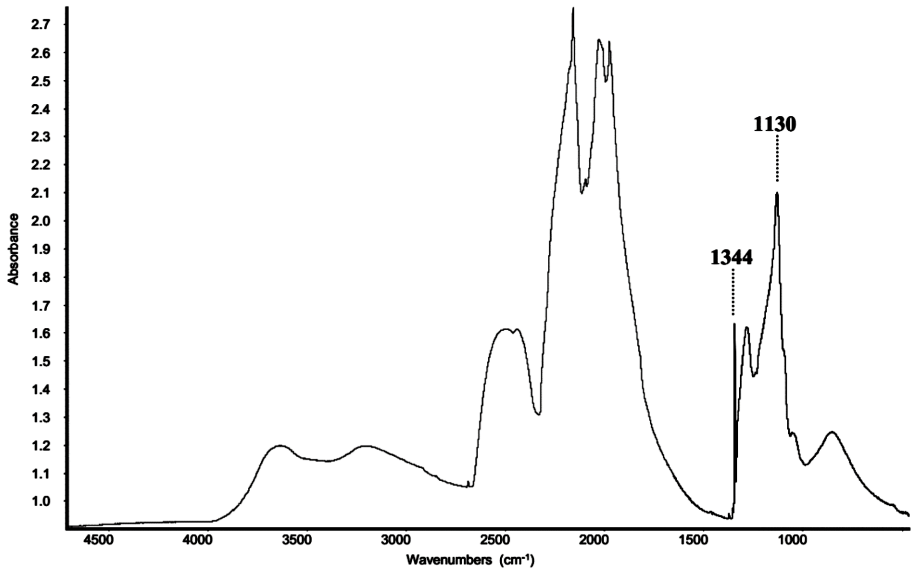

Figure 3.5 Infrared spectrum of type IaA diamond showing the presence of isolated substitutional nitrogen atoms (C centre) with peaks at 1130 and 1344 cm^{-1} [113].

3.2.1.1 A centre

The A centre represents the association of two substituted nitrogen atoms and has trigonal symmetry [114]. This centre is active in the infrared and inactive in the visible spectral region. In the infrared one-photon absorption region, the signature of the A centre in diamond is represented by a feature starting at 1332 cm^{-1}, in which the main peak is located at 1282 cm^{-1} and two additional broader peaks, at 1212 cm^{-1} and 482 cm^{-1}, respectively [115] as shown in Figure 3.6.

From a theoretical point of view, the gain in energy when two nitrogen atoms form a pair is between 2 and 4 eV [116, 117], which is relatively favorable. The absorption coefficient related to the band at 1282 cm^{-1} can be up to 85 cm^{-1} [106] which, in this case, makes it one of the most intense absorptions of the infrared spectrum of diamond.

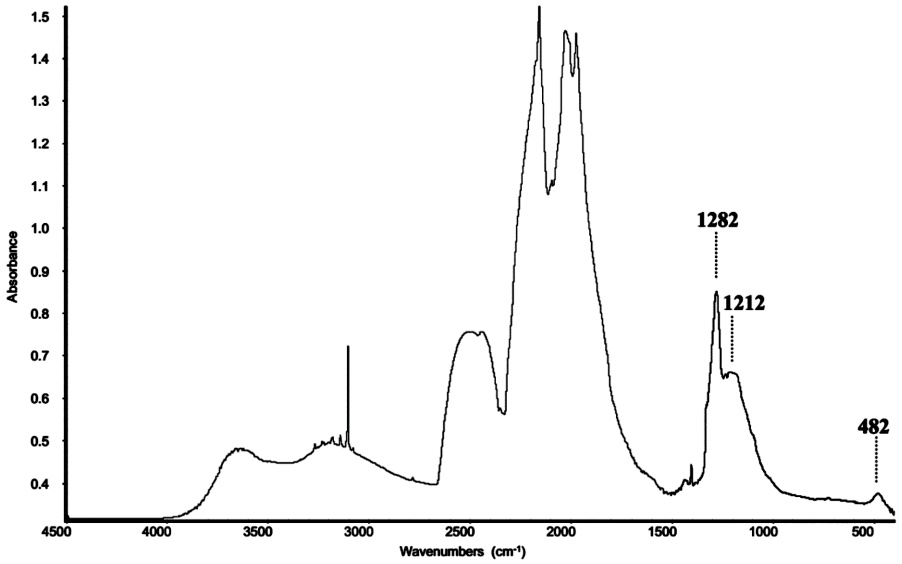

Figure 3.6 Infrared spectrum of type IaA diamond showing the A centre signature peaks at 1212 and 1282 cm^{-1} [113].

3.2.1.2 B centre

This aggregate is a combination of four nitrogen atoms arranged around a carbon vacancy (4N-V). It has Td symmetry. The activation energy for transforming A aggregates into B aggregates is between 6.5 and 7.6 eV [118]. The B centre is active in the infrared and inactive in the visible, and is not known to be responsible for luminescence. In the infrared one-phonon absorption region, the B centre is represented by an absorption feature starting just before the Raman band of diamond at 1332 cm^{-1}. The B centre has a sharp peak at 1332 cm^{-1} (superimposed with Raman peak of diamond), a broad peak at 1180 cm^{-1} with a shoulder at 1096 cm^{-1} and an additional broad peak at 1010 cm^{-1} as illustrated in Figure 3.7. Two additional broad absorption peaks at 754 cm^{-1} [119] and about 780 cm^{-1} [106] are also found on the infrared spectra of diamonds with B aggregates.

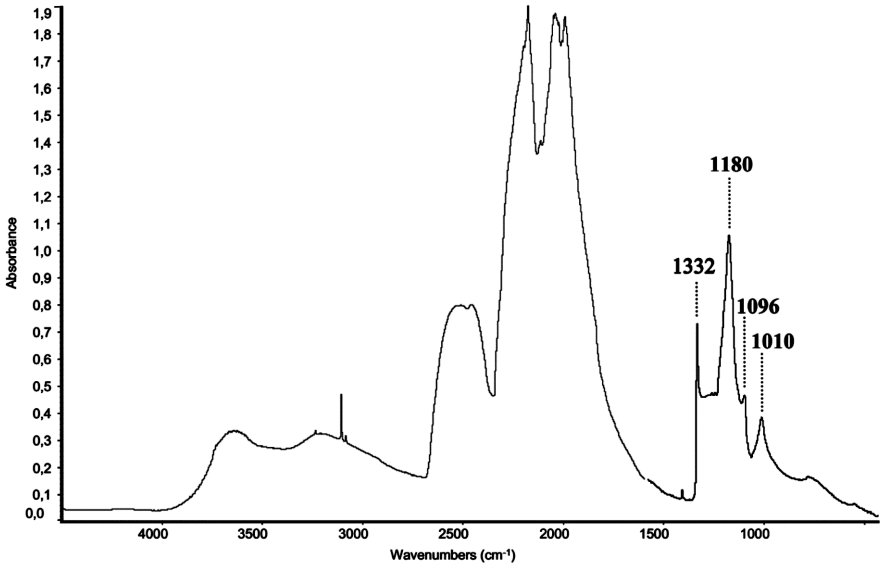

Figure 3.7 Infrared spectrum of type IaB diamond showing the B centre signature peaks at 1010,1096, 1180 and 1332 cm^{-1} [113].

3.2.1.3 Platelets

Platelets are defined as extended planar defects that appear in diamond containing aggregated forms of nitrogen. [120]. Diamonds that have platelets are therefore very rich in nitrogen. The size of these platelets varies from a few nanometers to a few micrometers. In the infrared, the peak correlated with these platelets is at about 1365 cm^{-1} (between 1375 and 1358 cm^{-1}), and is called B', the position varying according to the dimension of the platelet.

3.2.1.4 N9 centre

These centres occur naturally in nitrogen-containing diamonds in the form of B aggregates (B centre) whose intensity of the absorption band is proportional to the nitrogen concentration. The N9 centre has three very close absorption bands: 236 nm, 235.6 nm and 234.9 nm and energies of 5.252, 5.262 and 5.277 eV, respectively [106]. The most intense is close to 236 nm (5.252 eV). The relative intensities of these components depend on the temperature in the luminescence spectrum, but not on the absorption spectrum [106].

3.2.1.5 N3 centre

The N3 centre has an absorption peak at 415 nm. It consists of an aggregate of three substituted nitrogen atoms surrounding a vacancy [121]. It comes from the transformation of A aggregates into B aggregates, and occurs if there are many B aggregates. This centre is the signature of type Ia diamond since 95 % of diamond showing photoluminescence of the N3 centre belong to type Ia [122]. Field reported that the absorption intensity of N3 centre is proportional to the B-aggregates and the platelet peak [19]. N3 has several excited states in the band gap. One of them corresponds to a visible absorption at 478 nm, denoted N2. In type IIa diamond, the N3 centre can be created after nitrogen ion implantation followed by annealing at a temperature

above 1200 °C.

3.2.1.6 389 nm centre

The 389 nm centre is a defect induced by electron irradiation in all types of diamonds [106]. It is one of the common characteristic features of CVD diamonds. It has also been observed in some as-grown CVD diamond films [123]. Its luminescence is strongly enhanced after annealing at 550 °C. This defect has been suggested to involve an interstitial carbon atom and a single nitrogen atom [124]. Figure 3.8 shows a typical photoluminescence spectra of 389 nm centre.

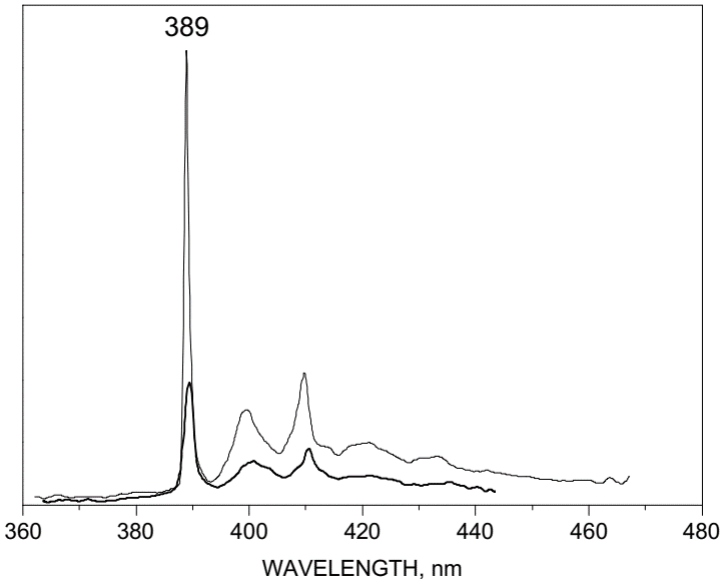

Figure 3.8 Typical photoluminescence spectra of 389 nm centre taken at low and room temperature (bold line) from as-irradiated CVD diamond [125].

3.2.1.7 TH5 centre

The TH5 centre (487.5 nm) is a defect induced after electron irradiation and subsequent annealing at temperature above 400 °C in type IIa and Ia diamonds [106]. The TH5 centre anneals out at

temperature above 1000 °C. This centre has been suggested to be an intrinsic defect containing a divacancy [43]. The emission peaks related to the TH5 centre are: 485.8 nm, 483.7 nm, 482.4 nm, 480 nm, 478.7 nm and 476.5 nm [106].

3.2.1.8 NV centre

Nitrogen vacancy centres (NV centre) is a naturally occurring defect in any nitrogen-containing diamonds. The NV centres can also be created artificially. It consists of a nitrogen atom in substitution of a carbon atom next to a vacancy as illustrated in Figure 3.9. It can exist in different charge states. The neutral form of the nitrogen-vacancy centre denoted as NV°, has a single electron, which is not involved in either a chemical bond or a non-binding pair associated with an atom. The negatively charged form, NV^{-} , has two free electrons. These electrons can undergo optical transitions. They confer photoluminescence properties on these two charge states of the NV centre.

- The **NV° centre** has a zero phonon line at 575 nm. In a high quality CVD diamond, the ZPL can be as narrow as 1 meV at nitrogen liquid temperature. Its symmetry can be either of trigonal (C_{3v}) or C_{2v}. It has an electronic transition between ^2E ground states of trigonal symmetry, to an excited state $^2A_1$, with a energy of 1.57 eV. There is also another transition (below the main transition) from $^2A_2$ to $^2A_1$.
- **NV^{-} centre** has a zero phonon line at 637 nm. It belongs to the C_{3v} point group. This association forms a fixed molecular system in a host matrix. The substitution of a carbon atom by a nitrogen atom brings an unpaired excess electron, which can stay localized on this defect. The NV^{-} behaves as a paramagnetic defect due to the unpaired electron. The electronic structure of the NV^{-} centre has been definitively established after several years of controversy. It is an electronic transition between a triplet ground state of spin 2, of symmetry ^3A, to an excited state of symmetry ^3E. Other levels of symmetry ^1E and ^1A,

have also been identified. Their energies are 0.44 eV and 1.67 eV respectively [106]. Since transitions to these levels are optically forbidden, they can act as traps [126].

The NV^- centre is not observable in photoluminescence or cathodoluminescence spectra recorded under excitation energy exceeding the band gap of diamond due to the fact that such excitation ionizes the negative centres which drives them to the neutral state [127].

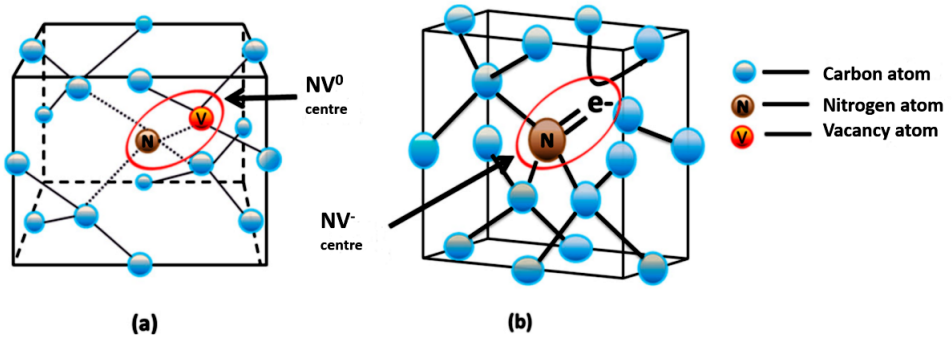

Figure 3.9 Illustration of NV centre in a diamond crystal lattice. (a) Neutral form of NV centre and (b) negatively charged state of NV centre [125].

3.2.1.9 H3 centre

The H3 centre (ZPL at 503.2 nm) is a common optical feature for most of the nitrogen containing diamonds. Its a typical radiation centre of diamond. This defect is produced after irradiation and subsequent annealing at temperatures above 550 °C. However, it is also observed naturally in some synthetic diamonds. The intensity of the luminescence of an H3 centre generated by low-energy electrons is proportional to the concentration of the B centre. This is explained by the fact that the nitrogen in the B centres favors creation of the vacancy near the A centres [106]. Its annealing behavior depends on the type of diamond and irradiation conditions. For ions implanted nitrogen-containing diamonds, the H3 centre becomes wider after annealing at the temperatures at which the centres are created. The luminescence intensity of the H3 centre

increases dramatically at low liquid nitrogen temperature with respect to room temperature measurements [128]. The H3 centre is formed from the A-aggregate of nitrogen and vacancies. The most widely accepted model of H3 centre is a pair of substitution nitrogen atoms separated by a vacancy (N-V-N), with a rhombic-I C_{2v} symmetry.

3.2.2 Carbon defects

3.2.2.1 Carbon vacancy centre

The centre related to the presence of the neutral vacancy (V°) is called General Radiation (GR). The largest electronic transition related to V° is named GR1 and has a zero phonon line at 740.9 nm. However, there is also a whole series of fine absorptions between 430.7 nm and 413.6 nm called GR2-8 that are linked to this centre. The GR1-related electron transition takes place between the ^{1}E (ground state) level and the $^{1}T_{2}$ (excited state) level of the Td symmetry defect [106].

The centre attributed to the presence of the negatively charged vacancy (V^{-} i.e. 5 electrons) is called ND1. This centre has a zero phonon line at 3.15 eV (394 nm). The V^{-} electron transition takes place between the $^{4}A_{2}$ (fundamental) level and the $^{4}A_{1}$ (excited state) level of the point symmetry T_{d} defect [129].

3.2.2.2 5RL centre

This system is a radiation damage centre occurring in type Ib, IIa and IIb diamonds of different origin. It can also be seen in as grown diamond samples [130]. It was initially observed by Wight [131]. Its luminescence spectrum is characterized by an intense zero phonon line, located at 270.6 nm (4,582 eV) accompanied by a shoulder extending over a few hundred meV from which two other zero phonon lines at 282.4 nm (4.380 eV) and 281.3 nm (4.407 eV) emerge as shown

in Figure 3.10. The whole spectrum comes from a site with a non-degenerate triplet electronic state and a singlet electronic state characterized by strong electron-phonon coupling with a local mode (237 meV). The 5RL centre has been observed only at nitrogen liquid temperatures and it almost vanishes at room temperature. In addition, it has been reported to be suppressed by the presence of oxygen [132]. The 5RL centre anneals out when a diamond is annealed at the temperatures above 900 °C [133]. The centre has been tentatively attributed to be related with the presence of carbon interstitials [123].

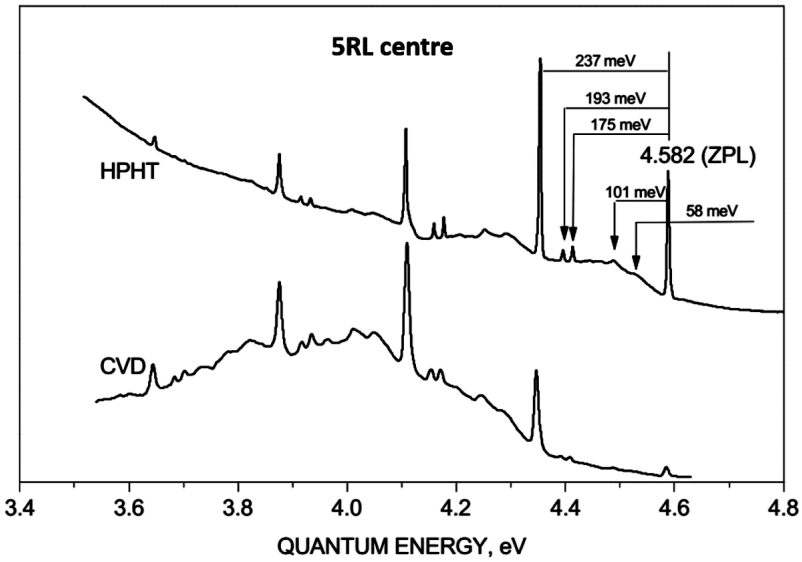

Figure 3.10 Typical CL spectra of 5RL centre recorded at liquid nitrogen temperature of as-irradiated CVD diamond film and single crystal diamond HPHT diamond. The 175, 193 and 237 meV are the three local vibrational modes [106].

3.2.2.3 TR12 centre

The TR12 centre (ZPL at 469.9 nm) is a typical radiation centre observed in all types of diamond after higher-energy irradiation [106]. The TR12 centre has been reported to occur in relatively pure diamond after electron irradiation [106, 134]. It is suppressed by hydrogenation in CVD

diamond films as-irradiated with ions [135]. In type II and low-nitrogen type Ia diamonds the intensity of the TR12 center is enhanced by heating at temperatures of 300-600 °C [136]. It has been reported that the TR12 centre anneals out at temperature above 700 °C and it is also strongly quenched by nitrogen including ion implanted nitrogen [106, 134, 137]. The centre has local vibration mode at 508.8 nm. The TR12 centre is attributed to a defect involving two vacancies and two interstitial carbon atoms in hexagonal positions [106].

3.2.3 Boron defect

Boron is easily incorporated as an impurity in the diamond lattice. The presence of boron leads to absorption in the visible and especially infrared, which result in the blue color of type IIb diamond. The main absorption lines attributed to boron in the infrared are: 1290 cm^{-1}, 2456 cm^{-1}, 2800 cm^{-1}, 2931 cm^{-1} and 4090 cm^{-1}. There are also several luminescence features involving boron atoms (More information can be found in ref [138]).

3.2.4 Hydrogen defect

This is the second most common impurity after nitrogen in diamonds. However, hydrogen is found primarily in type Ia diamonds, so it appears that this impurity is related to the presence of nitrogen [139]. In the infrared, the peaks due to the presence of hydrogen are superimposed on the diamond absorption. The hydrogen absorption is spread from the one phonon absorption to three phonon absorption regions. Natural diamonds show very sharp vibrational peaks attributed to various carbon-hydrogen vibrations. In particular, there are two vibrations at 3107 cm^{-1} (elongation of the C-H (= s) bond) and 1405 cm^{-1} ((angular deformation of the C-H (= b) bond). These vibrations produce combinations to:

- 2786 cm^{-1}: first harmonic of the angular deformation of C-H (= 2b)

- 4169 cm^{-1}: second harmonic of the angular deformation of C-H (= 3b)
- 4496 cm^{-1}: combination of elongation and angular deformation of C-H (= b + s)
- 3237 cm^{-1}: N-H bond.

When the absorption peak of the hydrogen at 3107 cm^{-1} is more intense than the intrinsic diamond band (2450 cm^{-1}), this diamond is called "H-rich diamond" [139].

3.2.5 Oxygen defects in diamond

Due to its size, which is very close to that of the carbon atom, oxygen is likely to be one of the major impurities in diamond [140]. However, there is less experimental data regarding oxygen related defects in diamond. This is due to the fact that it is a challenge to detect fingerprints of oxygen defects using most of the spectroscopy techniques commonly used, such as electron spin resonance or vibrational spectroscopy. For the reason that oxygen is a very light element, ^{16}O is the most abundant isotope of oxygen in nature and it is spinless [141]. However, there are some studies based on DFT calculations [3, 140–142] which provide a better understanding on the nature of oxygen defects in diamond.

An ab initio plane-wave pseudopotential calculation [3] has shown that as a substitutional dopant, oxygen introduces a defect level in the band gap and it is related to a non-degenerate a_1 state located in the middle of the band gap in diamond. The energy of this a_1 state is essentially the same for all charged forms of oxygen. The authors in [3] have also shown the emergence of other state (t_2) situated close to the conduction band edge. The positions of the energy levels of these defects were estimated and are given in the Table 3.1.

The theoretical work of Thiering et al. [141] revealed that the oxygen atom is likely to be on a substitutional site rather than an interstitial site. This is because the calculated formation

Table 3.1 Different positions of oxygen defect energy levels in the band gap, calculated with an energy gap at 4.5 eV [3].

Defect	E(a_1)	E(t_2)	ΔE
O^{2+}	1.18	3.36	2.18
O^{+}	1.50	3.50	2.00
O	1.96	4.13	2.17
O^{-}	1.98	3.87	1.89

energy of interstitial oxygen defect is higher compared to the substitutional one. In spite of its higher formation energy, an interstitial oxygen atom can still be created by means of oxygen ion implantation. However, oxygen in an interstitial site is optically and electrically inactive in diamond with a spin singlet ground state. This conclusion was made after the result of their DFT calculation showed that no defect state was created within the fundamental band gap of diamond after the incorporation of a single oxygen atom in the interstitial site. Furthermore, the energy barrier for diffusion has been calculated to be 3.13 eV [141]. This huge energy barrier suggests that the interstitial oxygen atom should not be mobile in diamond. The same authors confirm that oxygen as a substitutional defect occurs in different charged states, depending on the location of the Fermi level. These various charge states influence significantly the geometry of the ground state as shown in Figure 3.11.

The highest T_d point group symmetry is caused by the double positive charge of the oxygen. Its defect level lies within the valence band although the anti-bonding empty a_1 and t_2 orbital levels occur in the band gap (label as $1a_1$ and $2t_2$).

Another charge state of oxygen which can appear as a substitutional defect in diamond is the positively charge of $O(+)$ defect. This oxygen charge state has C_{3v} symmetry. Here, the t_2 state is divided into a_1 and e ($2a_1$ and $2e$). This separation of t_2 is caused by the distortion of T_d to

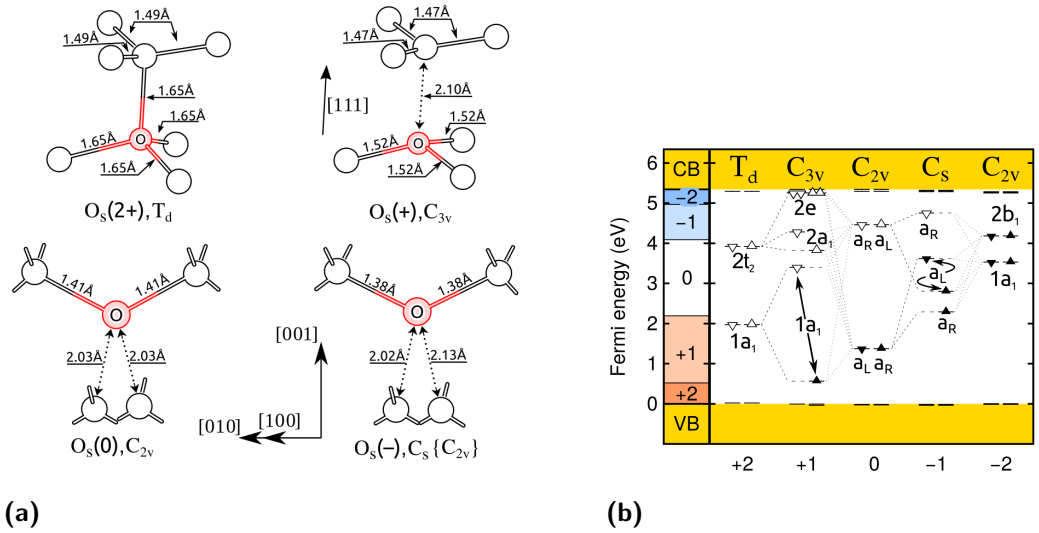

Figure 3.11 (a) Geometry of different charge states of substitutional oxygen defect (b) Symmetry and varous charge transition levels of substitution oxygen defects [141]

C_{3v} symmetry. In contrast to the doubly positively charge od defect, this state has S $= \frac{1}{2}$ electron spin, which makes it paramagnetic and consequently can be detected by electron spin resonance with the related hyperfine signal [141].

Neutral substitutional oxygen has C_{2v} symmetry. Here, the $2t_2$ state is splits to three different states namely: $2b_1$, $2b_2$ and $2a_1$. In this structure, the $2t_2$ level lies near to the $1a_1$ level while the $2b_2$ and $2a_1$ levels are resonant with the edge of the conduction band. They predicted a zero phonon line at 1.39 eV and this would have to be related to the neutral charge of the oxygen defect. In addition, according to the authors, the neutral oxygen charges should be found in nitrogen-contaminated diamond while the negative charge state should only exist in phosphorus doped diamond.

A vacancy can be combined with a substitutional oxygen to form oxygen-vacancy defect. In diamond, oxygen-vacancy defect has C_{3v} symmetry. According to the calculation done in [141], oxygen vacancy defects may form charge states from 2+ to 2-. However, the doubly positive

(2+) oxygen vacancy defect should only occur in boron-doped diamond while the doubly negative oxygen vacancy defect might only take place in p-doped diamond. In addition, the electronic structure of the neutral oxygen vacancy has been found to be similar to the negative charge of the nitrogen vacancy defect. Their calculations also revealed that oxygen vacancy defects in diamond exhibit three defect levels within the band gap: $1a_1$, $3a_1$ levels and a degenerate e level. In the neutral charge state, $1a_1$ level (one of the three state of the oxygen vacancy) is localized above the valance band edge, and within the valance band edge for the positive charge states.

In terms of experimental data, there are few luminescence structures attributed with oxygen defects in diamond. Among them are cathodoluminescence peaks at 484.12 nm, 463.3 nm and 454.9 nm associated to oxygen impurity by Ruan et al. [143]. These peaks were observed from their diamond films samples which were grown with 0.1 % O_2 in the gas mixture using microwave-plasma-enhanced CVD. These authors noticed also a decrease of intensity on some impurity-related luminescence peaks when the gas mixture was 0.1 % .

Mori et al. [144] attributed two features observed at 330.6 and 267.2 nm in their cathodoluminescence spectra to oxygen defects. These broad peaks were obtained after oxygen ions were introduced into a CVD diamond samples using a CrO_3 treatment followed by an exposure to a hydrogen plasma.

Gippius et al. [145] attributed the peaks at 584.8 nm, 598.3 nm, 836 nm and 845 nm in their photoluminescence spectra of implanted natural type IIa diamond samples to defects related to oxygen impurities. These luminescence features appeared after higher temperature annealing above 1500 °C. In addition, the luminescence intensity of these peaks were enhanced when the samples were annealed at 1650 °C after irradiation by 4 MeV electrons. According to the authors, the high temperature annealing allows the implanted oxygen atoms from some configurations where they were optically inactive, to become active after high temperature annealing.

3.3 Background on N-O complex in diamond

A study conducted by Eyre et al. [16] on multi-impurity complexes for n-type diamond has shown that the substitution nitrogen and oxygen atoms in a diamond lattice prefer nearest-neighbor sites and form deep donor defects [16]. Lowther [11] analyzed properties of various charge states of the nitrogen-oxygen pair in the diamond lattice using ab initio plane-wave calculations and found that N-O complexes are very stable defects in diamond. In particular when the concentrations of nitrogen or oxygen atoms are very high it results in the arising of the Fermi energy level in the material [11].

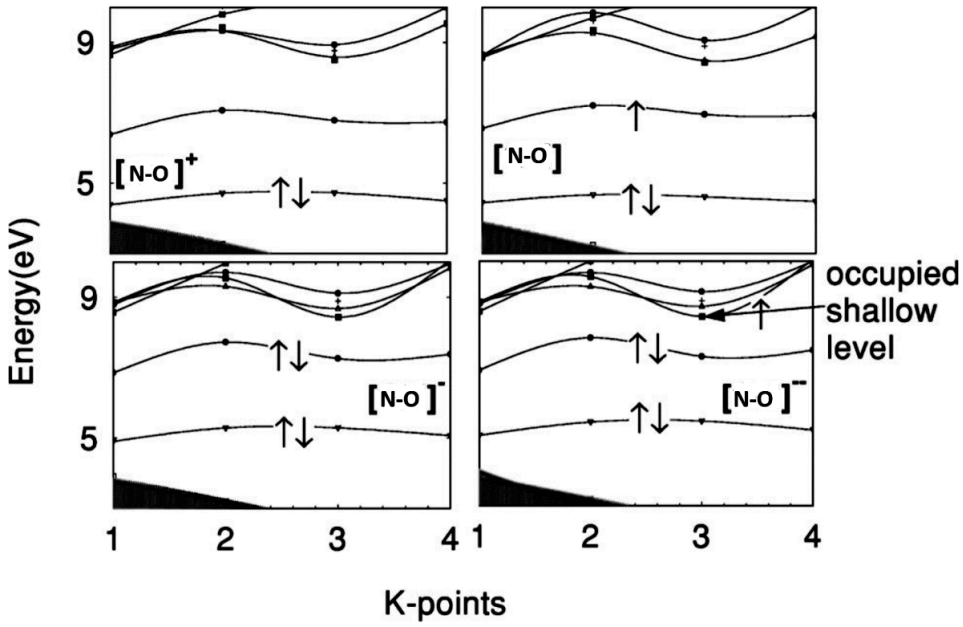

Figure 3.12 Defect related band structure of different charged froms of the nearest substitutional pair of N-O in diamond [11]. This figure shows the occupied shallow level which is less than 0.3 eV below the conduction band.

The aggregation energies of various charge states of N-O defects are given in Table3.2. The negative charge state of the N-O centre has been found to be the most stable and it exhibits

Table 3.2 Agregation energies for various charge states of the N-O defect in diamond. The values presented in this table have to be treated with some care as the band gap used for the calculation is 4.5 eV compared to the experimental value which is 5.47 eV. [11].

Defect	E_{ag} (eV)
$[N\text{-}O]^{++}$	-3.67
$[N\text{-}O]^{+}$	-2.38
[N-O]	-5.17
$[N\text{-}O]^{-}$	-4.08
$[N\text{-}O]^{--}$	-4.82

shallow n-type defect behavior. In fact the negative charge states of the N-O defect introduces significant local lattice distortion caused by the strong repulsion between N and O ions, which then consequently results in the shortening of C-N bonds. Furthermore, the repulsion between N and O atoms increases the electron charge density over that of pure diamond while lowering the value of both N-C and O-C bonds. As a result, there will be an accumulation of charge on the C-N bonds relative to that of a normal C-C bond. The shallow n-type character of the negative charge form of the N-O defect, associated with a strong charge accumulation adjacent to the C-N bond, should induce efficient electron emission. The occupied shallow level for the negative charge form of the N-O defect has been calculated to be less than 0.3 eV below the conduction band edge which is much shallower compared to nitrogen (1.7 eV) and phosphorus (0.6 eV). The shallow highest occupied state of the negative charge form of N-O is a degenerate level in the point group C_{3v} of the defect symmetry [11].

The density functional theory calculations of Etmimi et al. [142] revealed that the electronic structure of the N-O pair is a combination of the constituent parts and the N-O complex in diamond can have both donor and acceptor levels at $E_v + 3.7$ eV and $E_v + 1.5$ eV.

The N-O pair has been suggested to be responsible for two paramagnetic resonance centres

labelled N3 and Ok1, with N3 as the nearest-neighbour N-O pair [17] while Ok1 is the second nearest neighbour pair [18].

4. The Physics of ion implantation

Ion implantation is a powerful tool widely used for modification of the near surface composition of materials [146–148]. This technique involves the introduction of dopant impurities with enough energy (from several hundred eV to MeV) to penetrate the target sample surface in order to modify its electrical, chemical, optical and structural properties. Developed in 1954 by Shockley, ion implantation has undergone considerable development since the 1970s, with a view of its integration into the large-scale microelectronics industry.

The following sections give the principle of ion implantation, its advantages and disadvantages with respect to the diffusion doping method. In addition, the generation of defects by ion implantation and subsequent annealed are discussed, this includes the activation and diffusion of implanted species.

4.1 Principle of doping by ion implantation

Ion implantation is currently the most commonly used conventional technique for introducing a dopant into a semiconductor material. This technique is based on the acceleration of the dopant ions by an electric field to bombard a "target" material. The ions can be accelerated at a voltage of some keV (low energy implantation) to a few MeV (high energy implantation). Mass separation by magnetic sorting is used to specifically select a type of dopant ion, which provides the advantage of obtaining a pure beam. The depth of penetration and the fluence of the incorporated ions can be easily controlled by adjusting the energy transferred to the ion during acceleration and by modifying the implantation current, respectively.

During the implantation process, the element to be implanted is introduced (generally in gaseous form) into an ionization chamber. The most common technique for ionizing a gas is to emit

electrons from a filament. These will collide with the atoms of the gas and ionize them, creating a plasma, i.e. an electrically neutral ionized gas composed of molecules, atoms, ions and electrons. The resulting plasma can, in some cases, be confined magnetically by means of permanent magnets or electromagnets. An electric field makes it possible to extract the ions from the source and accelerate them towards the target material. Most ion implanters also use a magnetic mass separator to select a single ion type to implant.

Figure 4.1 shows all the interactions which usually occur between the implanted ions and the target material during implantation. At the beginning of their course in the target material, the implanted ions will have an almost rectilinear trajectory because of their high kinetic energy. They will gradually lose energy by interacting with the electrons of the target material. Once the implanted ions have lost most of their energy and speed, they will then interact with the atoms of the target material through elastic collisions.

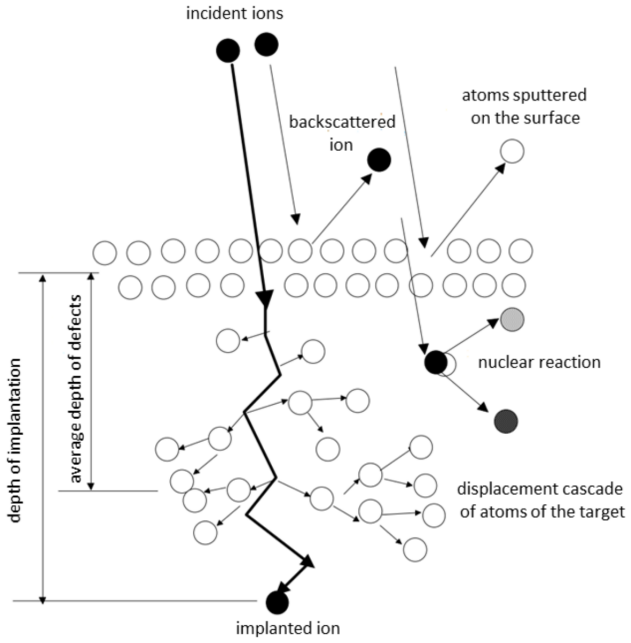

Figure 4.1 Diagram showing the interaction processes of the implanted ions with the target material [149].

An important phenomenon called sputtering may occur upon implantation. Indeed, under the effect of elastic collisions, atoms at the surface of the target material can be ejected, creating surface erosion. Depending on the nature and energy of the implanted ions, this phenomenon can be more or less accentuated, and induce a change in the concentration profile. It should be noted that for energies and ions used in the implantation regime for semiconductors, nuclear reactions do not occur.

A typical ion implantation scheme is given in Figure 4.2. It includes:

- an **ion source compartment** in which electrons emitted by a heating filament ionize a gas;
- a **primary electrostatic field** which is directly applied to the exit of the ionization chamber to allows the extraction of ions from the source compartment;
- a **mass spectrometer** in relation to the analyzing magnet is used to perform a physical analysis of the emitted ion beam. Each ion is derived according to its mass, speed, and magnetic field value. A slot (resolving aperture) placed at the exit allows to select a single species of ions with well defined energy;
- an **accelerator** for acceleration of the ion beam to energies between keV and up to several MeV (in the diagram shown the maximum energy of the ions would be 200 keV), before being focused on the sample;
- finally, a **system of electrostatic deflection (X and Y scan plates)**, which scans the beam uniformly across a large area before arriving at the target.

By measuring the charge accumulation on the target, the implanted ion fluence can be determined.

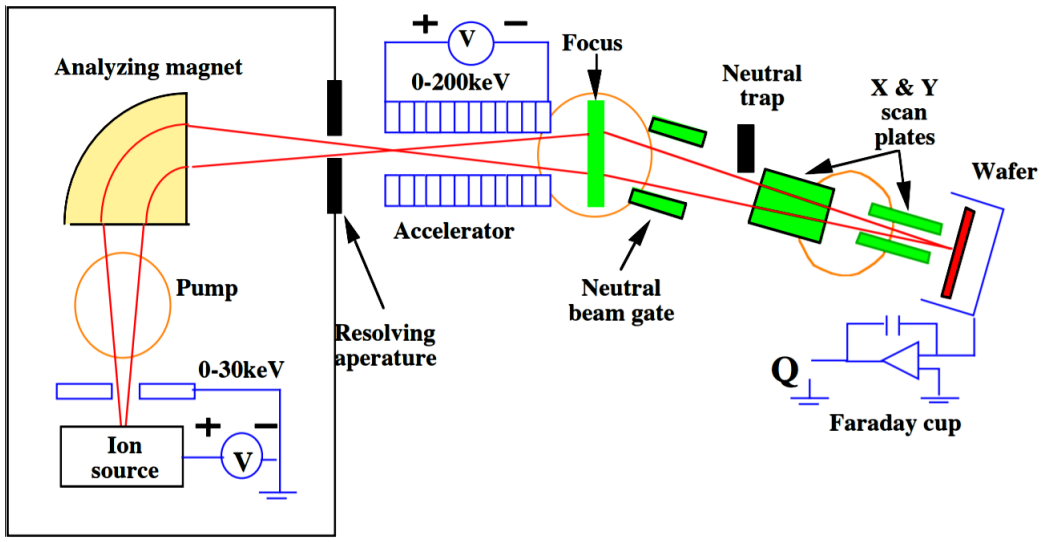

Figure 4.2 Typical diagram of an ion implanter [150].

4.2 Advantages and disadvantages of ion implantation techniques

The major advantages of ion implantation are [151, 152]:

- It can be applied to any type of substrate and any type of impurity;
- The total amount of ions introduced can be easily measured by integration of the ion current flowing through the substrate. It is, in fact, the only method of doping materials that actually counts the impurities arriving at the surface;
- The nature and the distribution depth of the implanted ions are easily controllable;
- Exceeding the solubility limit of the implanted element in a given material and/or introducing ions that could not be introduced by other methods (such as simple diffusion or epitaxy);

- By combining photolithography and implantation, it is possible to only dope only an extremely small selected area on the surface of a wafer. It is therefore a selective doping method.
- Improved surface properties without affecting the bulk properties of the materials.

Despite many advantages of this technique, it has a few disadvantages as mentioned below [153]:

- Presence of radiation damage, in the form of vacancies, interstitials and extensive defects. In the case of silicon, this is not a problem as it is recovered by post-implantation annealing. However, in the case of diamond, the situation is much more complex: the damage substantially modifies the physical properties of the material, and the various annealing steps do not necessarily restore them.
- Directional nature of the technique makes it difficulty to process objects with three dimensions.
- Often the gas sources used such as arsine (ASH_3), and phosphine (PH_3) are extremely toxic.
- Heavy equipment and very expensive.

4.3 Stopping power

The ions that penetrate the target will lose some of their kinetic energy during successive nuclear collisions. The slowdown of the ions in matter is characterized by its stopping power, note $\frac{dE}{dx}$, which corresponds to the quantity of energy lost during a course of length dx. We consider from the theory of implantation that this stopping power is the sum of two contributions, one nuclear

and the other electronic [154]. Thus, the energy lost involver the length dx can be written as:

$$\mathrm{S}(E) = \mathrm{S}_n + \mathrm{S}_e = \left(\frac{dE}{dx}\right)_{nuclear} + \left(\frac{dE}{dx}\right)_{electronic} \tag{4.3.1}$$

Among these two components, only the nuclear contribution participates in the generation of defects in diamond. The detailed characteristics of these two components are now discussed.

The nuclear stopping power interferes with atoms at low speeds. These collisions are elastic and standout from classical theory. The quantity $T_{(p)}$ of energy transferred to the target atom of mass M_2 by an incident ion with energy E and mass M_1 is calculated according to the classical formula given by:

$$T_{(p)} = \frac{4M_1 \cdot M_2}{(M_1 + M_2)^2} E \sin^2\left(\frac{\theta(p)}{2}\right) \tag{4.3.2}$$

$\theta(p)$ is the scattered angle and p the impact parameter (Fig 4.3).

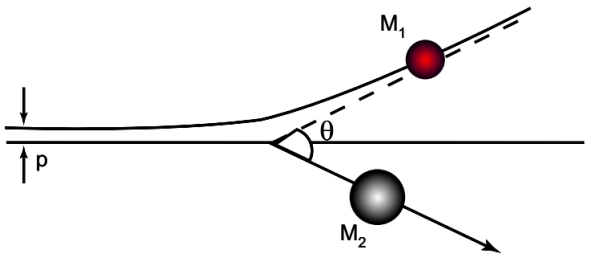

Figure 4.3 Schematic illustration of a collision between a projectile of mass M_1 and a target atom of mass M_2

In equation (4.3.1) the nuclear stopping power S_n can be derived from a screened Coulomb potential (Thomas-Fermi potential) using the reducing variables ϵ and ρ introduced by Linhard et al. [155], as follows:

$$\left(\frac{dE}{dx}\right)_{nuclear} = 509.6 \frac{\rho Z_1 Z_2 M_1 S_n(\epsilon)}{M_2(M_1 + M_2)\left(Z_1^{2/3} + Z_2^{2/3}\right)^{1/2}} \tag{4.3.3}$$

M_1 and M_2 are the masses for the incident ion and the atom of the host material, respectively. Z_1 and Z_2 are the correspond atomic numbers of the incident ion and the atom of the host material. ρ is density of the target material ($g \cdot cm^{-3}$) and $S_n(\epsilon)$ is the universal reducing nuclear stopping power which was introduced by Lindhard et al. [155].

Equation (4.3.3) can be simplified and replaced by an analytical expression proposed by Wilson et al. [156] It is based on a potential called Kr-C (Krypton-Carbon):

$$S_n(E) = \frac{0.5 \ln(1+\epsilon)}{\epsilon + 0.10718\epsilon^{0.37544}} \tag{4.3.4}$$

We distinguish two components for the electronic stopping power: local and non local stopping power. The ion passing through the crystal undergoes repulsive forces from multiple sources of electric fields.



Figure 4.4 Schematic illustration of (a) non-local electronic stopping power and (b) local electronic stopping power.

The electric field of the ions will then cause displacements of electrons involved in the bonds of the crystal. These electrons will strike the ion and the interactions will result in dipole moment that creates a polarized electric field in a direction opposite the velocity vector of ion [157]. The resultant force of this electric field applied to the ion is called the non-local electronic stopping power and it it illustrated in Figure 4.4a. Unlike the nuclear stopping power, which influences ions as they pass close to a target atom, the non-local electronic stopping power interferes with the

entire trajectory of the ion. Finally, when the ion approaches an atom, the electron cloud of the ion will interact with the core electrons of the atoms. The electrons of the ion can then transfer part of their kinetic energy to the electrons of the target, and their by inducing a decrease in the total energy of the ion. The force that results from this energy transfer is related to the local electronic stopping power [158] as illustrated in Figure 4.4b. Unlike the non-local electronic stopping power, the local component acts on the ion only during the period when the ion is close to the atom. In addition, the local electronic stopping power can (unlike the non-local) influence the trajectory of the incident ion (but to a much lesser degree compared to the nuclear stopping power). At higher energies, electronic stopping power dominates over the nuclear stopping power. In the field related to ion implantation, the electronic stopping power is described generally as [159]:

$$\left(\frac{dE}{dx}\right)_{electronic} = 231.6\ \rho Z_1^{1/6} \frac{Z_1 Z_2}{\left(Z_1^{2/3} + Z_2^{2/3}\right)^{3/2}} \sqrt{E\,(keV)} \tag{4.3.5}$$

In reduced notation, the effective electronic stopping power can be written as:

$$S_e\,(\epsilon) = 0.0793 Z_1^{1/6} \frac{Z_1^{1/2} Z_2^{1/6}\,(M_1 + M_2)^{3/2}}{\left(Z_1^{2/3} + Z_2^{2/3}\right)^{3/4} M_1^{2/3} M_2^{2/3}} \sqrt{\epsilon} \tag{4.3.6}$$

More information regarding the calculation of nuclear and electronic stopping power can be found in the textbook: Ion implantation science and technology [153].

4.3.1 Atomic displacements

A simple estimation of the number of displaced atoms can be obtained by considering a model of balls infinitely subjected to elastic collisions. Upon entering the crystal lattice, the incident ion of energy E_1 and mass M_1 strikes the first target particle of mass M_2. This is the primary shock for Figure 4.5.

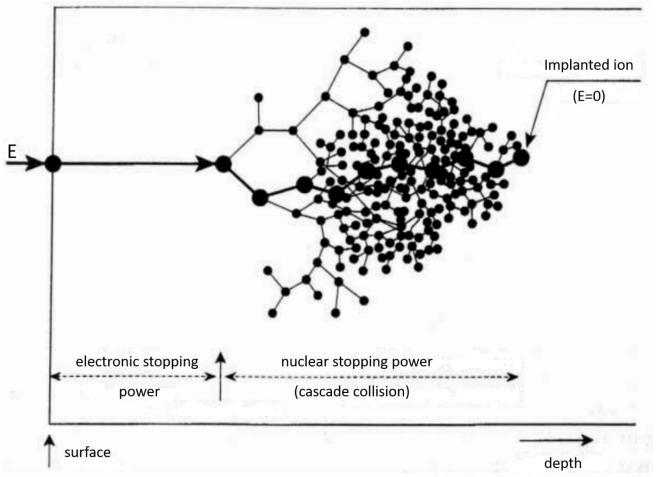

Figure 4.5 Representation of different displacements of atoms of the host material upon ion implantation [160].

During the collision, there is a transfer of energy $T_{(p)}$ from the incident ion to the atom of the host material that leads to a displacement of atoms whenever $T_{(p)}$ is greater than threshold displacement energy E_d (E_d is defined as the minimum energy necessary to move a host atom from its initial position, the theoretical value of E_d for diamond is 25 eV [161]). The displaced atom (mass M_2) will then hit a second atom of the target lattice and provide an average energy $\frac{T_{(p)}}{2}$.

At the third shock the transmitted energy will be $\frac{T_{(p)}}{4}$., then $\frac{T_{(p)}}{8}$, $\frac{T_{(p)}}{16}$, $\frac{T_{(p)}}{32}$,..., $\frac{T_{(p)}}{2^{n-1}}$. This will have a cascading effect where each displaced ion can move one or more ions. As long as the energy transmitted is greater than E_d, the energy transfer continues and the lattice is damaged. The average number of particles displaced per unit area is therefore :

$$\mathrm{N}_d = \frac{T_{(p)}}{2E_d}\Phi \tag{4.3.7}$$

Φ is defined as the total fluence implanted (cm^{-2}).

This relation is valid in the case of elastic collisions. To generalize it, the incident energy must be replaced by the energy lost by nuclear collisions. The equation of the density of defects per

unit volume is given by:

$$N_d(x) = \frac{\left(\frac{dE}{dx}\right)_n}{2E_d}\Phi \tag{4.3.8}$$

The maximum of the function $N_d(x)$ corresponds to $x = R_d$. If the implantation dose increases, the defect density increases to a value comparable to the atomic density of the target material:

$$N_d(x) \approx n_{atom}\left(\mathrm{cm}^{-3}\right)$$

It is said that there is amorphization when this concentration is reached. The corresponding implantation dose, called the critical dose of amorphization, $\Phi_{critical}$ is then given by the following expression:

$$\Phi_{critical} = \frac{2E_d n_{atom}}{\left(\frac{dE}{dx}\right)_{n,max}} \tag{4.3.9}$$

In practice, the number of atoms displaced and measured experimentally is lower than the theoretical estimation. This is mainly due to the channeling of particles which are dependent on the orientation of the target crystal lattice, the recombination defects interstitials-vacancy, the activation of the thermal diffusion of the defects, the isolated interstitials and vacancies by the warming of the target material upon ion implantation [162].

4.3.2 The stopping range

The stopping distance R, called the range, can be defined as the average distance traveled in the target by an incident ion energy E_i and it is given by the following expression:

$$R = \frac{1}{N}\int_E^0 \frac{dE}{\mathsf{S}_n(E) + \mathsf{S}_e(E)} \tag{4.3.10}$$

The distribution of ions can be estimated using a model based on Bohr's theory developed by Lindhard et al. [155]. This method known as the LSS theory, allows one to estimate the main parameters that characterize the ion implantation. These main parameters are: the trajectory of the ion inside the solid, R, its projections in the incident direction, Rp and perpendicularly $R_{\perp}$, as well as the corresponding standard deviations ΔR_p and $\Delta R_{\perp}$.

Due to the random nature of collisions in the material, at first approach, the distribution of the implantation atoms $n(x)$ can be described by a Gaussian function as given below:

$$n(x) = n(R_p) \exp\left(-\frac{(x - R_p)^2}{2(\Delta R_p)^2}\right) \tag{4.3.11}$$

where ΔR_p^2 is the quadratic root of the standard deviation of the projected range (ΔR_p is known as straggling).

The implanted fluence Φ corresponds to the number of ions introduced into the solid per unit area and is written as:

$$\Phi = \int_0^{\infty} n(x)\, dx \tag{4.3.12}$$

Using this expression, the maximum concentration of the implant atoms is written:

$$n(R_p) = \frac{\Phi}{\sqrt{2\pi}\Delta R_p} \tag{4.3.13}$$

In practice, the simple Gaussian approximation is very often insufficient to represent an implantation profile with the necessary precision. We then resort to simulation programs. In the framework of this work, we will use SRIM (Stopping and Range of Ions in Matter [97]) for the estimation of different parameters of the implantation.

4.4 Defects caused by ion implantation

The major disadvantage of the ion implantation technique is that it causes damage to the structure of the target or in our case, the diamond lattice by displacing atoms from the target. If the displaced atom acquires enough energy during the collision, it will again generate another collision and thus give rise to a cascade of collisions. The duration of a cascade being of the order of a picosecond. The displacement of the atoms of the crystal produces interstitial-vacancy pairs, also called Frenkel pairs.

During the relaxation time of the collision cascade, most of the Frenkel pairs will recombine to allow only a tiny fraction of the defects to survive. The probability of recombination is a function of the distance between an interstitial and a vacancy, the temperature and the number of traps present for the point defects. The number of interstitials and vacancies remaining after ion implantation is a function of the implantation conditions such as the mass of the implant ion, the implantation energy, the dose (or fluence), the temperature of the target and the implantation current.

The distribution of defects as a function of depth is very different from that of implanted ions. The defects are created at shallower depths. Indeed, the ion does not have enough energy, when it is at the end of its course, to move atoms away from their original site. The area where most of the defects are created, between the surface and the maximum implantation range (R_p), is called the "cascade zone". This is illustrated in Figure 4.6

Although many defects remain in the crystal after ion implantation, the crystallographic structure of the sample is not completely destroyed.

Depending on the degree of crystal damage, two types of ion implantations can be distinguished. Low fluence ion implantation damages the crystal causing many displacements of the target atoms but keeps its crystalline character. High fluence implantation will damage the crystal

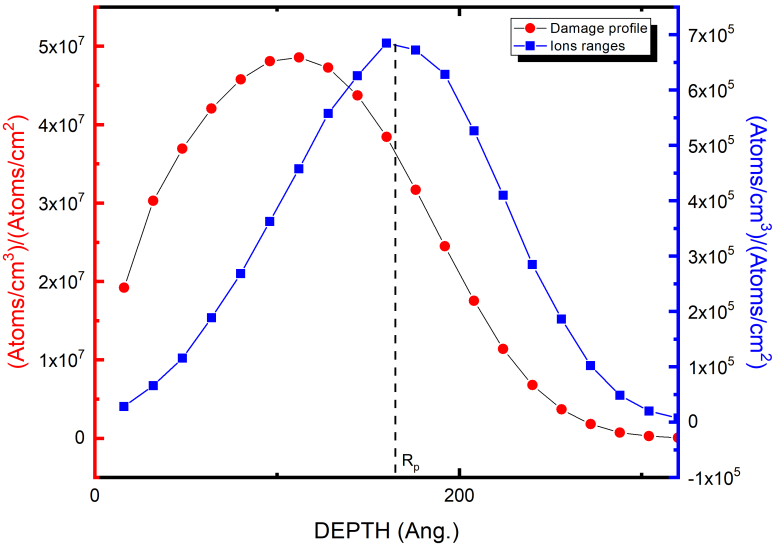

Figure 4.6 Transport of ions in matter (TRIM [97]) simulation showing the distribution of defects and implanted ions as a function of depth. TRIM simulation for 9 keV C^+ ion implantation in diamond

beyond a critical threshold and thus create an amorphous zone whose extent is determined by the implantation conditions. The thickness of this amorphous layer is sometimes greater than the average free path R_p and depends on the mass of the implant ion and its energy. The degree of amorphization has a great influence on the parameters of the thermal annealing. The most intuitive measurement of the thickness of the amorphous layer is Rutherforth BackScattering (RBS) or Transmission Electron Microscopy (TEM).

4.5 Simulation

Several numerical simulation softwares packages are used to calculate the kinetic phenomena associated with ion energy losses. One of them, SRIM, which has a Disk Operating System (DOS) accessible version called TRIM, is a set of programs that calculate the stopping range of an incident ion in a target material (up to 2 GeV / amu (= atomic mass units)). In this program,

developed by Ziegler and Biersack [97], the material is supposed to be isotropic. Calculations are performed using a Monte Carlo simulation, which individually follows a large number of ions at random collisions. An incident ion has a rectilinear trajectory with losses of electronic energies, then changes direction under the influence of nuclear collisions. When the energy of the ion is lower than its displacement energy E_d, it stops and there is dissipation of energy in the form of phonons.

This program allows you to calculate various parameters related to the implantation of ions in a target, among others:

- the spatial distribution of implanted ions (average depth, dispersion, lateral distribution);
- the distributions of electron and nuclear energy losses as a function of depth (these are the average distributions for an ion, they are expressed in eV/Å);
- the distribution of vacancies (displaced atoms) calculated from the modified Kinchin-Pease model [163].

However, there are some limitations to this program:

- the target does not keep any "memory effect" of one particle on the other: thus, the distribution of defects and the displacement of the recoil atoms do not take into account the previous defects calculated.
- the calculation does not take into account any chemical effects that can become significant when the energy of the incident ion is of the order of an eV at the end of its range.
- the simulation also does not take into account the effects of temperature rise due to irradiation;

- this program is better suited to massive targets than to stratified media: a limited number of layers of different composition can be represented at a time (up to 20 layers for SRIM 2000).

Apart from SRIM, there are other softwares packages which can be used to estimate the location of the implanted atoms and the displacement of the atoms of the target. The best-performing simulators use the two-atom collision approximation (Binary collision approximation).

- Marlowe, resulted from the work of Oen and Robinson [164], is able to simulate a very large number of experimental conditions related to implantation. Its adaptation to the most advanced problems of microelectronics is called UT-Marlowe [165].
- Silvaco tools have their own BCA program, developed at the University of Surrey by I.R. Chakarov [166], and provides both dopant and defect profiling.

4.6 Post-implantation thermal annealing

Post-implantation thermal annealing is essential. This allows to electrically activate the impurities introduced by placing them in substitutional positions, and secondly, it leads to a reduction in the concentration of defects created during the ion implantation.

Schematically, the ideal annealing process is shown in Figure 4.6.

4.6.1 Isothermal annealing

This annealing process has a duration that is long enough to have a uniform distribution of heat in the treated material. In this study the samples were isochronally annealed in a preheated graphite

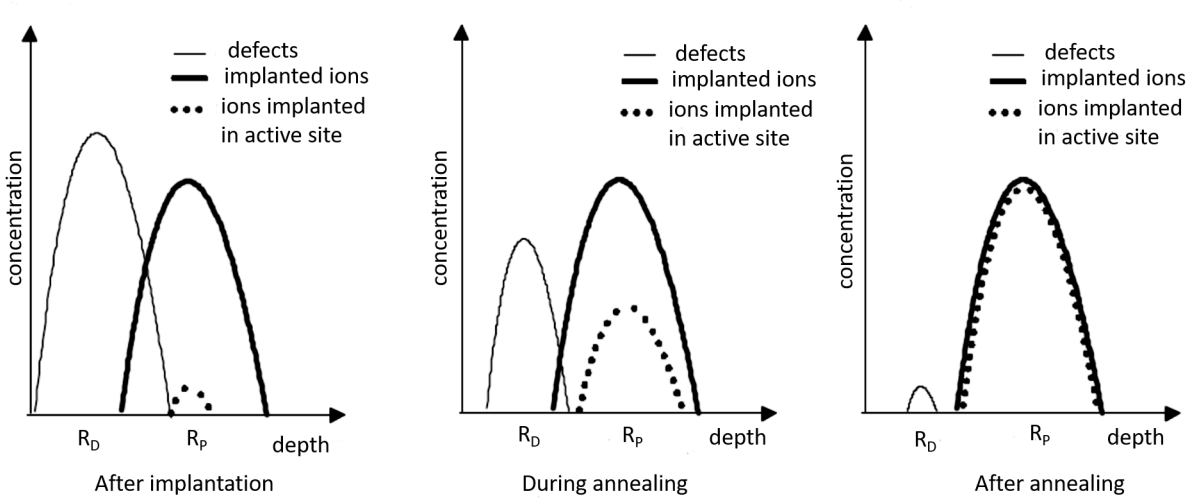

Figure 4.7 Schematic describing the evolution of the in-depth distribution of defects, implanted impurities and impurities on substitutional sites [160].

crucible. The samples were maintained at a predefined temperature for a duration of 30 minutes in an Ar atmosphere.

4.7 Channeling

In the case of a single crystal such as diamond, the atoms are organized regularly and periodically. A single crystal material therefore has an anisotropic structure in which the crystallographic orientation can play a very important role in ion implantation. During implantation, the ions that are confined in these channels will have little interaction with the material and will be implanted much more deeply. This penetration is more important since the size and mass of the implanted ion is small. This phenomenon is called "channeling".

In order to limit this phenomenon, it is possible to tilt the substrate relative to the ion beam in a configuration where these channels are reduced. This inclination is made by modifying two angles: The "tilt" angle between the incident beam and the normal surface of the substrate and

the "twist" angle of rotation of the substrate in its plane as illustrated in figure 4.8. In the case of a diamond orientation substrate (100), the usual angles used to reduce ion channeling are a 7° tilt and a 27° twist.

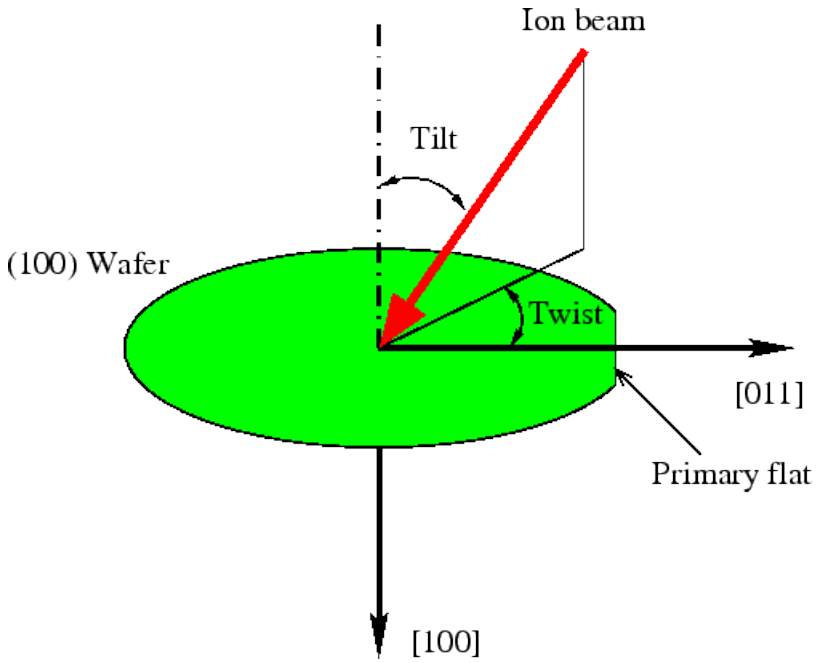

Figure 4.8 Schematic describing the tilt and twist angles used during the implantation in order to limit the channeling phenomenon [167].

5. Experimental and characterization techniques

This chapter describes the experimental techniques used in this thesis and the underlying theoretical principles. The first part discusses the sample preparation, the parameter details for the implantation performed in this study, as well as the post-annealing treatment. The second part focuses on various structural characterization techniques, the vibrational and optical characterization methods. The final part concludes with the description of the electrical characterization techniques.

5.1 Sample preparation

The samples used in this study were single crystal diamonds purchased from Element Six and were ready for use. Type IIa diamond samples had dimensions of $2.7 \times 2.7 \times 0.3$ mm^3 and $\sim 4.5 \times 4.5 \times 0.5$ mm^3, oriented in a $[100]$ direction. The typical nitrogen concentration for this batch of samples was given as < 1 ppm. The purchased diamond samples were polished on both sides and had a polished surface roughness of < 30 nm as specified by the manufacturer.

A Nd-YAG laser was used to make a groove cut (laser mark) near the top corner on one side of the samples prior to any implantation. This was done as an identification of the implanted side during the characterization of these samples. After being grooved, the diamond samples were boiled for 20 min, in an oxidizing acid solution composed of a 3:4:1 mixture of perchloric ($HClO_4$), sulphuric (H_2SO_4) and nitric (HNO_3) acid. This was done in order to etch away the graphite layer created after the groove cutting and to remove any impurities that may be on the surface of the samples.

Thereafter, the samples were cleaned with acetone and rinsed with distilled water using an ultrasonic bath. An electron microscope was used to examine the surface of the samples in order to make sure that they were clean and ready for implantation.

5.2 Ion implantation

A Varian 200-20A2F ion implanter located at iThemba LABS (Laboratory for Accelerator Based Sciences) was used to perform the implantations. Figure 5.1 shows an image of the 200-20A2F ion implanter. The principle and the physics behind ion implantation were discussed in the previous chapter (Chapter 4).

Two of the diamond samples were implanted with N-O ions with an energy of 18 keV and a fluence of 2×10^{16} ions/cm^2. The implants were performed at room temperature with a dose rate of $\sim\ 5 \times 10^{12}$ ions/s and an irradiation angle of $\sim 7^{\circ}$ to the surface normal. A radio frequency (RF) furnace was preheated to 600 °C and annealing of the samples was done by sliding the diamond down a quartz tube from ambient temperature into the preheated crucible. The used of 600 °C is motivated by the fact that it has been reported that 20 min annealing at 600 °C leads to a complete graphitization of the implanted layer in diamond [168]. After boiling it in an oxidizing acid solution, the graphitic carbon formed will be etched away and the remaining near surface layer will comprise a thin damaged diamond structure which is impervious to the oxidizing acid, and also contain the implanted ion. The annealing took place in an argon environment for 30 min. The setup of the furnace is described further below.

A third sample was implanted with 2×10^{16} ions/cm^2 carbon ions at 9 keV and annealed in order to distinguish the features observed in the N-O implanted samples from the implantation damage using the isochemical ions, which would produce a similar density of damage. The fourth sample which was not implanted was used as reference before and after annealing. A fifth diamond

(optical grade, nitrogen concentration not specified) of dimensions $\sim 4.5 \times 4.5 \times 0.5$ mm^3 was implanted with N and O ions at 9 keV to a fluence of 1×10^{16} ions/cm^2. In this case the diamond was implanted in two separate runs so that approximately half the surface was irradiated with N ions while the other half was masked. The N implanted area was subsequently masked and the other half of the diamond surface was implanted with O ions. The use of 9 keV for the C^+ , N^+ and O^+ ions as an implantation energy was motivated by the fact that the 18 keV used to implant N-O ions is split into approximately 9 keV for the N and O ions each since their mass difference is small. The energy of 9 keV for the C, N and O ions would thus create a similar implanted dopant and damage profile at more or less the same depth as the first sample implanted with N-O ions. The third, fourth and fifth diamonds were annealed for 30 minutes under argon flow at 600 °C. All samples that were annealed were cleaned by boiling them in an oxidizing acid solution and rinsed in deionized water after annealing.



Figure 5.1 Picture of the 200-20A2F ion implanter (iThemba LABS, Gauteng).

5.3 Radio frequency (RF) furnace

As discussed in section 4.6, the post-implantation thermal annealing treatment is essential since this activates introduced the impurities by trapping them in electrically active sites in the diamond crystal, and secondly, it leads to a reduction in the concentration of defects created during the ion implantation. In this study, a radio frequency (RF) furnace (Easy Heat 10 KW induction heating system) was used to anneal all the samples.

Electromagnetic induction heating which the RF furnace is based on is one of the electrothermal techniques used to heat a material without direct contact with a source of electrical energy. It involves immersing the material to be heated in a variable electromagnetic field over time, and the energy entering the material is dissipated in the form of heat.

The basic components of an electromagnetic induction heating system are:

- A generator (a source of high frequency electrical energy).
- A copper coil inductor to minimize electrical losses.
- A work-piece to be heated. It must be electrically conductive. In our case we used a graphite crucible lined with a quartz boat into which the diamond would be dropped.
- A cooling unit to cool the "inductor".

In a RF furnace, the generator passes a high-frequency alternating current through the inductor, which generates a very intense and fast changing magnetic field. When the work-piece is placed in the inductor, the magnetic field induces enormous currents, which are known as eddy currents, generating precise quantities of clean and localized heat without any physical contact between the inductor and the heated work-piece [169]. In addition, the high frequency used in induction heating gives rise to a phenomenon called "skin effect". This skin effect increases the flow of

alternating current in a thin layer of the surface of the heated work-piece. Therefore, it greatly increases the heating effect caused by the current induced in the work-piece. Figure 5.2 shows an image of RF furnace used in this study.

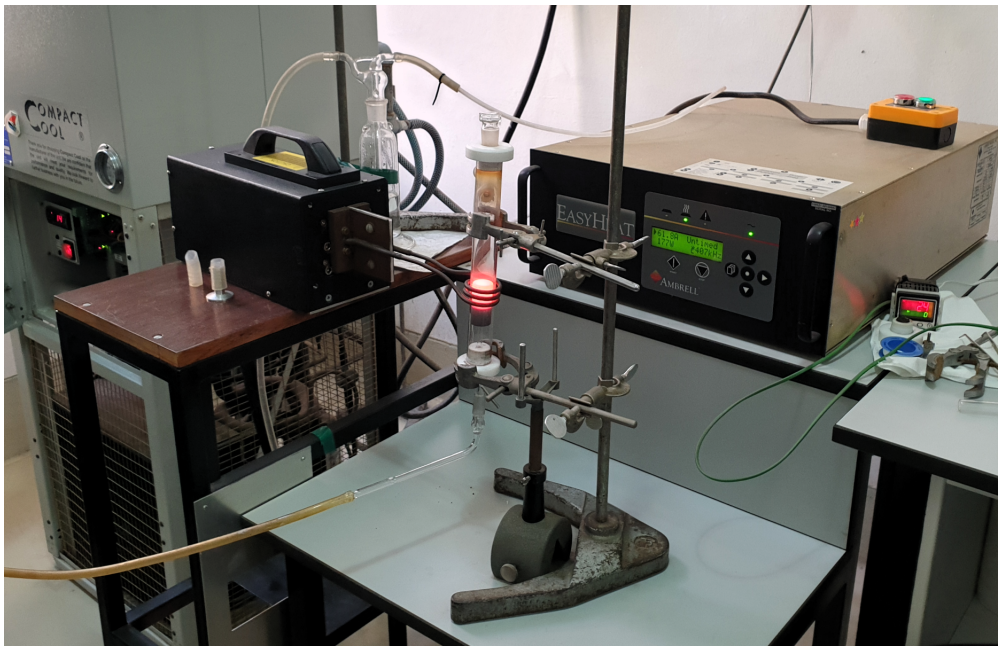

Figure 5.2 Image of RF furnace used for annealing.

5.4 Surface characterizations

5.4.1 Scanning electron microscopy

Scanning electron microscopy (SEM) is an imaging technique for characterizing the surface morphology of samples. This technique is based on electron-matter interactions. The principle of operation involves scanning the surface of the sample with a very fine beam of mono energetic electrons.

Under the influence of the electrons and following the electron-matter interactions, the sample

emits several types of radiation such as secondary electrons, retro-diffused electrons and X-ray photons. In the frame of our study, only images formed by the secondary electrons have been exploited. These are topographic images that represent the surface of the sample, up to very small scales of the order of a few tens of nanometers.

The SEM system comprises an electron gun for generating electrons by thermoelectric effect from a tungsten filament heated to high temperatures or by field effect from a very sharp metal tip. The so-called second optical focusing part makes it possible to focus the emitted electron beam in order to direct it towards the sample using magnetic lenses. Finally, the scanning system allows the beam to scan the entire surface of the sample using deflection coils. In order to improve the clarity and astigmatism, additional collimation coils are placed at the beam output.

The SEM analysis was carried out using a FEI Nova Nanolab 600 FEG-SEM/FIB with an acceleration voltage of 10 kV.

5.4.2 X-ray photoelectron spectroscopy

X-ray Photoelectron Spectroscopy (XPS) analysis provides access to the surface chemical composition of the sample analyzed. This technique was used to quantify the chemical species present on the surface and the electronic states of diamond.

XPS is a non-destructive surface characterization technique based on the use of the photoelectric effect discovered in 1887 by H.Hertz [170] and explained by A.Einstein in 1905 [171]. The current technology of the XPS was developed in the 1950s by K.Siegbahn, which earned him a Nobel Prize in Physics in 1981 [172].

Measurements of XPS are based on the study of the kinetic energy distribution of photoelectrons ejected from a sample under the impact of X-rays of known energy $h\nu$ as illustrated in Figure 5.3. The variation of the binding energy of photoelectrons as a function of the chemical environment

of the atoms from which they are derived is at the origin of the main interest of this technique.

XPS is used to determine the electronic structure and the chemical environment of the atoms present in a sample, but also quantify the components present in the various layers and even to perform chemical profile reconstructions when the instrument allows access to the angular information. This characterization technique is adapted to the surface study of the sample since the average free path of the photoelectrons emitted in the material is very small (i.e. of the order of one nanometer). Thus, the analysis depth does not exceed 10 nm [173].

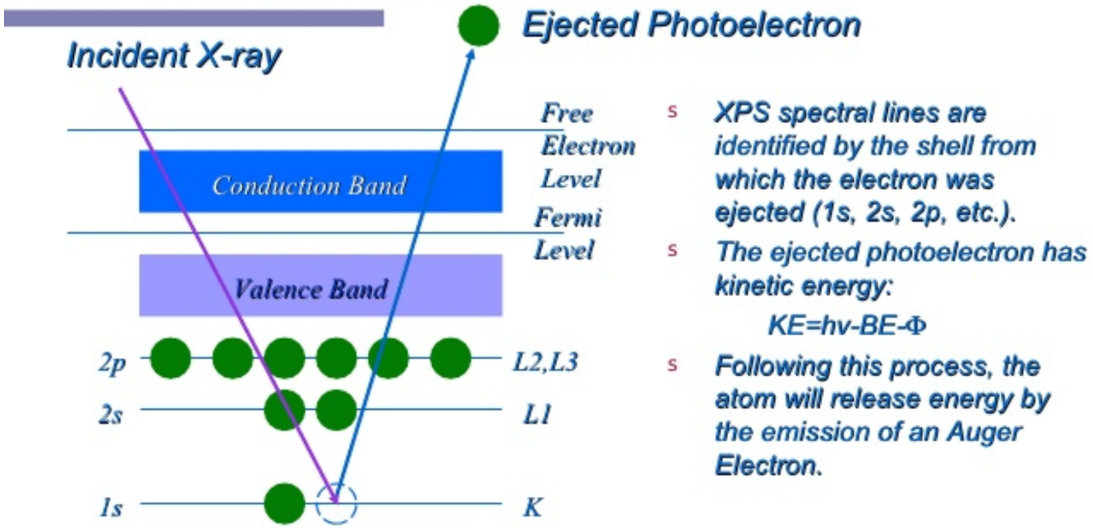

Figure 5.3 Illustration of the photoelectric process [174]

X-ray photoelectron spectroscopy is based on the principle of conservation of energy of the incident photon and is expressed as follows:

$$h\nu = E_c + E_L + \Phi \tag{5.4.1}$$

$h\nu$ is the energy of the incident photon with h being the Planck constant and ν the frequency of the incident photon. E_c and E_L are the kinetic energy of the photoelectron and the binding energy of the considered core level, respectively. Φ is the work function.

Thus, at the spectrometer, the conservation of energy is expressed as follows:

$$E_L = h\nu - E_{c,mes} - \Phi_{spec} \tag{5.4.2}$$

$E_{c,mes}$ and Φ_{spec} are the kinetic energy of the measured photoelectron and the work function of the spectrometer.

The work function of the spectrometer and the energy of the incident photons are known parameters of the experimental setup. By measuring the kinetic energy of the photoelectrons $E_{c,mes}$, it is then possible to determine the binding energy E_L of the electronic level from which the photoelectron originated. Each chemical element generates one or more characteristic peaks on the XPS spectrum. It is important to note that the binding energy is not a quantity associated with a single electronic level but it corresponds to the difference between the energy of electrons from the N non-ionized atom (initial state) and the energy of the $N-1$ electrons of the ionized atom (final state).

The final state of the atom therefore also affects the value of the binding energy:

$$E_L = E_{N-1}\,(final) - E_N\,(initial) \geq 0 \tag{5.4.3}$$

The XPS spectrum consists of several photoelectron emission peaks, characteristic of the electronic levels of the elements present in the material. Thus by identifying the energies associated with each peak, it is possible to determine not only the nature of the atoms present in this material but also their chemical environment.

The intensity of the XPS peaks is a function of the atomic concentration of the elements present in the sample and the photoionization cross section (the probability of ionizing an orbital by irradiation). While the photoionization itself is a function of the atom, the core level considered as well as the energy of the incident photons [175]. The full width at half maximum (FWHM) of these peaks depends on the lifetime of the ionized state (Lorentzian type profile) and instrumental

width (Gaussian type). The spectra are processed by removing the continuous background and the peaks are adjusted by a function containing a Gaussian component.

5.4.2.1 Deconvolution of XPS spectra

The deconvolution of XPS spectra allow the detection of the presence of carbon, oxygen and nitrogen (C1s, O1s and N1s) on the surface of CVD diamond sample.

The main peaks may have different chemical components and spin multiplets. The energy of the photoelectrons E_L is sensitive to the chemical environment of the excited atoms. It depends on the ability of the peripheral electrons to screen the positive charge created by the emission of the photoelectron. In particular, the extra-atomic relaxation due to the electrons of the valence and conduction bands contributes significantly to the chemical shift (depending on the electron density and the polarizability of the bonds). The main components present in an XPS spectrum of a CVD diamond are discussed below:

5.4.2.1.1 Carbon The XPS spectra of the carbon layers provide two types of information:

- the nature and proportion of the elements present in the layer;
- the state of hybridization of the carbon atoms.

In the literature, the study of the position of the carbon 1s peak (noted peak C1s) allows to measure the proportion of sp^2 and sp^3 hybridization in the sample. In general, the deconvolution takes place in two main components: one corresponding to the sp^2 bond, while the second corresponds to the sp^3 bond. The ratio of their respective surfaces gives the proportion of hybridizations in the layer. However, the interpretation of the C1s spectra is very complex due to the proximity of the binding energies of the bonding configurations. Therefore, this requires fairly accurate measuring equipment, with good resolution, in order to distinguish significantly

these different forms. This explains the diversity of results found in the literature where the interpretation of these peaks does not always converge.

The peak position corresponding to sp^3 carbons of the diamond matrix can vary from 283.8 eV to 284.8 eV according to references [176–178]. The component attributed to graphite-type sp^2 bonds can be observed with a negative displacement of 0.8 eV to 1.3 eV relative to the sp^3 carbon bonds of diamond [179–182].

Merel et al. [183] conducted a comparative study between natural diamond, graphite and amorphous carbon (Diamond Like Carbon (DLC)) which the results are presented in Figure 5.4). The deconvolution of the C1s peak for DLC films shown in Figure 5.4 was used to estimate the proportion of sp^3 and sp^2 carbon. They associated the binding energy at 284.4 eV with the sp^2 bond of the C = C type of graphite and the energy located at 285.2 eV with the C-C type sp^3 bond of diamond. The same results were found by Wilson et al. [184] for boron-doped polycrystalline diamond deposits.

In their investigation on in-situ detection of dopamine using nitrogen incorporated diamond nanowire electrode, Shalini et al. [185], after performing the deconvolution of their C1s spectra, attributed peaks at 285.9 and 286.7 eV to sp^2-hybridization bonding structures of C atoms bonded to N atoms (sp^2 C=N) and sp^3-hybridization bonding structures of C atoms bonded to N atoms (sp^3 C–N), respectively.

5.4.2.1.2 Oxygen The study of diamond O1s spectra is less common in the literature compared to the C1s spectra. In general, deconvolution of the oxygen O1s spectrum allows to identify three components. One at 531,4 eV attributed to the C-O bond, another at 532.5 eV attributed to the C-OH bond and a third at 533,3 eV, which is attributed either to the characteristic of the molecule of water (H_2O) absorbed on the surface, or to C-O-C [186, 187].

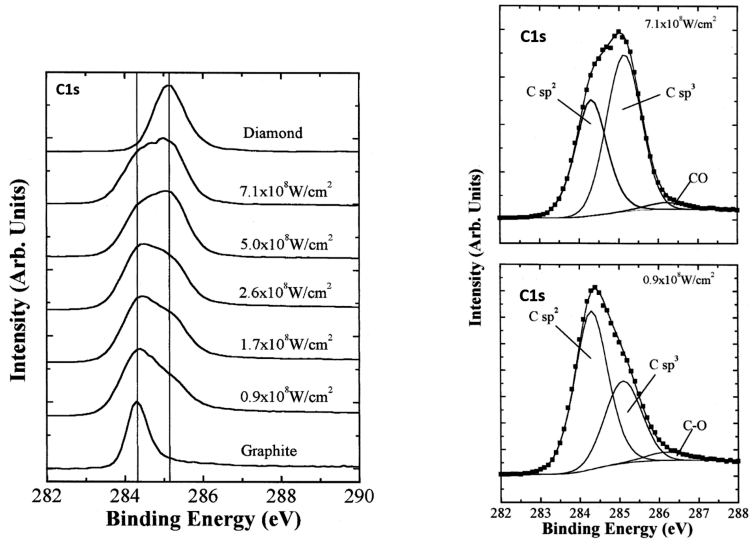

Figure 5.4 (a) Evolution of the binding energies of the 1s carbon peak for graphite, PECVD diamond film and DLC films obtained at different laser intensities,(b) XPS deconvolution of carbon peak C1s of a DLC film deposited a 7.1×10^8 and 0.9×10^8 W $\cdot$ cm^{-2} [183]

5.4.2.1.3 Nitrogen Generally, we note the appearance of peaks in some spectra in the energy field where they can be related to nitrogen. These peaks appear around 397 eV and in the vicinity of 407 eV. The different bonds and their bindings energies are summarized in Table 5.1:

Table 5.1 Binding energy of the 1s peak of nitrogen for different bonds.

Chemical environment	Binding energy (eV)	Reference
N-C	399-400	[173]
N-C	398	[188]
-C=N	398.2	[189]
N=C	400	[190]
N=N	400	[191]
N-O (NO_2)	402	[190]
N-O (NO_3)	407	[173]

5.4.2.2 Instrument

The device used in this thesis is a PHI 5000 Scanning ESCA Microprobe, equipped with a monochromatic Al Kα (1486.6 eV) X-ray source generated by a 25 W, 15 kV electron beam with a pass energy of 11 eV and a resolution of less than 0.5 eV. The emitted photoelectrons are detected at an angle of 90° and then analyzed to obtain an XPS spectrum. A low energy Ar^{+} ion gun and low energy neutralizer electron gun are utilized to reduce charging on the surface. It avoids the effects of differential loads related to the low conductive nature of our samples. The spectra are then processed using the Multipack version 9 software and the chemical compounds and their electronic states are derived using Gaussian-Lorentz fits.

5.5 Optical spectroscopy

Optical spectroscopy is the analysis of electromagnetic radiation emitted, absorbed or scattered by atoms or molecules. It provides information on the identity, structure and energetic levels of atoms and molecules due to the interaction of electromagnetic radiation with matter. When a sample is irradiated by electromagnetic radiation, some of the radiation passes through the sample (transmitted), a part of the incident radiation is absorbed by the sample, depending on the quantity and nature of the material; and a part is scattered (elastically or inelastically). The intensity of the part of the absorbed light is much greater than the scattering part. As molecules or atoms have quantified energy states, the atoms within the sample can only absorb or emit light when it makes a transition from one quantum mechanical state to another as shown in Figure 5.5. Consequently, the quantum states can now be probed from the wavelength of the light that has been absorbed or emitted, since this wavelength is directly related to the energy difference between these two quantum states.

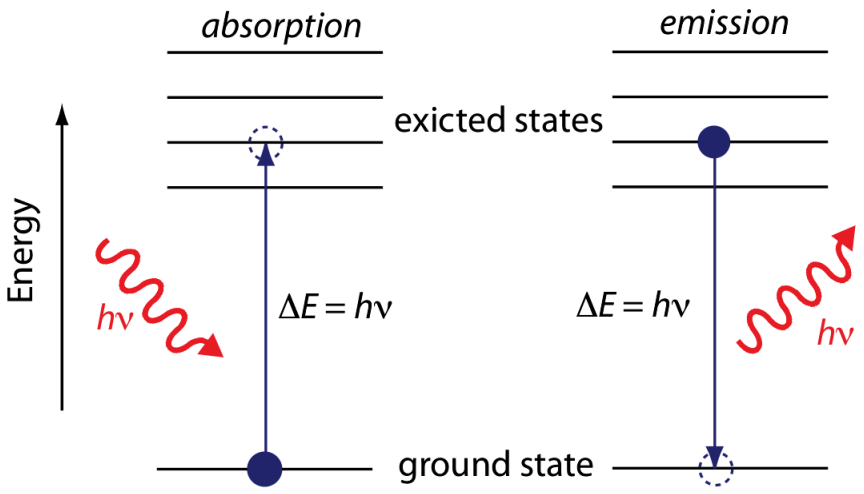

Figure 5.5 Diagrammatic illustration of absorption and emission of a photon by an atom or a molecule.

5.5.1 Raman spectroscopy

The Raman effect, on which Raman spectroscopy is based, consists of measuring a frequency shift of the light scattered by a sample subjected to monochromatic illumination. The advantages of this technique are that it is applicable to all samples regardless of its form (liquid, solid or gas), it is possible to work with small samples and no prior sample preparation is required. In the case of diamond, Raman spectroscopy provides reliable information on the crystalline quality of the samples by giving the state of stress of the material, its purity, the presence of impurities or graphitic phases.

5.5.1.1 Principle

The Raman effect is a physical phenomenon of scattering of monochromatic radiation by mono or polyatomic molecules causing a shift from the source radiation which is in the visible part of the electromagnetic spectrum. The difference in frequency between the incident photon and the scattered photon corresponds to a vibrational transition, and is characteristic of the chemical nature of the excited molecule and by extension of the analyzed material.

Under the effect of the excitation photons, the molecule scatters light which is composed of two types of radiation. Firstly, Rayleigh scattering which is an elastic scattering of the incident light. This involves a simple change in the direction of propagation of the light. The frequency of the scattered light is then equal to that of the incident light.

The other radiation is that of inelastically scattered light called Raman scattering. It corresponds to energy exchange between radiation and matter that induces a modification of the frequency. The Raman scattering represents a much smaller fraction of light compared to that of the Rayleigh scattering.

In the Raman scattering process, matter can either receive or yield energy to photons. Therefore,

the radiations can be shifted towards low frequencies or towards high frequencies. The set of scattered radiations forms the Raman spectrum of the sample. This consists of two symmetrical parts of both sides of the laser excitation frequency. They are called "Stokes Raman" (low frequencies) and "anti-Stokes Raman"(high frequencies). It should be noted that the intensity of the Stokes lines is greater ($\sim$ by a factor of 1000) than those of the anti-stokes lines [192]. Raman spectra are therefore generally studied in the Stokes line region and they are obtained by measuring the intensity of the Raman scattering as a function of the wavelength.

From a classical point of view, electromagnetic radiation of frequency ν, contains a sinusoidal magnetic field and perpendicular electric field E of the same frequency. This radiation can be coupled with any molecular movement involving a change in the state of electrical polarization of the molecule under consideration. This occurs when the frequency of the electromagnetic wave is different from the molecular vibration frequency. This concept of polarizability, which reflects the ability of the electron cloud to acquire an induced dipole moment is the basis of the Raman effect. In other words, the polarizability reflects the variation of the molecular vibration, i.e the oscillation induced dipoles. When a molecule is subjected to an electric field E, its electron cloud and nuclei will be polarized, which will result in an induced dipole moment P, defined by the following expression:

$$\mathrm{P} = \alpha \mathrm{E} \tag{5.5.1}$$

where E is the magnitude of the electric field of the incident electromagnetic wave oscillating at frequency ν. The strength of the electric field E of the incoming radiation is given by :

$$\mathrm{E} = \mathrm{E}_{\circ} \cos\left(2\pi\nu t\right) \tag{5.5.2}$$

The expression of the induced dipole moment can now be written as follows:

$$\mathrm{P} = \alpha \mathrm{E}_\circ \cos(2\pi\nu t) \tag{5.5.3}$$

The quantity α is the polarizability of the molecule and it is nothing more than the response of a medium to the applied electric field. It varies according to the inter-atomic distances. In particular, variations in polarizability associated with a natural vibration mode (phonon) can be written in terms of a Taylor expansion of the amplitude of vibration of the atoms as follow:

$$\alpha = \alpha_\circ + \left(\frac{\partial \alpha}{\partial \upsilon}\right)_{\upsilon=\upsilon_\circ} \upsilon + \frac{1}{2}\left(\frac{\partial^2 \alpha}{\partial \upsilon^2}\right)_{\upsilon=\upsilon_\circ} \upsilon^2 + \ldots \tag{5.5.4}$$

where υ is the displacement of the atoms with respect to their equilibrium position $\upsilon_\circ$ at a frequency Φ, and it is given by:

$$\upsilon = \upsilon_\circ \cos(2\pi\Phi t) \tag{5.5.5}$$

The substitution of equations 5.5.5 and 5.5.4 into 5.5.3 yields:

$$\begin{aligned} \mathrm{P} &= \left[\alpha_\circ + \left(\frac{\partial \alpha}{\partial \upsilon}\right)_{\upsilon_\circ} \upsilon_\circ \cos(2\pi\Phi t)\right] \mathrm{E}_\circ \cos(2\pi\nu t) \\ &= \alpha_\circ \mathrm{E}_\circ \cos(2\pi\nu t) + \left(\frac{\partial \alpha}{\partial \upsilon}\right)_{\upsilon_\circ} \upsilon_\circ \cos(2\pi\Phi t)\, \mathrm{E}_\circ \cos(2\pi\nu t) \end{aligned} \tag{5.5.6}$$

Using the trigonometric identity: $\cos a \cos b = \frac{1}{2}\left[\cos(a-b) + \cos(a+b)\right]$, equation 5.5.6 becomes :

$$\mathrm{P} = \alpha_\circ \mathrm{E}_\circ \cos(2\pi\nu t) + \left(\frac{\partial \alpha}{\partial \upsilon}\right)_{\upsilon_\circ} \frac{\upsilon_\circ E_\circ}{2} \left[\cos 2\pi(\nu - \Phi)\, t + \cos 2\pi(\nu + \Phi)\, t\right] \tag{5.5.7}$$

.

The expression of polarizability in equation 5.5.7 is fundamental in the classical approach. It shows the three frequency domains in which the scattered light is distributed. The first term on the right hand side of equation 5.5.7 represents the part of the light which is scattered at the same frequency (elastic scattering) as the incident light called Rayleigh scattering.

The second term represents an oscillating dipole corresponding to the emission of photons of frequencies $\nu - \Phi$ and $\nu + \Phi$ by creation or absorption of a phonon frequency of Φ. This is the first order Raman scattering. The photons of frequencies $\nu - \Phi$ and $\nu + \Phi$ are called Stokes and anti-Stokes, respectively.

It should noted that the term $\frac{\partial \alpha}{\partial \upsilon}$ in equation 5.5.7 must be non-zero. This condition is necessary for Raman scattering. It physically means that the vibrational displacement of the atoms corresponding to a particular vibrational mode lead to a change of polarizability.

The Raman spectrum contains various information. Each line or band can be characterized by its intensity and full width at half maximum. The intensity depends in particular on the density of elements and the Raman scattering cross-section of the studied structure. Since cross-sections vary between the different structures, direct comparisons of the intensities are not possible. The full width at half maximum provides information on the internal crystalline disorder in the structure. The position of the line or band in the spectrum is related to the natural frequency of a mode of vibration.

In the case of diamond, the desired structure is the sp^3 phase which is characterized by a wave number of 1332 cm^{-1}. The graphitic phase, or sp^2, is characterized by two components. Component D at about 1370 cm^{-1} corresponds to the expansion of the rings of sp^2 carbons. The G component located at $\sim 1570 cm^{-1}$ is due to vibration of sp^2 carbon bond.

The peak at 1332 cm^{-1} is the first order Raman of the diamond. This line corresponds to a T_{2g} symmetry vibration mode of the O_h group [193] with a full width at half height of 1.5 cm^{-1}. This band is allocated to LO = TO mode, where the longitudinal optical vibrations (LO) and

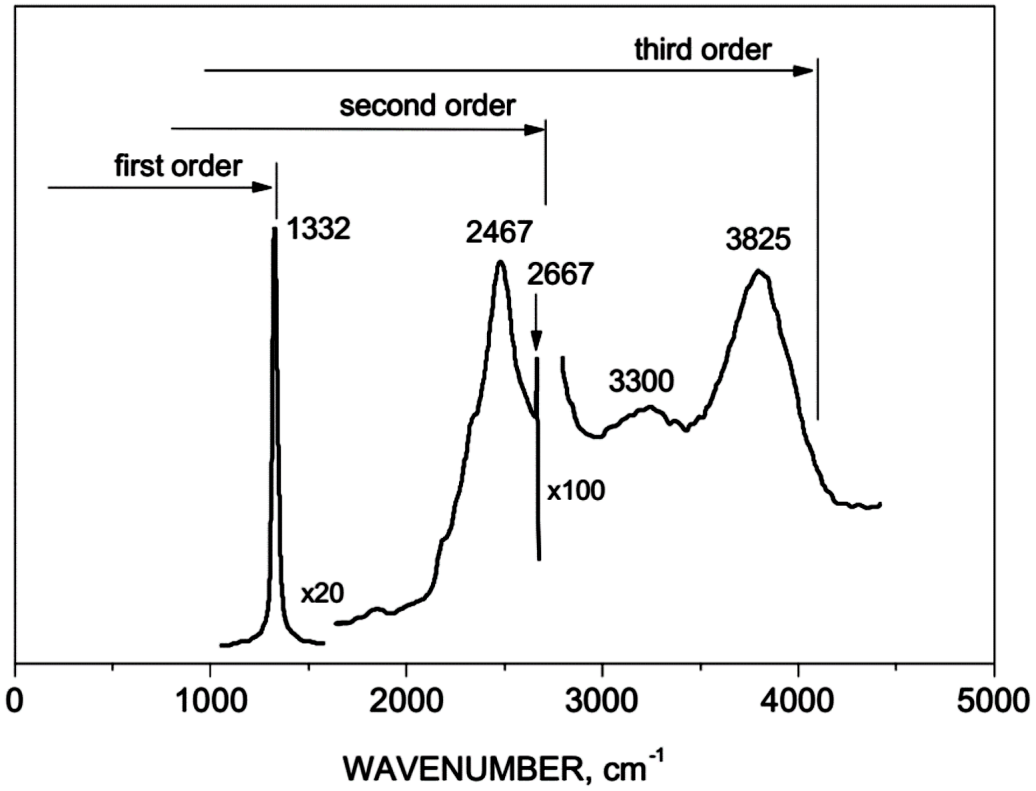

Figure 5.6 Typical Raman spectrum of diamond excited at 228.9 nm at room temperature showing first, second and third order Raman peaks [106].

transverse optical (TO) of the network are degenerate (have the same energy) due to the high symmetry of the diamond lattice [194].

5.5.1.2 Instrument

The analysis of our samples was performed at the Microscopy and Microanalysis Unit, University of the Witwatersrand. A Jobin Yvon T64000 spectrometer was used for Raman and photoluminescence measurements. This device allows the analysis of a point area (1 micron) by focusing the laser beam and facilitates the visual inspection of the impact of the laser at the sample level. This device is characterized by high speed data acquisition, high resolution and high sensitivity.

5.5.1.2.1 Spectrometer: The Jobin Yvon T64000 spectrometer consists of two stages: a pre-monochromator stage and a spectrograph stage as illustrated in Figure 5.7. The pre-monochromator stage has two monochromators with 1800 lines/mm gratings mounted in subtractive configuration. Its role is that of a filter for incident excitation. The spectrograph stage is a simple monochromator with a 600 lines/mm or 1800 lines/mm. Signal detection is provided by a CCD camera.

The spectrograph operating principle is to record a spectrum range by range. The light entering the spectrograph stage is dispersed by the grating onto the CCD. For each grating position a spectral range whose width depends on the energy of the scattered light and the grating used is recorded at the same time. This instrument is particularly well suited for weak signal measurements. In the case of intense signals its great advantage is the time saving in the acquisition of a spectrum. This instrument has different possibilities: It can be used in triple or single monochromator configuration according to the required experimental conditions. All measurements are performed under a microscope. The device is equipped with confocal optics that allows measurements on small samples and increased spatial, lateral and depth resolution. It is possible to limit the depth of the analysis area to less than 1 micron for transparent samples.

5.5.1.2.2 Exciting laser source: An argon laser as well as a ultra-violet lase were used as excitation source. The 514.5 and 458 nm excitation wavelength of the argon laser were used for Raman and photoluminescence measurements. The UV laser excitation line at 244 nm was also used for photoluminescence measurements. The incident laser beam is focused onto the sample using a BX40 Olympus microscope (several objectives were available, with magnification factors of $20\times$, $50\times$ and $100\times$), thus allowing measurement to be performed on small samples.

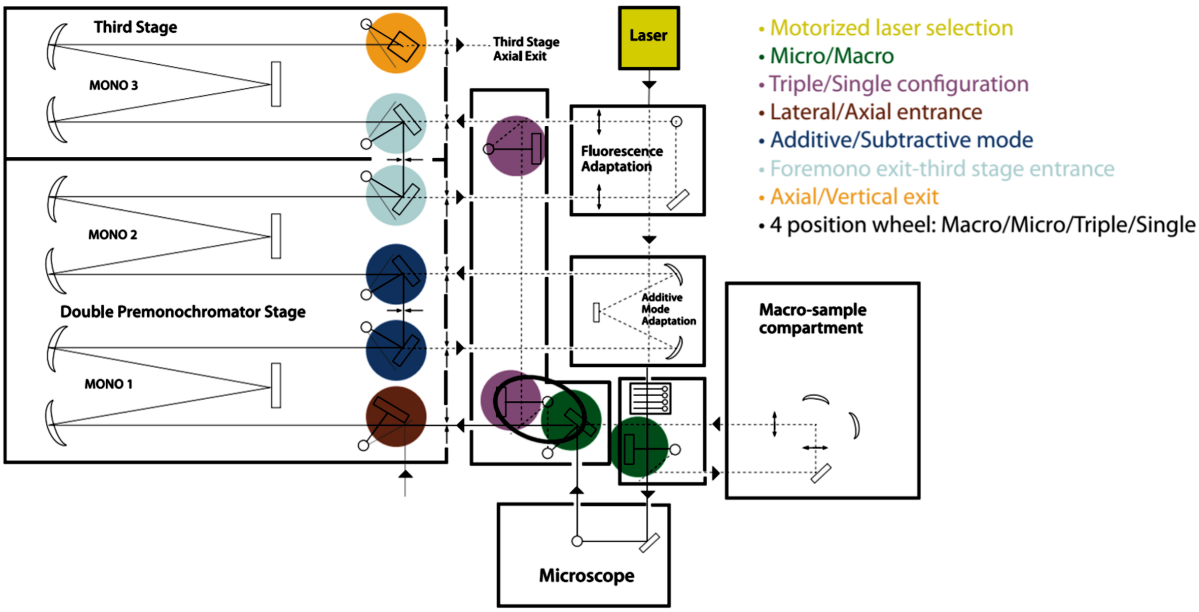

Figure 5.7 Optical path diagram showing the light path permutations of the Jobin-Yvon T64000 model spectrometer (T64000 User manual October 2009)

5.5.2 Absorption spectroscopy

Absorption spectroscopy is a non-destructive analysis technique which consists of measuring the intensity of the radiation coming from a light source, passing through a medium, and is attenuated when its wavelength coincides with that of a transition between two energy levels of one of the constituents of the probed medium. This technique is based on the Beer-Lambert law which establishes a proportionality relation between the absorption of a monochromatic light in a homogeneous and isotropic medium, the beam path length, and the concentration of a species according to the expression:

$$A = \log\left(\frac{I_\circ}{I}\right) = \varepsilon C l \tag{5.5.8}$$

where A is called absorbance and describes the decrease in the transmitted light. $I_\circ$ and I are

respectively the incoming intensity of light and light intensity after passing through the sample. l, ε and C are the beam path length, the molar attenuation coefficient and the concentration of a species, respectively.

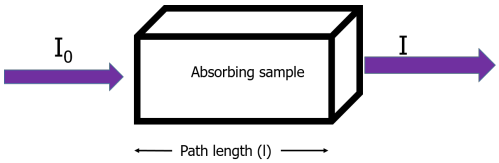

Figure 5.8 Diagrammatic illustration of principle of absorption methods.

In practice, radiation in the near-UV, visible and near-infrared range, which corresponds to the wavelength interval between 180 and 1000 nm is used to irradiate the sample. The intensities of the incident light $I_\circ$ and the transmitted light I are measured. Thereafter, the amount of the light that has been absorbed by the sample can be determined by using the Beer-Lambert law (equation 5.5.8).

In this study a Varian Cary 500 UV-Vis-NIR spectrophotometer was used to carry out room temperature measurements of diamond samples in the range of 200 to 800 nm. This spectrophotometer uses two different light sources: a deuterium lamp is used for emitting UV light while a tungsten filament lamp is used for the visible region. In addition, two detectors (PMT R928 and PbS detector) were used to record the signal according to the spectral range analyzed.

Figure 5.9 shows the components and the light path in the spectrophotometer. Light emitted by either deuterium lamp or tungsten filament goes through a filter in order to limit the noise signal before being focused onto a beam splitter inside the modulator. Two beams previously divided by the beam splitter emerge from the modulator. The first beam is passed through the reference cell while the second one is passed through the diamond sample. Both signals are then recorded by two photomultiplier tubes, and transferred to a computer where the amount of the light that has been absorbed by the sample can be calculated using the Beer-Lambert law.

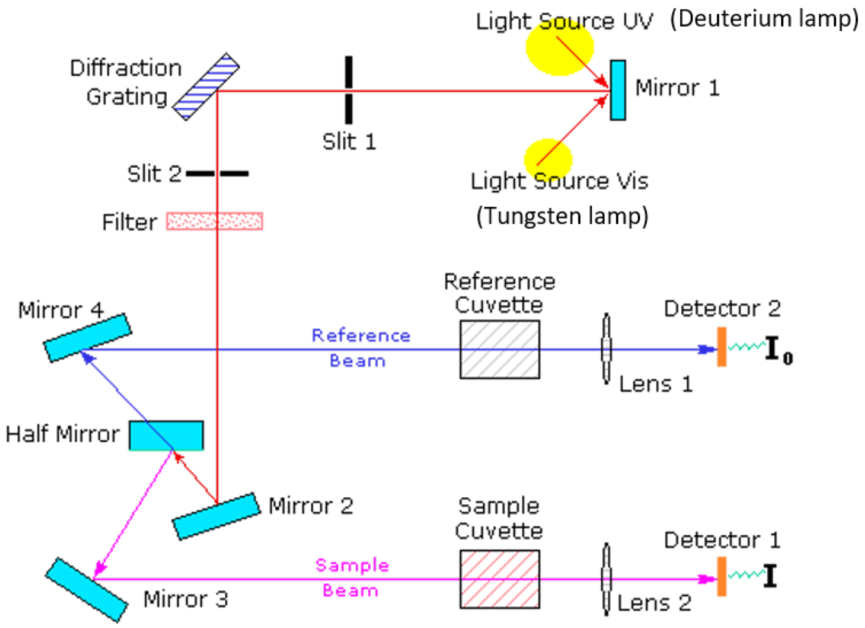

Figure 5.9 Illustration of a dual-beam UV-vis spectrophotometer.

5.5.3 Fourier-transform infrared spectroscopy

Infrared spectroscopy (IR) is one of the most widely used spectroscopic tools for the characterization of molecules. This technique studies the vibrations of a molecule when irradiated by an electromagnetic wave in the infrared range (about 0.8 μm to 1000 μm). The range of wave numbers generally used is 4000 to 400 cm^{-1} (wavelengths from 2.5 μm to 25 μm), since most of the molecules have their vibrational energies in this region.

The underlying principles of IR spectroscopy are very close to those governing UV-visible spectroscopy. The difference comes from the energy levels required by this technique, which are the molecular vibration energies. When changing the vibrational level, an electromagnetic wave can be absorbed (or emitted) only if there is simultaneously a change in the electric dipole moment. This technique involves forced the vibrations of the atoms of the material studied by causing a change in their dipole moments. Absorption described above can only be done for incident

photons having a frequency close to the vibration frequency of the studied system. In the case of intrinsic diamond, single-photon absorption is not allowed in contrast to two- or three-photon absorption. When an impurity is incorporated, the resonance frequency is then changed and it is possible knowing the resonant frequency to identify the nature of the chemical bond. By measuring the absorbance it is possible to trace the concentration of this defect.

5.5.3.1 IR spectra of diamond

The infrared region is of great importance in the study of diamond since diamonds exhibit significant absorption features in this particular region of electromagnetic spectrum. The IR absorption spectra of diamonds are usually subdivide in to three regions, namely: one, two and three phonon absorptions [195]. One phonon absorption is confined between 400 cm^{-1} and 1500 cm^{-1}. This region contains most of the absorption features related to nitrogen impurities. It is therefore used as a tool for identification of different types of diamonds [196]. Since the presence or absence of absorption features in this region indicates that the diamond samples belongs to either type I or II. The two phonon absorption region is confined between 1500 cm^{-1} and 2600 cm^{-1}. This region is characterized by the intrinsic diamond features, which is the fingerprint of diamond in the infrared region. The three phonon region contains some intrinsic diamond features and major features related to boron. Typical IR absorption spectra of all the types diamond films are presented in figure 5.10.

5.5.3.2 FTIR spectrometer

The IR spectra presented in this thesis were obtained using a Bruker tensor 27 Fourier transform spectrometer. A Fourier transform infrared spectrometer is based on the principle of light interference that modulates the amplitude of a signal as a function of the path difference between two interfering sources. An interferometer records the intensity of the light captured by the de-

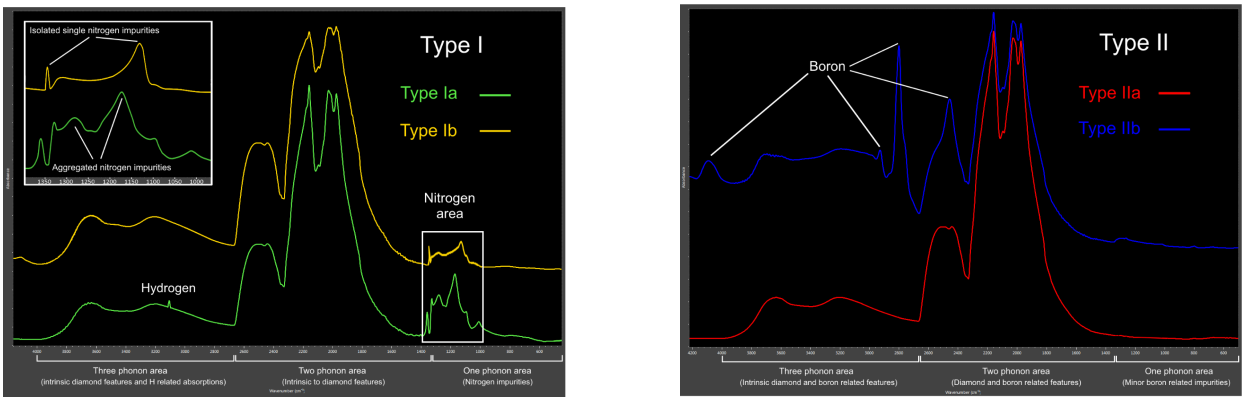

(a) **(b)**

Figure 5.10 Typical IR absorption spectra of different types of diamond films. (a) Type Ia and Ib diamonds samples, showing nitrogen related features. (b) Type IIa and IIb diamond samples, showing boron related features. Image courtesy: Magilabs Oy [196].

tector as a function of the path difference generated by the motion of a moving mirror. The measurement of the minimal displacement of this mirror is carried out by means of a laser beam which follows the same path as the infrared ray as shown in Figure 5.11. However, at this level, the interferogram refers to the position of the movable mirror and not to the wavelength that is of interest. The light from the IR source is directed through a beam splitter, which will split the incoming beam in equally two parts. The first half of the beam will be going to the fixed mirror and the other half to the moving mirror. From these mirrors, the IR light will reflect and recombine before reaching the detector. All the infrared frequencies travel at the same time in the interferometer and the rapid short-distance movements of the mirror allow the simultaneous formation of the entire infrared spectrum.

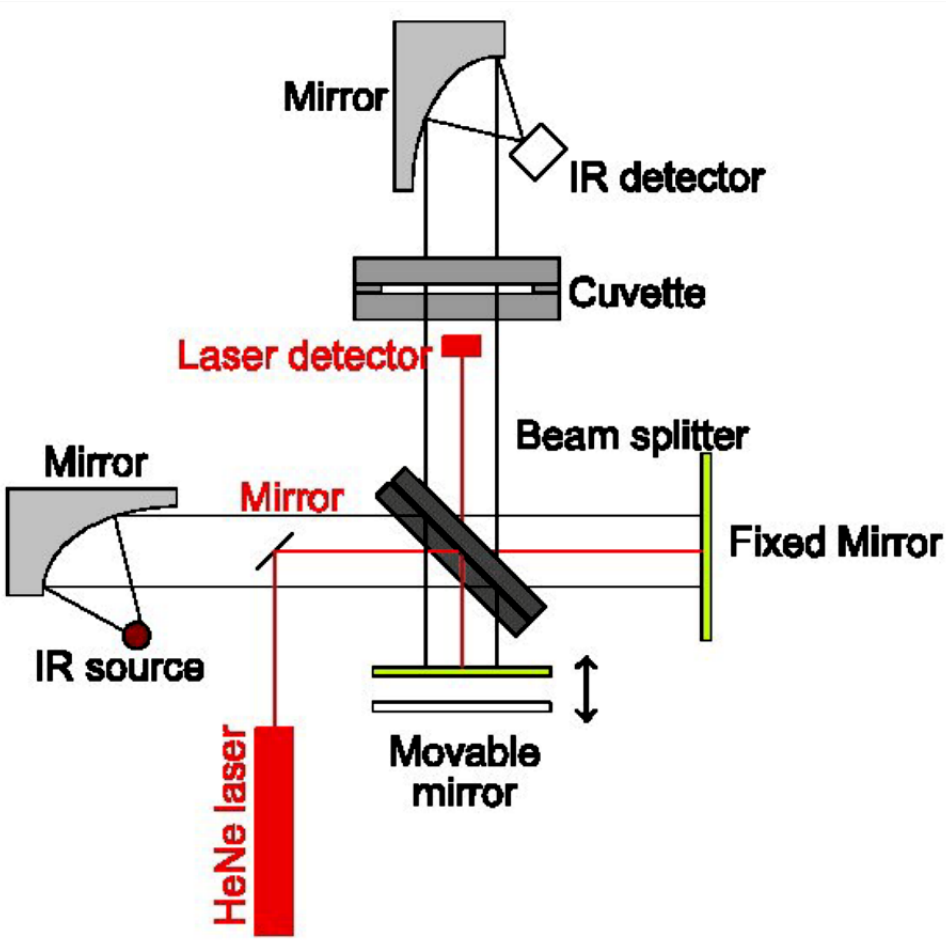

Figure 5.11 Schematic diagram of an FTIR spectrometer

The infrared beam from an HeNe laser source is directed to the Michelson interferometer which will modulate each wavelength of the beam at a different frequency. In the interferometer, the light beam will hit the beam splitter. Half of the beam is then directed to the fixed mirror while the remainder passes through the beam splitter and is directed to the mobile mirror. When the two beams recombine, destructive or constructive interferences appear depending on the position of the moving mirror. The modulated beam is then reflected from the two mirrors towards the sample, where absorptions occur. The beam then arrives on the detector to be transformed into

an electrical signal.

5.5.4 Photoluminescence spectroscopy

Photoluminescence spectroscopy is a technique that characterizes the intrinsic physical properties of semiconductor materials and also the quality of the latter by the study of defects and impurities that may exist in the band gap.

This technique is very similar to absorption spectroscopy, but here instead of considering the amount of light which is absorbed by the sample, the light emitted by atoms during their decay processes from excited states to their ground states is measured.

When excited atoms or molecules return to their initial states, they emit photons at particular wavelengths. The intensities and the associated wavelengths of the emitted light are related to donor-acceptor pair recombination processes, or other recombination mechanisms of energy states within the band gap. Indeed, the de-excitation of atoms can occur in many forms:

- non-radiative transitions with production of a large number of phonons (lattice vibrations) which causes local heating of the sample. These transitions cannot be observed in photoluminescence because no luminescence is produced.
- Band to band radiative transitions, with or without emission of phonons, depending on whether that semiconductor has a direct or indirect band gap. This causes the emission of a photon of energy $h\nu$ or less than the band gap energy E_g.
- Radiative transitions via donor and/or acceptor levels (intermediate levels in the band gap due to structural defects or impurities).
- Excitonic radiative transitions.

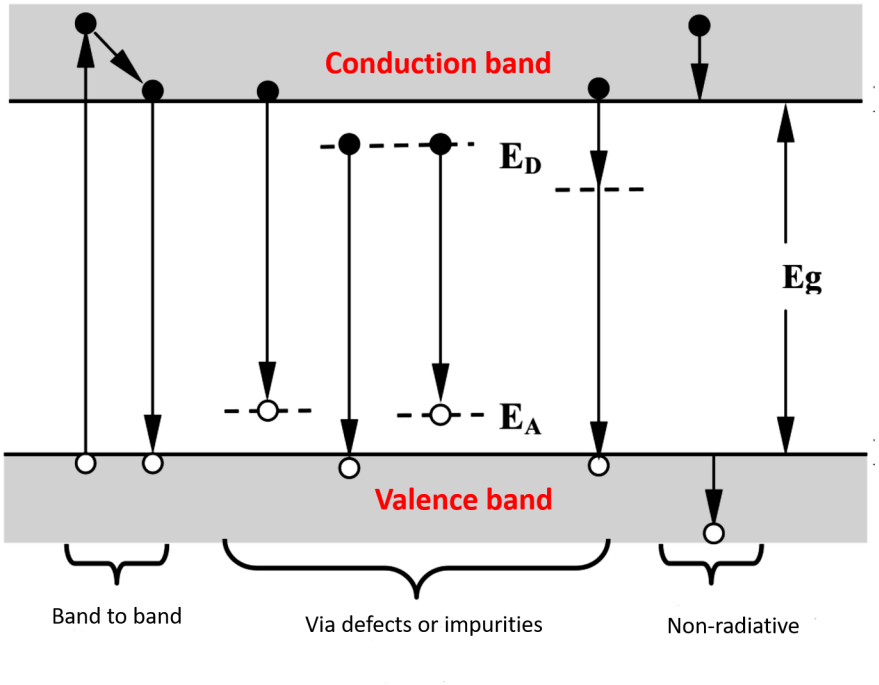

Figure 5.12 Different recombination processes in a semiconductor.

Figure 5.12 shows different recombination processes in a semiconductor.

Indeed, among the electron-hole pairs created in the semiconductor, some are likely to have their electrons and holes interact via the Coulomb interaction leading to the formation of a new state: the exciton. This electrostatic attraction between the hole (+q) and the electron (-q) lowers the energy of the pair through the formation of a bound state. The binding energy of this state will be denoted E_x. It is 80 meV in the case of diamond [197]. The free exciton in diamond is therefore stable at room temperature unlike for most semiconductors. In a doped semiconductor, excitons can also be localized around donors and neutral acceptors of the material. In that case they are called bound excitons. The localization energy E_b is defined as the binding energy between the impurity and the free exciton.

In an indirect band gap semiconductor such as diamond, the emission of a photon (providing

almost all of the energy) must be accompanied by the production of a phonon of energy $\hbar\omega$ and momentum $\hbar k$ so that the conservation of the wave vector is ensured. The radiative recombinations are therefore primarily with phonon emission as shown in Figure 5.13.

In diamond, the photon energies emitted during the radiative transitions considered are as follows:

- Band-band recombination: $h\nu = E_g - \hbar\omega$,
- Recombination of free excitons: $h\nu = E_g - \hbar\omega - E_x$,
- Recombination of bound excitons: $h\nu = E_g - \hbar\omega - E_x - E_b$

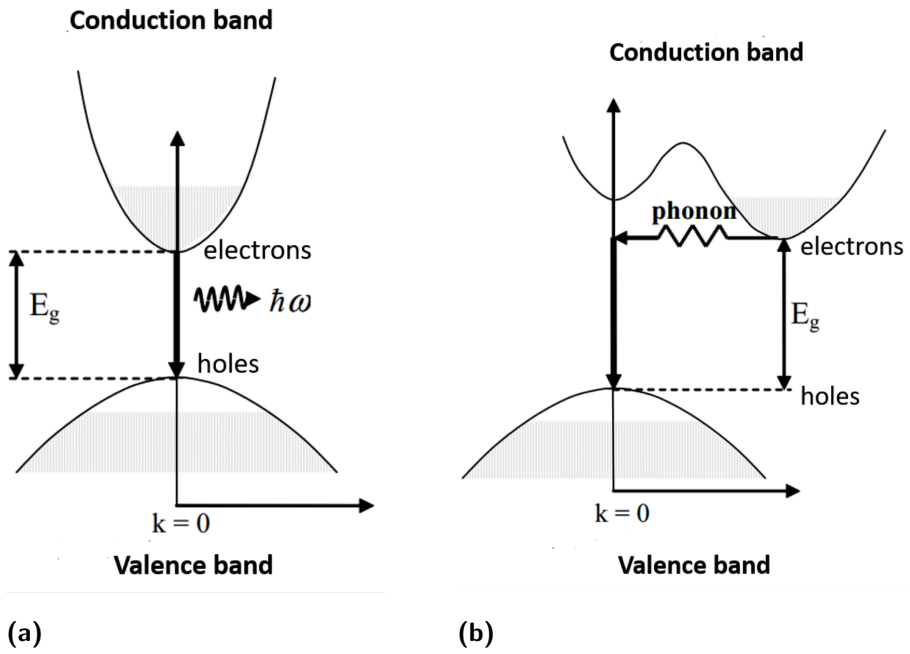

Figure 5.13 Photoluminescence scheme of (a) direct band gap semiconductor ,(b) an indirect band gap semiconductor. (Shaded areas indicate states that are occupied by electrons) [198].

The introduction of an impurity breaks the symmetry of the crystal. It also allows radiative recombinations without phonons.

There are many possibilities for radiative recombinations in diamond and several have been listed [106]. These recombinations compete with the excitonic recombinations and reduce their relative intensities [199, 200].

Instrument

For this study, a Horiba-Jobin-Yvon T64000 model spectrometer was used to perform the photoluminescence measurements. Details of this system are given in section 5.5.1.2. The measurements were recorded at room and liquid nitrogen (77K) temperatures using three different excitation wavelengths (244, 446 and 514.5 nm) from a frequency doubled Lexel argon ion laser.

5.5.5 Cathodoluminescence

Cathodoluminescence (CL) is by definition the luminescence induced by the interaction of an electron beam with the sample [106]. When a material is subjected to the energy of an incident electron beam, the electrons are slowed down by interactions with the electrons of the material. The electron-matter interaction then causes ejection of the following:

- secondary electrons, valence or conduction electrons due to ionization of deep levels; they are useful in the formation of topographical contrasts
- backscattered electrons depending on the atom that produced them; they are useful for the formation of chemical contrasts
- Auger electrons, outer shell electrons emitted by the de-excitation of electrons from inner shells
- X-ray photons also from electronic transitions involving the outer and inner shell

- visible, infrared or UV photons which are the source of the cathodoluminescence.

These photons can be emitted during the electronic transition between two states. Depending on the nature of these states, the luminescence will be either intrinsic (band to band) or extrinsic if the transition involves at least one localized state and is a characteristic of an impurity or defect.

Instrument

An Oxford MonoCL4 system attached to a JEOL JSM-7800F field emission scanning electron microscope was used for carrying out the cathodoluminescence measurements. The acceleration voltage was set at 10 kV for all the measurements. Exposure times for collecting data varied from 20-250 seconds depending on the intensity of CL obtained. The power supply voltage on the photomultiplier tube (PMT) was set at 1000 V for certain measurements. But we were obliged to change it to 700 V and 860 V for other measurements depending on the spectrum intensities obtained.

6. Results

This chapter entails results from different experimental analyses used to characterize the defect levels that arise from the implantation of nitrogen and oxygen into a diamond lattice. The Stopping and Range of Ions in Matter (SRIM) was used to predict the damage caused by implantation and the distribution profile of the implanted N-O ions. The chapter further goes on to look at the morphology of the sample surfaces before and after implantation and subsequent annealing using SEM analysis. The electronic states and surface chemical composition determined by XPS analysis are also presented. Raman spectroscopy (RS) analysis was used to determine the crystalline quality and to study the effects of implantation on the crystal structure. The recrystallization of these diamonds by heat treatment was investigated by RS. Room and nitrogen liquid temperature photoluminescence and cathodoluminescence measurements using different excitation sources allowed the identification of several defects present in the samples.

6.1 Simulation of damage caused by ion implantation

Simulations were done using the Stopping and Range of Ions in Matter (SRIM), to evaluate the damage created near the surface of the diamond samples during the implantation and to estimate the penetration depth of the implanted ions into the samples.

Figure 6.1 shows the SRIM simulation of N-O ion implantation into diamond. The calculations were done using the full damage cascade mode with a sample density of $3.52\mathrm{g/cm}^3$, an irradiation angle of 7° to the surface normal to the sample, and an acceleration energy of 9 keV for both N^+ and O^+ ions. The choice of 9 keV as the energy used in the simulation for both N and O ions was motivated by the fact that N-O ions were implanted at 18 keV. The N-O ions split when they enter the diamond and the N^+ and O^+ ions then have approximately 9 keV. An implant

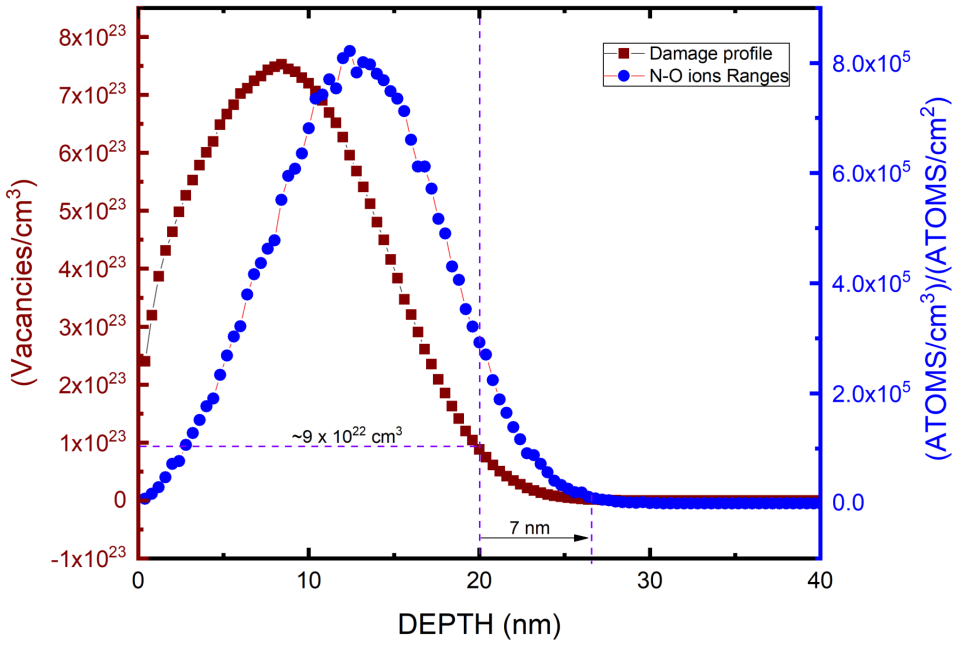

Figure 6.1 SRIM simulation showing the damage and N-O ion distribution profiles in diamond irradiated with 9 keV N^+ and O^+ ions. The damage peak is estimated at a depth of 8 nm while the ion distribution peak is approximately 13.2 nm from the sample surface. For a fluence of 1×10^{16} ions/cm^2 the simulated vacancy density is $\sim 2.4 \times 10^{23}$ vac/cm^3 at the surface of the diamond and this far exceeds the critical simulated damage density (amorphization threshold) of $5 - 9 \times 10^{22}$ vac/cm^3.

consisting of the isochemical species at 9 KeV was performed for control purposes.

In this study the implantation fluence and energy was deliberately chosen so that the TRIM damage distribution lies close to the surface. In previous studies for keV irradiation (50-200 keV) it has been shown in transmission electron microscopy (TEM) studies that when a simulated TRIM vacancy density of $\sim 5 - 9 \times 10^{22}$ vac/cm^3 is exceeded, then the diamond structure collapses upon annealing and an amorphous graphitic layer was formed [98, 201]. After boiling the diamond in an oxidizing acid solution it was observed that most of the graphitic carbon was removed and the remaining near surface layer comprise a thin damaged diamond structure which is impervious to the oxidizing acid, and also contain the implanted ion [202]. In our study this could be defects or defect complexes related to N-O, O, N and C ions. Based on the simulation made, the thickness of this layer is estimated to be 7 nm and it contains a density of N-O ions of about 3.7×10^{21} ions/cm^3, which is about 2.1 % of the atomic density of diamond (1.77×10^{23} cm^{-3}).

A summary of the diamonds and their implantation parameters is given in Table 6.1

Table 6.1 Implantations parameter

Sample	Implanted Ion	Ion energy (keV)	Fluence (ions/cm^2)
Sample 1 (N-O implanted sample)	N-O	18	2×10^{16}
Sample 2 (N-O implanted and annealed)	N-O	18	2×10^{16}
Sample 3 (Carbon implanted and annealed)	C	9	2×10^{16}
Sample 4 (Unimplanted and annealed)	-	-	-
Sample 5 (O implanted and N implanted and annealed)	Half (top): N^+	9	1×10^{16}
	Half (bottom): O^+	9	1×10^{16}

6.2 Surface morphology

A FEI Nova Nanolab 600 FEG-SEM with an acceleration voltage of 10 kV was used to characterize the surface morphology of the diamond samples under investigation. Figure 6.2 represents the SEM images showing the morphology of the surface of the unimplanted sample, N-O implanted sample, annealed carbon implanted sample and annealed N-O implanted sample.

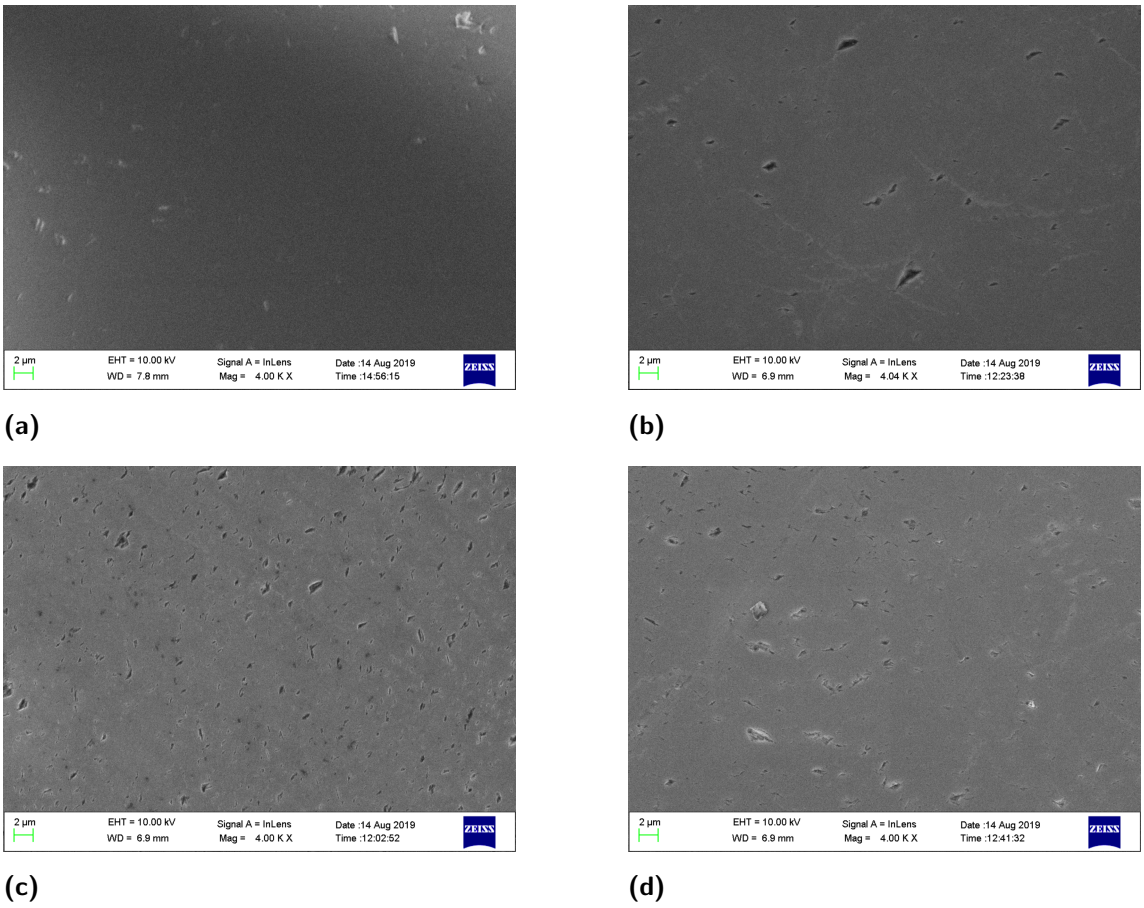

Figure 6.2 SEM images of (a) the unimplanted sample, (b) N-O implanted sample, (c) annealed carbon implanted sample and (d) N-O implanted and annealed sample.

A degradation of the diamond surface is observed on the implanted samples regardless of the ions used. This degradation is characterized by the appearance of "notches" on the sample surface. The appearance of these "notches" are caused by the high fluence used during the implantation and they are more visible on the annealed samples as show in Figures 6.2c and 6.2d. The surface of the unimplanted sample is smooth as there is no "notches" on its surface. However, one can observed some dust on the surface of this sample. Beside that, no noticeable difference are seen on these samples.

6.3 XPS analysis

Chemical analysis by X-ray photoelectron spectroscopy has been an extremely valuable tool in the work presented in this thesis. It allowed for the quantification of the chemical species, and especially to identify the nature of the bonds present on the surface of the diamond samples.

An Al X-beam of 25 W and 15 kV with a pass energy of 187 eV (1 eV/step) was used for acquisition of the wide-scan spectra (survey scans) with a resolution of 1 eV. The high resolution scan for the spectra of carbon, oxygen and nitrogen were recorded in the vicinity of the energy corresponding to each element in steps of 0.05 eV, with a resolution of 0.5 eV. The detection limit is estimated at less than 0.1 $\%$ atomic. The analysis was carried out in a vacuum of the order of 2.3×10^{-9} Torr. The XPS spectra were recorded before and after a slight argon etching of 1 min. This was done to overcome the surface contamination. The charge shift of all the spectra were corrected by referencing to the adventitious carbon C1s peak at 284.8 eV.

6.3.1 Analysis of survey spectrum

Figure 6.3 shows the wide-scan survey spectra obtained for each sample (unimplanted, N-O implanted sample, annealed N-O implanted sample) before and after argon sputtering recorded over a binding energy range of 0 to 1400 eV. These spectra are reproducible, both in intensity and in relative weight.

The analysis of the wide-scan survey spectra before sputtering mainly revealed the presence of carbon, oxygen, nitrogen and smaller proportions of calcium and silicon on the surface on these samples. The quantifications (ratio of the areas in atomic percentage) of each detected chemical species before and after sputtering are given in Table 6.2.

The detected carbon comes from the diamond and also from the carbon contamination which is

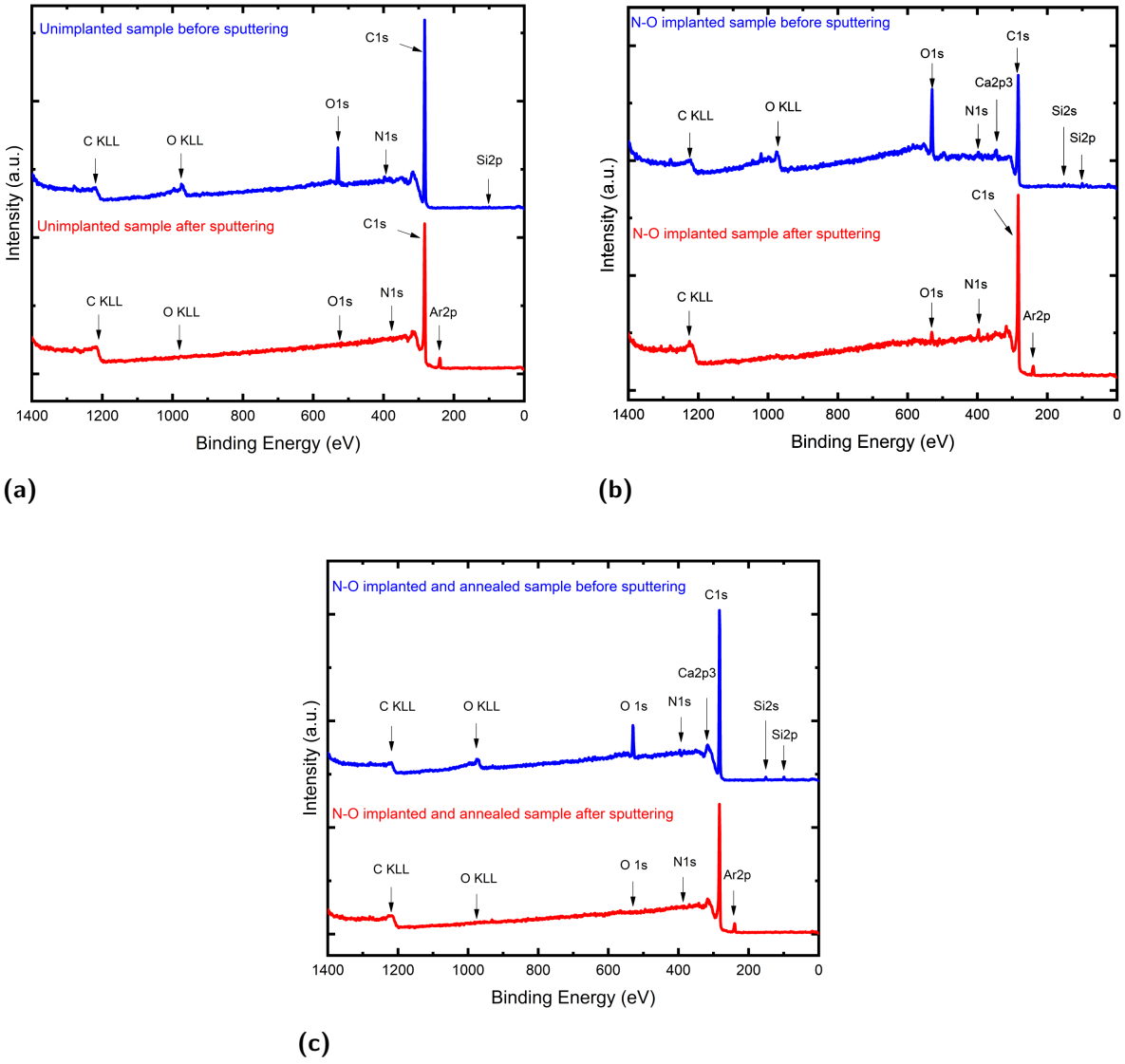

Figure 6.3 Wide-scan survey XPS of (a) unimplanted sample, (b) N-O implanted sample and (c) N-O implanted and annealed sample before (blue) and after (red) sputtering.

always present on the surface. This represents one of the major problems of the XPS analysis of the diamond. The higher oxygen value obtained on these samples (close to 10% on the unimplanted and annealed N-O implanted, and 20% on the N-O unannealed sample) comes also from the residual oxygen that is attached to the sample surface before Ar ion cleaning air contaminant. After sputtering the concentration of oxygen decreases on the N-O implanted sample and almost disappears on the unimplanted sample.

In addition, traces of calcium and silicon atoms disappeared after argon sputtering. This indicated the presence of these impurities as contamination on the surface and not in the bulk of the samples.

It is also observed that there is an appearance of argon atoms after sputtering. Peaks corresponding to Auger KLL electrons of carbon and oxygen are also observed.

The analysis of the wide-scan survey spectra revealed that the samples under investigation did not contain any other chemical impurities apart from nitrogen and oxygen which were implanted (considering that the nitrogen concentration provided from the supplier for these samples was less than 1 ppm). However, the wide-scan spectral analysis alone does not provide accurate information on the surface chemistry of the investigated diamond films. High resolution peak analysis is needed and gives more precise information about the chemical environment of each element. Thus, the decomposition of the peak C1s, O1s and N1s provided better information on the different chemical bonds present on the sample surfaces.

6.3.2 XPS high resolution spectra

The characterization of XPS high resolution spectra generated on the diamond surface is based on the deconvolution of the peaks associated with nitrogen, oxygen and carbon. The study of these elements allows us to extract information on the nature of the chemical bonds of the species detected as well as the structure of the films.

Table 6.2 Atomic concentrations of elements on the surface of the samples before and after sputtering

Samples	Atomic concentrations before sputtering (%)	Atomic concentrations after sputtering (%)
Unimplanted sample	C1s : 90.4	C1s : 97.3
	O1s : 9.30	O1s : <0.1
	N1s : 0.30	N1s : 0.8
	-	Ar2p : 1.8
N-O implanted Sample	C1s : 74	C1s : 92
	O1s : 20	O1s : 3.0
	N1s : 3.0	N1s : 3.7
	Si2p : 1.3	Ar2p : 1.3
	Ca2p : 1.3	-
N-O implanted and annealed sample	C1s : 86.2	C1s : 98.3
	O1s : 9.4	O1s : <0.1
	N1s : 3.2	N1s : <0.1
	Si2p : 1.2	Ar2p : 1.7

6.3.2.1 Carbon C1s

XPS analysis of the core level C1s recorded on the surface of the samples under investigation before argon sputtering are shown in Figure 6.4. These spectra were recorded at high resolution. The first observation that can be seen is the similarity of C1s peaks of the unimplanted and annealed N-O implanted samples. Their spectra look the same and they are almost symmetric, unlike the N-O implanted sample which had an asymmetrical shape.

Based on previous analysis performed on CVD implanted diamond samples and considering the shape of the spectra, these peaks were deconvoluted into four elementary components namely C1, C2, C3 and C4. The binding energies and full width at half maximum of each component are given in Table 6.3.

In each sample, the spectra shows the presence of a principal peak named C2 located around 284.84 eV. This peak unambiguously corresponds to the sp^3 hybridization of carbon in the diamond phase. This value is in agreement with the results found in literature [203–205].

The peak named C1 corresponds to sp^2 hybridized carbon-carbon (C=C) bonds. The position of the C1 varies with sample, as it is located at 283.8 eV for unimplanted and N-O implanted and annealed samples, while it is shifted to 284.46 eV for the N-O as-implanted sample (unannealed). All these sp^2 values are in agreement with literature, since it has been found that the component attributed to graphitic sp^2 bonds can be observed with a negative displacement of 0.8 eV to 1.3 eV relative to the diamond matrix (sp^3 C-C) [179–181].

The third component C3 peak is located at 285.5 eV for the unimplanted and N-O implanted and annealed samples, while it is centering at 285.9 eV in the N-O implanted sample (unannealed). This peak is attributed to the hybridization of sp^2 bonding structures of C atoms bonded to N atoms (C=N) [185, 204, 206]. The last component of the core level C1s named C4, is related to carbon-oxygen bonds. This peak is located between 286 eV and 290 eV. The presence of these

Table 6.3 Characteristics of the C1s peak components for the samples under investigation recorded before argon etched

Samples	Components	Peak (eV)	FWHM (eV)	Ratio (%)
Unimplanted sample	C1	283.71	0.93	8.28
	C2	284.79	0.85	82.23
	C3	285.65	0.83	8.11
	C4	286.76	0.95	1.38
N-O implanted Sample	C1	284.46	1.37	23.59
	C2	284.87	1.44	43.79
	C3	286.03	1.91	21.99
	C4	288.36	1.84	10.72
N-O implanted and annealed sample	C1	283.8	0.93	11.5
	C2	284.82	0.84	80.14
	C3	285.65	0.83	7.08
	C4	286.76	0.95	1.28

components linked to C-O bonds is consistent with the presence of the O1s peak around 533 eV [203, 206]. The C4 peak for the unimplanted and N-O implanted and annealed samples is located at 286.7 eV and shifts to 288.4 eV in the as-implanted N-O sample. It is much broader in this sample compared to the others samples.

Figure 6.5 represents the high resolution spectra of the C1s core level of the samples under investigation, recorded after cleaning the samples by argon etching for 1 min.

As expected, Ca and Si, which were present on the surface of the samples disappeared from the survey scan after the etching. However, a profound change is observed in the binding energy and the shape of the C1s peak. Argon ion etching caused a broadening of the carbon peaks due to

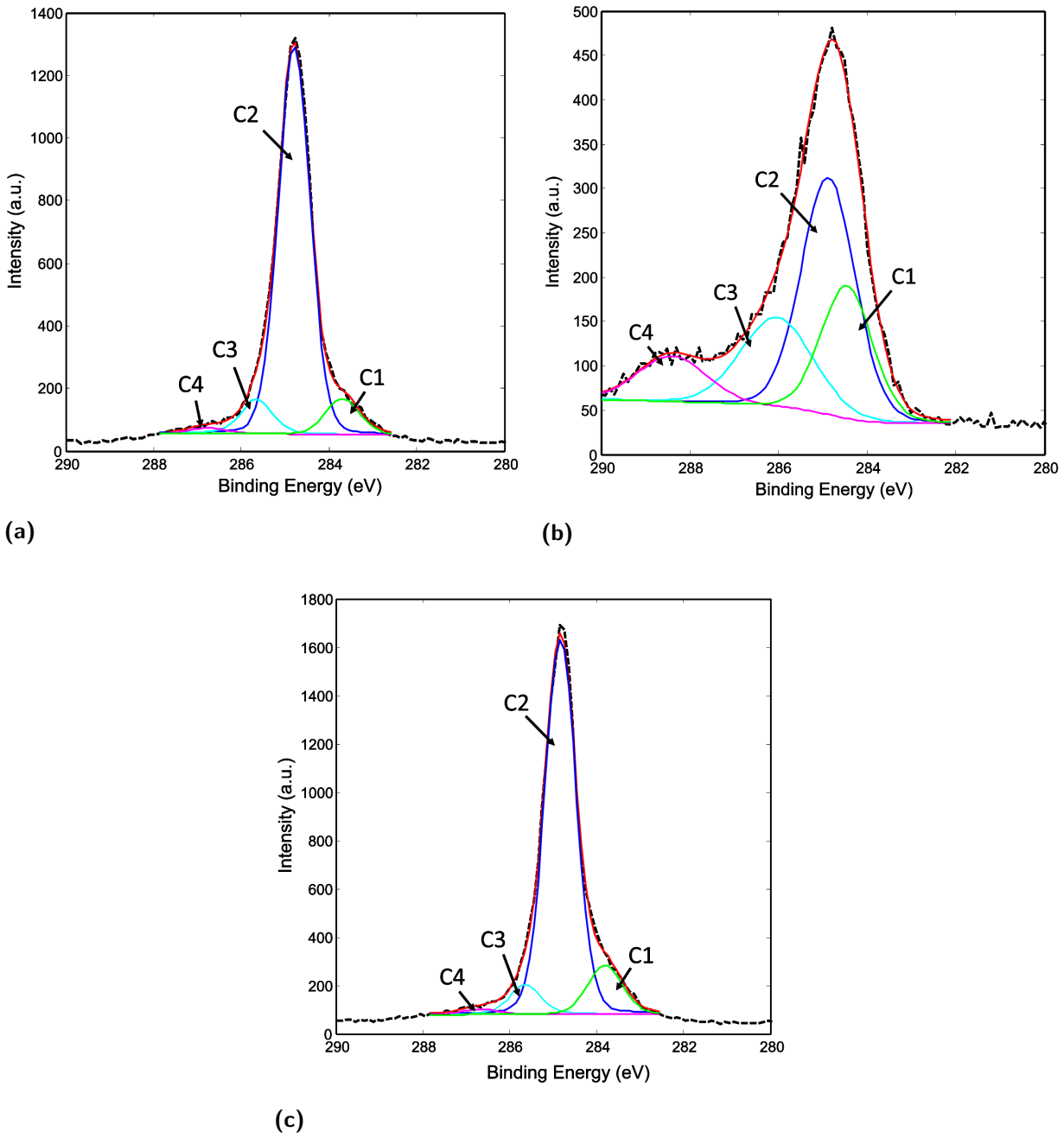

Figure 6.4 High resolution XPS spectra on C1s for (a) unimplanted sample, (b) N-O implanted sample and (c) N-O implanted and annealed sample recorded before the removal of air contaminant by argon etching.

surface rearrangement by the bombardment. This effect has been discussed in several studies where modification was noticed on the surface of the layer after the removal of impurities by Ar ion etching [207–209].

Lau et al. [210] have shown that the bombardment of a diamond sample caused a rearrangement of the bonds, and therefore the sp^3 /sp^2 ratio decreases with the bombardment, which explains why the sp^3 bonds are broken to form the sp^2 bonds. This is consistent with our observations, as it is observed through the broadening of all our spectra as shown in Figure 6.5). In addition, the contribution of the C2 peak (area of this component) which is attributed to sp^3 hybridization of carbon has been reduced in all the samples while the contribution of the C3 peak (sp^2 C=N) is increased as shown in Table 6.4. It is noticeable that the C1 peak which is assigned to hybridized sp^2 C-C bonds, shifted ($\simeq 0.4\ eV$) toward the lower energy for both unimplanted and N-O implanted and annealed samples, while it became more prominent on the N-O implanted sample compared to the other two samples. This is in agreement with our Raman results. The presence of more graphitic carbon phase on this sample is due to the fact that this sample was implanted with N-O ions and no post heating treatment was done on it.

In addition, we observed that the C4 component situated between 286 and 289 eV was present only on the N-O implanted (unannealed) sample. This component suffers a decrease in peak intensity compared to the one observed previously (before argon etching). This component is affected by the inclusion of contamination corresponding to the C-O bonds, but cannot entirely be substituted for "C-O" peaks.

6.3.2.2 Oxygen (O1s) and nitrogen (N1s) spectra

There are few studies of diamond O1s and N1s spectra reported in the literature compared to C1s spectra. However, the information that can be drawn from the study of these spectra is quite important. This helps in confirming or invalidating hypotheses formulated during the

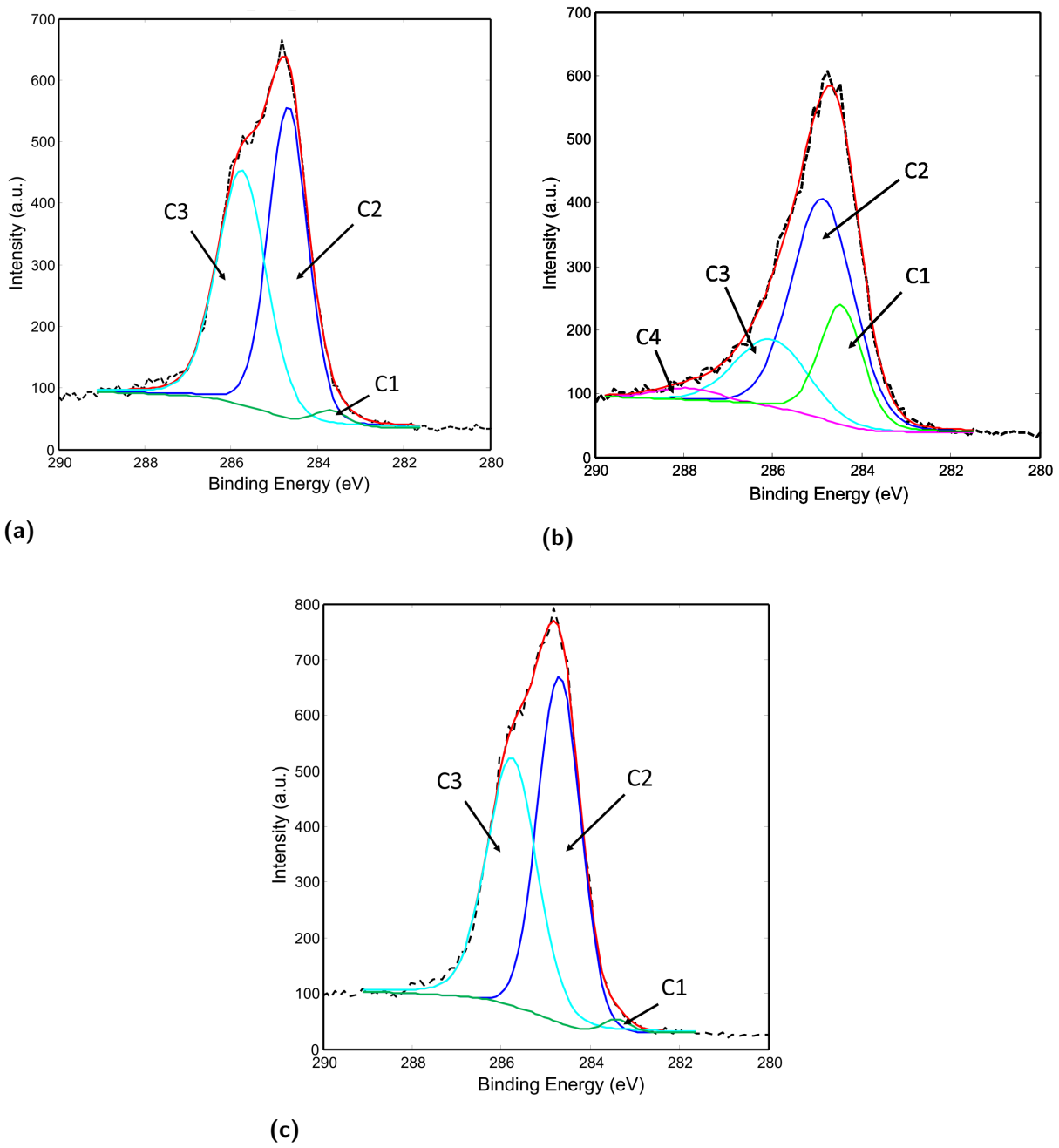

Figure 6.5 High resolution XPS spectra of C1s on (a) unimplanted sample, (b) N-O implanted sample and (c) annealed N-O implanted sample recorded after the removal of air contaminants by argon etching.

Table 6.4 Characteristics of the C1s peak components for the samples under investigation recorded after argon etched

Samples	Components	Peak (eV)	FWHM (eV)	Ratio (%)
Unimplanted sample	C1	283.71	0.95	2.17
	C2	284.67	1.07	49.82
	C3	285.75	1.34	48.01
	C4	286.76	0	0
N-O implanted sample	C1	284.4	1.14	21.66
	C2	284.87	1.64	55.25
	C3	286.03	1.91	19.87
	C4	287.91	1.72	3.21
N-O implanted and annealed sample	C1	283.41	0.72	1.28
	C2	284.69	1.33	51.56
	C3	285.75	1.14	47.17
	C4	286.76	0	0

deconvolution of C1s spectra and also to show evidence for the binding energy related to N-O on the surface of N-O implanted samples.

The XPS analysis performed in this section is mainly focused on the spectra recorded for the N-O implanted sample. This is due to the fact that after argon sputtering was carried out for 1 min in order to remove the air contaminants on the surface of the samples under investigation, the recorded spectra of N1s and O1s for the unimplanted and N-O implanted and annealed samples became hardly discernible and were therefore difficult to analyze.

For illustrative purposes, the spectra recorded on the N-O implanted and annealed sample before and after the removal of surface contamination are shown in Figure 6.6.

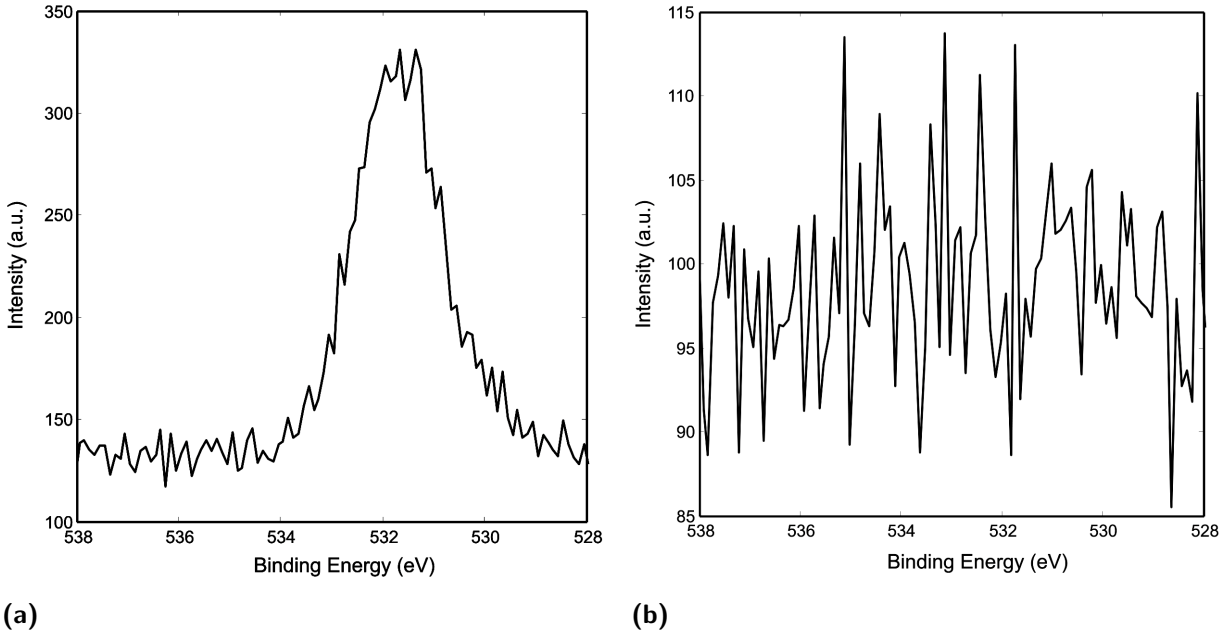

Figure 6.6 XPS spectra of O1s on N-O implanted and annealed sample (a) before argon etching and (b) after argon etching.

The recorded spectrum for the N-O implanted and annealed sample before the surface cleaning (Figure 6.6a) shows a broad peak of O1s and this is centered around 533 eV. Several components

may be included in the observed peak. However, the origin of this high amount of oxygen on the surface of these samples has been clearly identified to be contamination from the ambient environment. After 1 min of argon sputtering, the amount of oxygen and nitrogen on unimplanted and N-O implanted samples became less than 0.1 % (see Table 6.4). Thus, the intensity of the recorded signal for oxygen is too low (see Figure 6.6b) and not conclusive in relation to a possible N-O defect peak which would cause a shift in the peak position of the oxygen and nitrogen signatures in the XPS spectra.

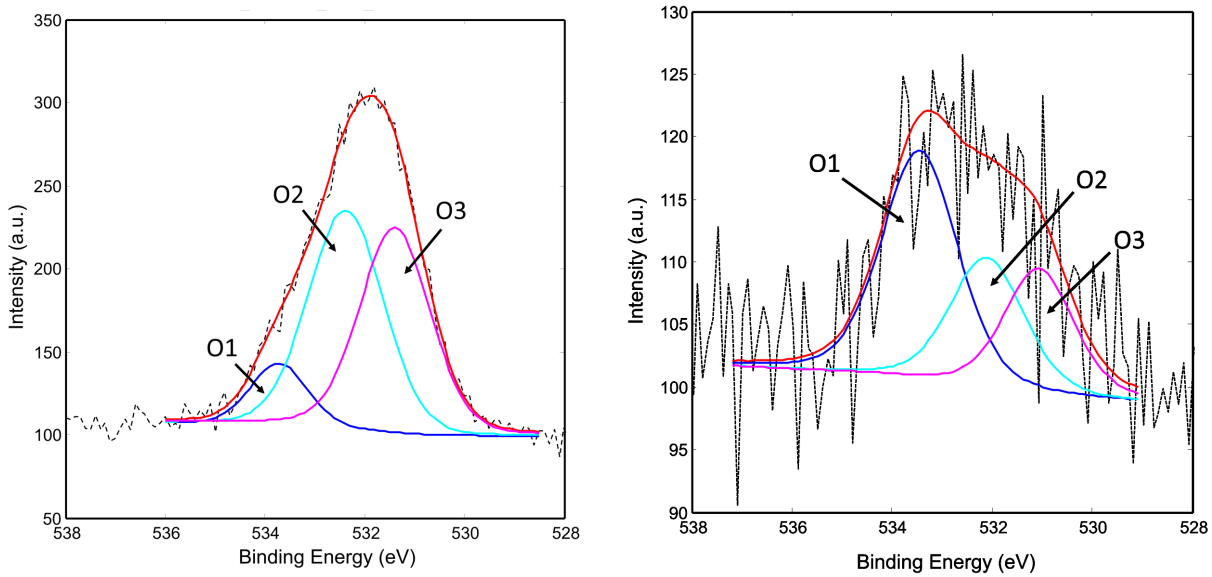

Figure 6.7 XPS spectra of O1s on N-O implanted sample (a) before argon etching and (b) after argon etching.

Figure 6.7 presents the characteristic high-resolution O1s spectra obtained in the analysis of the N-O implanted sample. The spectral decomposition of these peaks show three main contributions named O1, O2 and O3. The positions of these components for the spectrum recorded after the sample was cleaned are located at 533.4, 532.1 and 531.1 eV for O1, O2 and O3 respectively. It is observed there is a small energy shift ($\simeq 0.4$ eV) toward lower energies for the components

Table 6.5 Characteristics of the O1s peak components for the N-O implanted sample before and after argon etching

Samples	Components	Peak (eV)		FWHM (eV)		Ratio (%)	
		Before	After	Before	After	Before	After
N-O implanted Sample	O1	533.7	533.4	1.32	1.43	9.7	57.97
	O2	532.4	532.1	1.7	1.09	46.9	22.09
	O3	531.4	531.1	1.6	1.45	43.2	19.93

obtained on the spectrum recorded after argon etching. The O1 component is attributed to C-O-C [186, 187], while the O2 component has been tentatively attributed to C=O, C-O or C-HO by several authors [187, 211–213]. However, the NIST X-ray Photoelectron Spectroscopy database [214] attributed O2 peak at 532.1 eV to N-O. The last component O3 located at 531.1 eV is assigned to C-O bonds [187, 212]. These XPS results are in agreement with that found in [212].

The contribution to each component of O1s differs in the spectra recorded before and after argon etching. As seen in Table 6.5, the proportion of O2 and O3 in the O1s peak were about 46.9 % and 43.2 %, respectively. After argon etching, their contribution became less (22.09 % and 19.9 %). This shows that these components were enhanced from the contamination of the sample surface. However, the intensity of the first component (O1) did not change appreciably after argon etching.

Figure 6.8 presents the high-resolution N1s spectrum obtained in the analysis of the N-O implanted sample. This spectrum has been deconvoluted into four elementary components named N1, N2, N3 and N4. The characteristics and position of these peaks are given in Table 6.6. The first component N1 located at 398.4 eV is attributed to a nitrogen atom bonding with a carbon atom (N-C) [173]. This component becomes stronger after argon etching. The component N2

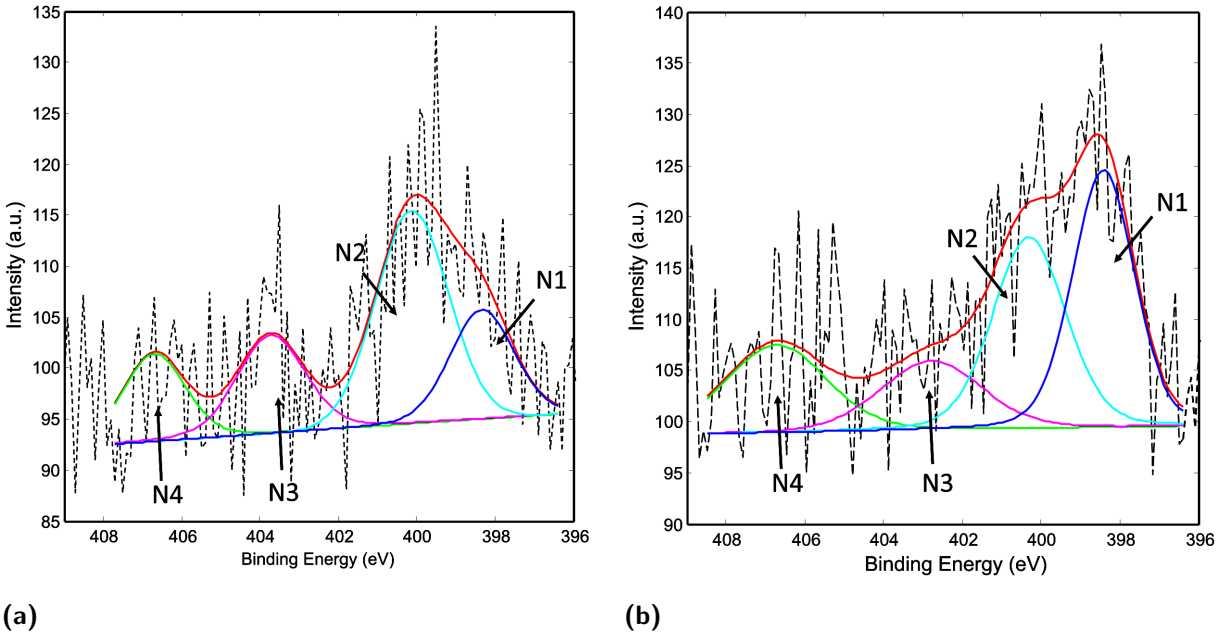

Figure 6.8 (a) O1s XPS spectra of N-O implanted before argon etching and (b) after argon etching.

located at 400 eV is assigned to N=C or N=N bonds [190, 191]. The last two components N3 and N4, are located at 402.7 and 406.9 eV, respectively. These components are attributed to the bonding between nitrogen and oxygen atoms (NO_2 and NO_3 for N3 and N4, respectively) [173, 190, 204, 215–217]. It is worth mentioning that a small energy shift in the order of 1 eV has been observed for the N3 position, since this component was at 403.7 eV before sputtering. However, after argon sputtering it shifted to 402.7 eV.

The XPS analysis done in this study enabled us to identify and quantify different chemical components present on the surface of the samples under investigation. The state of hybridization of carbon atoms were revealed by the analysis of C1s peaks. A change in the binding energy and the shape of the peak C1s was observed after cleaning the samples by argon etching of 1 min, which caused a broadening of the carbon peaks due to surface rearrangement by the bombardment. Other chemical bond structures between the atoms present within the samples (N, C and O) such as C=N, N=N, C-O, C-O-C, etc. have been observed. In addition, the analysis

Table 6.6 Characteristics of the N1s peak components for the N-O implanted sample after argon etching

Samples	Components	Peak (eV)		FWHM (eV)		Ratio (%)	
		Before	After	Before	After	Before	After
N-O implanted Sample	N1	398.4	398.4	1.90	1.84	20.36	34.47
	N2	400	400	2.19	2.20	49.43	30.71
	N3	403.7	402.7	2.04	3.04	20.24	15.38
	N4	406.8	406.9	1.86	3.04	16.40	19.43

of O1s and N1s spectra revealed evidence for the formation of N-O molecular complexes on the surface of the N-O implanted sample (not annealed). However, the XPS signal of N1s and O1s recorded on the annealed N-O implanted sample was weak which made it difficult to perform an analysis similar to the as-implanted N-O sample. It is probable that some N-O complexes were also formed on the surface of the samples but at a very low concentration. This speculation was verified with photoluminescence measurements (section 6.7) as this technique can detect impurities in diamond even at ppm concentration.

6.4 Raman measurements

Raman spectra of the unimplanted sample, N-O implanted sample, N-O implanted sample and annealed and carbon implanted sample before annealing are shown in Figure 6.9. These were recorded at room temperature with an Ar-laser line at 514.5 nm excitation wavelength.

These spectra are dominated by a sharp peak at 1332 cm^{-1} assigned to the first order Raman peak of diamond. The spectrum recorded from the unimplanted sample shows no other peaks

except the diamond peak. After ion implantation the 1332 cm^{-1} diamond Raman peak appears on a broad Raman band starting at 1150 cm^{-1} and peaking at 1520 cm^{-1} . This is shown in Figures 6.9b and 6.9d, which are the Raman spectra of the N-O implanted diamond sample and carbon implanted sample (both samples were not annealed). The broad band feature located at 1520 cm^{-1} is due to amorphous carbon and a disordered graphitic phase which is formed during ion implantation [98].

An implanted fluence of 1×10^{16}ions/cm^2 created a simulated damage density of $\sim 2.4 \times 10^{23}$vac/cm^3 at the surface of the diamond and reaches a maximum of $\sim 7.5 \times 10^{23}$vac/cm^3 at a depth of 8 nm, as shown in Figure 6.1. This was far greater than the critical damage density for diamond recovery [218]. After annealing, the intensity of the G peak was reduced significantly which indicates that the amorphous/graphitic phase that formed during the ion implantation was removed when the sample was annealed at 600 °C. Two additional peaks at 728.5 cm^{-1} and 1708.3 cm^{-1} were observed in the annealed N-O implanted sample. These peaks are from photoluminescence processes as they were not observed in the Raman spectra with a different excitation wavelength as shown in Figure 6.10. A peak at 540 cm^{-1} observed in the carbon implanted spectrum is also from a photoluminescence process. It is unusual for the G-peak intensity to reduce due to annealing and no acid boiling. After ion implantation, the surface of the diamond is visibly brown and after annealing, it becomes transparent. We postulate that because the damage profile was high on the surface, the graphitic/amorphous carbon is volatile and it evaporates during the annealing process.

Despite the diamond becoming lighter in colour after annealing, the Raman and PL spectra of all diamonds that were implanted and annealed in this study were recorded after cleaning the diamonds in an oxidizing acid solution. This was done to ensure that none of the observed features of the RS and PL were a result of artefacts that arise from the annealing environment.

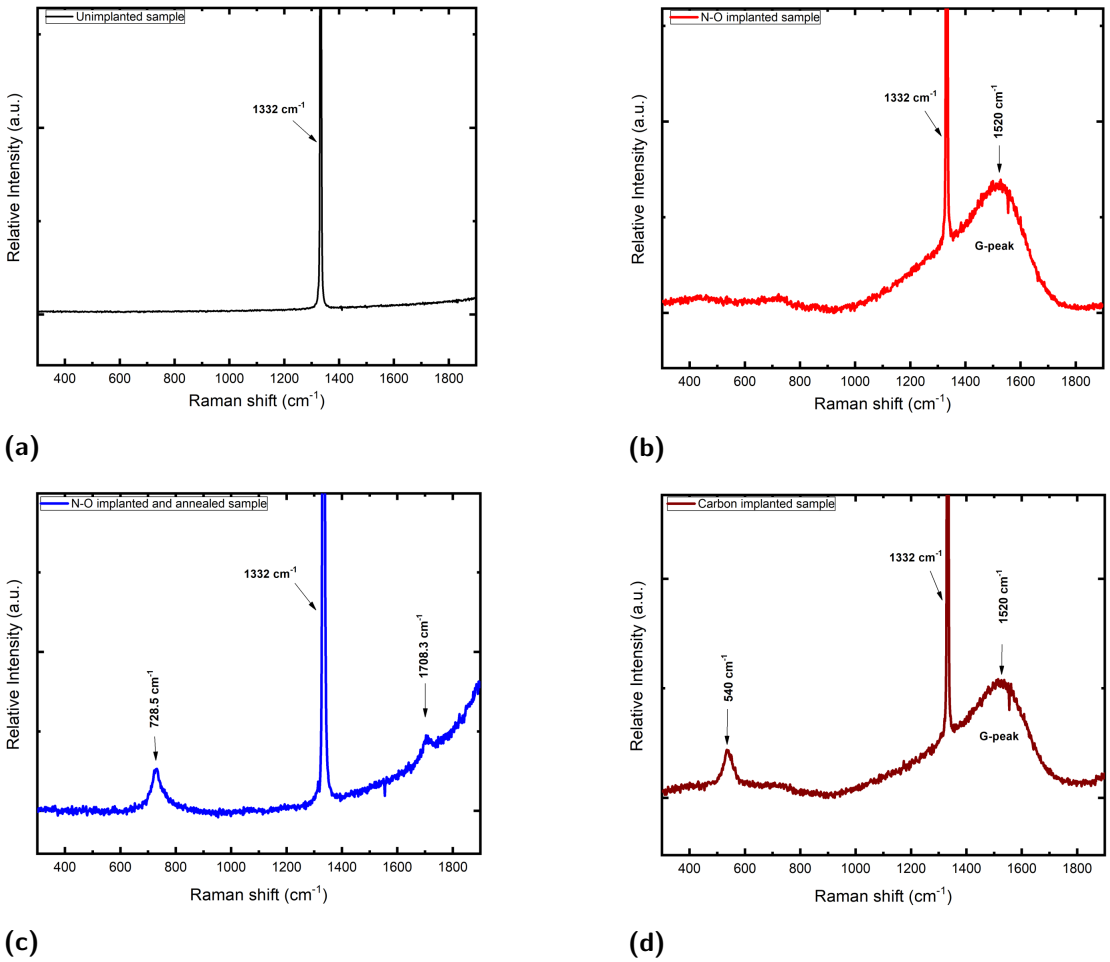

Figure 6.9 Raman spectra of (a) unimplanted sample, (b) N-O implanted sample, (c) N-O implanted and annealed sample and (d) carbon implanted sample recorded at room temperature with 514.5 nm excitation wavelength. The first order Raman peak at 1332 cm^{-1} is observed in all the samples. The N-O implanted sample shows the 1332 cm^{-1} diamond Raman peak on a broad Raman band starting at 1150 cm^{-1} and peaking at 1520 cm^{-1}. This is observed for high fluence ion implantation and the radiation damage is associated with amorphous carbon with a D band ($\sim 1350 cm^{-1}$) and G-band ($\sim 1500 - 1600$ cm^{-1}). The G mode arises from stretching from any pair of sp^2 sites from rings and chains, while the D mode is assigned to the breathing mode from sp^2 bonds in rings [98]

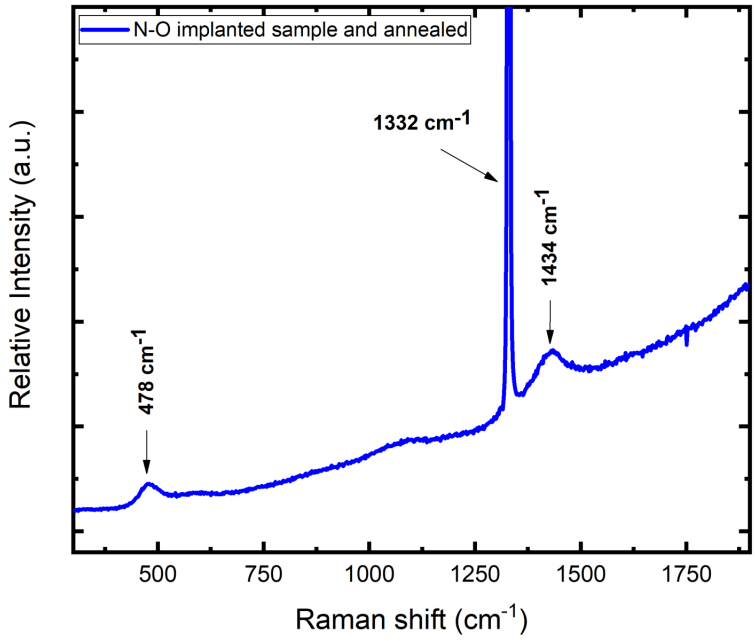

Figure 6.10 Raman spectrum of N-O implanted and annealed sample recorded at room temperature with 458 nm excitation wavelength. Peak at 1332 cm^{-1} is the first order Raman peak of diamond. Peaks observed previously at 728.5 and 1708.3 cm^{-1} on this sample while excited at 514.5 nm are not present anymore. However, new peaks can be observed at 478 and 1434 cm^{-1} and they are from photoluminescence lines.

6.5 UV-visible absorption measurements

A Varian Cary 500 UV-Vis-NIR spectrophotometer was used to carry out the room temperature absorption measurements of type IIa diamond samples used in this study in the range from 200 nm to 2500 nm. This was done in order to have complete absorption spectra of the samples under investigation.

Figures 6.11 and 6.12 show the spectra of carbon implanted, N-O implanted, unimplanted and N-O implanted and annealed samples in the ranges 200 nm to 800 nm and 800 nm to 2500 nm, respectively. All the spectra are characterized by an increase in absorption toward shorter wavelengths. This increase reaches a maximum at 223 nm (5.5 eV), which represents the intrinsic absorption edge of diamond.

The spectral line shapes of the unimplanted sample and the N-O implanted and annealed sample are very similar. The absorption intensities of their spectra tend to zero toward longer wavelengths and show no noticeable absorption feature. The observed structures in the spectra of all the samples between 2000 to 2500 nm is just noise and should not be taken as absorption features. In addition, the feature around 800 nm should not also be taken as absorption features since they are caused by the change between two detectors (photomultiplier tube) during the scans. On the other hand, the N-O implanted (unannealed) and the carbon implanted (unannealed) samples exhibit higher absorption in the recorded spectra range compared to the unimplanted and N-O implanted and annealed samples. This is normal since the surface of these samples is amorphous on the implanted side as no post implantation heating treatement was performed on these samples. Hence they are less transparent. Their spectra show an increase in absorption intensity between 250 to 600 nm. The origin of this increase in absorption is due to the absorption bands at 270 nm, 370 and 550 nm. The band at 270 nm is attributed to substitutional nitrogen atoms, while the band at 370 nm and 550 nm are attributed to the nitrogen vacancy centre [219].

The fact that there is no noticeable absorption feature in the spectrum of the unimplanted sample from 350 nm toward longer wavelengths is an indication of the high quality of the diamond films used in this study.

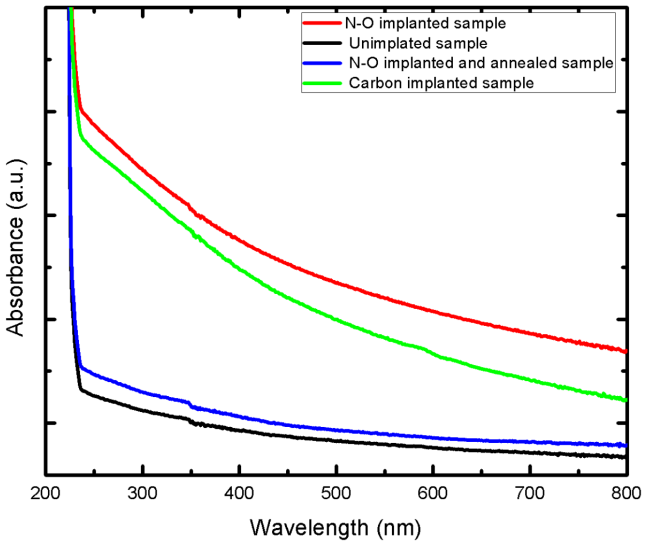

Figure 6.11 Absorption spectra of unimplanted, N-O implanted, N-O implanted annealed, carbon implanted samples in the range of 200 to 800 nm. These spectra show the intrinsic absorption edge of diamond at 223 nm (5.5 eV).

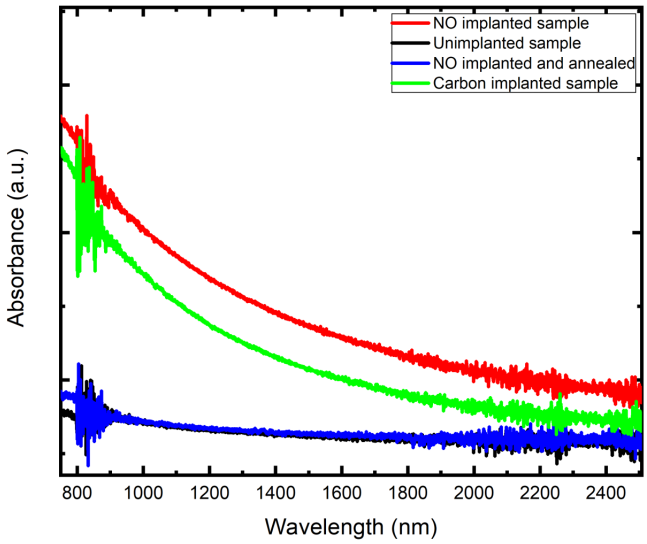

Figure 6.12 Absorption spectra of unimplanted, N-O implanted, N-O implanted annealed and carbon implanted samples in the range of 750 to 2500 nm.

6.6 Fourier-transform infrared spectroscopy measurements

Fourier-transform infrared spectroscopy (FTIR) is one of the most used techniques to identify impurities in diamond. It is used in this study to evaluate the quality of the four type IIa CVD diamond samples used in this study. The infra-red absorption spectra of diamond are usually subdivided into three regions, namely: one, two and three phonon absorptions. One phonon absorption is comprised between 400 cm^{-1} to 1500 cm^{-1}. This region contains most of the absorption features related to nitrogen impurities. The absorption feature in this range is used for classifying different types of diamond; viz type I or II. The two phonon absorption region, 1500 - 2600 cm^{-1}, is characterized by the intrinsic diamond features. The three phonon region contains some intrinsic diamond features and major features related to boron and hydrogen.

Figure 6.13 shows the IR absorption spectra in the range from 1000 cm^{-1} to 4000 cm^{-1} of the four CVD diamond samples used in this study. The spectra are dominated by absorption features

at 1970 cm^{-1}, 2030 cm^{-1}, 2160 cm^{-1} and 2500 cm^{-1}; these are the well known two-phonon intrinsic absorption peaks of diamond. The one and the three phonons absorption regions are featureless, as expected for any type IIa CVD diamond sample. However, magnification of these two regions shows some minor weak absorption peaks which are presented in figures 6.14 and 6.15

FTIR spectra in the range 800 cm^{-1} to 1600 cm^{-1} are shown in figure 6.14. Absorption features centered at 1047 cm^{-1}, 1175 cm^{-1}, 1280 cm^{-1}, 1510 cm^{-1} and 1562 cm^{-1} are observed in the spectra of each sample. There is also a peak at 1090 cm^{-1} which is more pronounced in the spectrum of the carbon implanted sample. The intensities of these features are weak and their shapes are totally different for most of the infrared absorption peaks reported previously in this wavenumber range by other authors (see Figures 3.6 and 3.7). The origin of these peaks are related to nitrogen defects. For instance the peak at 1090 cm^{-1} has been attributed to A and B aggregates of nitrogen by Sutherland et al. [106, 220], while the peak at 1510 cm^{-1} is reported to appear in synthetic and nitrogen-containing natural diamonds. According to Bokii and Malogolovet [112,221,222], the intensity of the 1510 cm^{-1} line is correlated with the concentration of single substitutional nitrogen atoms.

Figure 6.15 shows the expanded view of the spectra of Figure 6.13 in the range of 2707 to 4000 cm^{-1}. Absorption peaks at 2854 cm^{-1}, 2923 cm^{-1}, 2963 cm^{-1} and two absorption bands located at 3213 cm^{-1} and 3650 cm^{-1} were detected. The peak at 2953 cm^{-1} was observed in CVD diamonds previously and was attributed to asymmetrical stretching vibrations of sp^3 bonded CH_3 asymmetrical configurations [223–225]. Peaks at 2854 cm^{-1} and 2923 cm^{-1} have always been observed in CVD diamond films and they have been attributed to the asymmetrical and symmetrical C-H stretching modes of sp^3 bonded methylene groups $-CH_2-$ [112,226,227]. The broad absorption band located at 3650 cm^{-1} was previously seen in single-crystal CVD diamond films and was attributed to the one of the three-phonon absorption of diamond lattice [112,225]. The weak absorption features observed in one phonon absorption region are most likely due

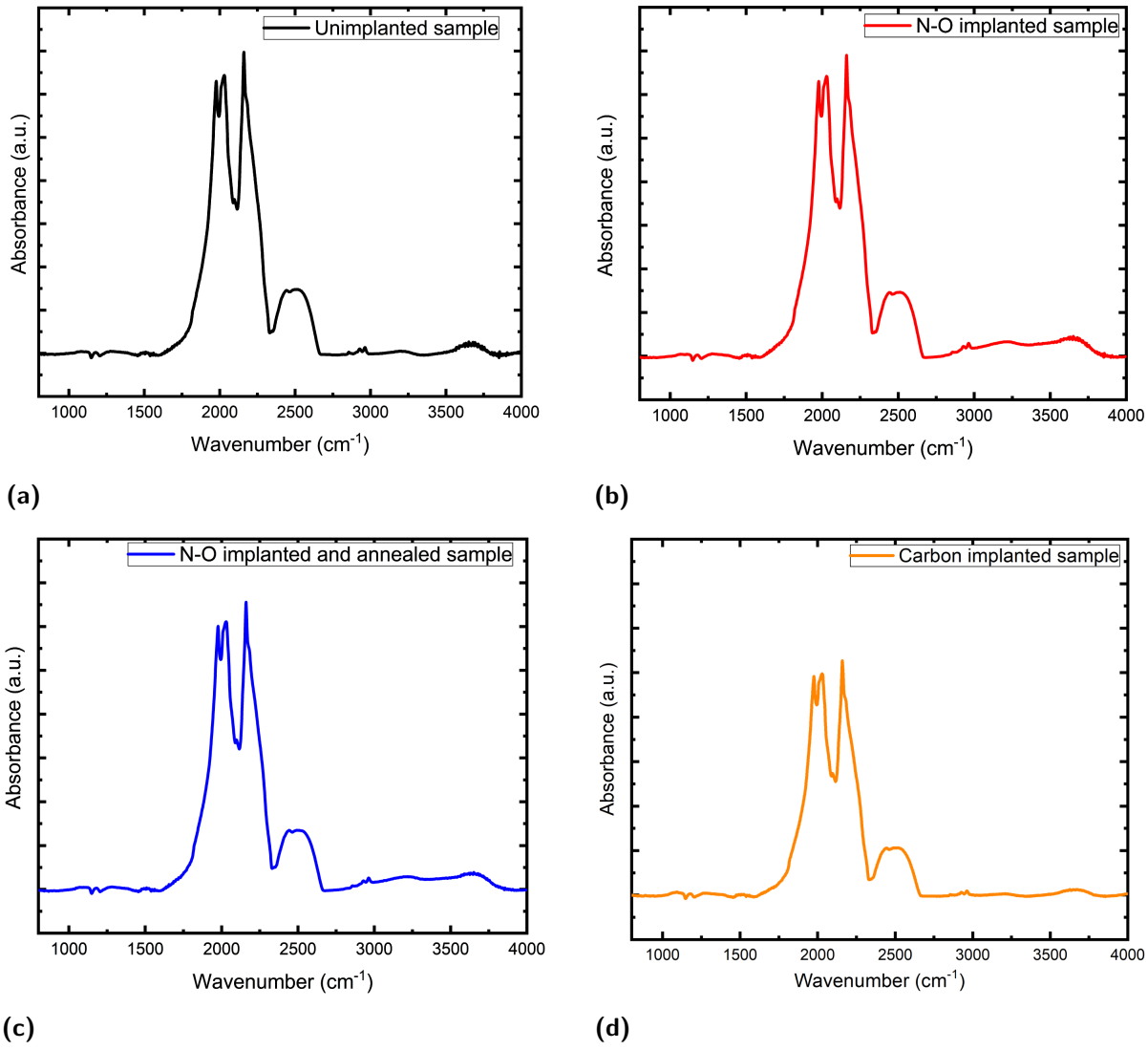

Figure 6.13 FTIR absorption spectrum of (a) unimplanted, (b) N-O implanted, (c) N-O implanted and annealed and (d) carbon implanted samples.

to intrinsic defects or to nitrogen related defects since it has been observed in all the samples regardless of their history (unimplanted or N-O/carbon implanted). In addition, the fact that we observed hydrogen related absorption features in these samples is not surprising because during the growth process there is a significant fraction of hydrogen.

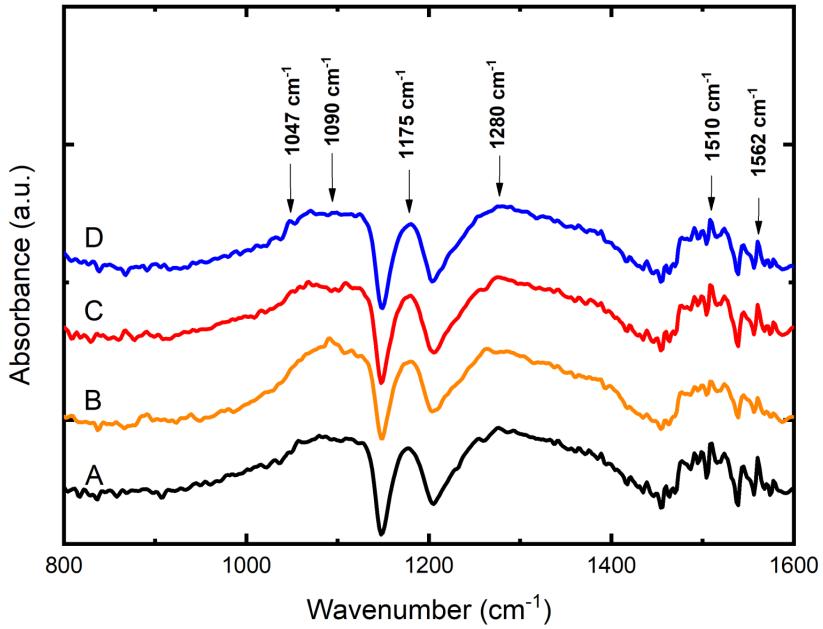

Figure 6.14 Expanded view of the FTIR spectra in the one-phonon absorption region, for (a) unimplanted, (b) N-O implanted, (c) N-O implanted and annealed and (d) carbon implanted samples.

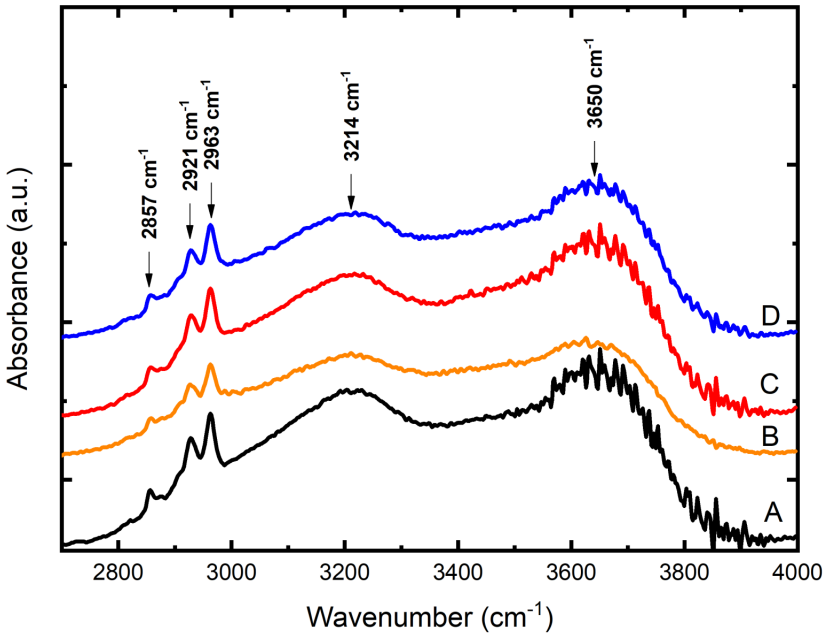

Figure 6.15 Expanded view of the FTIR spectra in the three-phonon absorption region, for (a) unimplanted, (b) N-O implanted, (c) N-O implanted and annealed and (d) carbon implanted samples.

Table 6.7 Summary of defects observed from FTIR measurements.

Defect position (cm^{-1})	**Origin of luminescence**
1970, 2030, 2160 and 2500	Absorption features characteristic of two-phonon intrinsic absorption of diamond [106].
1047, 1090, 1175, 1280, 1510 and 1562	Absorption features attributed to nitrogen defects [106, 112, 220–222].
2953	Absorption attributued to asymmetrical stretching vibration of sp^3 bonded CH_3 asymmetrical configurations [223–225].
2854 and 2923	Absorption features attributed to the asymmetrical and symmetrical C-H stretching modes of respectively of sp^3 bonded methylene groups $-CH_2-$ [112, 226, 227]
3650	Absorption feature attributed to the three-phonon absoprtion of diamond lattice [112, 225].

6.7 Photoluminescence measurements

Photoluminescence measurements conducted at room and liquid nitrogen temperature using different excitation wavelengths were used to investigate the nature and behavior of the defects induced by the implantation into diamond samples under different irradiation and annealing parameters of N-O ions into diamond sample followed by annealing at 600°C in argon atmosphere. A Jobin-Yvon T64000 spectrometer was used to record photoluminescence spectra using a 248 nm line of a He-Cd laser and 514.5 nm and 458 nm lines of an argon ion laser as excitation wavelength.

6.7.1 Room temperature photoluminescence measurements obtained with 248 nm excitation wavelength

Figure 6.16 shows typical room temperature PL spectra of the unimplanted sample, N-O implanted sample, N-O implanted and annealed sample and carbon implanted sample in the range of 260 to 750 nm obtained with 248 nm excitation wavelength. All the recorded spectra were measured under identical conditions and were normalized with the first order Raman peak at 251 nm.

These PL spectra have distinct peaks at 389 nm, 398 nm, 409.4 nm, 419.2 nm, 487.5 nm, 533 nm, 563 nm, 575 nm, 600 nm, 620 nm, 650 nm and 675 nm. The luminescence intensities of these peaks are low in the N-O implanted sample (without annealing) and carbon implanted sample as shown in Figure 6.17.

The peak at 389 nm is the ZPL of the 389 nm (3.188 eV) centre and has the highest intensity in the N-O implanted and annealed sample and the unimplanted sample. The peaks at 398 nm, 409.4 nm and 419.2 nm are its phonon sidebands (see section 3.2.1.6). The 389 nm centre

involves a carbon interstitial and a single nitrogen atom [123] as described in section 3.2.1.6.

The emission line at 487.5 nm is attributed to the TH5 centre, which is an intrinsic defect containing a divacancy observed in type Ia and IIa diamonds after electron irradiation followed by annealing at temperatures above 400 °C [106].

The peaks at 533 nm, 563 nm and 570 nm lines are reported to originate from a nitrogen related centre [106, 228, 229]. The 563 nm line was also reported in carbon irradiated diamond and was associated with interstitials [230, 231].

The peak at 575 nm corresponds to the emission line of the neutral charge state of the nitrogen-vacancy defect as described in section 3.2.2.2). The broad band peaks located at 600 nm, 620 nm, 650 nm and 675 nm are the associate phonon side bands.

Broad luminescence features are observed around 309 nm and 356 nm on unimplanted and N-O implanted (unannealed and annealed) samples. These broad band luminescence features are more intense for the annealed N-O implanted sample compare to other samples. This can be seen in Figure 6.17 where the PL spectra of all the samples under investigation are compared.

The origin of these broad luminescence features is unknown. The shape of these broad features indicates that it may contain several emission peaks which are unresolved because the measurements were carried out at room temperature. The room temperature PL measurements are characterized by a strong electron-phonon interaction which results in the overlapping of emission bands that are near each other and result in the broadening of luminescence emission bands.

The results for the photoluminescence measurements conducted at room temperature using the 458 and 514.5 nm lines of an argon ion laser as excitation sources are shown in appendix A and B.

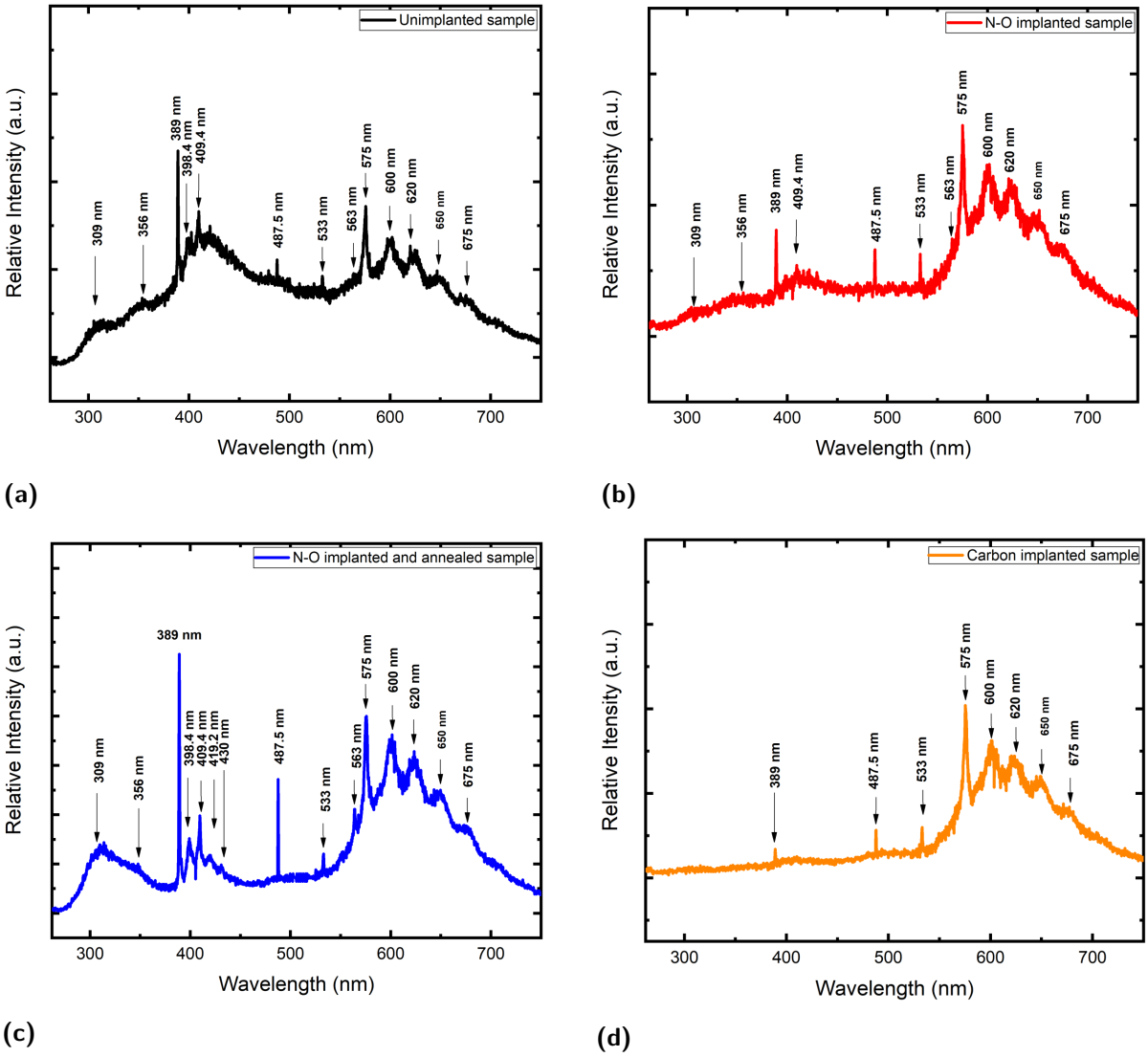

Figure 6.16 Typical PL spectra of (a) unimplanted sample, (b) N-O implanted sample, (c) annealed N-O implanted sample and (d) carbon implanted sample in the range 260 to 750 nm. These spectra were recorded at room temperature using 248 nm for excitation. All the spectra were normalized with the first order Raman peak at 251 nm.

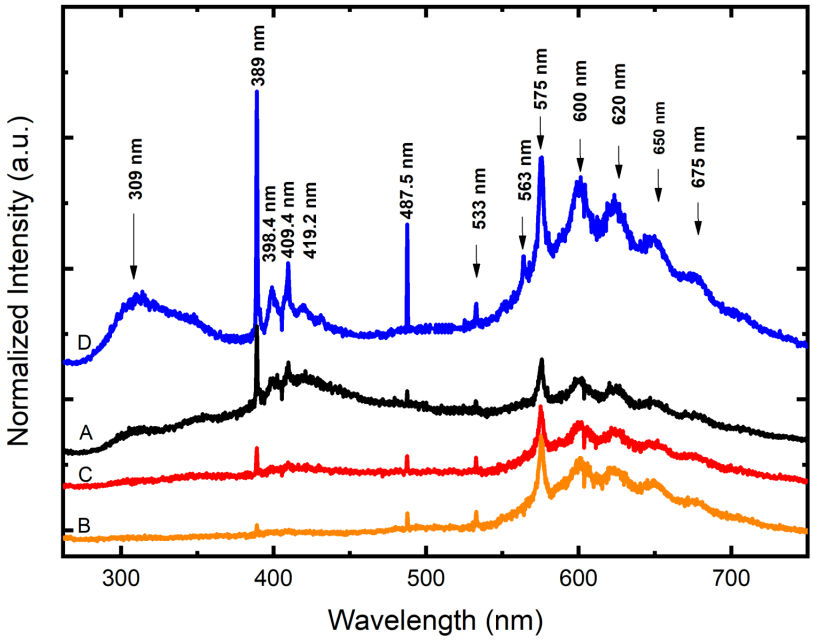

Figure 6.17 Comparison of PL spectra of unimplanted sample (spectrum A), carbon implanted sample (spectrum B), N-O implanted sample (spectrum C) and annealed N-O implanted sample (spectrum D). These spectra were recorded at room temperature using 248 nm for excitation. The spectra are vertically offset for more convenience and were normalized with the first order Raman peak at 251 nm.

6.7.2 Low temperature photoluminescence measurements obtained with 248 nm excitation wavelength

Conducting PL measurements at liquid nitrogen temperature will provide more information with regards to the observed broad band feature located at 309 nm, since at liquid nitrogen temperature, most of the carriers are completely frozen in and the lowest energy states can be easily seen.

Photoluminescence measurements were carried out at liquid nitrogen temperature for the unimplanted sample (annealed at 600°C), N-O implanted sample (without annealing), N-O implanted

and annealed (600°C) sample and the carbon implanted sample annealed at 800°C in the range of 260-800 nm. The reason why the carbon implanted sample was annealed at 800°C is given in section 6.7.3. All the recorded spectra were measured under identical conditions and were normalized with the first order Raman peak at 251 nm. For convenience, the recorded spectra were plotted in three ranges separately as follows: 262-330 nm, 330-450 and 450-660 nm.

Figure 6.18 presents the photoluminescence spectra measured at 77 K same samples in the range of 262 to 330 nm.

Broad PL emission bands were observed from all the samples with a maximum centred around 309 nm. This broad luminescence band is more prominent in the annealed N-O implanted sample. In addition, sharp emission peaks were observed at 270.3 nm, 278.1 nm, 281.5 nm, 285.1 nm, 301.5 nm, 319.7 nm and 328.3 nm in the spectrum of the unimplanted sample, annealed N-O implanted and carbon implanted samples. The luminescence intensities of these peaks are low in the unannealed N-O implanted sample as shown in Figure 6.19 where these spectra are compared. This indicates that these are intrinsic defects in the diamond material (as supplied) and the defect centres that give rise to these luminescent transitions are increased after annealing. The decrease in the optical activity on the N-O implanted sample (not annealed) is caused by the strain created in the implanted layer during the implantation process as a result of the displacement of the atoms from their lattices sites. The displaced atoms create defects which increase the non-radiative paths that excited electrons can follow. Annealing the sample leads to a decrease in strain in the implanted layer which then causes an increase in the PL activity in the sample [232]. The peaks at 290.5 nm and 330.4 nm are only present in the PL spectra of the N-O implanted and carbon implanted samples.

The peak at 270.3 nm is the zero phonon line of the 5RL system (see section 3.2.2.2) which is a common radiation damage centre observed in types IIa, IIb and Ib diamonds after high energy electron irradiation and ion implantation [106, 132]. The 5RL centre has also been observed in as-grown CVD diamond films [130, 233]. The peaks at 285.1 nm, 301.5 nm, and 319.7 nm are

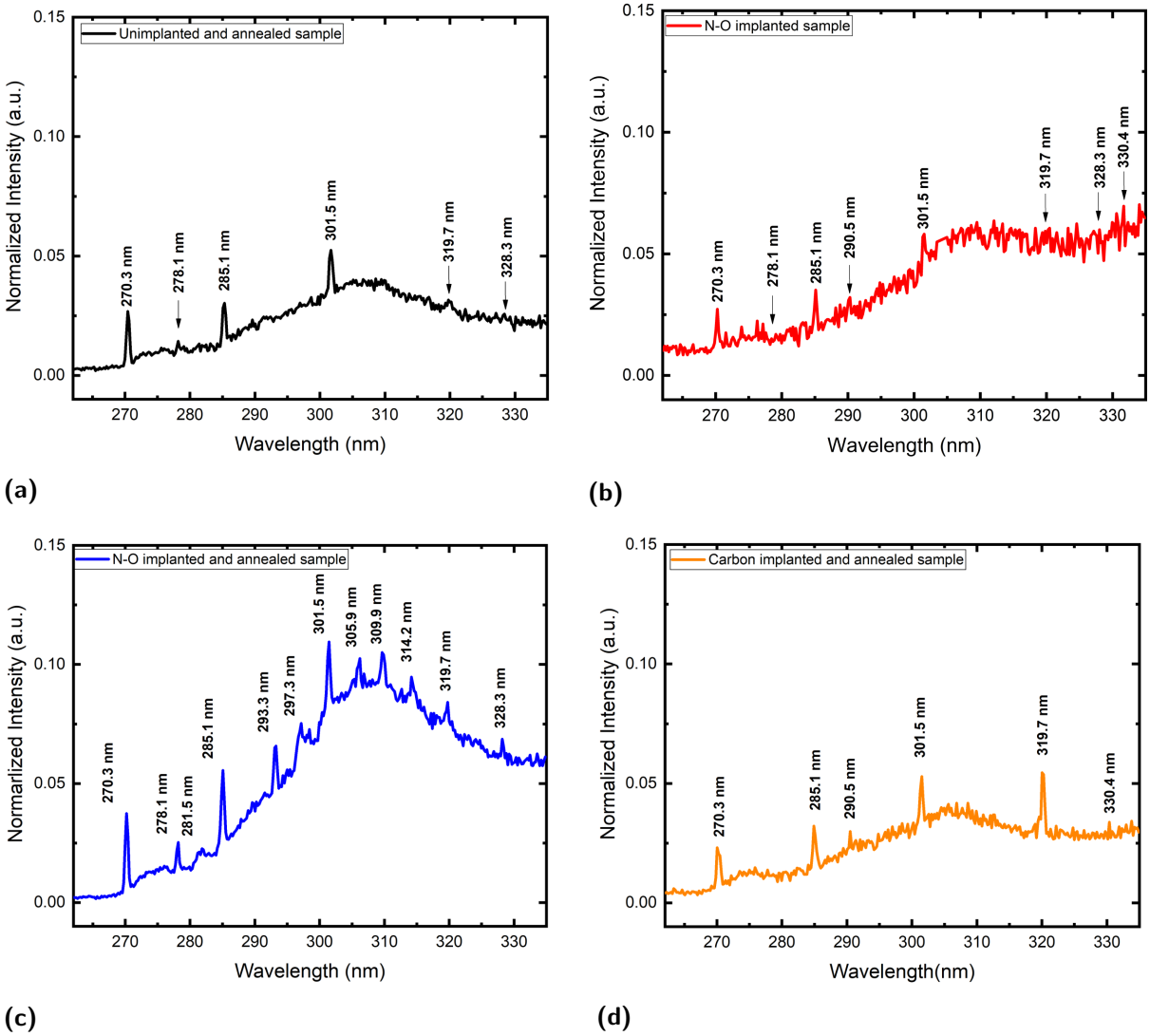

Figure 6.18 The typical PL spectra (262-335 nm) of (a) annealed unimplanted sample, (b) N-O implanted sample, (c) annealed N-O implanted sample and (d) annealed carbon implanted sample. These spectra were recorded at 77 K using 248 nm for excitation. All the spectra were normalized with the first order Raman peak at 251 nm

the local-mode phonon replicas of the 5RL centre as discussed in section 3.2.2.2. They are spaced at approximately 235 meV. These are in agreement with those previously reported by Collins and other authors [133, 228, 234]. The 328.3 nm peak was previously observed in low temperature cathodoluminescence measurements on a homoepitaxial (100) diamond film by Kadri et al. [235]. However, no information was given regarding the origin of this peak. The 278.1 nm, 281.5 nm and 328.3 nm lines are related to intrinsic defects since they are observed in the PL spectrum of the unimplanted samples (see Figure 6.18a). The peaks at 290.5 nm and 330.4 nm are related to radiation defects since they are observed in carbon and N-O implanted samples (see Figures 6.18b and 6.18d).

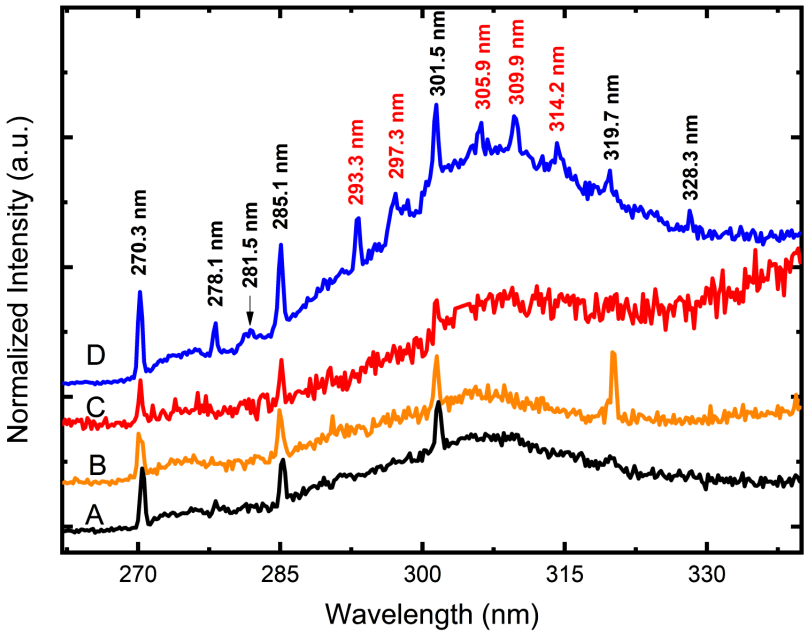

Figure 6.19 Comparison of PL spectra (262-335 nm) of annealed unimplanted sample (spectrum A), annealed carbon implanted sample (spectrum B), N-O implanted sample (spectrum C) and annealed N-O implanted sample (spectrum D). These spectra were recorded at 77 K using 248 nm for excitation. The spectra are vertically offset for convenience and were normalized to the first order Raman peak at 251 nm. Peaks at 293.3 nm, 297.3 nm, 305.9 nm, 309.9 nm and 314.2 nm are only present in the N-O implanted and annealed sample.

The peaks at 293.3 nm, 297.3 nm, 305.9 nm, 309.8 nm and 314.2 nm were observed only in the annealed N-O implanted sample. This sample did not show any other chemical impurities apart from nitrogen and oxygen as observed in X-ray photoelectron spectroscopy results (see section 6.3.1). It is therefore reasonable to speculate that these PL features are due to oxygen, nitrogen or aggregated defects due to N-O defect complexes as a result of the N-O ion implantation and subsequent annealing.

Defects related to nitrogen in diamond are well documented as they have been extensively studied [106]. The PL emission lines observed at 293.3 nm, 297.3 nm, 305.9 nm, 309.9 nm and 314.2 nm in the spectrum of N-O implanted and annealed sample are not among them.

On the other hand, there are few reports on the study of oxygen defects in diamond since oxygen has rarely been investigated. The reason is that oxygen-16 (^{16}O), the most abundant isotope of oxygen in nature, is spinless, thereby making detection of the oxygen fingerprint in diamond is a bit challenging [141]. Theoretical studies performed by Gali et al. [3] suggested that as a substitutional atom, oxygen gives rise to two defect-related energy states in the band gap in which one is in the middle of the band gap and the other is near the conduction band. Theiring and co-workers [141] have found that an oxygen atom in an interstitial site is optically and electrically inactive in diamond with a spin singlet ground state. Moreover, the neutral charge of the substitutional oxygen atom is likely to occur in nitrogen-containing diamonds and was predicted to have a zero phonon line at 1.39 eV (891.9 nm) [141]. Experimentally, there are few features which were tentatively attributed to oxygen defects. Among them are the cathodoluminescence (CL) peaks localized at 484.12 nm, 463.3 nm, 454.9 nm observed by Ruan et al. [143] from a diamond sample grown in 0.1% O_2. Two CL band structures located at 267.2 and 330.6 nm have been attributed to oxygen atoms or possible oxygen defect complexes by Mori et al. [144]. In addition Gippius [145] observed sharp photoluminescence peaks at 584.8 nm, 598.3 nm, 836 nm and 845 nm from oxygen implanted natural type IIa diamond after high temperature annealing (above 1500°C). Most of these peaks were in the visible range and those observed by

Mori et al. [144] are broader and cannot unambiguously be attributed to oxygen defects only. Furthermore, the density functional theory calculations of Etmimi et al. [142] revealed that the N-O complex in diamond can have both donor and acceptor levels at $E_v + 3.7$ eV and $E_v + 1.5$ eV [16, 142]. Based on the volume of information we have been able to read in both theoretical and experimental literature, we suggest that the PL emission lines observed at 293.3 nm, 297.3 nm, 305.9 nm, 309.9 nm and 314.2 nm are unlikely to be related to nitrogen or oxygen alone.

In order to assess the combined role of N, O ions and radiation-induced defects, and to eliminate any doubt regarding the origin of the observed features, the PL properties of the fifth sample that was irradiated with 9 keV N and O ions as described in section 5.2 with a fluence of 1×10^{16} ions/cm^2 were measured. The sample was annealed in Ar atmosphere at 600 °C, thereafter it was cleaned in an oxidizing acid solution.

Figure 6.20 shows the photoluminescence spectra of the annealed N-O implanted sample (spectrum D), the oxygen implanted sample (spectrum E), the nitrogen implanted sample (spectrum F) in the range of 265 to 335 nm. These PL spectra were characterized by the 5RL centre, and only the annealed N-O implanted sample still shows peaks at 293.3 nm, 297.3 nm, 305.9 nm, 309.9 nm and 314.2 nm after annealing and cleaning procedure in the boiling acid. This observation suggests that the aforementioned PL features for the annealed N-O implanted sample spectrum are not caused by radiation damage or any interaction with the radiation damage and native impurities, for the simple reason that they did not appear in the annealed carbon implanted sample. In addition, these defect peaks do not appear in the N or O ion implanted and annealed sample. These observations and arguments leads us to conclude that the PL features at 293.3 nm, 297.3 nm, 305.9 nm, 309.9 nm and 314.2 nm are likely to be related to a N-O complex in diamond.

Figures 6.21 and 6.22 present the photoluminescence spectra of unimplanted, N-O implanted, N-O implanted and annealed, carbon implanted, nitrogen implanted and oxygen implanted samples in the range of 335 to 450 nm.

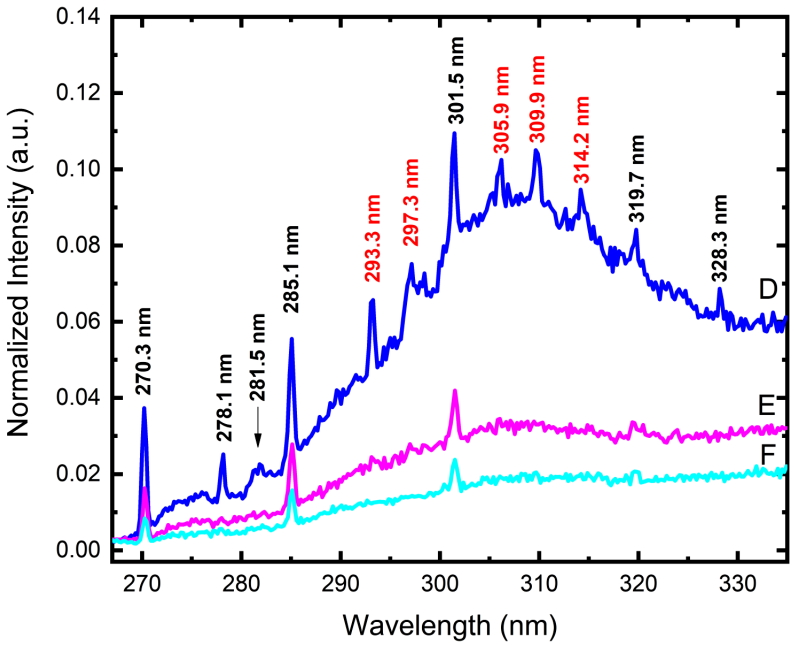

Figure 6.20 PL spectra (262-335 nm) of annealed N-O implanted sample (spectrum D), annealed oxygen implanted sample (spectrum E) and annealed nitrogen implanted sample (spectrum F). These spectra were recorded at 77 K using 248 nm for excitation. The spectra are arranged vertically for easy comparison and were normalized to the first order Raman peak at 251 nm. Peaks at 293.3 nm, 297.3 nm, 305.9 nm, 309.8 nm, and 314.4 nm do not appear in either the oxygen implanted sample or the nitrogen implanted sample.

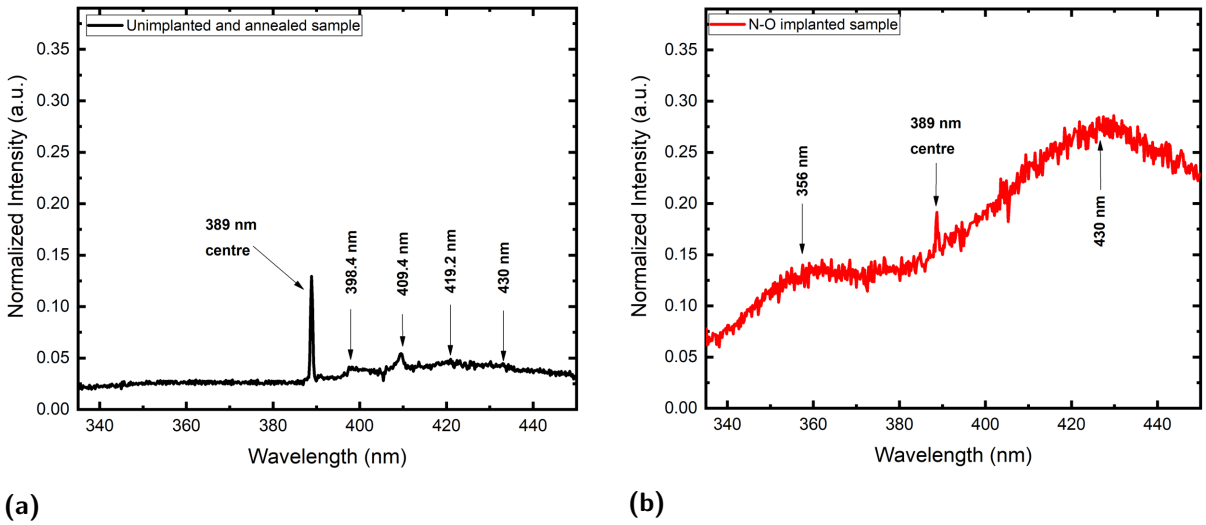

Figure 6.21 Typical photoluminescence spectra (335-450 nm) of (a) unimplanted sample and (b) N-O implanted sample, obtained at 77 K using 248 nm laser excitation. The spectra were normalized with the first order Raman peak at 251 nm.

Peaks at 389 nm, 398.4 nm, 409.4 nm and 419.2 nm are observed in all the spectra. However, 389 nm, 398.4 nm and 409.4 nm peaks are more intense in the spectra recorded on the unimplanted sample (Figure 6.21a), annealed N-O implanted sample (Figure 6.22a), annealed nitrogen implanted sample (Figure 6.22c and annealed oxygen implanted sample (Figure 6.22d). The N-O implanted sample (Figure 6.21b) and annealed carbon implanted sample (Figure 6.22b) are characterized by broad band luminescence features centred around 356 and 430 nm. These two PL bands (356 and 430 nm) are also observed for the N-O implanted and annealed sample, but are less intense.

The most prominent peak in the spectra of Figures 6.21 and 6.22 is the ZPL of the 389 nm (3.188eV) centre and its phonon sidebands at 398 nm and 409 nm (see section 3.2.1.6). The observation of the 389 nm centre provides evidence that these CVD diamond samples contain some nitrogen as the 389 nm centre involves a carbon interstitial and a single nitrogen atom [123].

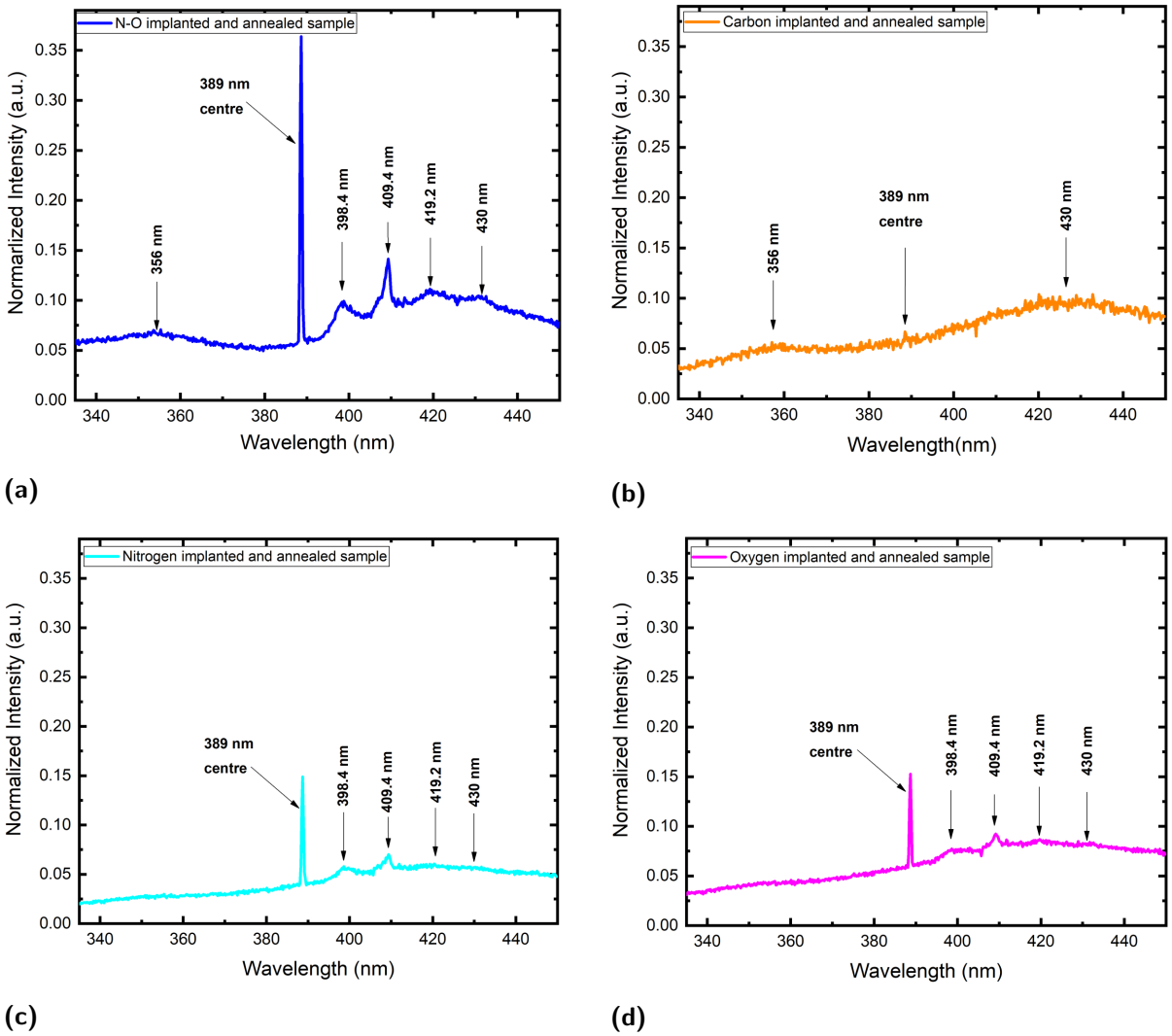

Figure 6.22 Typical photoluminescence spectra (335-450 nm) of (a) annealed N-O implanted sample, (b) annealed carbon implanted sample, (c) annealed nitrogen implanted sample and (d) annealed oxygen implanted sample, obtained at 77 K using 248 nm laser excitation. All the spectra were normalized to the first order Raman peak at 251 nm.

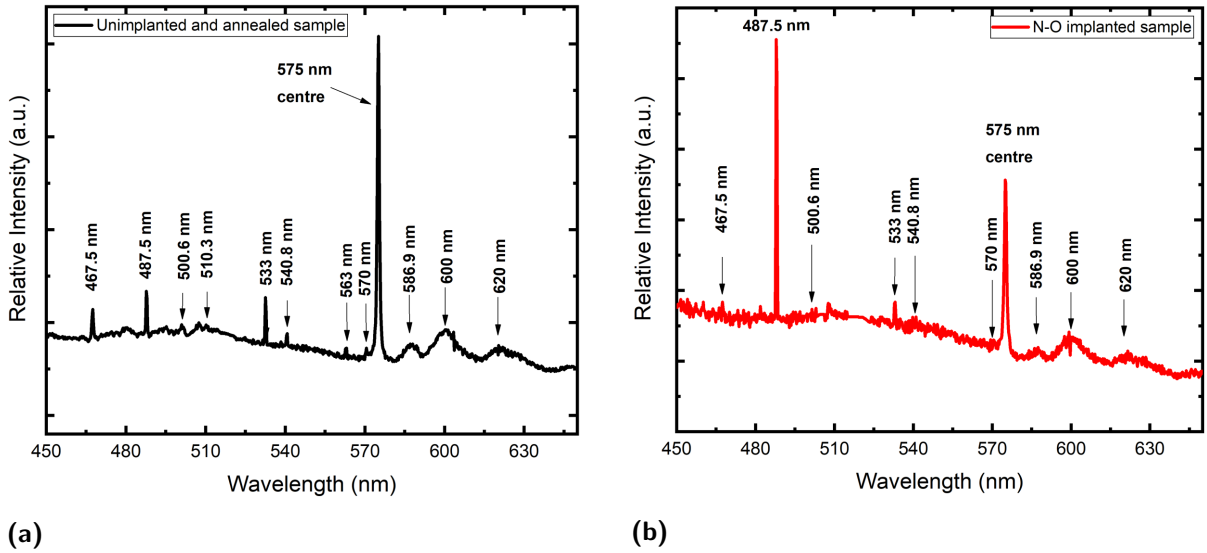

Figure 6.23 Photoluminescence spectra (450-650 nm) of (a) the annealed unimplanted sample and (b) N-O implanted sample obtained at 77 K using 248 nm laser excitation.

Figures 6.23 and 6.24 present the photoluminescence spectra of all the samples under investigation in the range of 450 to 650 nm. The most dominant feature observed in the PL spectra of all the samples is the zero phonon line of the neutral charge state of the nitrogen-vacancy defect at 575 nm (see section 3.2.2.2). In addition, there are several lines at 467.5 nm, 487.5 nm, 500.6 nm, 510.3 nm, 533 nm, 540.8 nm, 570 nm which are present in all the spectra. Broad peaks located at 586 nm, 600 nm and 620 nm are also seen in all the spectra.

The 467.5 nm, 533 nm, 563 nm and 570 nm lines are reported to originate from a nitrogen related centre [106, 228, 229]. The 563 nm line was also reported in carbon irradiated diamond and was associated with an interstitial-related defect [230, 231].

A peak at 540.8 nm has been observed in type IIa diamond implanted with Ni and has been tentatively ascribed to Ni atoms and carbon interstitial atoms [106]. The 540.8 nm peak is also observed in the PL spectra of our samples which do not show traces of Ni atoms (see section 6.3.1) and suggests that the 540.8 nm emission line should be associated to a nitrogen-related

defect or to carbon interstitial complexes. The peak at 510.3 nm is attributed to the S1 centre which is tentatively assigned to a single nitrogen atom bound to a vacancy [106]. The emission line at 500.6 nm has also been observed in the CL spectra of some diamond films by Collins and Kamo [236]. Its appearance seems to be unique to CVD diamond. The 487.5 nm emission line corresponds to the TH5 centre, which is an intrinsic defect containing a divacancy, observed in type Ia and IIa diamonds after electron irradiation followed by annealing at temperatures above 400 °C [106]. It is noticed that, the N-O implanted sample exhibits a strong the TH5 luminescence compared to other samples. This can be seen in Figure 6.25b where the unimplanted, N-O implanted (annealed and without annealing) samples are compared. The intensity of the TH5 centre for the N-O as-implanted sample is more than 3 times as intense as for the N-O implanted and annealed sample.

A sharp peak is observed at 556.7 nm which is only present on the annealed N-O implanted sample only (see Figure 6.25a). This peak has also been observed by Steeds [237] in diamond samples with a N-level of approximately 1 ppm. This peak was, however, absent from the material containing 10 ppm N or above and from ultra-pure single crystal CVD diamond. Further is needed in order to understand the behavior and origin of this emission line. It is worth mentioning that the negative charge state of the N-V defect centre (637 nm) does not appear in these spectra. According to Iakoubovskii et al. [127], the negative charge state of the N-V defect cannot be seen with excitation energy exceeding the band gap of diamond in the CL and PL processes due to the fact that such excitation ionizes the negative centres which drives them to the neutral state.

Based on the results shown in figures 6.22, 6.23 and 6.24, it is easily noticeable that no emission line which might be attributed to the N-O defects has been observed in the range of 450 to 650 nm. In addition, the reported oxygen related defect centres obtained from oxygen implanted type IIa diamond [145] have not been observed in either the oxygen or the N-O implanted sample. We do note that the annealing temperature is 600 °C for all the samples shown here, apart for the carbon implanted sample, and further PL measurements with sample annealed at different

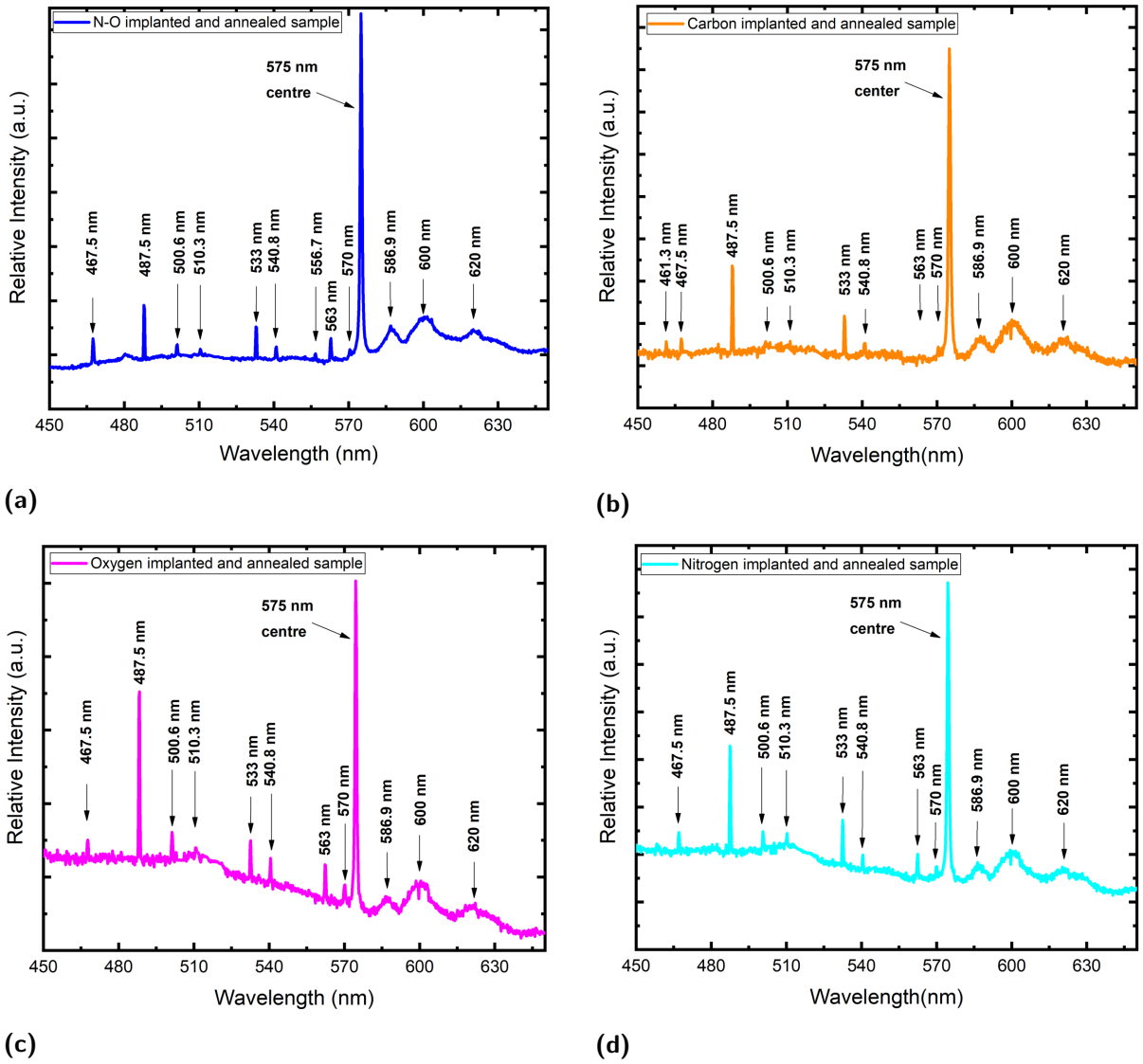

Figure 6.24 Photoluminescence spectra (450-650 nm) of (a) the annealed N-O implanted sample, (b) annealed carbon implanted sample, (c) annealed nitrogen implanted sample and (d) annealed oxygen implanted sample, obtained at 77 K using 248 nm laser excitation.

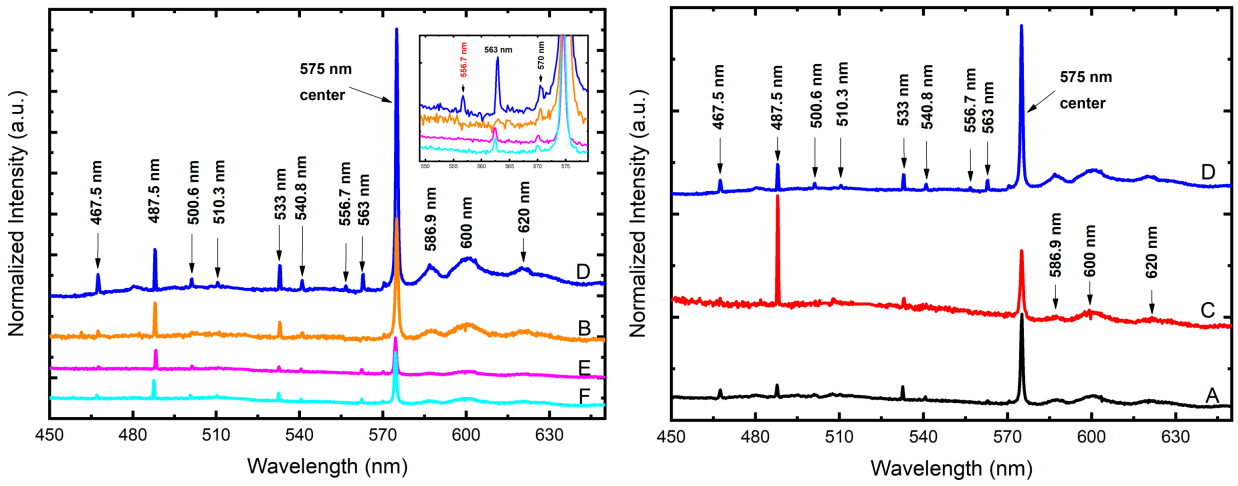

Figure 6.25 (a) Comparison of photoluminescence spectra (450-650 nm) of N-O implanted and annealed (spectrum D), annealed carbon implanted sample (spectrum B), annealed oxygen implanted sample (spectrum E) and annealed nitrogen implanted sample (spectrum F) obtained at 77 K using 248 nm laser excitation. The inset shows the peak at 556.7 nm, which is only present in the annealed N-O implanted sample. (b) PL spectra of annealed unimplanted sample (spectrum A), N-O implanted sample(spectrum C) and annealed N-O implanted sample (spectrum D).

temperature starting from 700 °C to 1600 °C are needed to fully understand the origin of the observations made thus far.

6.7.3 Low temperature photoluminescence measurements obtained with 458 nm excitation wavelength

Photoluminescence spectra of N-O implanted (unannealed), annealed N-O implanted, unimplanted (before and after annealing) and carbon implanted (before and after annealing) samples recorded at liquid nitrogen temperature using an excitation wavelength of 458 nm are shown in Figures 6.26 and 6.27.

The most prominent peaks in all the spectra shown in Figures 6.26 and 6.27 are the ZPL of the neutral charge state of the nitrogen-vacancy centre at 575 nm and the first order Raman peak at 487 nm.

There is also a sharp peak at 503.4 nm in the PL spectra of all the samples. This 503.4 nm peak is attributed to the H3 centre [106]. The luminescence intensities of the H3 centre are of similar height in the N-O doped samples, even though they are broader in the annealed sample. It is too weak to be observed in the unimplanted sample before annealing (spectrum C, Figure 6.28). However, an increase for luminescence intensity of the H3 centre was observed for the unimplanted sample after it was annealed at 600 °C.

In addition to these peaks, there were negative charge states of the nitrogen-vacancy defect centres at 637 nm and other peaks at 463 nm, 467.6 nm, 477 nm, 481 nm, 489.7 nm, 563 nm, 586.9 nm, 600 nm and 620 nm. All these peaks are present in the PL spectra of all the samples except the 489.7 nm peak (see Figure 6.28), which appears in both N-O implanted samples (unannealed and annealed). However, the luminescence of this peak is weak for the unannealed sample. The origin of this peak cannot be attributed to a N-O complex since it also appears in a

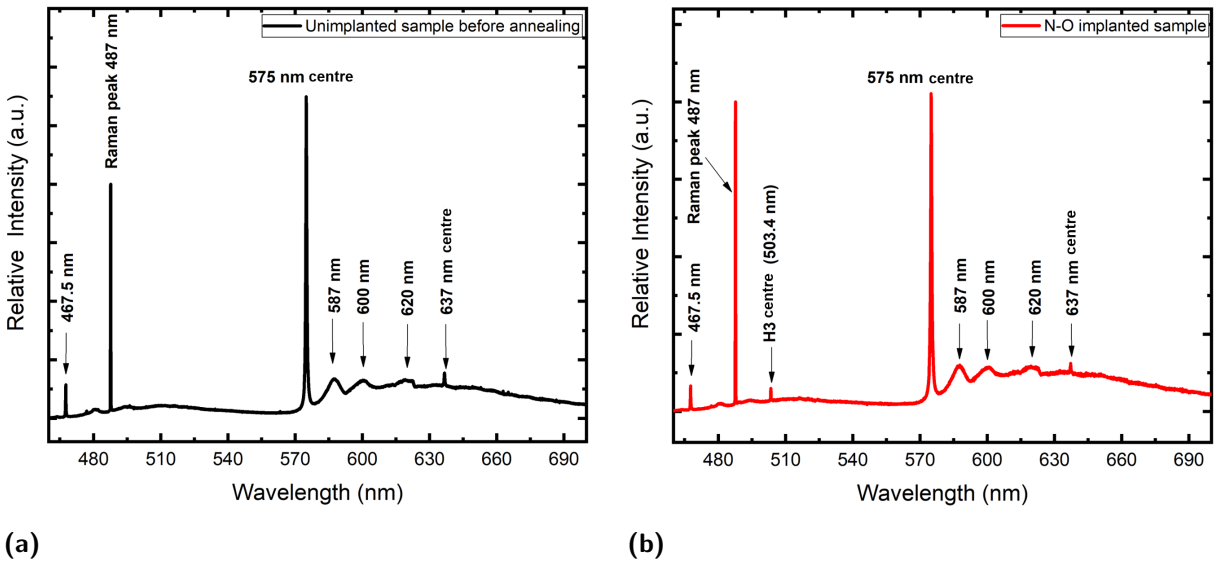

Figure 6.26 Typical 77 K PL spectra of (a) the unimplanted sample before annealing and (b) N-O implanted sample, recorded under 458 nm excitation.

sample that was implanted with carbon ions and is thus a radiation damage related defect. The 467.6 nm line has been tentatively attributed to a nitrogen-related defect containing interstitial carbon atoms [106]. Two new peaks appeared at 469.9 nm and 508.8 nm on the spectrum of the unimplanted sample after annealing (H). The 469.9 nm peak is the TR12 centre while the 508.8 nm is its local vibration mode. The TR12 centre is a typical radiation centre in diamond and it is attributed to a defect involving two vacancies and two interstitial carbon atoms in hexagonal positions [106]. The TR12 centre has been reported to occur in relatively pure diamond after electron irradiation [106, 134]. However, it is observed in the PL spectrum of the as-grown CVD type IIa diamond sample after annealing at 600 °C. The TR12 centre was not observed in the N-O implanted samples, and it has been reported to be strongly quenched after nitrogen ion implantation [106, 137]. The TR12 centre is also observed in the carbon implanted sample (B). In this study we annealed the carbon ion implanted sample at 800 °C in order to show that the TR12 centre is indeed the same centre observed by Walker [134] as it anneals away at 800 °C.

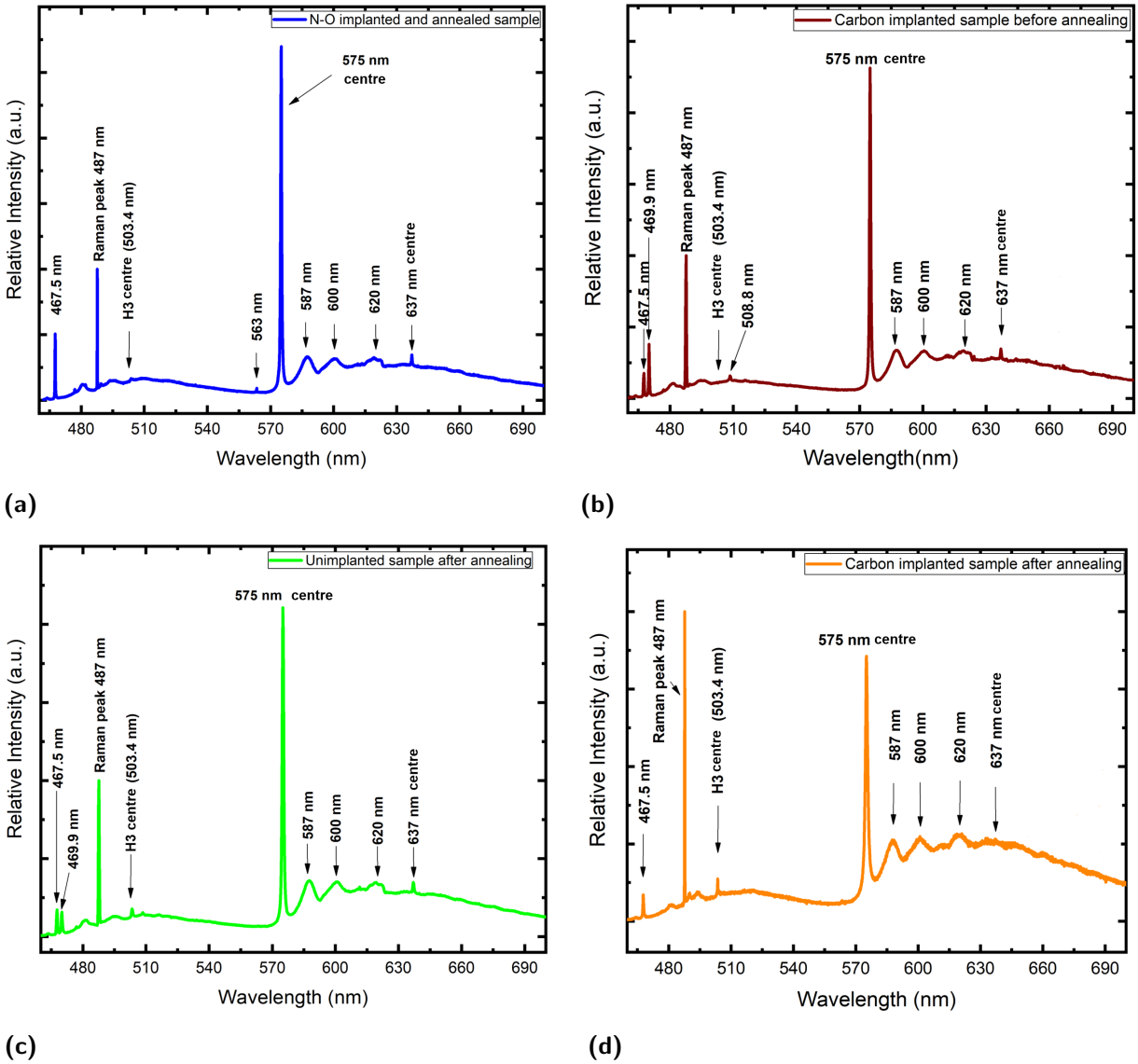

Figure 6.27 Typical 77K PL spectra of (a) annealed N-O implanted sample, (b) carbon implanted sample before annealing, (c) unimplanted sample after annealing and (d) annealed carbon implanted sample, recorded under 458 nm excitation.

This is observed as this peak does not appear in the carbon implanted sample after annealing at 800 °C. The H3 centre appears in the carbon implanted sample after annealing at 800 °C.

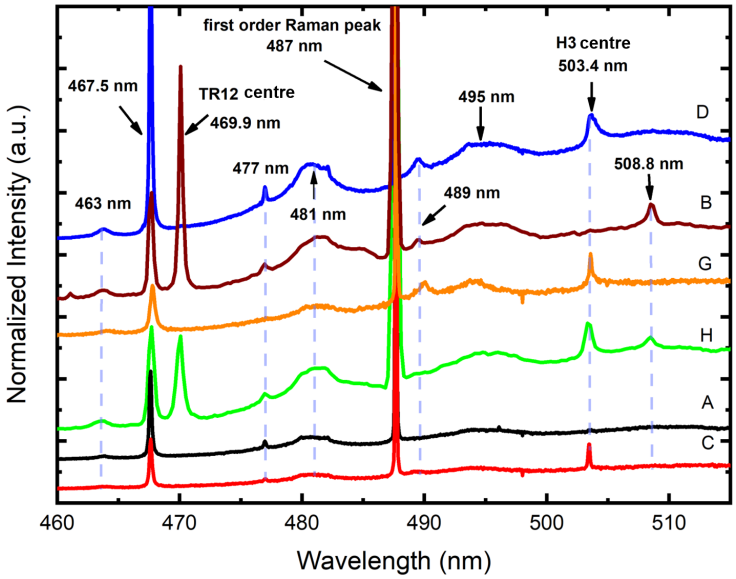

Figure 6.28 Comparison of PL spectra of unimplanted sample before annealing (spectrum A),carbon implanted sample before annealed (spectrum B), N-O implanted sample (spectrum C), annealed N-O implanted sample (spectrum D), annealed carbon implanted sample (spectrum G) and annealed unimplanted sample (spectrum H) obtained with 458 nm excitation wavelength in the range of 460 to 510 nm. All the spectra were normalized with the first order Raman peak at 487 nm

6.7.4 Low temperature photoluminescence measurements obtained with 514.5 nm excitation wavelength

PL spectra recorded with the 514.5 nm excitation wavelength show an increase in intensity of the negative charge state of the nitrogen-vacancy defect centre at 637 nm compared to the spectra obtained with the 458 nm excitation wavelength. This can be seen in Figures 6.29 and 6.30. Furthermore, a peak at 563 nm in the PL spectrum of the N-O implanted annealed sample is more intense (see Figure 6.30a), while it appears broader and less intense in the spectrum obtained

from the unimplanted sample after annealing (see Figure 6.31) and vanishes for carbon implanted samples (before and after annealing).

Two emission peaks were observed at 596.5 nm and 597.2 nm in the PL spectra of all the samples. These two peaks were first observed by Wang et al. [238] for their brown-to-gray and near-colorless single-crystal type IIa CVD synthetic diamond. According to Martineau et al. [239] these peaks are not seen in natural or HPHT-grown synthetic diamond. No concrete explanation for the origin of these peaks has been given. A small peak is also observed at 579 nm in PL spectrum D in Figure 6.31 of the N-O implanted annealed sample at liquid nitrogen temperature and is not present in spectra A, B, and C. The origin of the 579 nm peak is less likely to be associated with N-O ions since we observed a similar luminescence peak around 579 nm in the PL spectra of all our samples recorded at room temperature when exciting at a wavelength of 514.5 nm. However, this peak was not observed in the PL spectra of the unimplanted or annealed unimplanted samples at liquid nitrogen temperature. The 533 nm line shifted to 534.5 nm and it was only visible on the N-O implanted and annealed sample. There are two broad band features centered at 659 and 680 nm in all the spectra, which are the phonon sideband structures of the nitrogen-vacancy defect.

The peaks at 556.7 nm, 540.8 nm and 570 nm observed previously in the PL spectra when excited at 248 nm UV do not appear under visible excitation wavelengths (458 nm and 514.5 nm). This is an indication that these centres are due to a deep-lying intrinsic defect, since it requires high energy photons to be excited.

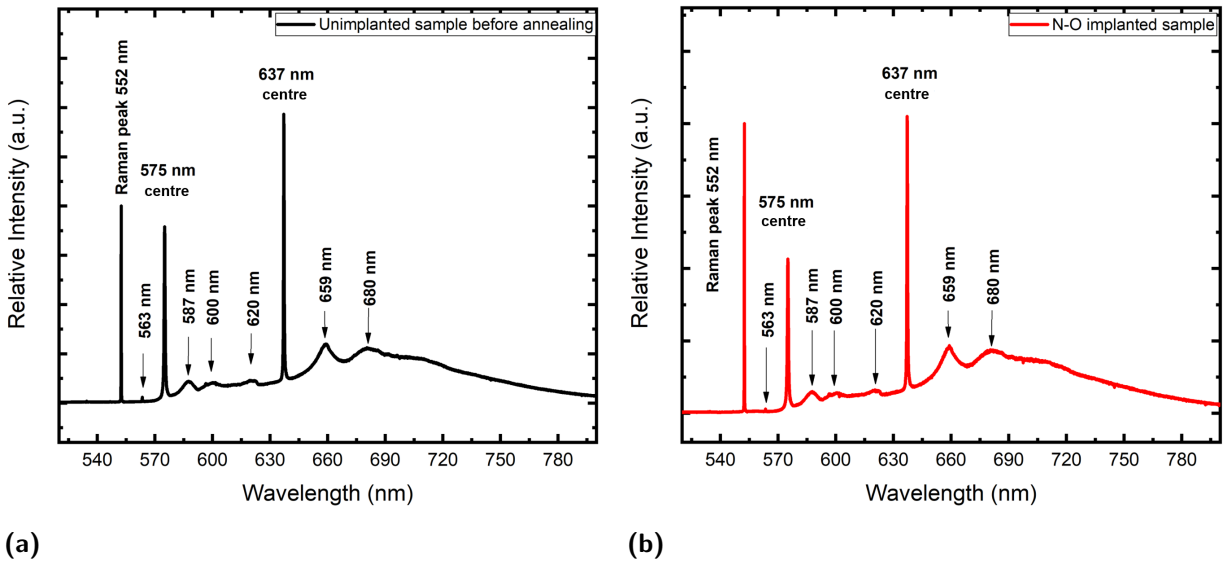

Figure 6.29 Typical 77 K PL spectra of unimplanted sample before annealing (a) and N-O implanted sample (b) recorded under 514.5 nm excitation.

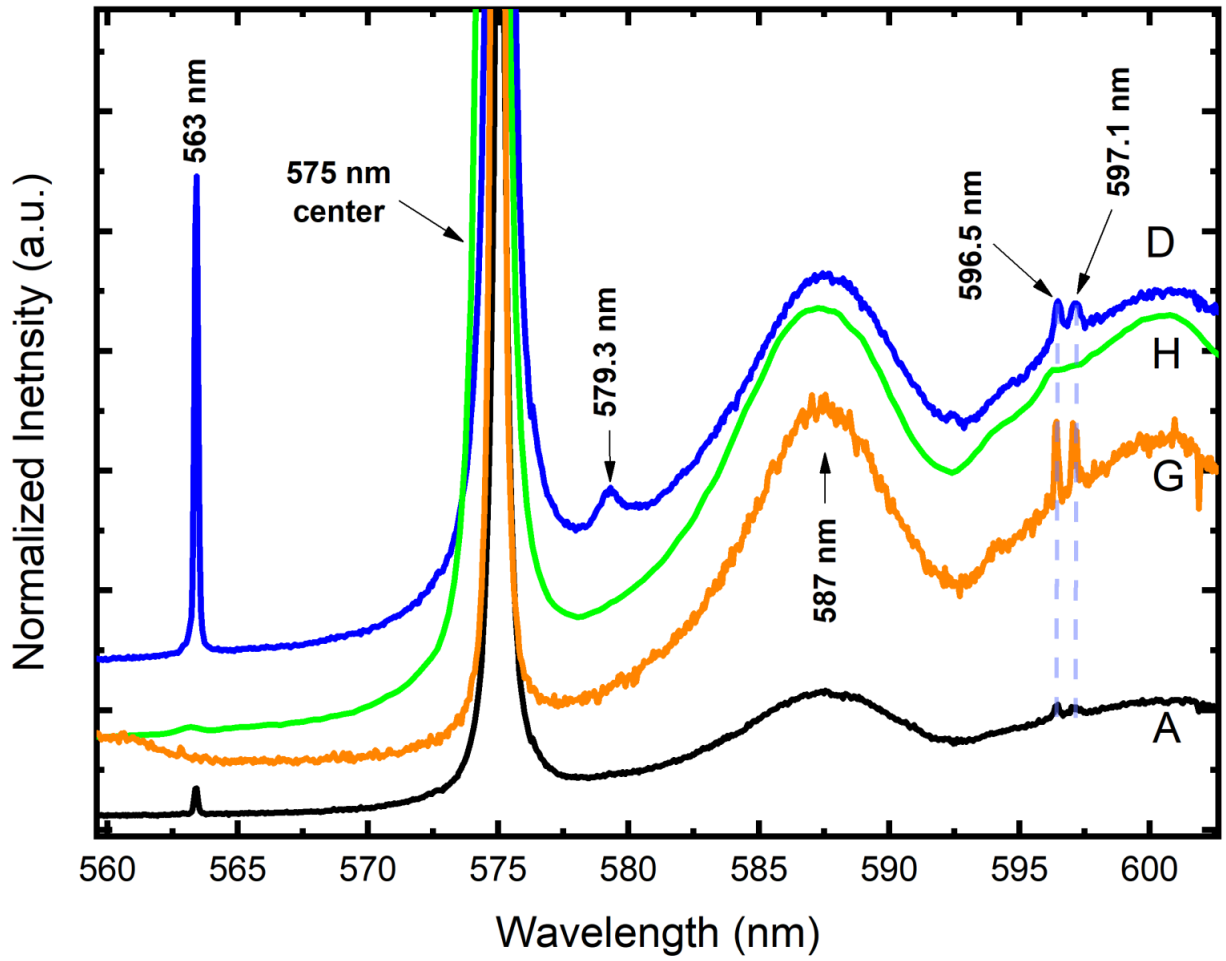

Figure 6.31 Comparison of the PL spectra at 77 K of (A) unimplanted sample before annealing, (G) carbon implanted sample after annealing, (H) unimplanted sample after annealing, (D) annealed N-O implanted sample obtained at 77 K with 514.5 nm excitation wavelength in the range of 560 to 620 nm. This figure shows a pair of lines at 596.5 and 597.1 nm in all the spectra and a peak at 579.3

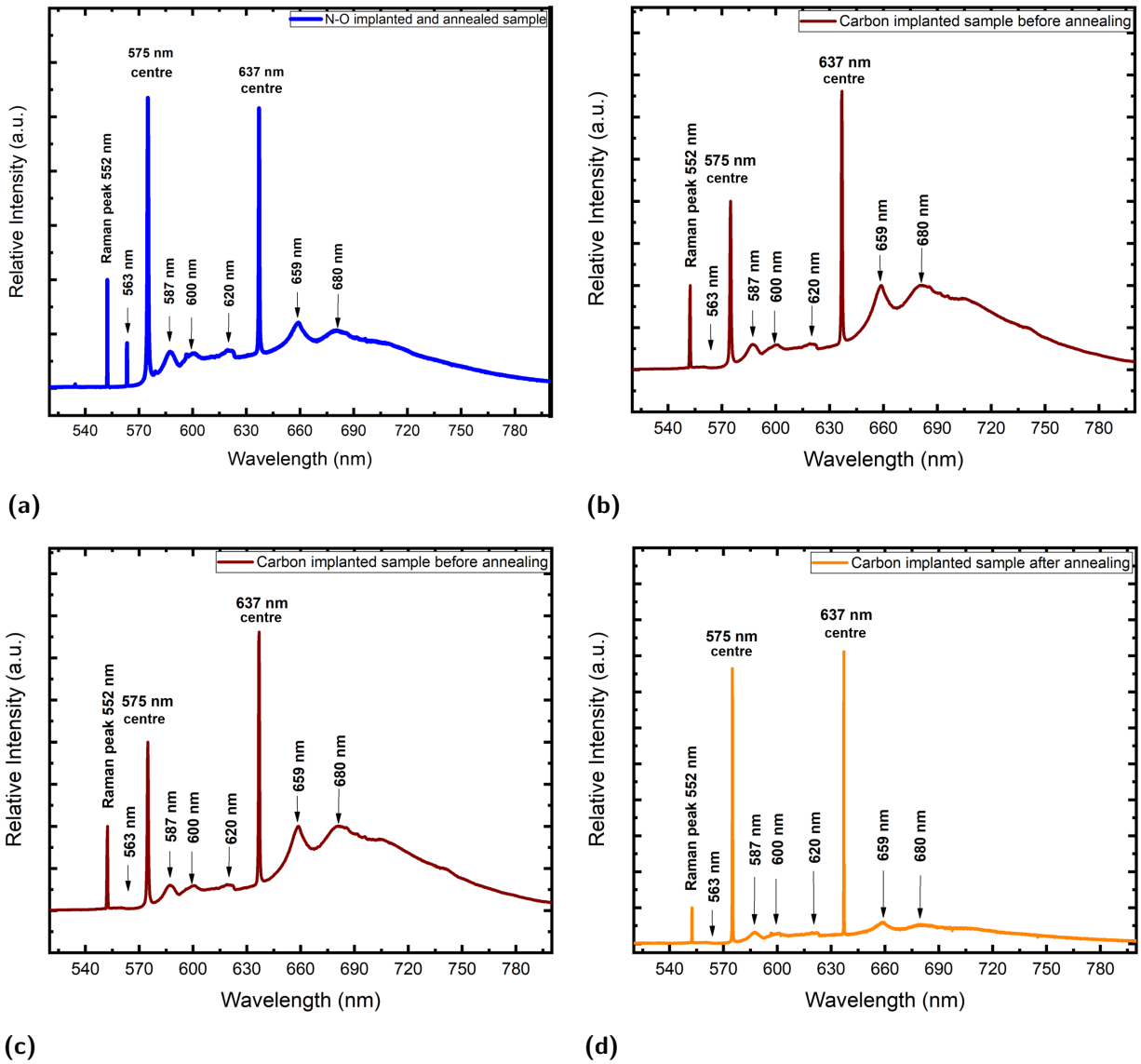

Figure 6.30 Typical 77 K PL spectra of (a) annealed N-O implanted sample , carbon implanted sample before annealing (b), unimplanted sample after annealing (c) and carbon implanted sample after annealing (d) recorded under 514.5 nm excitation.

Table 6.8 Summary of defects observed from CL and PL measurements.

Defect position (nm)	Methods ($\lambda_{excitation}$)	Origin of luminescence
270.3 , 285.1, 301.5 and 319.7 nm	PL (248 nm)	Emission lines attributed to the ZPL of the 5RL center and its local mode phonon replicas, respectively [106, 132].
278.1, 281.5 and 328.3	PL (248 nm)	Emission lines attributed to intrinsic defects [240].
290.5 and 330.4	PL (248 nm)	Emission lines observed in carbon and N-O implanted samples attributed to radiation defects [240].
293.3, 297.3 , 305.9, 309.9 and 314.2	PL (248 nm)	Emission lines observed only in the annealed N-O implanted sample attributed to N-O complex in diamond [240].
389, 398.4 , 409.4 and 419.2	PL (248 nm)	Emission lines attributed to the ZPL of 389 center and its phonon side bands. [123]
467.5 and 563	PL (248 and 458 nm)	Emission lines reported to originate from a nitrogen related center [230, 231].
469.9 and 508.8	PL (458 nm)	Emission lines observed in the spectra of unannealed carbon implanted sample and in annealed (600 °C) unimplanted sample attributed to the TR12 center and its local vibration mode, respectively [106].
489 nm and 517	CL	CL emission tentatively attributed to radiation damage related defects.
503.4	PL (458 nm)	Emission line attributed to the H3 center [106].
506	CL	Center often observed in combustion flame grown homoepitaxyial CVD diamond films [43, 106].
510.3	PL (248 nm)	Emission line attributed to the s1 center [106].
533	CL	Peak only observed on annealed N-O implanted sample, tentatively attributed to a radiation recombination of a shallow n-type defect and a deep lying p-type defect in the middle of the band gap.
533.8	PL (248, 458 nm) and CL	Emission line reported to originate from a nitrogen related center [106].
540.8	PL (248 nm)	Emission line ascribed to a nitrogen related defect or carbon interstitial complexes [106].
556.7	PL (248 nm) and CL	Peak observed only in annealed N-O implanted sample. It has also been observed in diamond samples with a N-level of approximately 1 ppm. But, was absent from the material containing 10 ppm N or above and from ultra-pure single crystal CVD diamond [240].
570	PL (248 nm)	Emission lines observed in all the spectra, reported to originate from a nitrogen related center [106].
575	PL (248, 458 and 514.5 nm) and CL	Emission lines observed in all the spectra, attributed to the ZPL of the NV° [106].
585	CL	Emission peak only observed on annealed N-O implanted sample, Center related to Oxygen defect center [145].
637	PL (458 and 514.5 nm)	Emission line attributed to the ZPL of the NV^{-} [106]
619	CL	De-excitation related to intrinsic defect in the band gap that are deep lying states which were ionized by the electron beam [106].
659 and 680	PL (458 and 514.5 nm)	The phonon sidebands structure of the nitrogen vacancy defect [106].

6.7.5 Proposed mechanism of electronic transitions leading to PL emission of N-O

The first step in the formation of the N-O centres in a type IIa diamond sample is by the incorporation of nitrogen and oxygen atoms in the diamond lattice by means of ion implantation. Irradiation of samples during ion implantation process leads to production of lattice vacancies. Annealing the samples at a temperature of 600 °C causes the migration of vacancies, nitrogen, oxygen and interstitials as they become more mobile. Upon the migratory movement of atoms and vacancies in the lattice, N and O atoms may find themselves in nearest-neighbor substitutional sites. The recombination of nitrogen and oxygen atoms could then take place to form N-O complexes. When the sample is excited with UV laser light at 248 nm, only defects and impurities within the band gap are excited since the 5 eV photon energy used is small compared to the 5.4 eV energy band gap of diamond. Upon excitation, electrons in the ground state of N-O are promoted to an excited state. As a result of constant vibrational and rotational motion taking place within the N-O molecule in the excited state, different radiative relaxations by spontaneous emission of photons can occur depending on the transition probabilities. Figure 6.32 is a simplified energy diagram showing electron transitions when the samples are excited at 248 nm (see Figure 6.19). Due to the lack of theoretical data on N-O complexes, we are unable to assign the exact electronic transition, however we postulate that electrons are excited from the valence band to N-O excited energy states, followed by non-radiative transitions to lower excited energy states and finally by radiative transitions to the ground state. The emissions at 293.3 nm and 297.3 nm are ascribed to a ZPL and its phonon replica, respectively. The 305.9 nm emission might also be a ZPL with two phonon replicas at 309.9 and 314.2 nm, since these centres occurred at intervals spaced at approximately 53 meV.

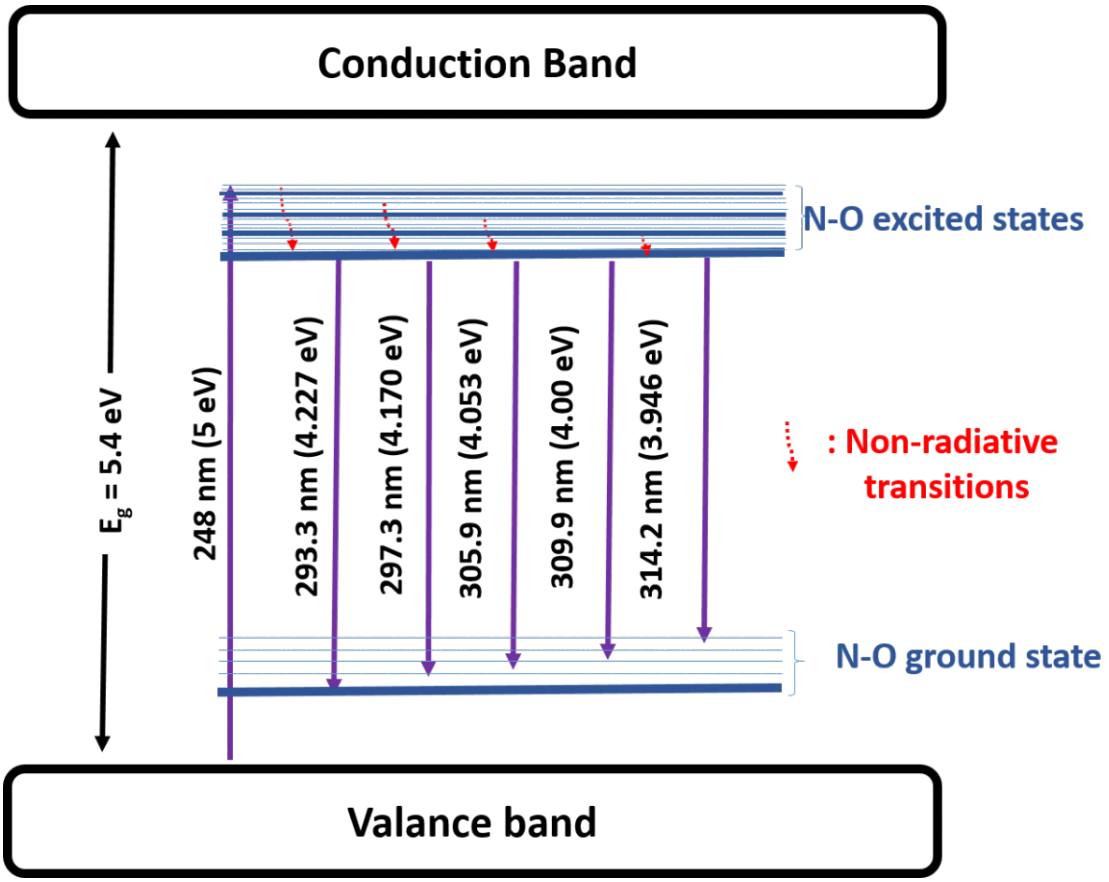

Figure 6.32 Schematic diagram of energy levels of N-O centre corresponding to photoluminescence spectra.

6.8 Cathodoluminescence (CL) measurements

Cathodoluminescence measurements were performed using an Oxford MonoCL4 system attached to a JEOL JSM-7800F field emission scanning electron microscope at the University of the Free State (UFS). The acceleration voltage for all the recorded spectra was set at 10 kV. Data was collected for 20-180 seconds depending on the intensity of the CL signal and a power supply voltage of either 860 V or 1000 V was used for the photomultiplier tube. The spectra were recorded at room temperature.

Figure 6.33 presents the typical cathodoluminescence spectra of the unimplanted sample, N-O implanted sample, N-O implanted and annealed sample and carbon implanted sample recorded at room temperature and in vacuum environment. The parameters for data acquisitions for these spectra are as follows:

- Unimplanted sample : exposure time 50 seconds and 180 seconds, PMT set at 1000 V
- N-O implanted sample : exposure time 20 seconds and 100 seconds, PMT set at 1000 V
- N-O implanted and annealed sample : exposure time 20 seconds, PMT set at 860 V
- Carbon implanted sample : exposure time 100 seconds, PMT set at 860 V.

A similarity is observed in the shape of CL spectra of unimplanted, N-O implanted and carbon implanted samples while the spectrum obtained from the N-O implanted and annealed sample is clearly different. The three similar spectra are dominated by a broad band centered at 619 nm. Two broad bands located around 450 and 534 nm are discernible in the CL spectrum obtained from the unimplanted sample. Peaks at 506 nm, 517 nm and 534.5 nm are observed for both carbon and N-O implanted samples (unannealed) but their appear to be more prominent for the carbon implanted sample. Slight differences are noted in the carbon implanted sample which has

a distinct peak at 577 nm, while the N-O implanted sample has a small peak located at 585 nm. The origin of the luminescence band centered at 619 nm is de-excitation related to intrinsinc defects in the band gap, that are deep lying states which were ionized by the electron beam. The peak at 506 nm present in the spectrum of the carbon implanted sample is a centre which is often observed in combustion flame grown homoepitaxial CVD diamond films [43, 106]. The luminescence emission peak at 577 nm on the CL spectrum of carbon implanted sample should be related to the neutral nitrogen vacancy centre which usually appears at 575 nm [106]. The neutral nitrogen vacancy centre should be also present in the spectra of other samples, however, it is not observed because of the strong emission intensity of the band at 619 nm. The 534.5 nm peak observed on N-O implanted and carbon implanted samples is attributed to nitrogen-containing defects and normally appears at 533.8 nm [106]. The small broad band observed around 586 nm (see Figure 6.33b) on N-O implanted sample is probably related to an oxygen defect centre, since it has been observed from oxygen implanted natural type Ia and type IIa diamonds [145]. The 489 nm weak band and the peak at 517 nm present in the CL spectra of carbon implanted and N-O implanted samples are attributed to radiation damage related defects as they are only appear on the implanted samples (unannealed).

The CL spectra of the sample doped with N-O and annealed at 600°C as shown in Figure 6.33c, shows significant differences in position and intensity of its broad band compared to the other samples. Its spectrum is characterized by an intense broad luminescence band which starts at 482 nm and maximizes at 533 nm. In addition, the intensity of the CL obtained from this sample was so high that the exposure times used for data collection were reduced to 20 seconds and the power supply of the PMT was set at 860 V in order to prevent saturation of the analogue to digital converter. This can be seen in Figure 6.35b were a comparison of the CL intensities of all the samples under investigation has been made.

The deconvolution of the broad luminescence spectrum observed in the CL spectrum of annealed N-O implanted sample revealed four elementary components centred at 517 nm, 533 nm, 556.7

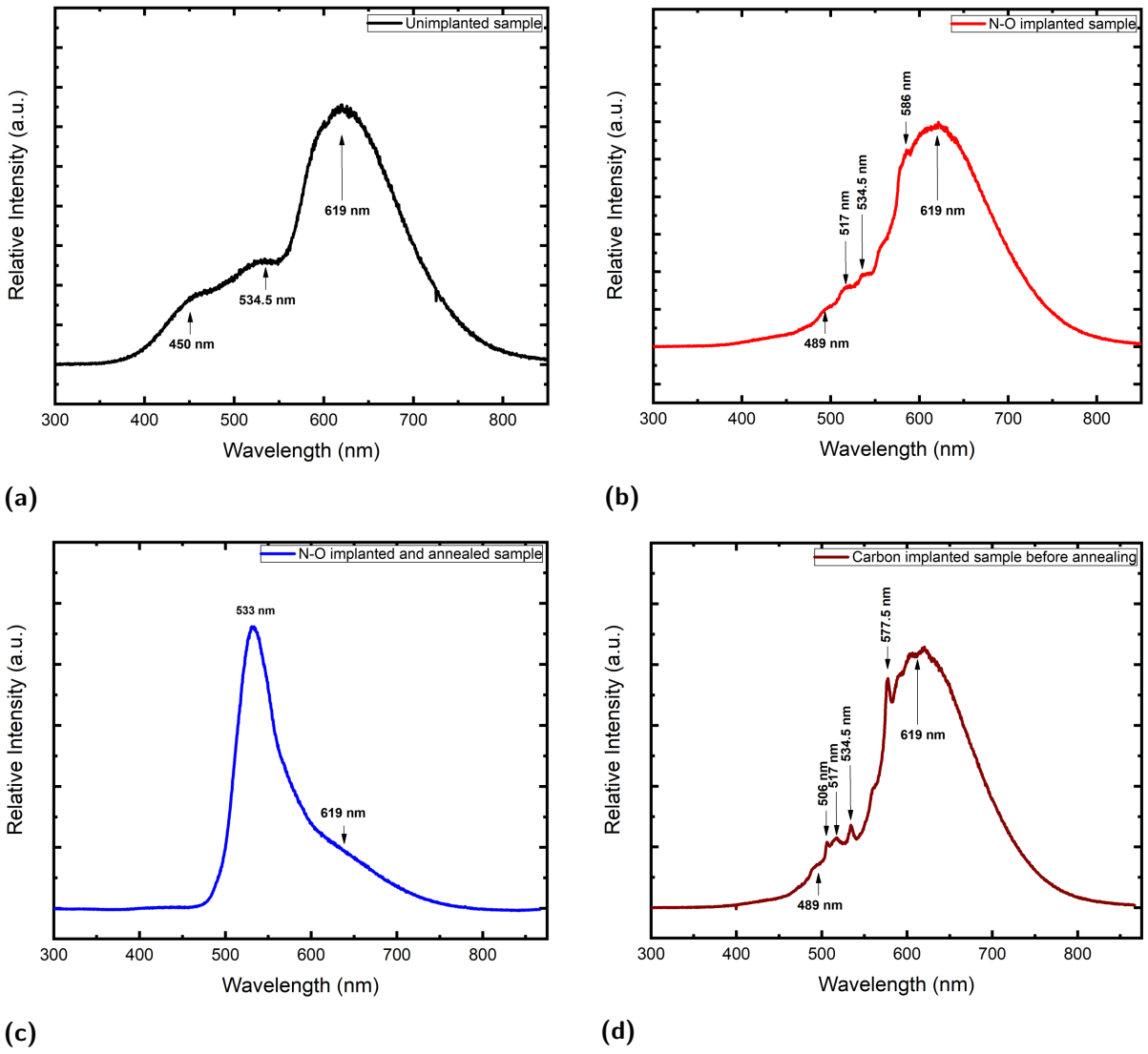

Figure 6.33 CL spectra of (a) unimplanted sample,(b) N-O implanted sample, (c) annealed N-O implanted sample and (d) carbon implanted sample, recorded at room temperature with the acceleration voltage set at 10 kV for all the measurements.

nm and 619 nm as shown in Figure 6.34. The 556.7 nm broad peak present only in this sample was also observed in the PL spectrum of this sample taken at low temperature (77 K) under UV excitation (248 nm) only but was absent under visible excitation (458 nm and 514.5 nm) see Figure 6.24. The origin on this peak is discussed in detail in the photoluminescence section (section 6.7).

The component at 533 nm could be the 534.5 nm centre, which is attributed to nitrogen-containing defects or possibly nitrogen-vacancy complex [106, 241, 242]. This peak was also observed in the PL spectrum of all the samples taken at low (77 K) and room temperature under UV excitation (248 nm). The difference in the intensity of this peak in the PL spectra was negligible as shown in Figure 6.17 and 6.25. However, it exhibits a strong CL intensity on the annealed N-O implanted sample only as shown in Figure 6.35. This unusual behavior infers that the defect responsible for this luminescence feature could come from another centre rather nitrogen-vacancy only. The behavior of this peak suggest that it could be a deep-lying defect located either close to the band edge or higher in energy than the conduction band edge. Hence we propose that this peak should be attributed to a radiative recombination of a shallow n-type defect and a deep lying p-type defect in the middle of the band gap, associated with vacancies-related states. For the reason that, it has been theoretically found that the nearest-neighbor pair of nitrogen and oxygen ions in the diamond lattice introduce several defect levels in the band gap [11]. The lower energy states of these defect levels are associated with vacancies-related states. The occupied shallow level is found to be located at < 0.3 eV below the conduction band edge and it is associated with a strongly compressed nitrogen-carbon bond. Thus, we postulate that the defect responsible for the 533 nm peak in the CL spectrum of the annealed N-O implanted sample should be attributed to a radiative recombination of the lower and shallow states induced by N-O pair in the band gap of this sample.

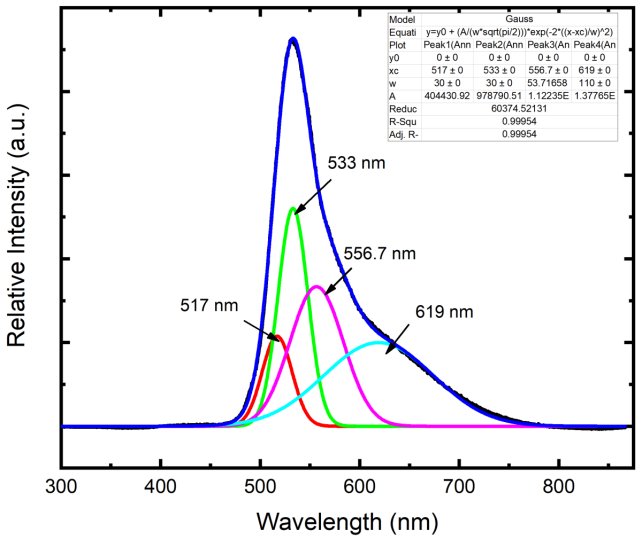

Figure 6.34 Deconvolution of the CL spectrum of the annealed N-O implanted sample, showing different components of the 533 nm feature.

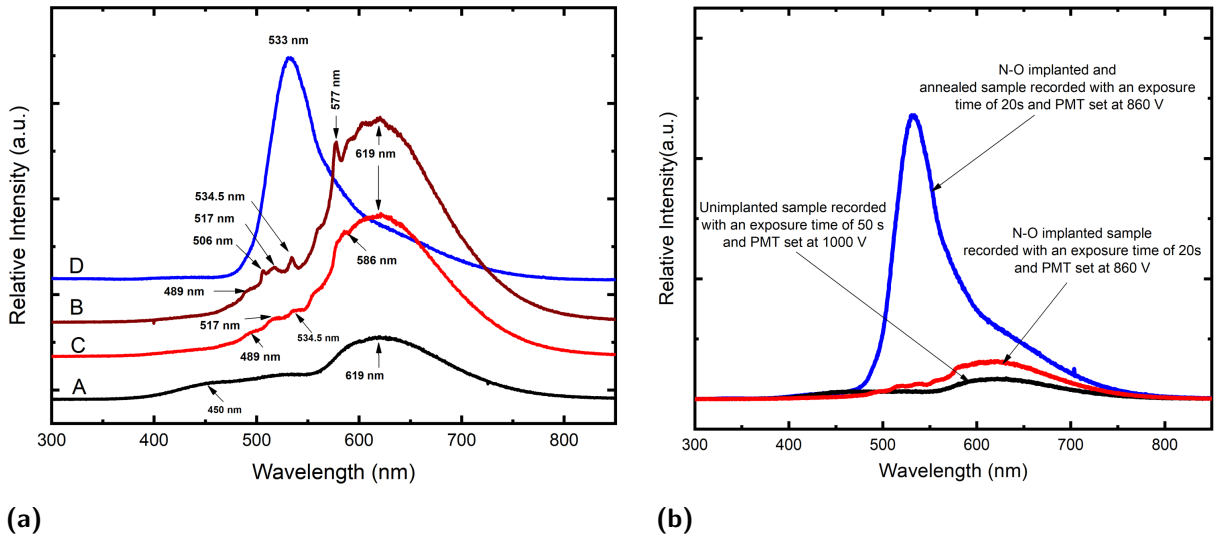

Figure 6.35 (a) Comparison of CL spectra of (A) unimplanted sample, (B) Carbon implanted sample, (C) N-O implanted sample and (D) annealed N-O implanted sample. The spectra are vertically offset for more convenience. (b) Comparison of the intensities of CL spectra of unimplanted sample, N-O implanted sample and annealed N-O implanted sample.

7. Conclusion

7.1 Summary

This research project focused on the defect levels arising from the implantation of nitrogen and oxygen into a diamond lattice. The aim was to investigate whether or not nitrogen and oxygen ions form molecular N-O complexes in diamond, and if they could lead to n-type conductivity.

A 7 nm layer of higher density of N-O ions was formed on the surface of type IIa diamond samples ($2.7 \times 2.7 \times 0.3$ mm^3, oriented in a $[100]$ direction). The formation of this layer was achieved by means of ion implantation technique, with a meticulous choice of higher fluence and low energy parameters. The sample was annealed by sliding the diamond down a quartz tube from ambient temperature into a crucible of a radio frequency (RF) furnace which was preheated to 600 °C. The annealing took place in an argon environment for 30 min, thereafter, the sample was cleaned and rinsed by boiling it in an oxidizing acid solution and deionized water to etch away the graphite layer created on the surface of the sample after the annealing process.

Surface characterization, optical spectroscopy measurements were carried out to investigate defects occurring from the implantation of N-O ions by comparing the responses obtained from the annealed N-O implanted sample with five other samples of which the first one was a pristine (unimplanted) and the others were implanted with carbon, oxygen, nitrogen and N-O (unannealed).

From the surface characterization, the XPS analysis showed that there were no other chemical impurities present on the surface of the samples apart from nitrogen and oxygen. The analysis of O1s and N1s core level spectra revealed evidence of the formation of the N-O molecular complex on the surface of the N-O implanted sample (not annealed). The XPS signals of N1s and O1s recorded on the annealed N-O implanted sample were weak, and thus made it

impossible to conclude on the presence or formation of the N-O molecular complexes. However, we believe that some N-O complexes were also formed on the surface of the samples but at a very low concentration. This hypothesis was verified with photoluminescence measurements as this technique can detect impurities in diamond even at ppm concentration. In addition, the state of hybridization of carbon atoms were revealed by the analysis of C1s peaks. A change in the binding energy and the shape of the peak C1s was observed after cleaning the samples using 1 min argon etching, which caused a broadening of the carbon peaks due to surface rearrangement by the bombardment. Other chemical bonds structures between the atoms present within the samples (N, C and O) such as C=N, N=N, C-O, C-O-C were observed. SEM analysis done on the samples revealed the damage on the samples surface after higher fluence implantation. This damage was characterized by the appearance of "notches" on the surface of the implanted samples.

FTIR analysis performed on the samples under investigation showed weak absorption features on the one-phonon absorption region of all the samples. These weak features are more likely to be related to intrinsic defects or to nitrogen related defect since it has been observed in all the samples regardless their history (unimplanted or N-O/carbon implanted).

Room temperature cathodoluminescence measurements performed on the samples under investigation revealed an intense broad band emission centred at 533 nm on the annealed N-O implanted sample only. The deconvolution of this broad emission band revealed peaks at 517 nm, 533 nm, 556.7 nm and 619 nm. The origin of the CL peak at 533 nm has been tentatively attributed to a radiative recombination of a shallow n-type defect and a deep lying p-type defect in the middle of the band gap, associated to vacancy-related states.

Photoluminescence measurements conducted at room temperature using different excitation wavelengths were used to investigate the nature and behavior of the defects induced by the implantation into the diamond under the different irradiation and annealing parameters. Severals centers characteristics of nitrogen contain type IIa diamond such has NV°, NV^{-}, H3 and 389

nm or radiation damage centers such as TR12 have been observed. However, the observation of an intense broad band feature located at 309 nm led us to conduct the PL measurements at nitrogen liquid temperature as at that temperature, most of the carriers are completely frozen and the lowest energy states can be easily seen.

The low temperature measurements were done using 248 nm, 458 nm and 514.5 nm excitation wavelengths. Our low temperature PL measurements revealed luminescence peaks from an interaction with an excitation source of 248 nm at 293.3 nm, 297.3 nm, 305.9 nm, 309.8 nm, and 314.2 nm in the annealed N-O implanted sample only. These defects were related to the presence of N-O. In addition, no emission line which might be related to N-O defect has been observed in the range of 450 nm to 650 nm on the PL measurements. Futhermore, the reported oxygen related defect centers obtained from oxygen implanted type IIa diamond [145] have not been observed in either the oxygen or the N-O implanted sample. It was therefore reasonable to conclude that nitrogen and oxygen ions formed molecular N-O complexes in diamond. The mechanism of electronic transitions that lead to photoluminescence emission ascribed to the N-O molecular defects in diamond was proposed.

7.2 Conclusion

This study extended the knowledge on defects leading to shallow n-type dopants in diamond. An approach on how to form molecular N-O complexes in diamond by ion implantation was presented. It has been theoretically argued that nitrogen-oxygen pair in diamond can form a shallow defect which leads to n-type behavior [11].

Based on low temperature photoluminescence measurements and room temperature cathodoluminescence, we were able to identify a unique optical center which we relate to the presence of N-O. Therefore, we believe that this thesis creates a paradigm for future studies on the search

for alternative suitable shallow dopants, which is the sine qua non for potential application of diamond-based electronic devices.

7.3 Future work

The approach used in this study to create a layer containing high density of N-O ions with low energy and high fluence damages the sample interface as revealed by the SEM analysis. Therefore, for future work a new approach must be adopted. The sample should be implanted with low fluence and energy in order to not exceed the critical threshold value which is $\sim 5 - 9 \times 10^{22}$ vac/cm^3. This is to ensure that during post during annealing, the diamond structure will be recovered without damaging the surface of the sample. Thereafter, the same process must be repeated until one obtains a higher density of N-O ions near the surface of the sample. In that way, one can increase the concentration of N-O ions in the diamond surface without leaving too much damage. In addition, resistivity measurements using the Van der Pauw method and temperature dependent Hall measurements should be done in order to extract the activation energy of N-O ions and having a reliable measurements of Hall mobility of the created layer. Electron paramagnetic resonance measurements could also be done in order to get more details information regarding N-O complexes in diamond.

Appendix A. Room temperature photoluminescence measurements obtained with 458 nm excitation wavelength

Figure A.1 shows a typical room temperature PL spectra of the unimplanted sample, N-O implanted sample, annealed N-O implanted sample and carbon implanted sample in the range of 460 to 700 nm obtained with 458 nm excitation wavelength. All the recorded spectra were measured under identical conditions and were normalized with the first order Raman peak at 487 nm. The luminescence peaks are observed at 487 nm, 503.4 nm, 563 nm, 575 nm, 587 nm, 600 nm, 620 nm, and 637 nm. The origins of these luminescence emission have been discussed in section 6.7.3 of Chapter 6. The broad luminescence band centering at 492 nm observed in the spectra of carbon implanted sample and N-O as implanted sample shown in Figure A.2 is caused by the implantation.

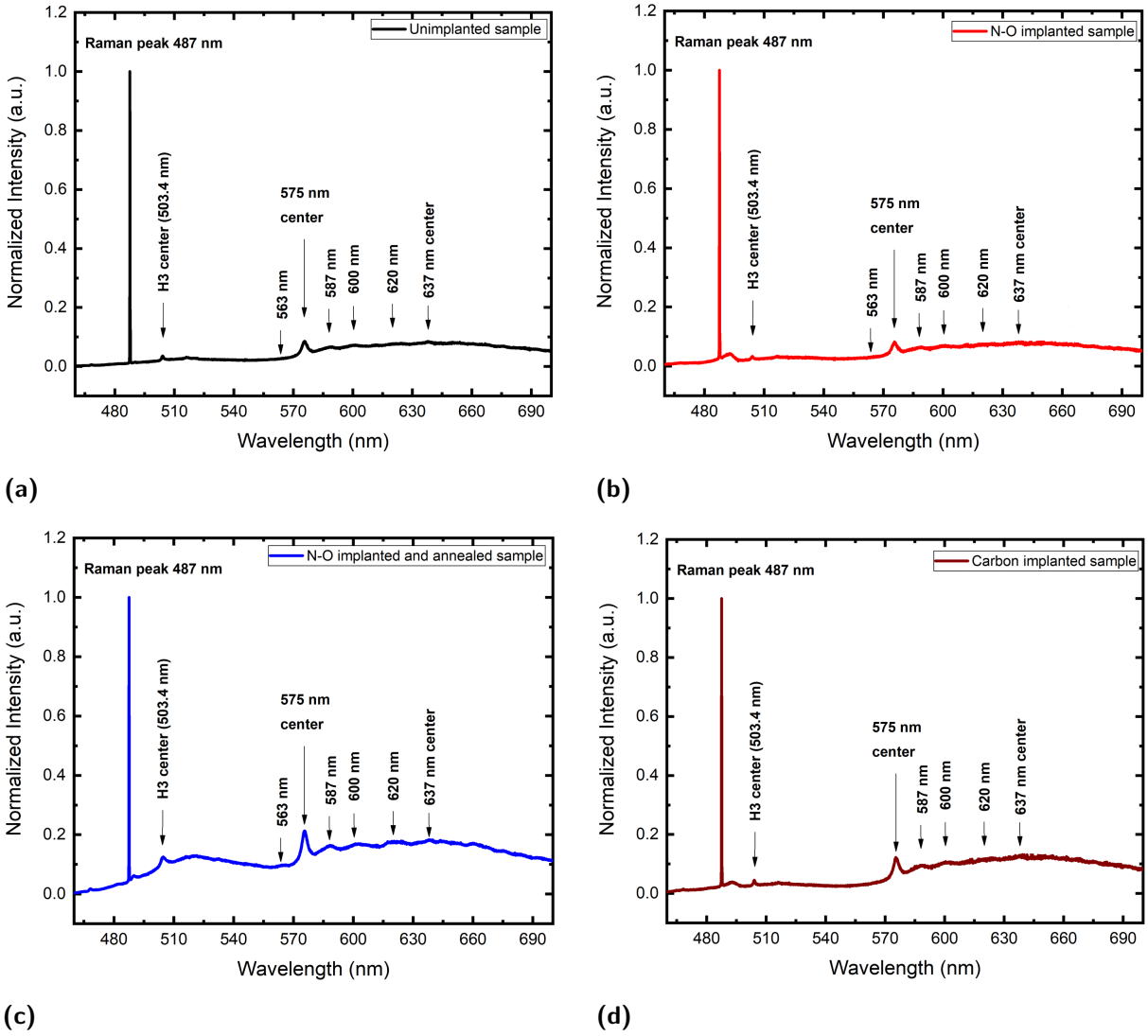

Figure A.1 Typical PL spectra of (a) unimplanted sample, (b) N-O implanted sample, (c) annealed N-O implanted sample and (d) carbon implanted sample in the range 460 to 700 nm. These spectra were recorded at room temperature using 458 nm for excitation. All the spectra were normalized with the first order Raman peak at 487 nm

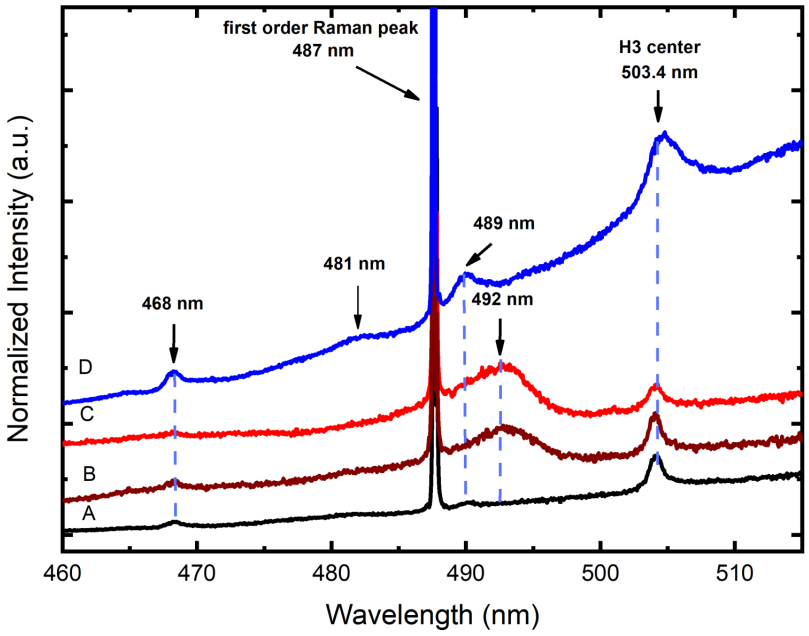

Figure A.2 Comparison of PL spectra of unimplanted sample (spectrum A), carbon implanted sample (spectrum B), N-O implanted sample (spectrum C) and annealed N-O implanted sample (spectrum D). These spectra were recorded at room temperature using 458 nm for excitation. The spectra are vertically offset for more convenience and were normalized with the first order Raman peak at 487 nm.

Appendix B. Room temperature photoluminescence measurements obtained with 514 nm excitation wavelength

Figure B.1 shows a typical room temperature PL spectra of the unimplanted sample, N-O implanted sample, annealed N-O implanted sample and carbon implanted sample in the range of 520 to 900 nm obtained with 514 nm excitation wavelength. All the recorded spectra were measured under identical conditions and were normalized with the first order Raman peak at 552 nm. The luminescence peaks are observed at 533 nm, 575 nm, 587 nm, 600 nm, 620 nm, 637 nm, 660 nm and 684 nm. The origins of these luminescence emission have been discussed in section 6.7.4 of Chapter 6. The broad luminescence band centering at 557 nm observed in the spectra of carbon implanted sample and N-O as implanted sample is caused by the implantation.

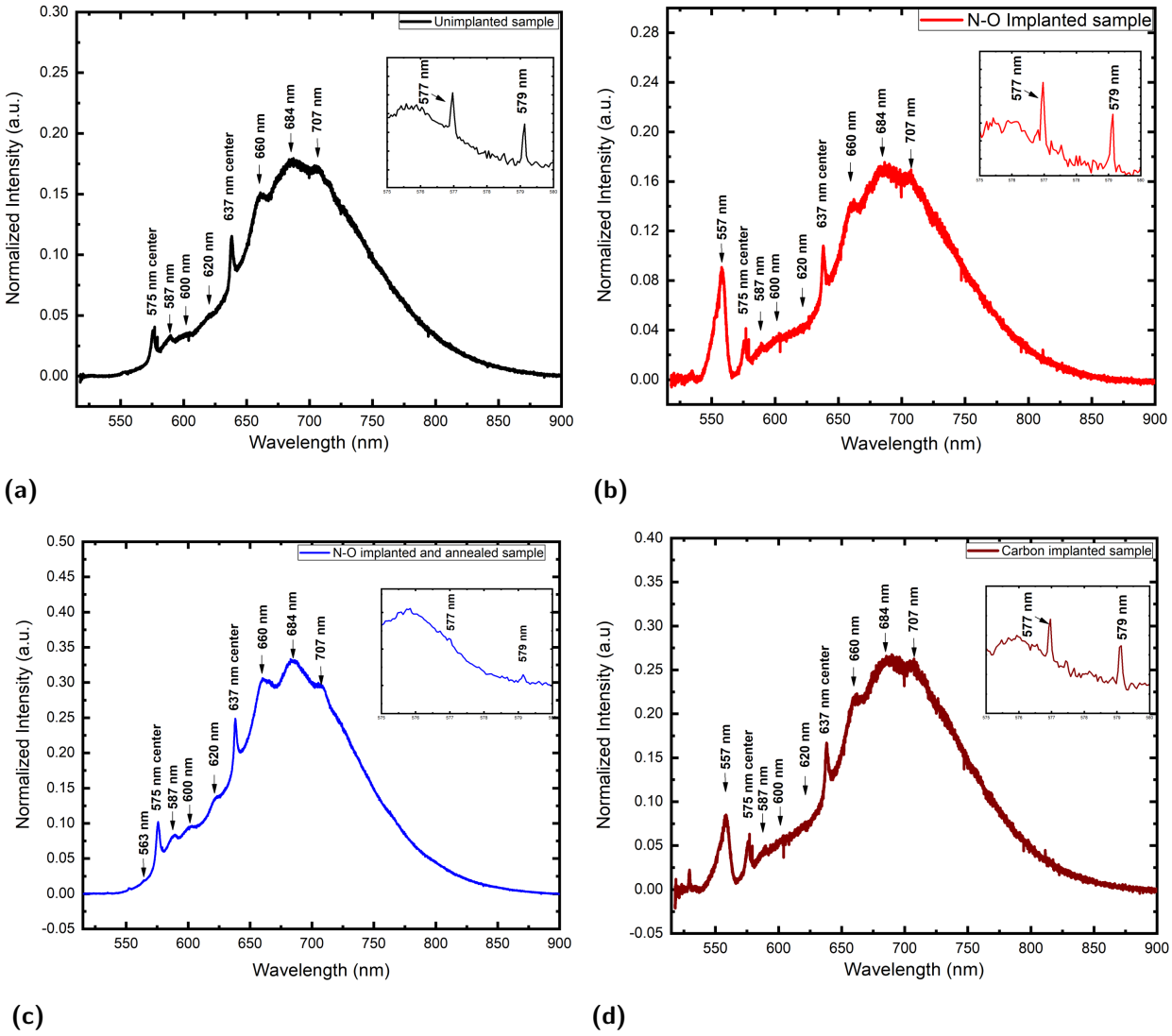

Figure B.1 Typical PL spectra of (a) the unimplanted sample, (b) N-O implanted sample, (c) annealed N-O implanted sample and (d) carbon implanted sample. recorded under 514 nm excitation. All the spectra were normalized with the first order Raman peak at 552 nm. The inset shows peak at 577 nm and 579 nm.

Contributions

Publication

1. **T.M. Matindi**, S.R Naidoo O.M Ntwaeaborwa *Luminescence induced by NO ion implantation into diamond* Diamond and Related Materials **96** (2019). Ref [240].

Conferences

- March 21, 2019, **CoE-SM/ AMSEN Annual Students Presentations** University of Witwatersrand. Poster presentation with the title: *Luminescence induced by N-O ion implantation into diamond.*
- June 25-29, 2018, **The 63rd Annual Conference of the South African Institute of Physics (SAIP), University of the Free State** . Poster presentation with the title: *Defects in diamond created by NO^+ ion implantation.*
- March 22, 2018, **CoE-SM/ AMSEN Annual Students Presentations** University of Witwatersrand. Poster presentation with the title: *Investigation of defects in Diamond Implanted N-O molecular ions.*
- Nov 27-28, 2017, **THE SOUTH AFRICAN RAMAN WORKSHOP 2017**, Hosted by Stellenbosch Institute for Advanced Studies (STIAS). Poster presentation with the title: *Investigation of defects in diamond Implanted N-O molecular ions*.
- May 11, 2017, **CoE-SM/ AMSEN Annual Students Presentations**, University of Witwatersrand. Poster presentation with the title: *Optical Characterization of N-O molecular ion implanted CVD diamond*.

- May 2-3, 2017, **United Kingdom- South Africa workshop**, on the theme: Low Diamensional Nanomaterials. Hosted by University of Cape Town. Poster presentation with the title: *Optical Characterization of N-O molecular ion implanted CVD diamond*.
- May 26, 2016, **CoE-SM/ AMSEN Annual Students Presentations**, University of Witwatersrand. Poster presentation with the title: *A Implantation of the N-O molecular ion in Diamond*.
- September 10-11, 2015, **NECSA-Wits workshop on radiation, Material Sciences and High Energy Physics**. Oral presentation with the title: *Co-implantation of N-O complex in Diamond*.

Research Visit

- **June 2016**, *Laser research Institute, Stellenbosch University*
- **September 2016**, *Department of Physics, University of free state*
- **March 2017**, *Department of Physics, University of free state*
- **October 2017**, *Department of Physics, University of free state*

References

[1] S. Pearton and F. Ren, "Devices for high-frequency applications," 2016.

[2] D. Zhou, F. Stevie, L. Chow, J. McKinley, H. Gnaser, and V. Desai, "Nitrogen incorporation and trace element analysis of nanocrystalline diamond thin films by secondary ion mass spectrometry," *Journal of Vacuum Science & Technology A: Vacuum, Surfaces, and Films*, vol. 17, no. 4, pp. 1135–1140, 1999.

[3] A. Gali, J. Lowther, and P. Deak, "Defect states of substitutional oxygen in diamond," *Journal of Physics: Condensed Matter*, vol. 13, no. 50, p. 11607, 2001.

[4] A. A. Gippius, "Impurity-defect reactions in ion-implanted diamond," in *Materials Science Forum*, vol. 83, pp. 1219–1224, Trans Tech Publ, 1992.

[5] P. May, W. Ludlow, M. Hannaway, P. Heard, J. Smith, and K. Rosser, "Raman and conductivity studies of boron-doped microcrystalline diamond, facetted nanocrystalline diamond and cauliflower diamond films," *Diamond and Related Materials*, vol. 17, no. 2, pp. 105–117, 2008.

[6] X. Liu, X. Chen, D. J. Singh, R. A. Stern, J. Wu, S. Petitgirard, C. R. Bina, and S. D. Jacobsen, "Boron–oxygen complex yields n-type surface layer in semiconducting diamond," *Proceedings of the National Academy of Sciences*, vol. 116, no. 16, pp. 7703–7711, 2019.

[7] M. Ullah, E. Ahmed, F. Hussain, A. M. Rana, R. Raza, and H. Ullah, "Electronic structure calculations of oxygen-doped diamond using dft technique," *Microelectronic Engineering*, vol. 146, pp. 26–31, 2015.

[8] S. Sque, R. Jones, J. Goss, and P. Briddon, "Shallow donors in diamond: chalcogens, pnictogens, and their hydrogen complexes," *Physical review letters*, vol. 92, no. 1, p. 017402, 2004.

[9] D. Segev and S.-H. Wei, "Design of shallow donor levels in diamond by isovalent-donor coupling," *Physical review letters*, vol. 91, no. 12, p. 126406, 2003.

[10] K. Muzyka, J. Sun, T. H. Fereja, Y. Lan, W. Zhang, and G. Xu, "Boron-doped diamond: current progress and challenges in view of electroanalytical applications," *Analytical methods*, vol. 11, no. 4, pp. 397–414, 2019.

[11] J. Lowther, "Substitutional oxygen-nitrogen pair in diamond," *Physical Review B*, vol. 67, no. 11, p. 115206, 2003.

[12] S. Kajihara, A. Antonelli, and J. Bernholc, "Impurity incorporation and doping of diamond," *Physica B: Condensed Matter*, vol. 185, no. 1, pp. 144–149, 1993.

[13] S. Koizumi, M. Kamo, Y. Sato, H. Ozaki, and T. Inuzuka, "Growth and characterization of phosphorous doped {111} homoepitaxial diamond thin films," *Applied physics letters*, vol. 71, pp. 1065–1067, 1997.

[14] S. Koizumi and M. Suzuki, "n-type doping of diamond," *physica status solidi (a)*, vol. 203, no. 13, pp. 3358–3366, 2006.

[15] J. F. Prins, "n-type semiconducting diamond by means of oxygen-ion implantation," *Physical review B*, vol. 61, no. 11, p. 7191, 2000.

[16] R. Eyre, J. Goss, P. Briddon, and M. Wardle, "Multi-impurity complexes for n-type diamond: a computational study," *physica status solidi (a)*, vol. 204, no. 9, pp. 2971–2977, 2007.

[17] J. Van Wyk, J. Loubser, M. Newton, and J. Baker, "Endor and high-temperature epr of the n3 centre in natural type ib diamonds," *Journal of Physics: Condensed Matter*, vol. 4, no. 10, p. 2651, 1992.

[18] D. A. McNeil and M. C. Symons, "Electron spin resonance spectra of two naturally occurring paramagnetic centres in diamond," *Journal of Physics and Chemistry of Solids*, vol. 38, no. 4, pp. 397–400, 1977.

[19] J. E. Field, *The properties of natural and synthetic diamond*. Academic Press, 1992.

[20] J. Wilks and E. Wilks, *Properties and applications of diamond*. Butterworth-Heinemann Oxford, 1991.

[21] A. Petitfils, *Propriétés thermoluminescentes du diamant CVD. Applications à la dosimétrie des rayonnements ionisants*. PhD thesis, Université Toulouse III-Paul Sabatier, 2007.

[22] R. Heimann, S. Evsyukov, and Y. Koga, "Carbon allotropes: a suggested classification scheme based on valence orbital hybridization," *Carbon*, vol. 35, no. 10-11, pp. 1654–1658, 1997.

[23] H. O. Pierson, "Handbook of carbon, graphite, diamond and fullerenes: processing, properties and applications," *Aufl. Park Ridge: Noyes Publications*, 1993.

[24] P. Scharff, "New carbon materials for research and technology," *Carbon*, vol. 36, no. 5-6, pp. 481–486, 1998.

[25] R. Heimann, S. Evsyukov, and Y. Koga, "Carbon allotropes: a suggested classification scheme based on valence orbital hybridization," *Carbon*, vol. 35, no. 10-11, pp. 1654–1658, 1997.

[26] W. Kaiser and W. Bond, "Nitrogen, a major impurity in common type i diamond," *Physical Review*, vol. 115, no. 4, p. 857, 1959.

[27] K. Lonsdale, "Formation of lonsdaleite from single-crystal graphite," *American Mineralogist: Journal of Earth and Planetary Materials*, vol. 56, no. 1-2, pp. 333–336, 1971.

[28] F. Bundy and J. Kasper, "Hexagonal diamond—a new form of carbon," *The Journal of Chemical Physics*, vol. 46, no. 9, pp. 3437–3446, 1967.

[29] R. Hanneman, H. Strong, and F. Bundy, "Hexagonal diamonds in meteorites: implications," *Science*, vol. 155, no. 3765, pp. 995–997, 1967.

[30] C. Frondel and U. B. Marvin, "Lonsdaleite, a hexagonal polymorph of diamond," *Nature*, vol. 214, no. 5088, p. 587, 1967.

[31] T. Sekine, M. Akaishi, N. Setaka, and K.-I. Kondo, "Diamond synthesis by weak shock loading," *Journal of materials science*, vol. 22, no. 10, pp. 3615–3619, 1987.

[32] M. Michel, H. Gnägi, and M. Müller, "Diamonds are a cryosectioner's best friend," *Journal of Microscopy*, vol. 166, no. 1, pp. 43–56, 1992.

[33] S. Evans, *Emis. Datareviews series n°9*, p. 64. INSPEC, IEE, 1994.

[34] M. E. Thomas and W. J. Tropf, "Optical properties of diamond," *Johns Hopkins APL Technical Digest*, vol. 14, pp. 16–23, 1993.

[35] A. Petitfils, *Propriétés thermoluminescentes du diamant CVD. Applications à la dosimétrie des rayonnements ionisants*. PhD thesis, Université Toulouse III-Paul Sabatier, 2007.

[36] A. BenMoussa, U. Schühle, K. Haenen, M. Nesládek, S. Koizumi, and J.-F. Hochedez, "Pin diamond detector development for lyra, the solar vuv radiometer on board proba ii," *physica status solidi (a)*, vol. 201, no. 11, pp. 2536–2541, 2004.

[37] G. Davies, "Charge states of the vacancy in diamond," *Nature*, vol. 269, no. 5628, p. 498, 1977.

[38] J. E. Field, *The properties of natural and synthetic diamond*. Academic Press, 1992.

[39] A. Collins, S. Lawson, G. Davies, and H. Kanda, "Indirect energy gap of c 13 diamond," *Physical review letters*, vol. 65, no. 7, p. 891, 1990.

[40] C. E. Nebel, "Electronic properties of cvd diamond," *Semiconductor science and technology*, vol. 18, no. 3, p. S1, 2003.

[41] S. Koizumi, H. Umezawa, J. Pernot, and M. Suzuki, *Power Electronics Device Applications of Diamond Semiconductors*. Woodhead Publishing, 2018.

[42] A. Neves and M. H. Nazaré, *Properties, growth and applications of diamond*. No. 26, IET, 2001.

[43] I. Gordon Davies, "Properties and growth of diamond," *INSPEC publication, Institution of Electrical Engineers*, 1994.

[44] J. Hartmann, M. Costello, and M. Reichling, "Influence of thermal barriers on heat flow in high quality chemical vapor deposited diamond," *Physical review letters*, vol. 80, no. 1, p. 117, 1998.

[45] C. J. Wort and R. S. Balmer, "Diamond as an electronic material," *Materials Today*, vol. 11, no. 1-2, pp. 22–28, 2008.

[46] G. A. Denu, J. H. Mirani, J. Fu, Z. Liu, and H. Wang, "Fem thermal analysis of cu/-diamond/cu and diamond/sic heat spreaders," *AIP Advances*, vol. 7, no. 3, p. 035102, 2017.

[47] A. Lostetter, K. Olejniczak, W. Brown, and A. Elshabini, "The utilization of diamond and diamond-like-carbon substrates for high performance power electronic packaging applications," in *2001 EPE Conference*, 2001.

[48] O. ims, "Material sound velocities," 2019.

[49] L. Le Brizoual and O. Elmazria, "Fem modeling of aln/diamond surface acoustic waves device," *Diamond and related materials*, vol. 16, no. 4-7, pp. 987–990, 2007.

[50] H. Nakahata, S. Fujii, K. Higaki, A. Hachigo, H. Kitabayashi, S. Shikata, and N. Fujimori, "Diamond-based surface acoustic wave devices," *Semiconductor science and technology*, vol. 18, no. 3, p. S96, 2003.

[51] R. A. Freitas Jr, "Nanomedicine, volume iia: Biocompatibility. landes bioscience, georgetown, tx, 2003," 2003.

[52] M. S. Humayun, J. D. Weiland, G. Y. Fujii, R. Greenberg, R. Williamson, J. Little, B. Mech, V. Cimmarusti, G. Van Boemel, G. Dagnelie, *et al.*, "Visual perception in a blind subject with a chronic microelectronic retinal prosthesis," *Vision research*, vol. 43, no. 24, pp. 2573–2581, 2003.

[53] C. Veraart, C. Raftopoulos, J. T. Mortimer, J. Delbeke, D. Pins, G. Michaux, A. Vanlierde, S. Parrini, and M.-C. Wanet-Defalque, "Visual sensations produced by optic nerve stimulation using an implanted self-sizing spiral cuff electrode," *Brain research*, vol. 813, no. 1, pp. 181–186, 1998.

[54] P. Bergonzo and R. B. Jackman, "Diamond-based radiation and photon detectors," in *Semiconductors and Semimetals*, vol. 77, pp. 197–309, Elsevier, 2004.

[55] F. Bundy, H. T. Hall, H. Strong, and R. W. Jun, "Man-made diamonds," *nature*, vol. 176, no. 4471, p. 51, 1955.

[56] F. Bundy, "Methods and mechanisms of synthetic diamond growth," *Chem. and Phys. Carbon*, vol. 10, pp. 213–263, 1973.

[57] F. Bundy, W. Bassett, M. Weathers, R. Hemley, H. Mao, and A. Goncharov, "The pressure-temperature phase and transformation diagram for carbon; updated through 1994," *Carbon*, vol. 34, no. 2, pp. 141–153, 1996.

[58] F. P. Bundy, "The p, t phase and reaction diagram for elemental carbon, 1979," *Journal of Geophysical Research: Solid Earth*, vol. 85, no. B12, pp. 6930–6936, 1980.

[59] R. Abbaschian, H. Zhu, and C. Clarke, "High pressure–high temperature growth of diamond crystals using split sphere apparatus," *Diamond and related materials*, vol. 14, no. 11-12, pp. 1916–1919, 2005.

[60] P. Bridgman, "Synthetic diamonds," *Scientific American*, vol. 193, no. 5, pp. 42–47, 1955.

[61] B. Derjaguin, D. Fedoseev, V. Lukyanovich, B. Spitzin, V. Ryabov, and A. Lavrentyev, "Filamentary diamond crystals," *Journal of Crystal Growth*, vol. 2, no. 6, pp. 380–384, 1968.

[62] J. C. Angus, H. A. Will, and W. S. Stanko, "Growth of diamond seed crystals by vapor deposition," *Journal of Applied Physics*, vol. 39, no. 6, pp. 2915–2922, 1968.

[63] T. A. Grotjohn and J. Asmussen, "Microwave plasma-assisted diamond film deposition," *Diamond films handbook*, pp. 243–260, 2002.

[64] J. Butler, Y. A. Mankelevich, A. Cheesman, J. Ma, and M. Ashfold, "Understanding the chemical vapor deposition of diamond: recent progress," *Journal of Physics: Condensed Matter*, vol. 21, no. 36, p. 364201, 2009.

[65] A. Gicquel, F. Silva, C. Rond, N. Derkaoui, O. Brinza, J. Achard, G. Lombardi, A. Tallaire, A. Michau, M. Wartel, *et al.*, "Ultrafast deposition of diamond by plasma-enhanced cvd," 2014.

[66] M. Schwander and K. Partes, "A review of diamond synthesis by cvd processes," *Diamond and related materials*, vol. 20, no. 9, pp. 1287–1301, 2011.

[67] N. Tranchant, *Synthèse et caractérisation de diamants monocristallins pour applications de détecteur de rayonnements*. PhD thesis, Rennes, INSA, 2008.

[68] E. Fritsch and K. Scarratt, "Natural-color nonconductive gray-toblue diamonds," *Gems & Gemology*, vol. 28, no. 1, pp. 35–42, 1992.

[69] D. Pearson, D. Canil, and S. Shirey, "Mantle samples included in volcanic rocks: xenoliths and diamonds," *Treatise on geochemistry*, vol. 2, p. 568, 2003.

[70] G. Woods, "The'type'terminology for diamond," *Properties and growth of diamond*, pp. 83–84, 1992.

[71] J. I. Koivula, *The Microworld of Diamonds: A Visual Reference Guide*. Gemworld International, Incorporated, 2000.

[72] J. Wilks and E. Wilks, *Properties and applications of diamond*. Butterworth-Heinemann Oxford, 1991.

[73] A. Collins and A. Williams, "The nature of the acceptor centre in semiconducting diamond," *Journal of Physics C: Solid State Physics*, vol. 4, no. 13, p. 1789, 1971.

[74] R. Haubner, S. Bohr, and B. Lux, "Comparison of p, n and b additions during cvd diamond deposition," *Diamond and related materials*, vol. 8, no. 2-5, pp. 171–178, 1999.

[75] R. Haubner, S. Bohr, and B. Lux, "Comparison of p, n and b additions during cvd diamond deposition," *Diamond and related materials*, vol. 8, no. 2-5, pp. 171–178, 1999.

[76] H. Spicka, M. Griesser, H. Hutter, M. Grasserbauer, S. Bohr, R. Haubner, and B. Lux, "Investigations of the incorporation of b, p and n into cvd-diamond films by secondary ion mass spectrometry," *Diamond and Related Materials*, vol. 5, no. 3-5, pp. 383–387, 1996.

[77] J.-P. Lagrange, A. Deneuville, and E. Gheeraert, "Activation energy in low compensated homoepitaxial boron-doped diamond films," *Diamond and Related Materials*, vol. 7, no. 9, pp. 1390–1393, 1998.

[78] K. Ushizawa, K. Watanabe, T. Ando, I. Sakaguchi, M. Nishitani-Gamo, Y. Sato, and H. Kanda, "Boron concentration dependence of raman spectra on {100} and {111} facets of b-doped cvd diamond," *Diamond and related materials*, vol. 7, no. 11-12, pp. 1719–1722, 1998.

[79] S. Yamanaka, H. Watanabe, S. Masai, D. Takeuchi, H. Okushi, and K. Kajimura, "High-quality b-doped homoepitaxial diamond films using trimethylboron," *Japanese journal of applied physics*, vol. 37, no. 10A, p. L1129, 1998.

[80] S. Yamanaka, D. Takeuchi, H. Watanabe, H. Okushi, and K. Kajimura, "Low-compensated boron-doped homoepitaxial diamond films," *Diamond and Related Materials*, vol. 9, no. 3-6, pp. 956–959, 2000.

[81] J. P. Goss, R. J. Eyre, and P. R. Briddon, "Theoretical models for doping diamond for semiconductor applications," *physica status solidi (b)*, vol. 245, no. 9, pp. 1679–1700, 2008.

[82] T. Zimmermann, M. Kubovic, A. Denisenko, K. Janischowsky, O. A. Williams, D. Gruen, and E. Kohn, "Ultra-nano-crystalline/single crystal diamond heterostructure diode," *Diamond and related materials*, vol. 14, no. 3-7, pp. 416–420, 2005.

[83] S. Koizumi, M. Kamo, Y. Sato, S. Mita, A. Sawabe, A. Reznik, C. Uzan-Saguy, and R. Kalish, "Growth and characterization of phosphorus doped n-type diamond thin films," *Diamond and related materials*, vol. 7, no. 2-5, pp. 540–544, 1998.

[84] S. Koizumi, T. Teraji, and H. Kanda, "Phosphorus-doped chemical vapor deposition of diamond," *Diamond and Related Materials*, vol. 9, no. 3-6, pp. 935–940, 2000.

[85] M. Nesladek, K. Meykens, K. Haenen, L. Stals, T. Teraji, and S. Koizumi, "Photocurrent and optical absorption spectroscopic study of n-type phosphorus-doped cvd diamond," *Diamond and related materials*, vol. 8, no. 2-5, pp. 882–885, 1999.

[86] H. Kato, S. Yamasaki, and H. Okushi, "n-type doping of (001)-oriented single-crystalline diamond by phosphorus," *Applied Physics Letters*, vol. 86, no. 22, p. 222111, 2005.

[87] H. Kato, W. Futako, S. Yamasaki, and H. Okushi, "Homoepitaxial growth and characterization of phosphorus-doped diamond using tertiarybutylphosphine as a doping source," *Diamond and related materials*, vol. 13, no. 11-12, pp. 2117–2120, 2004.

[88] K. Bharuth-Ram, H. Quintel, M. Restle, C. Ronning, H. Hofsäss, and S. Jahn, "Lattice sites of arsenic ions implanted in diamond," *Journal of applied physics*, vol. 78, no. 8, pp. 5180–5182, 1995.

[89] F. Maier, M. Riedel, B. Mantel, J. Ristein, and L. Ley, "Origin of surface conductivity in diamond," *Physical review letters*, vol. 85, no. 16, p. 3472, 2000.

[90] M. Kubovic, M. Kasu, I. Kallfass, M. Neuburger, A. Aleksov, G. Koley, M. Spencer, and E. Kohn, "Microwave performance evaluation of diamond surface channel fets," *Diamond and related materials*, vol. 13, no. 4-8, pp. 802–807, 2004.

[91] C. Nebel and J. Ristein, *Thin-Film Diamond I:(part of the Semiconductors and Semimetals Series)*, vol. 76. Academic Press, 2003.

[92] W. Tsai, M. Delfino, D. Hodul, M. Riaziat, L. Ching, G. Reynolds, and C. Cooper, "Diamond mesfet using ultrashallow rtp boron doping," *IEEE electron device letters*, vol. 12, no. 4, pp. 157–159, 1991.

[93] O. B. Krutko, P. B. Kosel, R. Wu, S. Fries-Carr, S. Heidger, and J. Weimer, "P-type polycrystalline diamond layers by rapid thermal diffusion of boron," *Applied Physics Letters*, vol. 76, no. 7, pp. 849–851, 2000.

[94] V. Vavilov, "Ion implantation into diamond," *Radiation Effects*, vol. 37, no. 3-4, pp. 229–236, 1978.

[95] S. Prawer and R. Kalish, "Ion-beam-induced transformation of diamond," *Physical Review B*, vol. 51, no. 22, p. 15711, 1995.

[96] C. Uzan-Saguy, C. Cytermann, R. Brener, V. Richter, M. Shaanan, and R. Kalish, "Damage threshold for ion-beam induced graphitization of diamond," *Applied Physics Letters*, vol. 67, no. 9, pp. 1194–1196, 1995.

[97] J. F. Ziegler, M. D. Ziegler, and J. P. Biersack, "Srim–the stopping and range of ions in matter (2010)," *Nuclear Instruments and Methods in Physics Research Section B: Beam Interactions with Materials and Atoms*, vol. 268, no. 11-12, pp. 1818–1823, 2010.

[98] E. Nshingabigwi, T. Derry, S. Naidoo, J. Neethling, E. Olivier, J. O'Connell, and C. Levitt, "Electron microscopy profiling of ion implantation damage in diamond: Dependence on fluence and annealing," *Diamond and Related Materials*, vol. 49, pp. 1–8, 2014.

[99] C. Nebel and J. Ristein, *Thin-Film Diamond I:(part of the Semiconductors and Semimetals Series)*, vol. 76. Academic Press, 2003.

[100] J. F. Prins, "Point-defect interactions when annealing diamonds implanted at low temperatures," *Physical Review B*, vol. 44, no. 6, p. 2470, 1991.

[101] J. F. Prins, "Activation of boron-dopant atoms in ion-implanted diamonds," *Physical Review B*, vol. 38, no. 8, p. 5576, 1988.

[102] C. Kittel, P. McEuen, and P. McEuen, *Introduction to solid state physics*, vol. 8. Wiley New York, 1976.

[103] F. Agulló-López, C. R. A. Catlow, and P. D. Townsend, *Point defects in materials*. Academic press, 1988.

[104] L. J. Bond, "Point defects." 2012, 09 2012.

[105] T. L. libraries, "Defects in crystals," 2019.

[106] A. M. Zaitsev, *Optical properties of diamond: a data handbook*. Springer Science & Business Media, 2013.

[107] F. V. Kaminsky and G. K. Khachatryan, "Characteristics of nitrogen and other impurities in diamond, as revealed by infrared absorption data," *The Canadian Mineralogist*, vol. 39, no. 6, pp. 1733–1745, 2001.

[108] A. T. Collins, M. Kamo, and Y. Sato, "A spectroscopic study of optical centers in diamond grown by microwave-assisted chemical vapor deposition," *Journal of Materials Research*, vol. 5, no. 11, pp. 2507–2514, 1990.

[109] W. G. Clark C.D, Collins A.T, *Absorption and luminescence spectroscopy*, pp. 35–79. 1992.

[110] G. Davies, "The a nitrogen aggregate in diamond-its symmetry and possible structure," *Journal of Physics C: Solid State Physics*, vol. 9, no. 19, p. L537, 1976.

[111] T. Evans and Z. Qi, "The kinetics of the aggregation of nitrogen atoms in diamond," *Proceedings of the Royal Society of London. A. Mathematical and Physical Sciences*, vol. 381, no. 1780, pp. 159–178, 1982.

[112] A. M. Zaitsev, *Optical properties of diamond: a data handbook*. Springer Science & Business Media, 2013.

[113] L. Massi, *Étude des défauts dans les diamants bruns et les diamants riches en hydrogène*. PhD thesis, Ph. D. Thesis. Université de Nantes, Faculté des Sciences et des Techniques . . . , 2006.

[114] G. Davies, "The a nitrogen aggregate in diamond-its symmetry and possible structure," *Journal of Physics C: Solid State Physics*, vol. 9, no. 19, p. L537, 1976.

[115] W. G. S, *The "type" terminology for diamonds*, pp. 83–84. 1992.

[116] A. Mainwood, "Nitrogen and nitrogen-vacancy complexes and their formation in diamond," *Physical Review B*, vol. 49, no. 12, p. 7934, 1994.

[117] T. Miyazaki, H. Okushi, and T. Uda, "Shallow donor state due to nitrogen-hydrogen complex in diamond," *Physical review letters*, vol. 88, no. 6, p. 066402, 2002.

[118] T. Evans, *Aggregation of nitrogen in diamond*, pp. 259–290. 1992.

[119] N. Ferrer and J. Nogues-Carulla, "Characterisation study of cut gem diamond by ir spectroscopy," *Diamond and related materials*, vol. 5, no. 6-8, pp. 598–602, 1996.

[120] L. Speich, S. Kohn, G. Bulanova, and C. Smith, "The behaviour of platelets in natural diamonds and the development of a new mantle thermometer," *Contributions to Mineralogy and Petrology*, vol. 173, no. 5, p. 39, 2018.

[121] L. Bursill and R. Glaisher, "Aggregation and dissolution of small and extended defect structures in type ia diamond," *American Mineralogist*, vol. 70, no. 5-6, pp. 608–618, 1985.

[122] A. Yelisseyev and V. Nadolinny, "Photoinduced absorption lines related to nickel impurity in annealed synthetic diamonds," *Diamond and related materials*, vol. 4, no. 3, pp. 177–185, 1995.

[123] A. T. Collins, "The characterisation of point defects in diamond by luminescence spectroscopy," *Diamond and related materials*, vol. 1, no. 5-6, pp. 457–469, 1992.

[124] L. Robins, L. Cook, E. Farabaugh, and A. Feldman, "Cathodoluminescence of defects in diamond films and particles grown by hot-filament chemical-vapor deposition," *Physical Review B*, vol. 39, no. 18, p. 13367, 1989.

[125] A. Haque and S. Sumaiya, "An overview on the formation and processing of nitrogen-vacancy photonic centers in diamond by ion implantation," *Journal of Manufacturing and Materials Processing*, vol. 1, no. 1, p. 6, 2017.

[126] A. Dräbenstedt, L. Fleury, C. Tietz, F. Jelezko, S. Kilin, A. Nizovtzev, and J. Wrachtrup, "Low-temperature microscopy and spectroscopy on single defect centers in diamond," *Physical Review B*, vol. 60, no. 16, p. 11503, 1999.

[127] K. Iakoubovskii, G. Adriaenssens, and M. Nesladek, "Photochromism of vacancy-related centres in diamond," *Journal of Physics: Condensed Matter*, vol. 12, no. 2, p. 189, 2000.

[128] H. Dyer and I. Matthews, "The fluorescence of diamond," *Proceedings of the Royal Society of London. Series A. Mathematical and Physical Sciences*, vol. 243, no. 1234, pp. 320–335, 1958.

[129] D. Twitchen, D. Hunt, V. Smart, M. Newton, and J. Baker, "Correlation between nd1 optical absorption and the concentration of negative vacancies determined by electron paramagnetic resonance (epr)," *Diamond and related materials*, vol. 8, no. 8-9, pp. 1572–1575, 1999.

[130] A. Collins, M. Kamo, and Y. Sato, "Optical centres related to nitrogen, vacancies and interstitials in polycrystalline diamond films grown by plasma-assisted chemical vapour deposition," *Journal of Physics D: Applied Physics*, vol. 22, no. 9, p. 1402, 1989.

[131] D. Wight and P. Dean, "Extrinsic recombination radiation from natural diamond: exciton luminescence associated with the n 9 center," *Physical review*, vol. 154, no. 3, p. 689, 1967.

[132] W. D. Partlow, J. Ruan, R. E. Witkowski, W. Choyke, and D. S. Knight, "Cryogenic cathodoluminescence of plasma-deposited polycrystalline diamond coatings," *Journal of Applied Physics*, vol. 67, no. 11, pp. 7019–7025, 1990.

[133] A. Collins and P. Spear, "Optical studies of the 5rl centre in diamond," *Journal of Physics C: Solid State Physics*, vol. 19, no. 34, p. 6845, 1986.

[134] J. Walker, "An optical study of the tr12 and 3h defects in irradiated diamond," *Journal of Physics C: Solid State Physics*, vol. 10, no. 16, p. 3031, 1977.

[135] H. Yagyu, M. Deguchi, J. H. Won, Y. Mori, A. Hatta, M. Kitabatake, T. Ito, T. Hirao, and A. Hiraki, "Ion implantation in cvd diamond and plasma treatment effect," *Diamond and related materials*, vol. 4, no. 5-6, pp. 575–579, 1995.

[136] L. Allers, A. T. Collins, and J. Hiscock, "The annealing of interstitial-related optical centres in type ii natural and cvd diamond," *Diamond and related materials*, vol. 7, no. 2-5, pp. 228–232, 1998.

[137] A. Gippius, A. Zajtsev, and V. Vavilov, "Formation annealing and interaction of defects in ion-implanted natural diamond layers," *Fizika i Tekhnika Poluprovodnikov*, vol. 16, no. 3, pp. 404–411, 1982.

[138] S. William, "Forming semiconductive devices by ionic bombardment," Apr. 2 1957. US Patent 2,787,564.

[139] E. Fritsch, K. Scarratt, A. Collins, R. Messier, J. Glass, J. Butler, and R. Roy, "Optical properties of diamonds with an unusually high hydrogen content," in *Materials Research Society International Conference Proceedings, Second International Conference on New Diamond Science and Technology, Washington DC, Sept*, pp. 23–27, 1991.

[140] K. Etmimi, P. Briddon, A. Abutruma, A. Sghayer, and S. Farhat, "Density functional theory study of substitutional oxygen in diamond," *arXiv preprint arXiv:1609.04697*, 2016.

[141] G. Thiering and A. Gali, "Characterization of oxygen defects in diamond by means of density functional theory calculations," *Physical Review B*, vol. 94, no. 12, p. 125202, 2016.

[142] K. Etmimi, J. Goss, P. Briddon, and A. Gsiea, "A density functional theory study of models for the n3 and ok1 epr centres in diamond," *Journal of Physics: Condensed Matter*, vol. 22, no. 38, p. 385502, 2010.

[143] J. Ruan, W. Choyke, and K. Kobashi, "Oxygen-related centers in chemical vapor deposition of diamond," *Applied physics letters*, vol. 62, no. 12, pp. 1379–1381, 1993.

[144] Y. Mori, N. Eimori, H. Kozuka, Y. Yokota, J. Moon, J. Ma, T. Ito, and A. Hiraki, "Oxygen diffusion into diamond induced by hydrogen microwave plasma," *Applied physics letters*, vol. 60, no. 1, pp. 47–49, 1992.

[145] A. A. Gippius, "Luminescent characterization of radiation damage and impurities in ion-implanted natural diamond," *Diamond and Related Materials*, vol. 2, no. 5-7, pp. 640–645, 1993.

[146] J. Adler, A. Silverman, N. Ierushalmi, A. Sorkin, and R. Kalish, "Simulation and visualization of ion-implantation in diamond," in *Journal of Physics: Conference Series*, vol. 487, p. 012015, IOP Publishing, 2014.

[147] P. Townsend, "Optical effects of ion implantation," *Reports on Progress in Physics*, vol. 50, no. 5, p. 501, 1987.

[148] S. G. L. Z. Z. Sioxiao and W. B. L. X. J. Jinyun, "An implantation facility for surface modification of metals,"

[149] S. Merabet, "Simulation à l'aide d'un modèle dit de" monté carlo" des profils de bore implantés requis pour la réalisation des jonctions courtes utilisées dans les processus de haute densité d'intégration (phdi)," 2009.

[150] O. ims, "Material sound velocities," 2019.

[151] C. Chabrol, "Implantation ionique," *Les Techniques de l'ingénieur. M*, vol. 1, p. 219, 1989.

[152] S. Blanqué, *Optimisation de l'implantation ionique et du recuit thermique pour SiC*. Universitat Autònoma de Barcelona,, 2005.

[153] J. F. Ziegler, *Ion implantation science and technology*. Elsevier, 2012.

[154] J. Williams, "Materials modification with ion beams," *Reports on Progress in Physics*, vol. 49, no. 5, p. 491, 1986.

[155] J. Lindhard, M. Scharff, and H. E. Schiøtt, *Range concepts and heavy ion ranges*. Munksgaard Copenhagen, 1963.

[156] Y. Pauleau, *Materials surface processing by directed energy techniques*. Elsevier, 2006.

[157] J. Lindhard, A. Winther, *et al.*, *Stopping power of electron gas and equipartition rule*. Munksgaard, 1964.

[158] O. Firsov, "A qualitative interpretation of the mean electron excitation energy in atomic collisions," *Zhur. Eksptl'. i Teoret. Fiz.*, vol. 36, 1959.

[159] J. Lindhard and M. Scharff, "Energy dissipation by ions in the kev region," *Physical Review*, vol. 124, no. 1, p. 128, 1961.

[160] P.-N. Favennec, *L'implantation ionique: pour la microélectronique et l'optique*. Masson, 1993.

[161] J. Koike, D. Parkin, and T. Mitchell, "Displacement threshold energy for type iia diamond," *Applied physics letters*, vol. 60, no. 12, pp. 1450–1452, 1992.

[162] M. B. Lazar, *Etude du Dopage par Implantation Ionique d'Aluminium dans le Carbure de Silicium pour la Réalisation de Composants de Puissance*. PhD thesis, Lyon, INSA, 2002.

[163] G. Kinchin and R. Pease, "The displacement of atoms in solids by radiation," *Reports on progress in physics*, vol. 18, no. 1, p. 1, 1955.

[164] M. T. Robinson and I. M. Torrens, "Computer simulation of atomic-displacement cascades in solids in the binary-collision approximation," *Physical Review B*, vol. 9, no. 12, p. 5008, 1974.

[165] S. Morris, B. Obradovic, S.-H. Yang, and A. Tasch, "Modeling of boron, phosphorus, and arsenic implants into single-crystal silicon over a wide energy range (few kev to several mev)," in *International Electron Devices Meeting. Technical Digest*, pp. 721–724, IEEE, 1996.

[166] I. Chakarov and R. Webb, "Crystal-binary collision simulation of atomic collisions and dynamic damage buildup in crystalline silicon," *Radiation Effects and Defects in Solids*, vol. 130, no. 1, pp. 447–452, 1994.

[167] O. ims, "Material sound velocities," 2019.

[168] R. Kalish, A. Reznik, S. Prawer, D. Saada, and J. Adler, "Ion-implantation-induced defects in diamond and their annealing: experiment and simulation," *physica status solidi (a)*, vol. 174, no. 1, pp. 83–99, 1999.

[169] V. Rudnev, D. Loveless, and R. L. Cook, *Handbook of induction heating*. CRC press, 2017.

[170] H. Hertz, "Ueber einen einfluss des ultravioletten lichtes auf die electrische entladung," *Annalen der Physik*, vol. 267, no. 8, pp. 983–1000, 1887.

[171] A. Einstein, "Über einen die erzeugung und verwandlung des lichtes betreffenden heuristischen gesichtspunkt," *Annalen der physik*, vol. 322, no. 6, pp. 132–148, 1905.

[172] K. Siegbahn and C. Nordling, "Esca, atomic, molecular and solid state structure studied by means of electron spectroscopy," *Nov. act. uppsaliensis*, 1967.

[173] M. P. Seah and D. Briggs, *Practical Surface Analysis: Auger and X-ray Photoelectron Spectroscopy*. John Wiley & Sons, 1990.

[174] O. ims, "Material sound velocities," 2019.

[175] C. S. Fadley, "Basic concepts of x-ray photoelectron spectroscopy. electron spectroscopy: theory, techniques, and applications, vol. 2," 1978.

[176] L. Demuynck, J. Arnault, R. Polini, and F. Le Normand, "Cvd diamond nucleation and growth on scratched and virgin si (100) surfaces investigated by in-situ electron spectroscopy," *Surface science*, vol. 377, pp. 871–875, 1997.

[177] S. Ghodbane, D. Ballutaud, F. Omnès, and C. Agnes, "Comparison of the xps spectra from homoepitaxial $\{111\}$,$\{100\}$ and polycrystalline boron-doped diamond films," *Diamond and Related Materials*, vol. 19, no. 5-6, pp. 630–636, 2010.

[178] R. Bogdanowicz, M. Sawczak, P. Niedzialkowski, P. Zieba, B. Finke, J. Ryl, J. Karczewski, and T. Ossowski, "Novel functionalization of boron-doped diamond by microwave pulsed-plasma polymerized allylamine film," *The Journal of Physical Chemistry C*, vol. 118, no. 15, pp. 8014–8025, 2014.

[179] R. Graupner, F. Maier, J. Ristein, L. Ley, and C. Jung, "High-resolution surface-sensitive c 1 s core-level spectra of clean and hydrogen-terminated diamond (100) and (111) surfaces," *Physical Review B*, vol. 57, no. 19, p. 12397, 1998.

[180] H. Girard, N. Simon, D. Ballutaud, M. Herlem, and A. Etcheberry, "Effect of anodic and cathodic treatments on the charge transfer of boron doped diamond electrodes," *Diamond and Related Materials*, vol. 16, no. 2, pp. 316–325, 2007.

[181] W. Kulisch, C. Petkov, E. Petkov, C. Popov, P. N. Gibson, M. Veres, R. Merz, B. Merz, and J. P. Reithmaier, "Low temperature growth of nanocrystalline and ultrananocrystalline diamond films: a comparison," *physica status solidi (a)*, vol. 209, no. 9, pp. 1664–1674, 2012.

[182] R. Bertoncello, A. Casagrande, M. Casarin, A. Glisenti, E. Lanzoni, L. Mirenghi, and E. Tondello, "Tin, tic and ti (c, n) film characterization and its relationship to tribological behaviour," *Surface and Interface Analysis*, vol. 18, no. 7, pp. 525–531, 1992.

[183] P. Merel, M. Tabbal, M. Chaker, S. Moisa, and J. Margot, "Direct evaluation of the sp3 content in diamond-like-carbon films by xps," *Applied Surface Science*, vol. 136, no. 1-2, pp. 105–110, 1998.

[184] J. Wilson, J. Walton, and G. Beamson, "Analysis of chemical vapour deposited diamond films by x-ray photoelectron spectroscopy," *Journal of Electron Spectroscopy and Related Phenomena*, vol. 121, no. 1-3, pp. 183–201, 2001.

[185] J. Shalini, K. J. Sankaran, C.-L. Dong, C.-Y. Lee, N.-H. Tai, and I.-N. Lin, "In situ detection of dopamine using nitrogen incorporated diamond nanowire electrode," *Nanoscale*, vol. 5, no. 3, pp. 1159–1167, 2013.

[186] S. Ferro, M. Dal Colle, and A. De Battisti, "Chemical surface characterization of electrochemically and thermally oxidized boron-doped diamond film electrodes," *Carbon*, vol. 43, no. 6, pp. 1191–1203, 2005.

[187] Y. Liu, L. Zhou, Y. Li, R. Deng, and H. Zhang, "Highly fluorescent nitrogen-doped carbon dots with excellent thermal and photo stability applied as invisible ink for loading important information and anti-counterfeiting," *Nanoscale*, vol. 9, no. 2, pp. 491–496, 2017.

[188] H. Schmiers, J. Friebel, P. Streubel, R. Hesse, and R. Köpsel, "Change of chemical bonding of nitrogen of polymeric n-heterocyclic compounds during pyrolysis," *Carbon*, vol. 37, no. 12, pp. 1965–1978, 1999.

[189] I. Gouzman, R. Brener, and A. Hoffman, "Nitridation of diamond and graphite surfaces by low energy n+ 2 ion irradiation," *Surface science*, vol. 331, pp. 283–288, 1995.

[190] J. Shirafuji, Y. Sakamoto, A. Furukawa, H. Shigeta, and T. Sugino, "X-ray photoelectron spectroscopy analysis of plasma-treated surfaces of diamond films," *Diamond and related materials*, vol. 4, no. 7, pp. 984–988, 1995.

[191] R. DeClements and G. M. Swain, "The formation and electrochemical activity of microporous diamond thin film electrodes in concentrated koh," *Journal of the Electrochemical Society*, vol. 144, no. 3, pp. 856–866, 1997.

[192] J. Botsoa, "Synthèse de nanostructures de carbure de silicium et étude de leurs propriétés optiques," *Lyon: INSA de Lyon*, 2008.

[193] D. S. Knight and W. B. White, "Characterization of diamond films by raman spectroscopy," *Journal of Materials Research*, vol. 4, no. 2, pp. 385–393, 1989.

[194] L. Nasdala, D. C. Smith, R. Kaindl, and M. A. Ziemann, "Raman spectroscopy: analytical perspectives in mineralogical research," *Spectroscopic methods in mineralogy*, vol. 6, pp. 281–343, 2004.

[195] C. M. Breeding and J. E. Shigley, "The "type" classification system of diamonds and its importance in gemology," *Gems & Gemology*, vol. 45, no. 2, pp. 96–111, 2009.

[196] A. Scarani, M. Åström, and M. G. Instruments, "Application note: Diamond classification–the diamond types," 2015.

[197] K. Takahashi, A. Yoshikawa, and A. Sandhu, "Wide bandgap semiconductors," *Springer-Verlag Berlin Heidelberg.*, p. 239, 2007.

[198] M. Fox, "Optical properties of solids," 2002.

[199] B. Yacobi and D. Holt, "Cathodoluminescence scanning electron microscopy of semiconductors," *Journal of applied physics*, vol. 59, no. 4, pp. R1–R24, 1986.

[200] H. Watanabe and H. Okushi, "Nonlinear effects excitonic emission from high quality homoepitaxial diamond films," *Japanese Journal of Applied Physics*, vol. 39, no. 8B, p. L835, 2000.

[201] D. Hickey, K. Jones, and R. Elliman, "Amorphization and graphitization of single-crystal diamond—a transmission electron microscopy study," *Diamond and Related Materials*, vol. 18, no. 11, pp. 1353–1359, 2009.

[202] S. Naidoo and J. Prins, "Electroluminescence from electron injection junctions created by carbon and phosphorus ion implantation," *Diamond and related materials*, vol. 8, no. 8-9, pp. 1502–1507, 1999.

[203] D. Ballutaud, T. Kociniewski, J. Vigneron, N. Simon, and H. Girard, "Hydrogen incorporation, bonding and stability in nanocrystalline diamond films," *Diamond and Related Materials*, vol. 17, no. 7-10, pp. 1127–1131, 2008.

[204] S. Bhattacharyya, J. Hong, and G. Turban, "Determination of the structure of amorphous nitrogenated carbon films by combined raman and x-ray photoemission spectroscopy," *Journal of applied physics*, vol. 83, no. 7, pp. 3917–3919, 1998.

[205] H. G. Zanin, A. C. Peterlevitz, R. F. Teófilo, H. J. Ceragioli, and V. Baranauskas, "Synthesis and characterization of magnetic nanocrystalline diamond films," *Ferroelectrics*, vol. 436, no. 1, pp. 96–100, 2012.

[206] P. Niedziakowski, T. Ossowski, P. Ziba, A. Cirocka, P. Rochowski, S. Pogorzelski, J. Ryl, M. Sobaszek, and R. Bogdanowicz, "Poly-l-lysine-modified boron-doped diamond electrodes for the amperometric detection of nucleic acid bases," *Journal of Electroanalytical Chemistry*, vol. 756, pp. 84–93, 2015.

[207] Y. Kawabata, J. Taniguchi, and I. Miyamoto, "Xps studies on damage evaluation of single-crystal diamond chips processed with ion beam etching and reactive ion beam assisted chemical etching," *Diamond and related materials*, vol. 13, no. 1, pp. 93–98, 2004.

[208] Y. Fan, A. Fitzgerald, P. John, C. Troupe, and J. Wilson, "X-ray photoelectron spectroscopy studies of cvd diamond films," *Surface and Interface Analysis: An International Journal devoted to the development and application of techniques for the analysis of surfaces, interfaces and thin films*, vol. 34, no. 1, pp. 703–707, 2002.

[209] B.-E. Jun, C.-S. Kim, H.-K. Kim, J.-N. Kim, Y.-H. Hwang, and J.-S. Chae, "Ar-ion etching effects on the xps spectra of the ferroelectric potassium lithium niobate crystal," *J. Korean Phys. Soc*, vol. 46, pp. 100–103, 2005.

[210] W. Lau, L. Huang, I. Bello, Y. Yiu, and S.-T. Lee, "Modification of surface band bending of diamond by low energy argon and carbon ion bombardment," *Journal of applied physics*, vol. 75, no. 7, pp. 3385–3391, 1994.

[211] I.-Y. Jeon, H.-J. Choi, M. J. Ju, I. T. Choi, K. Lim, J. Ko, H. K. Kim, J. C. Kim, J.-J. Lee, D. Shin, *et al.*, "Direct nitrogen fixation at the edges of graphene nanoplatelets as efficient electrocatalysts for energy conversion," *Scientific reports*, vol. 3, p. 2260, 2013.

[212] N. W. Makau, *Foreign atoms on the three low index diamond surfaces*. PhD thesis, 2008.

[213] Z. Xing, Z. Ju, Y. Zhao, J. Wan, Y. Zhu, Y. Qiang, and Y. Qian, "One-pot hydrothermal synthesis of nitrogen-doped graphene as high-performance anode materials for lithium ion batteries," *Scientific reports*, vol. 6, p. 26146, 2016.

[214] S. W. G. Alexander V. Naumkin, Anna Kraut-Vass and C. J. Powell, "Nist x-ray photoelectron spectroscopy database." 2015, 09 2015.

[215] K. Yamamoto, Y. Koga, and S. Fujiwara, "Xps studies of amorphous sicn thin films prepared by nitrogen ion-assisted pulsed-laser deposition of sic target," *Diamond and related materials*, vol. 10, no. 9, pp. 1921–1926, 2001.

[216] D. Marton, K. Boyd, A. Al-Bayati, S. Todorov, and J. Rabalais, "Carbon nitride deposited using energetic species: a two-phase system," *Physical Review Letters*, vol. 73, no. 1, p. 118, 1994.

[217] A. Dementjev, A. De Graaf, M. Van de Sanden, K. Maslakov, A. Naumkin, and A. Serov, "X-ray photoelectron spectroscopy reference data for identification of the c3n4 phase in carbon–nitrogen films," *Diamond and related materials*, vol. 9, no. 11, pp. 1904–1907, 2000.

[218] R. Spits, J. Prins, and T. Deny, "A determination of the critical damage density required for "amorphisation" of ion-implanted diamond," *Nuclear Instruments and Methods in Physics Research Section B: Beam Interactions with Materials and Atoms*, vol. 85, no. 1-4, pp. 347–351, 1994.

[219] Q. Liang, C.-s. Yan, Y. Meng, J. Lai, S. Krasnicki, H.-k. Mao, and R. J. Hemley, "Enhancing the mechanical properties of single-crystal cvd diamond," *Journal of Physics: Condensed Matter*, vol. 21, no. 36, p. 364215, 2009.

[220] G. Sutherland, "Gbbm sutherland, de blackwell, and wg simeral, nature 174, 901 (1954)," *Nature*, vol. 174, p. 901, 1954.

[221] V. Malogolovets, A. Gontar, A. Vishnevskij, and V. Khivrich, "Optical and electric properties of monocrystalline synthetic diamond irradiated by neutrons," *Ukrainskij Fizicheskij Zhurnal*, vol. 23, no. 5, pp. 860–863, 1978.

[222] G. Bokii, G. Bezrukov, Y. A. Klyuev, A. Naletov, and V. Nepsha, "Natural and synthetic diamonds," *Science*, 1986.

[223] A. Dehbi-Alaoui, A. James, and A. Matthews, "A comparison of the properties of hard carbon films produced by direct gas deposition and plasma-assisted evaporation," in *Metallurgical Coatings and Thin Films 1990*, pp. 88–98, Elsevier, 1990.

[224] C. Wild, N. Heres, J. Wagner, P. Koidl, and T. Anthony, "Optical and structural characterization of cvd diamond," in *Proceedings of the First International Symposium on Diamond and Diamond-Like Film*, 1989.

[225] G. Janssen, W. Van Enckevort, W. Vollenberg, and L. Giling, "Characterization of single-crystal diamond grown by chemical vapour deposition processes," *Diamond Relat. Mater*, vol. 1, pp. 789–800, 1992.

[226] R. Erz, W. Dötter, K. Jung, and H. Ehrhardt, "Investigation of boron and hydrogen concentrations in p-type diamond films by infrared spectroscopy," *Diamond and related materials*, vol. 4, no. 4, pp. 469–472, 1995.

[227] F. Fuchs, C. Wild, K. Schwarz, and P. Koidl, "Hydrogen-related ir absorption in chemical vapour deposited diamond," *Diamond and related materials*, vol. 4, no. 5-6, pp. 652–656, 1995.

[228] A. T. Collins, "Intrinsic and extrinsic absorption and luminescence in diamond," *Physica B: Condensed Matter*, vol. 185, no. 1-4, pp. 284–296, 1993.

[229] V. Vavilov and A. Gippius, "Investigation of the cathodoluminescence of epitaxial diamond films," *Sov. Phys. Semicond.*, vol. 14, no. 9, pp. 1078–1079, 1980.

[230] J. Steeds, S. Charles, T. Davis, A. Gilmore, J. Hayes, D. Pickard, and J. Butler, "Creation and mobility of self-interstitials in diamond by use of a transmission electron microscope and their subsequent study by photoluminescence microscopy," *Diamond and related materials*, vol. 8, no. 1, pp. 94–100, 1999.

[231] J. Forneris, S. D. Tchernij, A. Tengattini, E. Enrico, V. Grilj, N. Skukan, G. Amato, L. Boarino, M. Jakšić, and P. Olivero, "Electrical control of deep nv centers in diamond by means of sub-superficial graphitic micro-electrodes," *Carbon*, vol. 113, pp. 76–86, 2017.

[232] P. Sullivan and R. Baragiola, "Ion beam induced luminescence in natural diamond," *Journal of applied physics*, vol. 76, no. 8, pp. 4847–4852, 1994.

[233] J. Won, A. Hatta, T. Ito, T. Sasaki, and A. Hiraki, "The investigation of defect formation in chemical vapor deposited diamond using photoluminescence by ultraviolet synchrotron radiation," *Applied physics letters*, vol. 69, no. 27, pp. 4179–4181, 1996.

[234] J. Ruan, W. Choyke, and W. D. Partlow, "Cathodoluminescence and annealing study of plasma-deposited polycrystalline diamond films," *Journal of applied physics*, vol. 69, no. 9, pp. 6632–6636, 1991.

[235] M. Kadri, D. Araujo, M. Wade, A. Deneuville, and E. Bustarret, "Effect of oxygen on the cathodoluminescence signal from excitons, impurities and structural defects in homoepitaxial (100) diamond films," *Diamond and related materials*, vol. 14, no. 3-7, pp. 566–569, 2005.

[236] A. T. Collins, M. Kamo, and Y. Sato, "A spectroscopic study of optical centers in diamond grown by microwave-assisted chemical vapor deposition," *Journal of Materials Research*, vol. 5, no. 11, pp. 2507–2514, 1990.

[237] J. Steeds. personal communication, 2018.

[238] W. Wang, T. Moses, R. C. Linares, J. E. Shigley, M. Hall, and J. E. Butler, "Gem-quality synthetic diamonds grown by a chemical vapor deposition (cvd) method," *Gems Gemol*, vol. 39, no. 4, pp. 268–83, 2003.

[239] P. M. Martineau, S. C. Lawson, A. J. Taylor, S. J. Quinn, D. J. Evans, and M. J. Crowder, "Identification of synthetic diamond grown using chemical vapor deposition (cvd)," *Gems & Gemology*, vol. 40, no. 1, pp. 2–25, 2004.

[240] T. B. Matindi, S. R. Naidoo, and O. M. Ntwaeaborwa, "Luminescence induced by no ion implantation into diamond," *Diamond and Related Materials*, vol. 96, pp. 11–19, 2019.

[241] J. Ruan, W. Choyke, and W. D. Partlow, "Cathodoluminescence and annealing study of plasma-deposited polycrystalline diamond films," *Journal of applied physics*, vol. 69, no. 9, pp. 6632–6636, 1991.

[242] L. Robins, L. Cook, E. Farabaugh, and A. Feldman, "Cathodoluminescence of defects in diamond films and particles grown by hot-filament chemical-vapor deposition," *Physical Review B*, vol. 39, no. 18, p. 13367, 1989.